RATIONAL DESIGN OF SEMICONDUCTOR HETEROSTRUCTURES FOR ENERGY CONVERSION

A Dissertation

by

JUNSANG CHO

Submitted to the Office of Graduate and Professional Studies of
Texas A&M University
in partial fulfillment of the requirements for the degree of

DOCTOR OF PHILOSOPHY

Chair of Committee,	Sarbajit Banerjee
Committee Members,	Marcetta Y. Darensbourg
	Xin Yan
	Miladin Radovic
Head of Department,	Simon North

December 2018

Major Subject: Chemistry

ABSTRACT

Increasing worldwide energy consumption has imposed strain on natural energy sources and given rise to an energy crisis on our society. The development of efficient solar energy conversion to augment other renewable energy approaches is one of the grand challenges in our time. Water splitting, or the disproportionation of H_2O into energy-dense fuels, H_2 and O_2, is undoubtedly a promising strategy. However, solar water splitting has been a long challenge in the scientific community since the process involves the concerted transfer of four electrons and four protons, which requires the synergistic operation of solar light harvesting, charge separation, mass and charge transport, and redox catalysis processes.

In the first thrust, we explore the development of tunable and programmable heterostructures comprised of $M_xV_2O_5$ nanowires (where M = Pb^{2+}, Sn^{2+}) and cadmium chalogenide quantum dots (QDs: CdS, CdSe, and CdTe) designed to extract photoexcited holes from the valence band of quantum dot to mid-gap state of $M_xV_2O_5$ nanowires to facilitate water oxidation at low overpotentials. Thermodynamic energetic band offsets and the relative band alignment of $M_xV_2O_5$/QD heterostructures have been studied by hard X-ray photoelectron spectroscopy and density functional theory, whereas the dynamics of charge transfer kinetics has been examined by ultrafast transient absorption spectroscopy. These heterostructures demonstrate the remarkable utility of stereoactive lone pairs of post-transition-metal (p-block) cations in mediating solar energy conversion by dint of precise tunability of their energy positioning.

In the second thrust, we develop an alternative palette of light harvesting semiconductors through the establishment of dimensional control over lead halide perovskites. The nucleation and growth processes are finely tuned with the help of added surface ligands in order to precisely control size and thus optical properties of the nanocrystals. Dimensional control is a key to engineering optical, electronic, and magnetic properties of materials owing to quantum confinement effects, selective elimination of symmetry elements, and the pronounced role of surface energy. Utilizing ligand-mediated synthetic approaches, such as ligand-assisted reprecipitation and hot colloidal methods, allows for control over nucleation/growth kinetics and consequently enables precise modulation of nanocrystal dimensions. In this dissertation, we have been successful at synthesizing precisely tunable 2D methylammonium lead bromide ($MAPbBr_3$) nanoplatelets by controlling the surface-capping ligands. Utilizing a variety of spectroscopic tools, we have derived mechanistic understanding and structure—function correlations of the role of surface-capping ligands in mediating the growth of all-inorganic 2D $CsPbBr_3$ nanoplatelets as a function of reaction temperature and concentration.

DEDICATION

There are many people who have inspired and guided me toward my success throughout my Ph.D. life and journey in chemistry at Texas A&M University. This dissertation is foremost dedicated to my loving wife Yujin Jeong, my bright son Nathan Geonwoo Cho, and my beautiful daughter Lauren Yeonwoo Cho, who have been always on my side at every single step of my graduate student life. I incredibly appreciate their endless love and support. This dissertation is also dedicated to my father, mother, and brother by my side as well as father-in-law, mother-in law, sister-in-law, and brother-in-law. Without their encouraging love and support, I could not finish this Ph.D. journey. Finally, thanks to all other friends and family.

ACKNOWLEDGEMENTS

First, I would like to thank my advisor, Prof. Sarbajit Banerjee, for the years of guidance, mentorship, and support of my Ph.D. research. His devotion toward nanoscience, his motivation and inspiration for nanochemistry, and his pursuit of immense knowledge has instilled in me a strong passion for science to perform at my best. Without him I would not be prepared for my career as a scientist.

I would also like to thank my committee members, Prof. Marcetta Y. Darensbourg, Prof. Xin Yan, and Prof. Miladin Radovic for their guidance and support throughout the course of this research. Over the years, I have been collaborating with several research groups. To this extent, I would like to express my gratitude to Prof. David F. Watson at the University at Buffalo, with whom I have been able to involve in many exciting projects for rational design of the next generation photocatalytists. I also want to thank Dr. Jin Ho at Los Alamos National Laboratory for the single particle photoluminescent emission measurements to physically resolve the energy-quantized emission of lead halide perovskite with different unit cell layer.

Thanks also goes to friends, colleagues, department faculty, and staff for making my time at Texas A&M University a great experience. Finally, thanks all the past and present Banerjee Group members for their support and friendship through my graduate career.

CONTRIBUTORS AND FUNDING SOURCES

Contributors

The work in this dissertation was guided by a dissertation committee comprised of Professor Sarbajit Banerjee (advisor), Professor Marcetta Y. Darensbourg, Professor Xin Yan of the Department of Chemistry and Professor Radovic Miladin of the Department of Materials Science and Engineering.

I acknowledge that much of the characterization and data in this dissertation is obtained using a variety instruments in Materials and Characterization Facilities (MCF) for UV/vis absorption spectroscopy and spectrofluorometer and Microscopy and Imaging Center (MIC) for scanning electron microscopy and transmission electron microscopy. Some of data in Chapter 5 was provided by the Center for Functional Nanomaterials (CFN) at Brookhaven National Laboratory (BNL) using ultrafast transient absorption spectroscopy with assistance from Dr. Matthew Y. Sfeir.

Some of characterization of Chapter 7 and mechanical testing measurements for cement samples was made possible by Dr. Kai-Wei (Victor) Liu at the Texas A&M Transportation Institute.

Funding Sources

This work in this dissertation was supported by National Science Foundation under DMREF 1627197 and additionally by Cenovus Energy, Inc.

.

TABLE OF CONTENTS

LIST OF FIGURES

Page

LIST OF TABLES

Page

CHAPTER I

INTRODUCTION AND MOTIVATION

I.1 Rational Design of Semiconductor Heterostructures

The catastrophic environmental impact of our reliance on geological deposits of hydrocarbons[1, 2] as our primary source of energy makes solar energy conversion arguably the greatest scientific and technological challenge of our generation.[3, 4] Solar-to-electrical energy conversion, using photovoltaics, is essential but insufficient. Variable insolation also necessitates the storage of solar energy through the generation of fuels.[3] Water splitting, or the disproportionation of H_2O into H_2 and O_2, is the most promising strategy, given that it yields hydrogen, a high-energy-density fuel that can be combusted to release energy, with water as the only byproduct (**Figure I. 1**).[3-5] Water splitting is fundamentally challenging, however, as it requires the concerted transfer of four electrons and four protons[4, 6] and necessitates remarkable synergy between thermodynamics and kinetics in a manner that is intuitively difficult to predict.

Water-splitting photocatalysts must promote the following processes: (1) absorption of the solar spectrum to yield electrons at potentials sufficiently negative to reduce protons and holes at potentials sufficiently positive to oxidize water, (2) separation of charges and accumulation at catalytic sites, (3) generation and separation of H_2 and O_2, and (4) transport of four equivalents of protons from the oxidation site to the reduction site (**Figure I. 2**). A single material or molecule that can mediate this entire sequence of light-harvesting, charge-transfer, and mass-transport processes may never be

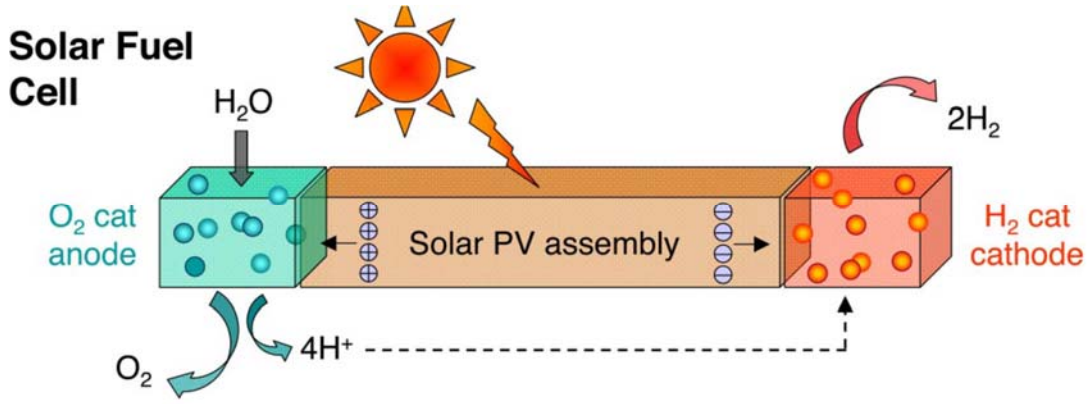

Figure I. 1 Photoelectrochemical cell for water splitting. Water is split into O_2 and H_2 upon solar radiation to solar photoelectrochemical cell assembly as four proton and four electrons are moving.[3] Reprinted with permission from Ref. 3. Copyright 2006 PNAS Science Journal.

identified. Instead, a promising strategy is to develop hybrid systems in which different components perform the various functions required to split water.[6, 7] This approach mimics photosynthesis, in which oxidation and reduction occur in separate photosystems with seamless "division of labor".

Semiconductor-based photocatalyst constructs have been investigated for decades[6]; however, real-world water-splitting applications have been precluded by poor light harvesting, inefficient redox catalysis, long-term instability, and high cost. The vexingly high overpotential of the water-oxidation half-reaction has often necessitated the use of wide-bandgap metal oxide semiconductors, with valence band-edge potentials up to 2 V positive of the water-oxidation potential, as photocatalysts.[6] Such materials are poor harvesters of visible light, and free energy is thrown away *via* the unnecessarily large driving force for water oxidation. Moreover, simple binary and ternary

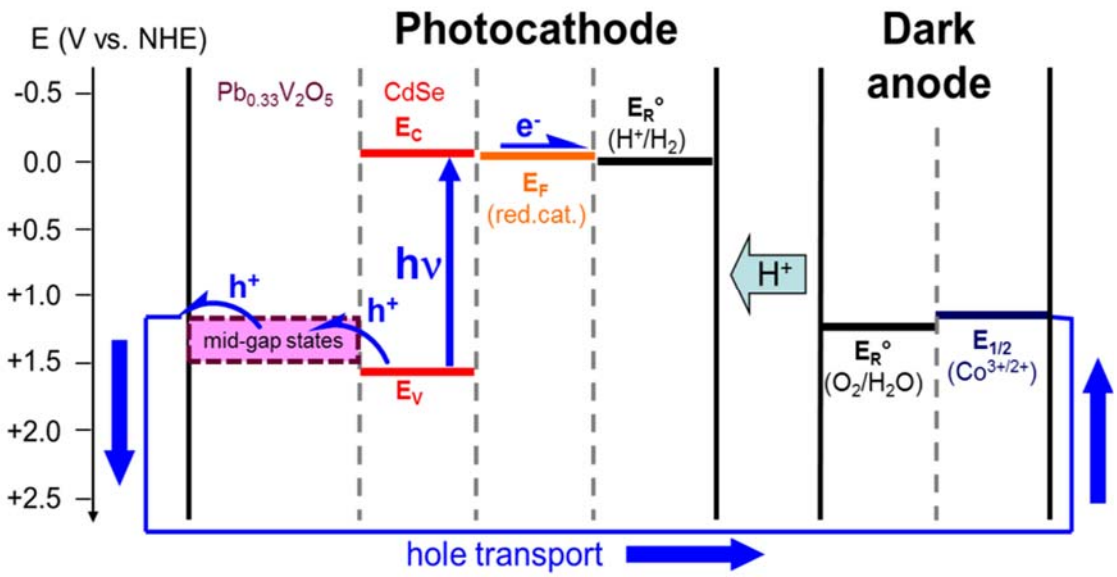

Figure I. 2 Water-splitting mechanism of proposed PECs with CdSe QDs and Pb0.33V2O5 NWs as a representative example. Holes are injected from photoexcited QDs to the NWs, then transported to the dark anode to oxidize water. Excited-state electrons are transferred to a reduction catalyst at which H_2 is evolved. The $Co^{3+/2+}$ potential corresponds to that of Nocera's catalyst.[5]

semiconductors such as TiO_2, SnO_2, WO_3, and $SrTiO_3$, which have traditionally been studied for photovoltaics and photocatalysis, exhibit clearly-defined valence and conduction band edges separated by a fixed bandgap. The ability to tune light-harvesting properties, electronic structure, and charge-transfer reactivity is thus immutably limited.

We have undertaken an alternative approach. Our effort involves the rational design of hybrid photocatalyst architectures exhibiting programmability of absorption spectra, interfacial electronic structure, energetic offsets, and thermodynamic driving forces for charge transfer.[8-10] These photocatalysts consist of single-crystalline $M_xV_2O_5$ nanowires (NWs), where M is an intercalated cation with stoichiometry defined by x,[11-13] functionalized with II-VI semiconductor quantum dots (QDs). Unique properties of

$M_xV_2O_5$/QD interfaces render them intriguing for incorporation into hybrid photocatalyst constructs. First, several examples of $M_xV_2O_5$ NWs possess mid-gap electronic states situated several hundred millivolts positive of the water-oxidation potential.[11-13] These states are derived not from defects or dopants but from the intrinsic crystal structure of the NWs and are reconfigurable by changing the specific intercalated cations in the open-framework structures.[13] Second, the energetic dispersion and occupancy of the mid-gap states of $M_xV_2O_5$ NWs are tunable through the stoichiometry and identity of the intercalating cation, whereas the potentials of excitonic and surface states of QDs are tunable through size, composition, and surface functionalization. These effects enable systematic control of light harvesting, driving forces for charge transfer, and interfacial electronic coupling. Third, $M_xV_2O_5$ NWs exhibit reversible mid-gap-state-mediated electrochemistry and are not susceptible to anodic corrosion.[9] Thus, these novel NW/QD heterostructures exhibit programmable absorption, charge-transfer, and charge-transport properties for photocatalysis. This strategy to involve intercalative mid-gap states in interfacial charge transfer while exploiting quantum confinement to tune charge-transfer reactivity represents a new approach to photocatalysis and solar energy conversion and yields a richly diverse design space that can be efficiently navigated using an iterative combination of theory and experiment as illustrated in **Figure I. 3.**

The accessible design space comprises a vast matrix of potential NW/QD heterostructures, differing in composition and interfacial properties, enabling broad tunability of electronic properties as well as both the thermodynamics and kinetics of excited-state charge transfer. Variables include the type of V_2O_5 framework (*e.g.*, single-

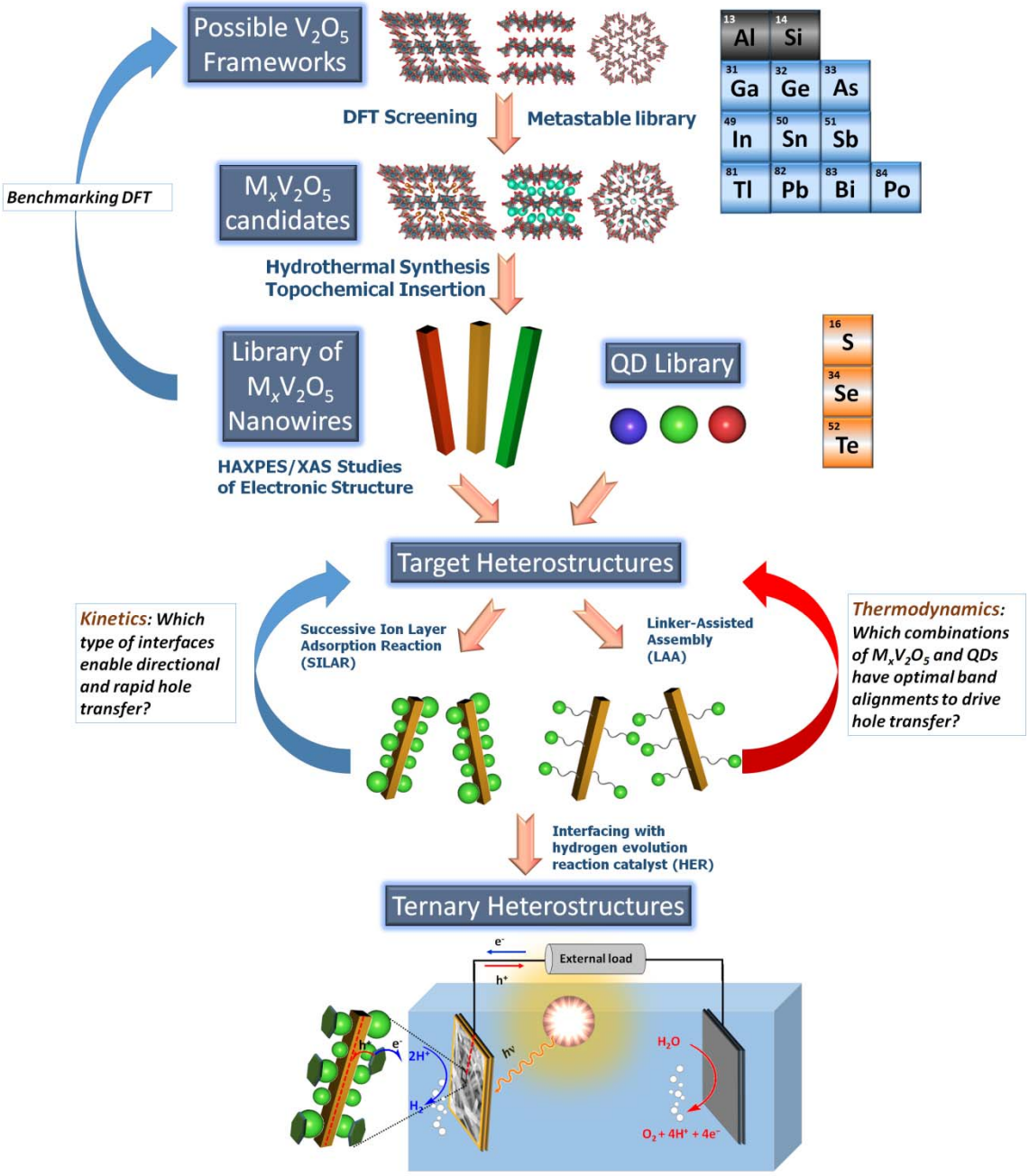

Figure I. 3 Schematic illustration of our strategy for the design and synthesis of $M_xV_2O_5$/QD heterostructures with programmable energetic offsets and kinetics of charge transfer that underpins our evolutionary approach to photocatalyst design. p-block cations are particularly of interest for positioning of states derived from filled s-subshells at the top of the valence band to facilitate hole extraction from photoexcited QDs. The integration of first-principles modeling, diversified material synthesis, interfacial functionalization, and analytics allows for effective exploitation of the opportunities for programmability available in the design space.

layered α- and γ'-, double-layered ε', and tunnel-structured ζ-phases)[14], the specific cation (M) that yields a mid-gap state, the stoichiometry (*x*) of the cation, the composition and size of QDs, and the nature of the interface between NWs and QDs (**Figure I. 3**). These variables provide tremendous versatility and are central to the development of heterostructures with programmable light harvesting, energetics, and charge transfer. However, the complexity of this multidimensional parameter space represents a daunting challenge, which complicates the prediction and rational design of interfacial energetic offsets and electronic coupling, as well as the rate constants of charge-transfer processes central to photocatalysis. This challenge is difficult to resolve using a purely Edisonian approach. Therefore, we are instead utilizing a predictive decision-making framework involving the iterative integration of theory and experiment to converge on optimal catalyst architectures (Figure I. 3).

In this introduction, we outline our evolutionary design scheme as well as summarize our computational and experimental research involving the synthesis of first-generation heterostructures consisting of β-$Pb_{0.33}V_2O_5$ NWs interfaced with cadmium chalcogenide QDs. The prediction and measurement of the electronic structure of such heterostructures is delineated, highlighting favorable energetic offsets for interfacial charge separation and the experimental characterization of their excited-state charge-transfer dynamics and photocatalytic performance. Additionally, we report on the theory-guided design of second-generation $Sn_xV_2O_5$/QD heterostructures with electronic structure programmed to engender excited-state charge transfer and photocatalysis. The programmability of this interfacial coupling approach epitomizes the versatility of

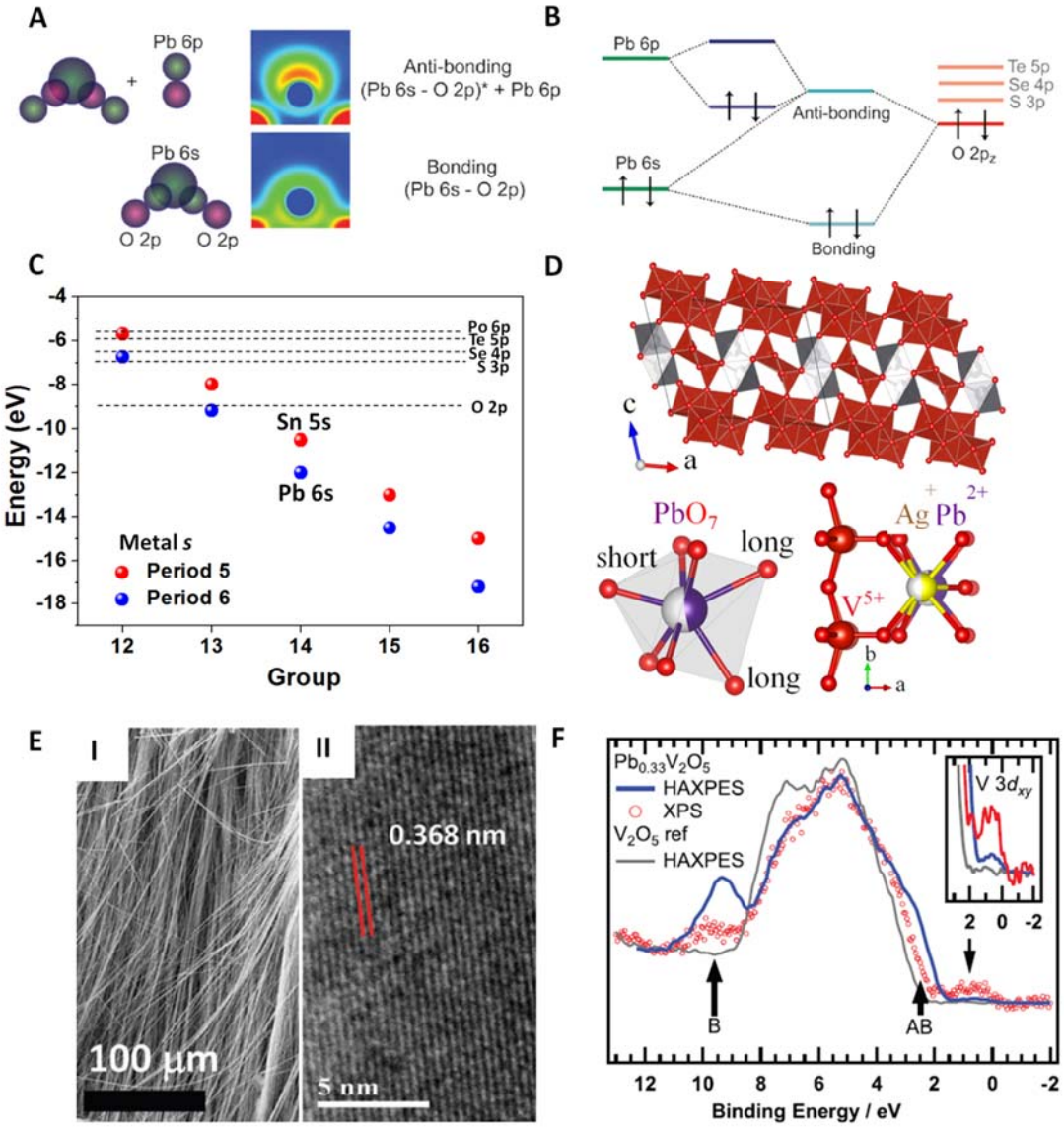

Figure I. 4 Mid-gap states derived from p-block cations. (A) Hybridization of p-block ns^2np^0 cations with anionic p-states as per the "revised lone pair model".[16] (B) Energy level diagram of cation s and anion p orbitals calculated from DFT (Kohn-Sham eigenvalues are depicted). (C) Comparison of the crystal structures of d-block β-$Ag_{0.33}V_2O_5$ and p-block β-$Pb_{0.33}V_2O_5$ indicating the lone-pair-induced distortion; (D) SEM and TEM images of β-$Pb_xV_2O_5$ nanowires; (E) HAXPES valence band spectra of β-$Pb_xV_2O_5$; (E) DFT calculation and HAXPES measurements at two different energies acquired for β-$Pb_xV_2O_5$. Panel (A,B) is reprinted and panel (C) is adapted with permission from ref 16. Copyright 2011 Royal Society of Chemistry; Panel (D,F) is reprinted with permission from ref 12. Copyright 2014 American Physical Society; Panel (E) is reprinted with permission from ref 11. Copy right 2013 Wiley-VCH.

$M_xV_2O_5$ frameworks and underscores the centrality of electronic structure design, achieved through integration of theory and electronic structure measurements, to facilitate the rational design of heterostructures and the systematic improvement of their properties and photocatalytic performance.

At the heart of our programmable design of electronic structure is the ability to reconfigure periodic $M_xV_2O_5$ solid-state compounds through facile topochemical methods.[14, 15] A variety of V_2O_5 frameworks can be stabilized with intercalated cations through hydrothermal synthesis; the energy positioning of the valence and conduction bands of these compounds is determined by the V—O connectivity and the local vanadium coordination environment, whereas the hybridization of the intercalated cations with the V_2O_5 frameworks gives rise to states with variable energy dispersion depending on the mode of interaction. The conduction band edges are typically V 3d in origin (with their specific splitting dictated by the vanadium coordination geometry and their resulting hybridization with O 2p states), whereas the valence band edges are primarily O 2p in origin.[15] The topochemical leaching of cations from $M_xV_2O_5$ at low temperatures stabilizes metastable V_2O_5 frameworks, many of which are located only slightly higher in energy as compared to the thermodynamically stable α-V_2O_5 phase. Tunnel-structured ζ-V_2O_5 and puckered layered γ'-V_2O_5 are two prominent examples of kinetically trapped compounds that are considerably modified in structure and covalency from the layered α-V_2O_5 phase[15]; the installation of entirely different cations within these frameworks through intercalation chemistry provides a powerful means of reconfiguring electronic structure and thereby energetic offsets in our photocatalytic

platform. Of particular interest for photocatalytic applications are the filled s-subshells of post-transition-metal cations with the $(n\text{-}1)d^{10}ns^2np^0$ electronic configuration (Figure I. 1), which have the potential to yield mid-gap states derived from their stereoactive lone pairs of electrons. Such states are typically positioned at the top of the valence band, where they can extract photogenerated holes from QDs if the appropriate energetic offsets can be established within heterostructures.

The filled s-subshell of p-block cations is manifested prominently in distinctive structural distortions of solid-state compounds, seen for example, in the litharge structures of SnO and PbO, which have historically been ascribed to a second-order Jahn—Teller effect mediated by the hybridization of cationic *ns* and *np* states.[17] A more recent view, the "revised lone pair model", derived from extensive quantum chemical calculations and X-ray emission spectroscopy measurements of the valence band structure paints a more complex picture. These filled subshells are not in fact inert in character and tend to be strongly hybridized with anion p-states giving rise to filled bonding and anti-bonding states as sketched in **Figure I. 4**.[16, 18] The antibonding states can further hybridize with empty cation np^0 states with a distortion of the local coordination geometry away from a centrosymmetric environment when the electronic stabilization thus derived offsets the destabilization resulting from coordinative undersaturation.[16] The projected electron density of the stabilized anti-bonding state has classical "lone pair" character[19] and is positioned at the top of the valence band. In order to have effective orbital overlap with cation 5p or 6p states, which is necessary to facilitate a pronounced distortion, a major constraint is that the hybrid antibonding

cation-s—anion-p-states must have substantial 5s/6s-character. In turn, this necessitates the effective mixing of the cation 5s/6s and anion p-states, the extent of which strongly diverges as a function of the anion electronegativity and resultant energy positioning of the anion-p states (Figure I. 2C).[16] Two important consequences that result from this constraint are that (a) oxides are considerably more amenable to pronounced lone pair effects as compared to chalcogenides (as a result of the sharp change in electronegativity and energy positioning of p-states in going from oxygen to sulfur) and that (b) $5s^2$ (Sn^{2+}) states that show the least differential in energy exhibit the most pronounced lone-pair distortions in oxides since $6s^2$ (Pb^{2+}) states are relegated to even lower energies as a result of relativistic effects. The order of stability of lone-pair distortions arising from anti-bonding states at the top of the valence band is predicted to follow: Sn>Pb>Sb>Bi>Te>Po.[16] Figure I. 2D shows the pronounced lone-pair-induced structural distortion observed around the intercalating cation in β-$Pb_xV_2O_5$ that is not observed in its d-block counterpart β-$Ag_xV_2O_5$. Figures I. 2E and F illustrate the pronounced anti-bonding and bonding states with considerable Pb 6s character observed by high-energy X-ray photoemission spectroscopy (HAXPES) measurements at the edge and deep valence band of β-$Pb_xV_2O_5$, respectively. The ability to modulate the energy positioning of the lone-pair states at the top of the valence band provides an important design tool for the construction of heterostructures whereby such states can be positioned to accept holes from interfaced photoexcited QDs.

The ability to access this design space is greatly facilitated by our recent discovery of topochemical extraction and intercalation methods wherein treatment with

acid or an appropriate oxidizing agent facilitates cation extraction from $M_xV_2O_5$ bronzes, stabilizing a metastable V_2O_5 framework that can be filled with other cations. As a remarkable demonstration of this approach, Ag-ions have been extracted from β-$Ag_{0.33}V_2O_5$ by acid treatment, stabilizing the metastable ζ-V_2O_5 phase with open 1D tunnels, which are subsequently filled with Mg-ions by reaction with di-*n*-butylmagnesium or by electrochemically magnesiation using a $Mg(TFSI)_2$ electrolyte to stabilize a β-$Mg_{0.33}V_2O_5$ phase inaccessible from direct synthesis.[20] Such an "etch-a-sketch" approach to swapping cations through intercalation chemistry provides unprecedented control over electronic structure of the hole acceptor and thereby facilitates tuning of energetic offsets within heterostructures (Figure I. 1).

In our proposed design, light harvesting by the II-VI QDs is immediately followed by charge separation on ultrafast timescales such that photoexcited electrons are extracted by a hydrogen evolution catalyst and used to reduce protons in aqueous media, whereas photogenerated holes are transferred to the abovementioned mid-gap states of $M_xV_2O_5$ nanowires for transport to a water oxidation catalyst. **Figure I. 5** illustrates two distinctive methods for the preparation of NW/QD heterostructures: (1) linker-assisted assembly (LAA)[21], in which bifunctional ligands tether colloidal QDs to NWs with the specific binding preferences explicable based on principles of hard-soft acid—base interactions and differences in surface potentials, and (2) successive ionic layer adsorption and reaction (SILAR)[22] wherein NWs are immersed sequentially into ionic precursor solutions of cadmium and chalcogenide precursors. The former method allows for well-defined preformed chalcogenide nanocrystals to be tethered to NWs with

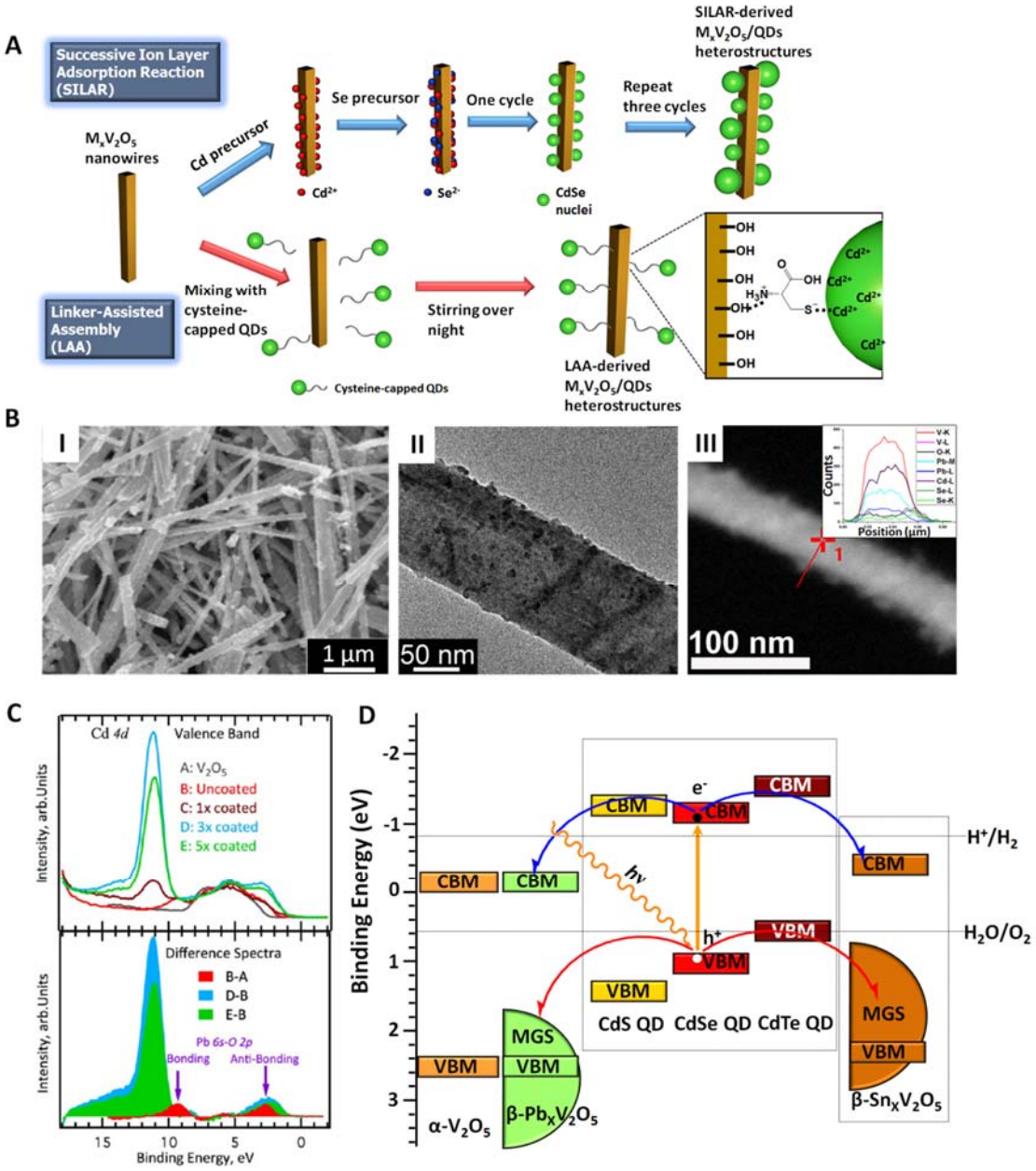

Figure I. 5 Synthetic strategies and energetic band offsets of $M_xV_2O_5$/QDs heterostructures. (A) Schematic illustration of SILAR and LAA routes for constructing $M_xV_2O_5$/QDs heterostructures; (B) SEM image for (I) SILAR-derived and (II) LAA-derived β-$Pb_xV_2O_5$/CdSe heterostructures, and (III) TEM image of SILAR-derived β-$Pb_xV_2O_5$/CdSe; (C) valence band spectra of β-$Pb_xV_2O_5$/CdSe heterostructures; (D) energetic offsets of $M_xV_2O_5$/QDs heterostructures illustrating the thermodynamic driving forces for charge transfer. Panel (B,C) are reprinted with permission from ref 8. Copyright 2015 American Chemical Society.

separations controllable by the chain lengths and functionalities of linker molecules.[21] Precise control of QD size and composition allows for tunability of light harvesting, whereas the ability to modulate the interfacial separation based on choice of molecular linker provides control over the dynamics of hole and electron transfer.[21] In turn, the SILAR method is facile and yields nanostructured chalcogenide QDs directly bonded through quasi-epitaxial interfaces with the NWs with thickness tunable by the number of SILAR cycles. **Figure I. 5B** illustrates scanning electron microscopy (SEM) and transmission electron microscopy (TEM) images of β-$Pb_{0.33}V_2O_5$/CdSe heterostructures. HAXPES measurements allow for delineation of energetic offsets and are shown for β-$Pb_{0.33}V_2O_5$/CdSe heterostructures in **Figure I. 5C**.

Holes generated in II-VI QDs upon photoexcitation relax to the valence band edges, which are comprised primarily of chalcogenide p-states. Concordant with Fajan's rules, the extent of mixing of cationic and anionic states is increased down a group, reflecting the relatively greater covalency of the heavier chalcogenide lattices.[23] As a result, the energy positioning of the p-states that constitute the valence band follows periodic trends in electronegativity as per: S > Se > Te.[24] The deeper valence-band edges of CdS are more optimally situated to facilitate hole transfer to mid-gap states of β-$Pb_xV_2O_5$ NWs and indeed represent our most successful first-generation heterostructures (**Figure I. 5D**). However, owing to their larger bandgap, these QDs are relatively inefficient at harvesting the solar spectrum[10] and furthermore there is a 0.48 eV barrier to hole transfer from the valence band edge to the mid-gap states of the β-$Pb_xV_2O_5$ NWs. Based on the considerations outlined above and the expected energy positioning of $5s^2$

states relative to $6s^2$ states sketched in Figure I. 4, β-$Sn_xV_2O_5$/QD heterostructures are anticipated to resolve both issues, allowing for thermodynamically favorable hole transfer from the valence band edges of CdS and CdSe QDs (Figure I. 3D) and further enabling utilization of CdTe QDs that are particularly efficient at harvesting the visible region of the solar spectrum in view of their smaller bandgap. An important additional lever to control driving forces for electron transfer to a HER catalyst arises from quantum confinement effects, which primarily modify the conduction band edges of QDs[25] but have relatively little influence on the valence band edges. In summary, the thermodynamic driving forces for electron and hole transfer are amenable to tuning in our heterostructures through variation of QD size, compositional modulation of the QD lattice, and the specific p-block cation selected for the NW component.

I.2 Efficient Light Harvesting with Type II Semiconductors Heterostructures

Harvesting solar energy and storing the energy in the chemical form or by generating electric current is of tremendous importance to modern technology given the predominant role of fossil fuels in the current economy.[26-28] For effective solar energy conversion, not only must a semiconductor absorb a large portion of the incident solar radiation but also the photoexcited electron−hole pairs must be further separated and transported across interfaces.[27, 29] Efficient charge separation and transport across interfaces is predicated on both thermodynamic energy offsets as well as the kinetics of charge transfer; based on Marcus theory considerations, the latter relies on the interfacial structure and distance as well the thermodynamic driving force or relative energetic

offset.[29-31] Charge separation, interfacial charge transfer, and transport from the interface must outcompete charge recombination to maximize conversion efficiencies. Recently, we have designed and developed reconfigurable β-$Pb_xV_2O_5$/QDs with programmable interfacial energetic offsets, wherein electron and hole charge carriers can be separated from direct photoexcitation.[8, 32] Desired charge transfer processes must outcompete with deleterious charge recombination pathways to improve a photocatalytic efficiency. Furthermore, this platform can be potentially used as ideal platform water splitting exploiting a distinctive feature in the electronic structure of ternary vanadium oxide bronzes: the presence of intrinsic midgap states, derived from the intercalating cations, which are situated between the valence-and conduction-band edges. The intrinsic mid-gap states derived from antibonding Pb 6s–O 2p interactions and are situated between the conduction and valence bands.[11, 33] There is a vast matrix of potential material compositions and interface structures that can be envisioned with some obvious variables being the specific cation (M) bearing a stereoactive lone pair, the stoichiometry (x) of the cation, the specific II-VI QDs, the size of the QDs, and the mode of coupling between the NWs and the QDs.[8, 12, 32, 34]

To increase charge carrier lifetimes (and facilitate more thermodynamic favorable charge transfer), controlling the energetic offsets within heterostructures is imperative since thermodynamics energetic band offsets can dictate interfacial charge transfer kinetics (**Figure I. 6**). The heterostructures with type II band alignment (staggered configuration) is more desirable rather than with type I band alignment

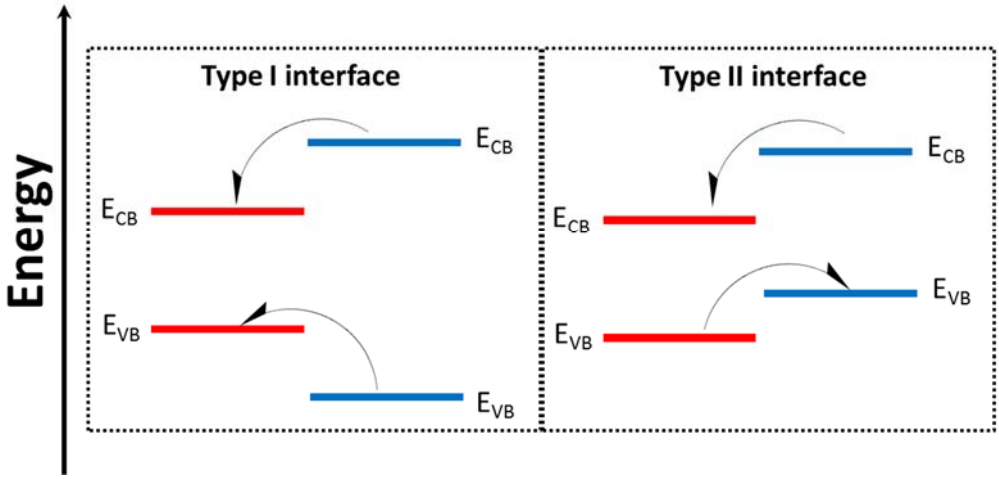

Figure I. 6 Energetic offset and relative band alignment of type I and type II interfaces. In type I interface, both electrons and holes are localized in a single component whereas in type II interface, electrons and holes are spatially separated.

(sandwiched configuration) as a result of excited-state charge separation and longer electron-hole lifetimes.[35, 36] Typically, in type I band alignment, both valence (VB) and conduction band (CB) of one component are entirely sandwiched by VB and CB of the other wider energy bandgap materials. As a result, excited-state electrons and holes are only localized in one of the component. However, in type II heterostructures, as depicted in **Figure I. 6,** the VB and CB edge of one component are staggered with the other component, located either lower or higher than the other component energy level. Type II energetic alignment thus facilitates spatial charge separation and localization of electrons and holes in different location; the hole is localized on the component with the higher (more negative) valence band edge, and the electron is localized on the component with the lower (more positive) conduction band edge. As a result of charge separation, type II configuration substantially increase carrier lifetimes by diminishing

radiative electron-hole recombination processes, thereby allowing carriers to be deployed for catalytic reactions.

I.3 Dimensional Control over Lead Halide Perovskite

Colloidal semiconductor quantum dots (QDs) have attracted tremendous research interest over the last two decades owing to their distinctive optical properties such as size-dependent photoluminescence emission, narrow band-edge absorption, and high quantum yields, which are derived from quantum confinement effects.[37, 38] Establishing precise dimensional control over these systems thus provides a means to tune their electronic, optical, and sometimes magnetic properties. The strong absorption cross-sections of QDs renders these materials intriguing candidates for harvesting of solar radiation but require the efficient separation of photoexcited holes and electrons.

While well-established chalcogenide nanocrystals have been used as the light-harvesting components of heterojunctions, they are plagued by numerous challenges such as a high density of trap states, poor overlap with the solar spectrum for sulfides and selenides, and tendency to stabilize defects such as stacking faults that deleteriously impact carrier transport. We have sought to expand an alternative palette of semiconductor nanocrystals based on remarkably defect tolerant cesium lead halides. In Chapters II—IV, we detail our efforts to establish compositional, dimensional, and morphological control through mechanistic understanding of the influence of added ligands.

Lead halide perovskites have attracted considerable research interests recently because they have emerged as the next generation of photovoltaics with efficiencies approaching 22.1% in 2016.[39, 40] Lead halide perovskites have ABX_3 crystal structure (where A = Cs^+, $CH_3NH_3^+$, $CH_2(NH_2)^+$; B = Sn^{2+}, Pb^{2+}; X = Cl^-, Br^-, I^-) and have been extensively studied over a couple of years since lead halide perovskite are a versatile class of materials with highly tunable optical and electronic properties through compositional and dimensional confinement (**Figure I. 7**).[41] The phase of ternary A-B-X perovskites are substantially invested in terms of ionic exchange reactions in monovalent "A", divalent "B", and "X" sites, respectively, as well as dimensional confinement as a result of quantum confinement effect. Apart from compositional variation in cationic or anionic sites, dimensional control is an alternative to engineering optical, electronic, and magnetic properties of materials owing to quantum confinement effects, selective elimination of symmetry elements, and the pronounced role of surface energy. Utilizing ligand-mediated synthetic approaches, such as ligand-assisted reprecipitation[42] and hot colloidal methods[43], allows for control over nucleation/growth kinetics and consequently enables precise modulation of nanocrystal dimensions.[44] Establishing precise dimensional control over these systems thus provides a means to tune their electronic, optical, and sometimes magnetic properties. The strong absorption cross-sections of lead halide perovskites renders these materials intriguing candidates for harvesting of solar radiation but require the efficient separation of photoexcited holes and electrons.

In the nanoscale regime, when the material size is decreased below the exciton Bohr radius (CdSe: 5.4 nm, $MAPbBr_3$: 2.5 nm, and $CsPbBr_3$: 3.5 nm), the optical and

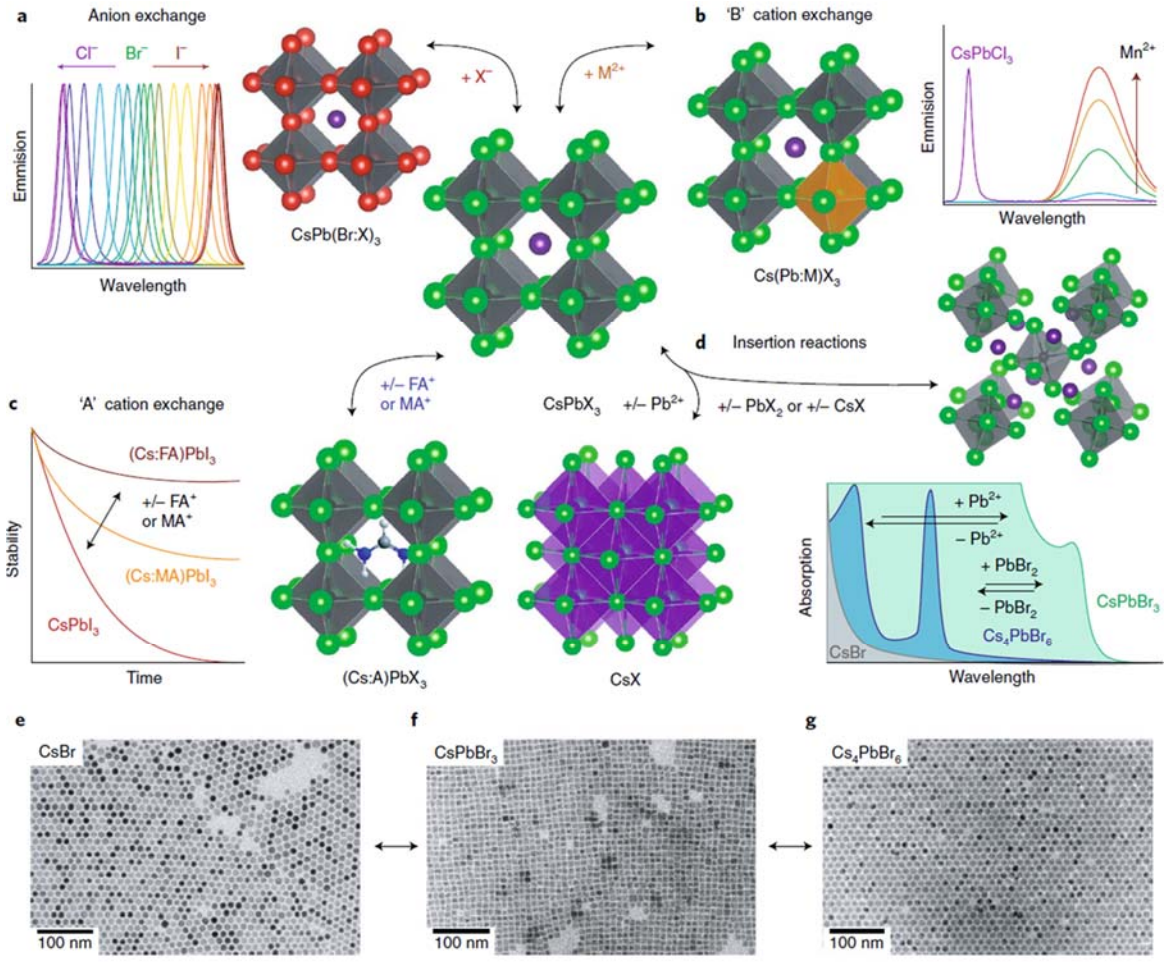

Figure I. 7 Structural and compositional modulation of lead halide perovskites. (A) Anion exchange exchange by changing 'X' halide anion (B) 'B' cation exchange reaction (C) 'A' cation exchange eraction (D) Phase transformation from $CsPbX_3$ to Cs_4PbX_6 and CsX via reactions with Pb^{2+} or PbX_2. (E–G) TEM images of nanocrystals obtained through the phase transformations in the ternay Cs–Pb–Br compounds. Reprinted with permission from ref. 41. Copyright 2018 Nature Publishing Group.

electronic properties are drastically altered as a result of quantum confinement effects wherein electron and hole wavefunctions are three-dimensionally confined in 0D nanocrystals.[37, 38, 41] Surface-capping ligands are generally used to establish synthetic control over nanocrystal dimensions. The ligand-mediated synthesis of nanocrystals has been intensively studied since initial reports of the colloidal synthesis of CdSe quantum

dots in 1993.[45] In a similar manner, perovskite nanocrystals are rapidly precipitated and crystallized through ligand-mediated synthesis wherein the surface-capping ligands can play a crucial role in mediating the extent of supersaturation and confining the layer-by-layer crystal growth of nanoplatelets by binding to the basal planes of $PbBr_6$ corner-sharing nanoplatelets.[42, 43, 46] Mechanistic elucidation of the role of surface-capping ligands is imperative to precisely modulate nanocrystal dimensions and will be the focus of the Chapter II—III.

I.4 References

(1) Su, J.; Vayssieres, L., A Place in the Sun for Artificial Photosynthesis? *ACS Energy Lett.* **2016,** 1, 121-135.

(2) Takanabe, K., Photocatalytic Water Splitting: Quantitative Approaches toward Photocatalyst by Design. *ACS Catal.* **2017,** 7, 8006-8022.

(3) Lewis, N. S.; Nocera, D. G., Powering the planet: Chemical challenges in solar energy utilization. *Proc. Natl. Acad. Sci.* **2006,** 103, 15729-15735.

(4) Cook, T. R.; Dogutan, D. K.; Reece, S. Y.; Surendranath, Y.; Teets, T. S.; Nocera, D. G., Solar energy supply and storage for the legacy and nonlegacy worlds. *Chem. Rev.* **2010,** 110, 6474-6502.

(5) Kanan, M. W.; Yano, J.; Surendranath, Y.; Dinca, M.; Yachandra V. K.; Nocera, D. G., Structure and Valency of a Cobalt−Phosphate Water Oxidation Catalyst Determined by in Situ X-ray Spectroscopy. *J. Am. Chem. Soc.* **2010**, 132, 13692-13701

(6) Sun, J.; Zhong, D. K.; Gamelin, D. R., Composite photoanodes for photoelectrochemical solar water splitting. *Energ. Environ. Sci.* **2010,** 3, 1252-1261.

(7) Selinsky, R. S.; Ding, Q.; Faber, M. S.; Wright, J. C.; Jin, S., Quantum dot nanoscale heterostructures for solar energy conversion. *Chem. Soc. Rev.* **2013,** 42, 2963-2985.

(8) Pelcher, K. E.; Milleville, C. C.; Wangoh, L.; Chauhan, S.; Crawley, M. R.; Marley, P. M.; Piper, L. F.; Watson, D. F.; Banerjee, S., Integrating β-$Pb_{0.33}V_2O_5$ Nanowires with CdSe Quantum Dots: Toward Nanoscale Heterostructures with Tunable Interfacial Energetic Offsets for Charge Transfer. *Chem. Mater.* **2015,** 27, 2468-2479.

(9) Milleville, C. C.; Pelcher, K. E.; Sfeir, M. Y.; Banerjee, S.; Watson, D. F., Directional Charge Transfer Mediated by Mid-Gap States: A Transient Absorption Spectroscopy Study of CdSe Quantum Dot/β-$Pb_{0.33}V_2O_5$ Heterostructures. *J. Phys. Chem. C* **2016,** 120, 5221-5232.

(10) Pelcher, K. E.; Milleville, C. C.; Wangoh, L. W.; Cho, J.; Sheng, A.; Chauhan, S.; Sfeir, M. Y.; Piper, L. F.; Watson, D. F.; Banerjee, S., Programming Interfacial Energetic Offsets and Charge Transfer in β-$Pb_{0.33}V_2O_5$/Quantum-Dot Heterostructures: Tuning Valence Band Edges to Overlap with Midgap States. *J. Phys. Chem. C* **2016**, 28992-29001.

(11) Marley, P. M.; Stabile, A. A.; Kwan, C. P.; Singh, S.; Zhang, P.; Sambandamurthy, G.; Banerjee, S., Charge Disproportionation and Voltage-Induced Metal–Insulator Transitions Evidenced in β-PbxV2O5 Nanowires. *Adv. Funct. Mater.* **2013,** 23, 153-160.

(12) Wangoh, L.; Marley, P.; Quackenbush, N.; Sallis, S.; Fischer, D.; Woicik, J.; Banerjee, S.; Piper, L., Electron lone pair distortion facilitated metal-insulator transition in β-$Pb_{0.33}V_2O_5$ nanowires. *Appl. Phys. Lett.* **2014,** 104, 182108.

(13) Marley, P. M.; Abtew, T. A.; Farley, K. E.; Horrocks, G. A.; Dennis, R. V.; Zhang, P.; Banerjee, S., Emptying and filling a tunnel bronze. *Chem. Sci.* **2015,** 6, 1712-1718.

(14) De Jesus, L. R.; Andrews, J. L.; Parija, A.; Banerjee, S., Defining Diffusion Pathways in Intercalation Cathode Materials: Some Lessons from V_2O_5 on Directing Cation Traffic. *ACS Energy Lett.* **2018,** 3, 915-931.

(15) Parija, A.; Waetzig, G. R.; Andrews, J. L.; Banerjee, S., Traversing Energy Landscapes Away from Equilibrium: Strategies for Accessing and Utilizing Metastable Phase Space. *J. Phys. Chem. C* **2018**.

(16) Walsh, A.; Payne, D. J.; Egdell, R. G.; Watson, G. W., Stereochemistry of post-transition metal oxides: revision of the classical lone pair model. *Chem. Soc. Rev.* **2011,** 40, 4455-4463.

(17) Orgel, L. E., 769. The stereochemistry of B subgroup metals. Part II. The inert pair. *J. Chem. Soc.* **1959**, 3815-3819.

(18) Fabini, D. H.; Laurita, G.; Bechtel, J. S.; Stoumpos, C. C.; Evans, H. A.; Kontos, A. G.; Raptis, Y. S.; Falaras, P.; Van der Ven, A.; Kanatzidis, M. G., Dynamic Stereochemical Activity of the Sn^{2+} Lone Pair in Perovskite $CsSnBr_3$. *J. Am. Chem. Soc.* **2016,** 138, 11820-11832.

(19) Stoltzfus, M. W.; Woodward, P. M.; Seshadri, R.; Klepeis, J.-H.; Bursten, B., Structure and bonding in $SnWO_4$, $PbWO_4$, and $BiVO_4$: lone pairs vs inert pairs. *Inorg. Chem.* **2007,** 46, 3839-3850.

(20) Andrews, J. L.; Mukherjee, A.; Yoo, H. D.; Parija, A.; Marley, P. M.; Fakra, S.; Prendergast, D.; Cabana, J.; Klie, R. F.; Banerjee, S., Reversible Mg-Ion Insertion in a Metastable One-Dimensional Polymorph of V_2O_5. *Chem* **2018,** 4, 564-585.

(21) Watson, D. F., Linker-Assisted Assembly and Interfacial Electron-Transfer Reactivity of Quantum Dot−Substrate Architectures. *J. Phys. Chem. Lett.* **2010,** 1, 2299-2309.

(22) Li, J. J.; Wang, Y. A.; Guo, W.; Keay, J. C.; Mishima, T. D.; Johnson, M. B.; Peng, X., Large-scale synthesis of nearly monodisperse CdSe/CdS core/shell nanocrystals using air-stable reagents via successive ion layer adsorption and reaction. *J. Am. Chem. Soc.* **2003,** 125, 12567-12575.

(23) Swesi, A. T.; Masud, J.; Liyanage, W. P.; Umapathi, S.; Bohannan, E.; Medvedeva, J.; Nath, M., Textured $NiSe_2$ Film: Bifunctional Electrocatalyst for Full Water Splitting at Remarkably Low Overpotential with High Energy Efficiency. *Sci. Rep.* **2017,** 7, 2401.

(24) Chen, E. M.; Stoyko, S. S.; Aitken, J. A.; Poudeu, P. F. P., Tuning the optical, electronic and thermal properties of $Cu_3NbS_{4-x}Se_x$ through chemical substitution. *Inogr. Chem. Front.* **2017,** 4, 1493-1500.

(25) Lee, J. R.; Meulenberg, R. W.; Hanif, K. M.; Mattoussi, H.; Klepeis, J. E.; Terminello, L. J.; van Buuren, T., Experimental observation of quantum confinement in the conduction band of CdSe quantum dots. *Phys. Rev. Lett.* **2007,** 98, 146803.

(26) Grätzel, M., Photoelectrochemical cells. *Nature* **2001,** 414, 338-344.

(27) Kamat, P. V., Quantum dot solar cells. The next big thing in photovoltaics. *J. Phys. Chem. Lett.* **2013,** 4, 908-918.

(28) Nocera, D. G., The artificial leaf. *Acc. Chem. Res.* **2012,** 45, 767-776.

(29) Bridewell, V. L.; Alam, R.; Karwacki, C. J.; Kamat, P. V., CdSe/CdS Nanorod Photocatalysts: Tuning the Interfacial Charge Transfer Process through Shell Length. *Chem. Mater.* **2015,** 27, 5064-5071.

(30) Goodman, S. M.; Singh, V.; Ribot, J. C.; Chatterjee, A.; Nagpal, P., Multiple Energy Exciton Shelves in Quantum-Dot–DNA Nanobioelectronics. *J. Phys. Chem. Lett.* **2014,** 5, 3909-3913.

(31) Nagpal, P.; Klimov, V. I., Role of mid-gap states in charge transport and photoconductivity in semiconductor nanocrystal films. *Nat. Commun.* **2011,** 2, 486.

(32) Milleville, C. C.; Pelcher, K. E.; Sfeir, M. Y.; Banerjee, S.; Watson, D. F., Directional Charge Transfer Mediated by Mid-Gap States: A Transient Absorption Spectroscopy Study of CdSe Quantum Dot/β-$Pb_{0.33}V_2O_5$ Heterostructures. *J. Phys. Chem. C* **2016,** 120, 5221-5232.

(33) Yamauchi, T.; Ueda, H.; Ueda, Y.; Kikuchi, J., Rich phase transitions under pressure in β-$A_{0.33}V_2O_5$ (A= Ca and Pb). *Physica C: Superconductivity and its applications* **2007,** 460, 532-533.

(34) Pelcher, K. E.; Milleville, C. C.; Wangoh, L. W.; Cho, J.; Sheng, A.; Chauhan, S.; Sfeir, M. Y.; Piper, L. F.; Watson, D. F.; Banerjee, S., Programming Interfacial

Energetic Offsets and Charge Transfer in β-$Pb_{0.33}V_2O_5$/Quantum-Dot Heterostructures: Tuning Valence Band Edges to Overlap with Midgap States. *J. Phys. Chem. C* **2016**.

(35) Kamat, P. V., Meeting the Clean Energy Demand: Nanostructure Architectures for Solar Energy Conversion. *J. Phys. Chem. C* **2007,** 111, 2834-2860.

(36) Baxter, J. B.; Richter, C.; Schmuttenmaer, C. A., Ultrafast Carrier Dynamics in Nanostructures for Solar Fuels. *Ann. Rev. Phys. Chem.* **2014,** 65, 423-447.

(37) Kovalenko, M. V.; Manna, L.; Cabot, A.; Hens, Z.; Talapin, D. V.; Kagan, C. R.; Klimov, V. I.; Rogach, A. L.; Reiss, P.; Milliron, D. J., Prospects of nanoscience with nanocrystals. *ACS Nano* **2015,** 9, 1012–1057.

(38) Talapin, D. V.; Lee, J.-S.; Kovalenko, M. V.; Shevchenko, E. V., Prospects of colloidal nanocrystals for electronic and optoelectronic applications. *Chem. Rev.* **2009,** 110, 389-458.

(39) Zhou, H.; Chen, Q.; Li, G.; Luo, S.; Song, T.-b.; Duan, H.-S.; Hong, Z.; You, J.; Liu, Y.; Yang, Y., Interface engineering of highly efficient perovskite solar cells. *Science* **2014,** 345, 542-546.

(40) Yang, W. S.; Noh, J. H.; Jeon, N. J.; Kim, Y. C.; Ryu, S.; Seo, J.; Seok, S. I., High-performance photovoltaic perovskite layers fabricated through intramolecular exchange. *Science* **2015,** 348, 1234-1237.

(41) Akkerman, Q. A.; Raino, G.; Kovalenko, M. V.; Manna, L., Genesis, challenge and opportunities for colloidal lead halide perovskite nanocrystals. *Nat. Mater.* **2018**, 17, 395–405.

(42) Zhang, F.; Zhong, H.; Chen, C.; Wu, X.-g.; Hu, X.; Huang, H.; Han, J.; Zou, B.; Dong, Y., Brightly Luminescent and Color-Tunable Colloidal $CH_3NH_3PbX_3$ (X = Br, I, Cl) Quantum Dots: Potential Alternatives for Display Technology. *ACS Nano* **2015,** 9, 4533-4542.

(43) Schmidt, L. C.; Pertegás, A.; González-Carrero, S.; Malinkiewicz, O.; Agouram, S.; Mínguez Espallargas, G.; Bolink, H. J.; Galian, R. E.; Pérez-Prieto, J., Nontemplate Synthesis of $CH_3NH_3PbBr_3$ Perovskite Nanoparticles. *J. Am. Chem. Soc.* **2014,** 136, 850-853.

(44) Cho, J.; Choi, Y.-H.; O'Loughlin, T. E.; De Jesus, L.; Banerjee, S., Ligand-Mediated Modulation of Layer Thicknesses of Perovskite Methylammonium Lead Bromide Nanoplatelets. *Chem. Mater.* **2016,** 28, 6909-6916.

(45) Murray, C.; Norris, D. J.; Bawendi, M. G., Synthesis and characterization of nearly monodisperse CdE (E= sulfur, selenium, tellurium) semiconductor nanocrystallites. *J. Am. Chem. Soc.* **1993,** 115, 8706-8715.

(46) Akkerman, Q. A.; D'Innocenzo, V.; Accornero, S.; Scarpellini, A.; Petrozza, A.; Prato, M.; Manna, L., Tuning the Optical Properties of Cesium Lead Halide Perovskite Nanocrystals by Anion Exchange Reactions. *J. Am. Chem. Soc.* **2015,** 137, 10276-10281.

CHAPTER II

LIGAND-MEDIATED MODULATION OF LAYER THICKNESSES OF METHYLAMMONIUM LEAD BROMIDE NANOPLATELETS*

II.1 Introduction

Organic metal halide perovskites with the composition ABX_3 (where A is a short-chain alkylammonium cation; B is a main-group, usually divalent, metal cation; and X is a halide anion), have been heralded as being transformative for the next generation of photovoltaic devices given the outstanding device efficiencies that are accessible even with solution-cast thin films.[1-5] These materials show exceptional promise as semiconductors and are characterized by high diffusion lengths, small exciton binding energies, and long-lived as well as high-quantum-yield photoluminescence.[6-8] Such properties have further led to interest in these materials for applications in light-emitting diodes (LEDs) and electroluminescent (EL) devices.[9, 10] The band gap, exciton binding energy, and absorption cross-section of these materials are tunable to some extent by partial or complete substitution of the A, B, and X sites with analogous cations or anions albeit it is worth noting that unlike oxide perovskites, the lower charge of the halide anions constrain the oxidation states and ionic radii permissible at the B site (for instance, entirely excluding transition metals).[11-15] The A site is furthermore sensitive to size as well as charge distribution constraints and is thus far restricted to Cs^+, $CH_3NH_3^+$,

*Reprinted with permission from "Ligand-Mediated Modulation of Layer Thicknesses of Perovskite Methylammonium Lead Bromide Nanoplatelets" by J. Cho, Y-H. Choi, T. E. O'Loughlin, L. D. Jesus, S. Banerjee, *Chem Mater,* 2016, **28**, 6909-6916.

and $HC(NH)_2^+$. [15-17] As with other semiconductors, dimensional confinement in proximity of the Böhr radius (estimated to be in the range of 1.36—2 nm[18-20] for these materials) provides an important additional means of tuning the energy positioning and separation of conduction and valence band edges and thus optical and electronic properties.

As polar extended solids, perovskite organic lead halides are readily crystallized from solvent mixtures containing the constituent ions.[15, 21] The use of capping ligands, analogous to methods deployed in the synthesis of colloidal quantum dots, has gained increasing prominence as a means of dimensionally confining crystal growth.[22-24] For instance, Schmidt *et al.* have reported the preparation of 0D colloidal methylammonium lead bromide ($MAPbBr_3$) nanocrystals that are ca. 6 nm in diameter using octyl- or octadecyl-alkylammonium ions as capping ligands.[25, 26] As a result of the larger steric footprint of longer alkyl chain (R) quaternary ammonium salts and their specific charge distribution, such cations are unable to occupy the A sites of ABX_3 perovskites and instead stabilize layered perovskites with the structure $(RNH_3)_2PbI_4$.[27-29] The addition of mixed ligands, for instance, methylammonium and long chain alkylammonium ligands results in segregation of the capping ligands such that the former is incorporated within the crystal structure, whereas the latter serves as the terminating layer where it is electrostatically bound to sheets of corner-shared $PbBr_6$ octahedra. As an example of this approach, a ligand-assisted reprecipitation method has been developed wherein the addition of octylamine facilitates the stabilization of colloidal $MAPbX_3$ perovskite nanocrystals exhibiting photoluminescence quantum yields of up to 70%.[30, 31] Recently,

surface termination with long-chain alkylammonium cations has been utilized in the synthesis of quasi-2D perovskite nanoplatelets with a layered structure; the 2D morphology allows for modulation of the extent of quantum confinement along the vertical direction depending on the number of layers and holds great potential for fabrication of colloidal analogs of epitaxally grown 2D quantum well architectures.[32-35] Depending on the relative ratios of $CH_3NH_3^+$ and the long-chain alkylammonium cations, the proportion of interior unit cells incorporating the former and terminal surface planes binding the latter can be modulated to obtain nanoplatelets that span no more than unit cell (of $MAPbBr_3$) in thickness with the longer chain capping ligands electrostatically bound on both sides of the platelets. The 2D nanoplatelets show increased exciton binding energies, decreased photoluminescence decay times, and improved absorption cross-sections.[28, 36-38] Particularly striking and distinctive thickness-dependent optical properties are observed for 2D platelets that are confined to being one- or two unit cells thick, which have dimensions below the Böhr radius, and are thus within the strongly quantum confined regime in terms of their vertical dimensions. [28, 38] While several synthetic and fractionation protocols to prepare phase-pure samples of few-layered thick nanoplatelets have become available[18], mechanistic understanding of the factors affecting nucleation and growth have thus far not been elucidated.

In this paper, we demonstrate that tuning the chain length and concentration of the longer chain alkylammonium cation in ligand-assisted reprecipitation allows for fine modulation of the stacking of $MAPbBr_3$ nanosheets. The vertical oligomerization of the nanosheets is directly correlated to diffusion constants of the alkylammonium species

and allows for broad tunability of optical absorption and emission features in the range of 430—520 nm.

II.2 Experimental

Synthesis of 2D $MAPbBr_3$ perovskite nanoplatelets. Methylammonium lead bromide nanoplatelets were prepared by modifying a previously published ligand-assisted reprecipitation method.[31] Briefly, a precursor solution was prepared by dissolving 0.016 mmol of CH_3NH_3Br and 0.016 mmol of $PbBr_2$ in 1 mL of DMF (a good solvent for the perovskite organic metal halides) and mixing in 0.5 mL of oleic acid and the appropriate amount of alkylamine (RA). Alkylamines with different alkyl chain lengths were employed such as BA (C4), HA (C6), OA (C8), DA (C12), and OLAm (C18). The MA:Pb ratio was kept constant at 1:1, whereas the MA:RA ratio was varied in the range between 1:0.5 to 1:8. Next, the precursor solution was rapidly added into 10 mL of toluene (a poor solvent for the polar perovskite organic metal halides) under vigorous stirring resulting in stabilization of a precipitate. The precipitate was collected by centrifugation at 10—15k rpm for 10 min and then resuspended in toluene solution. Three such centrifugation and resuspension cycles were used to obtain a colloidal dispersion of the nanoplatelets in toluene for further characterization.

Characterization. Powder X-ray diffraction (XRD) measurements were performed using a Bruker D8-Focus Bragg-Brentano X-ray Powder Diffractometer with a Cu Kα radiation source (λ = 1.5418 Å). Powder XRD data was acquired in the range of 10—60°. Bright-field transmission electron microscopy (TEM) images were obtained using a

JEOL JEM-2010 instrument operated at an accelerating voltage of 200 kV; high-resolution TEM (HRTEM) images were obtained using a FEI Tecnai G2 F20 ST instrument operating at 200 kV. Field emission scanning electron microscopy (FE-SEM) images were acquired using a JEOL JSM-7500F instrument at an accelerating voltage at 10 kV. Atomic force microscopy (AFM) images were acquired using a Bruker Dimension Icon instrument using silicon tips in tapping mode. Small angle X-ray scattering (SAXS) measurements were performed using a Rigaku S-Max3000 Pinhole SAXS Camera. UV-Vis absorption spectra were measured using a Hitachi U-4100 UV-Vis-NIR spectrophotometer, whereas photoluminescence spectra were obtained using a Horiba PTI Quanta-Master series spectrofluorometer with a Xenon arc lamp as the source and a photomultiplier tube (PMT) as the detector.

Calculation of Diffusion Coefficients. Diffusion coefficients of various alkylamine (C4, C6, C8, C12, and C18) were calculated as per:[39]

$$\boldsymbol{D = \frac{kT}{6\pi\eta a}\ln\left(\frac{2a}{b}\right)\ldots} \qquad \text{(II. 1)}$$

where D is the diffusion coefficient, k_B is Boltzmann's constant, T is the absolute temperature, η is the viscosity of the solvent, a is the radius of long axis, and b is radius of short axis of freely rotating prolate ellipsoids of the alkylamine. The dimensions were calculating from molecular models of the amines constructed using the Avogadro molecular modeling package.[40] The viscosity was extrapolated from experimentally determined values measured for DMF (0.92 cP) and toluene (0.59 cP) at room

temperature. A 1:10 stoichiometry ratio of DMF:toluene was used to calculate the values shown in Figure II. 1b.

II.3 Results and Discussion

As a polar solvent, DMF is able to dissolve all of the precursors; however, addition of the precursor solution to non-polar toluene at room temperature immediately induces precipitation and crystallization of $MAPbBr_3$ as indicated by the incipient turbidity of the solvent mixture. The $MAPbBr_3$ crystals are formed immediately at room temperature and thus nucleation and growth of the precursors is not well separated in time.[41, 42] However, the long chain RA ligands clearly influence the morphology and layer thicknesses of the obtained nanoplatelets. As noted above, the thinnest platelets that can be stabilized are only one unit cell thick; the strong exciton binding energy of these systems partially counteracts the effects of quantum confinement and such monolayer (n = 1) species have been reported to exhibit a characteristic photoluminescence emission maximum at 427 nm and a sharp excitonic absorption feature blue-shifted by a small Stokes shift.[18] The spectral signatures are red-shifted stepwise by discrete energies with increasing number of layers (n = 2, 3, 4, etc.) up until the bulk limit ($n = \infty$) characterized by a photoluminescence emission maximum at 519 nm and an absorption onset of 528 nm.[18, 43] These well-established thickness-dependent spectral signatures of few-layered $MAPbBr_3$ thus enable mapping of the layer thicknesses of the prepared materials as a function of the concentration and chain length of the long chain alkylammonium groups, which in turn can be correlated to the extent of supersaturation of the precursors in the

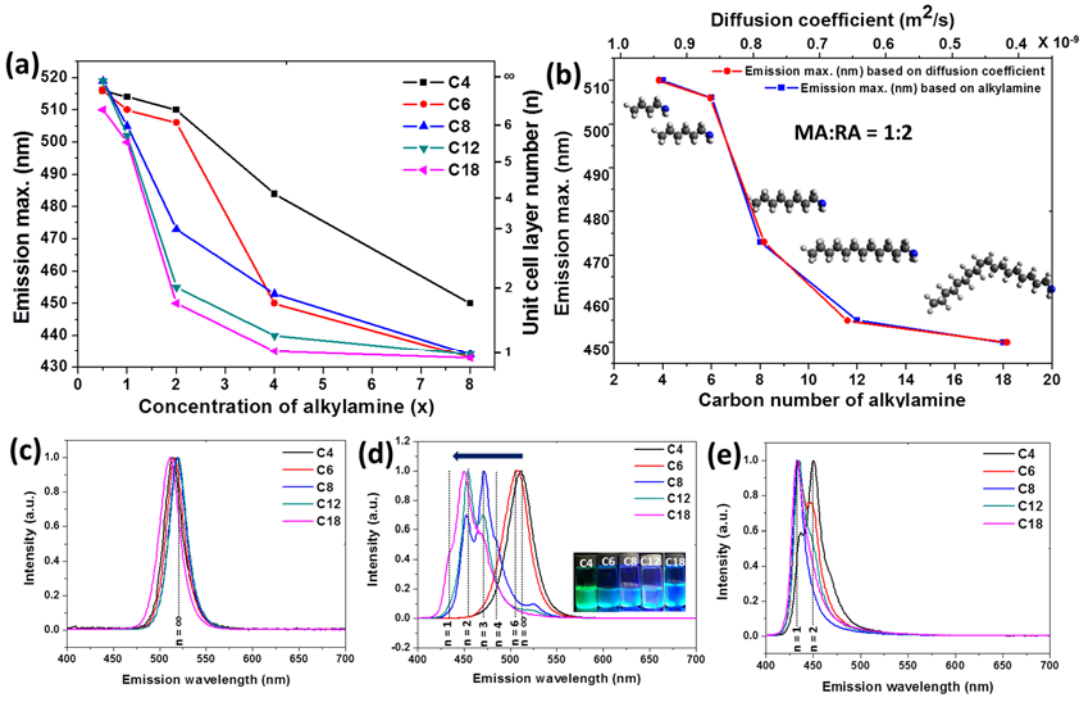

Figure II. 1 (a) Photoluminescence maximum of $MAPbBr_3$ nanoplatelets plotted as a function of the number of carbon atoms in the alkyl chain of long chain RA groups added as capping ligands. The photoluminescence maxima at different MA:RA concentrations are plotted. (b) Photoluminescence emission maxima plotted as a function of the calculated diffusion constant and the number of carbon atoms at a MA:RA ratio of 1:2. Photoluminescence emission spectra at MA:RA ratios of 1:*x* for different chain lengths of the capping ligand plotted at (c) $x = 0.5$, (d) $x = 2$, and (e) $x = 8$. The photoluminescence spectra have been normalized to a unitary intensity at their peak maxima. The inset to (c) indicates a digital photograph of toluene dispersions of the 2D nanoplatelets prepared using different capping ligands upon excitation with a UV light source at 365 nm.

solvent mixture as buffered by the capping ligands.[19, 20, 24, 44] **Figure II. 1a** indicates the evolution of the photoluminescence emission maxima measured for nanoplatelets obtained using different alkyl chain lengths of the alkylammonium cations (C4—C18) at varying precursor ratios of MA:RA = 1:*x* ($x = 0.5$—8). At a low concentration, 1:0.5 of MA:RA, the photoluminescence emission maxima for all of the alkylammonium cations

collapse to a single peak in the range of 510—520 nm, indicative of the nanoplatelets approaching the bulk limit in terms of the number of layers. The small differences in PL maxima across the different ligands likely relate to the dielectric constants of the electrostatically bound layers and their extent of aggregation. In stark contrast, at the highest RA concentration (MA:RA = 1:8) examined here, for all but the butylamine-capped nanoplatelets, the photoluminescence maxima collapse to a singular peak at 433 nm, which can be attributed to the emission of strongly quantum confined single-layered nanoplatelets.

The photoluminescence maximum of the butylamine-capped nanoplatelets is observed at 450 nm, corresponding to nanoplatelets that span two unit cells in thickness (n = 2). These two data sets are illustrative of the critical influence of the longer chain alkylammonium cations in mediating the vertical oligomerization of $MAPbBr_3$ platelets. The addition of toluene to the DMF solution induces supersaturation of $MAPbBr_3$ and results in a rapid burst nucleation that yields monomers, likely single-layered $MAPbBr_3$ that span only a few unit cells in terms of lateral dimensions. The extent of supersaturation is mediated by the long-chain alkylammonium groups that passivate the surfaces of these monomers. At high RA concentrations, the longer-chain alkylammonium cations are electrostatically bound to the entire surface of the monolayer nuclei and preclude vertical oligomerization, thereby yielding nanoplatelets that are constrained to being a single unit cell thick and limiting crystal growth to the increase of lateral dimensions via mechanisms such as oriented attachment.[18, 45] Monomers can continue to add along the uncapped edges enabling the growth of the nanoplatelets in the

ab plane.[44, 46] The shorter butylammonium cation is clearly less effective at constraining growth and thus a high density of bilayered (n = 2) platelets are stabilized. In contrast, at low RA concentrations, the surfaces of the monomers are not entirely covered, and thus under conditions of high supersaturation, unconstrained growth yields bulk-like crystals (although note the blue shift of the photoluminescence maxima for crystals grown using the longest chain OLAm moiety, which suggests some weak dimensional confinement).

The effects of chain length are greatly emphasized in the intermediate concentration regime where MA:RA = 1:2 (**Figure II. 1b**) and 1:4. **Figures II. 1c—e** contrast the photoluminescence spectra acquired at MA:RA ratios of 1:0.5, 1:2, and 1:8, respectively, for different alkyl chain lengths. At intermediate concentrations of the capping group, the extent of supersaturation is greatly decreased and a 2D layer-by-layer mode of crystal growth becomes accessible yielding few-layered nanoplatelets with layer thicknesses as ascribed in **Figure II. 1d**.[44, 47-49] Nanoplatelets prepared using the C4 RA as the capping group show a photoluminescence maximum at 510 nm, suggesting the stabilization of multilayered nanoplatelets approaching the bulk limit; the C6 RA moiety yields a single peak at 506 nm, ascribed to 2D nanoplatelets with n = 6; the C8 RA yields a primary peak at 474 nm that can be ascribed to n = 3 nanoplatelets with shoulders showing distributions of both bilayered and four-layered nanoplatelets; the C12 RA is characterized by an emission band centered at 455 nm assigned to bilayered nanoplatelets with a minority population of n = 3 nanoplatelets; and finally, for C18 RA the photoluminescence maximum shifts to 450 nm, which can be ascribed to layer thicknesses of n = 2 with minority populations of monolayer (at 433 nm) and trilayered

nanoplatelets (at 474 nm). **Table A. 1** lists the spectral assignments to layer thicknsses and cites the assignments available in the literature.[18, 28, 51] **Figure A. 1** shows the corresponding absorption spectra that furthermore corroborate the influence of the chain length and concentration. The MA:RA = 1:8 samples are characterized by pronounced excitonic absorption features at 427 nm, corresponding to monolayer $MAPbBr_3$, whereas samples prepared using MA:RA = 1:0.5 have broad absorption features characteristic of the bulk material. **Figure A. 2** shows powder X-ray diffraction patterns acquired for the materials grown at MA:RA ratios of 1:2 with varying chain lengths of the alkylammonium cations. The diffraction patterns exclusively show (*00l*) reflections, which is further indicative of the stabilization of 2D nanoplatelets. Scherrer broadening is observed for the 2D nanoplatelets

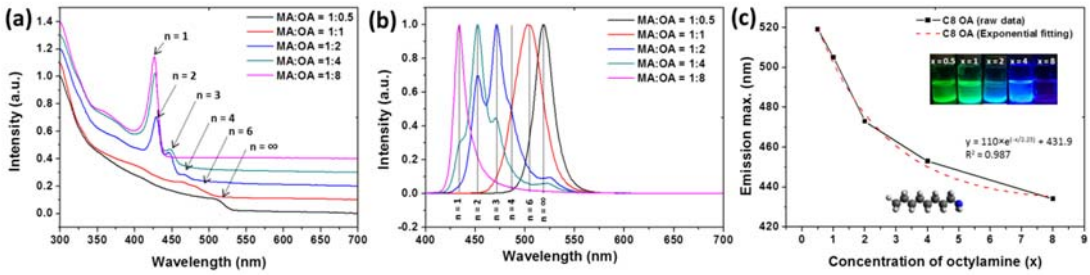

Figure II. 2 (a) UV-visible absorption spectra and (b) photoluminescence emission spectra plotted for varying MA:RA ratios when C8 OA is used as the capping ligand. The photoluminescence spectra have been normalized to a unitary intensity to exhibit variations of the peak maxima. (c) Plot of the peak position of the primary photoluminescence emission band as a function of the relative OA concentration. An exponential fit to the data yields a R^2 value of 0.987. The inset to (c) indicates a digital photograph of 2D nanoplatelets capped with OA prepared at different concentrations of the capping ligand upon excitation with a 365 nm UV light source.

grown using C8, C12, and C18 RA groups indicative of strong dimensional confinement along the crystallographic *c* direction. Notably, the intensities of the Bragg reflections are

greatly diminished for the latter two samples that span only a couple of unit cells in thickness.

Since the monomeric single-layered $MAPbBr_3$ nanosheets are capped by the RA groups, crystal growth in layer-by-layer mode becomes dependent on the diffusion constant of the capping ligand, which in turn is dependent on the alkyl chain length. Indeed, Figure II. 1b suggests a direct correlation between the calculated diffusion coefficients of the RA moieties[39] and the PL maxima, which in turn reflects the number of layers at a MA:RA ratio of 1:2 (**Figure II. 1d**). It is evident from this figure that at these RA concentrations, oligomerization proceeds through a diffusion controlled regime. Notably, the diffusion constant serves as a proxy for several physical parameters. Under conditions of dynamic equilibrium, interactions between surface-bound ligands will greatly affect the grafting density and consequently the ease of monomer diffusion. In general, when considering the packing of long-chain alkylaimines on surfaces, the aggregation enthalpy is increased with increasing number of carbon atoms as a result of a higher number of dispersive interactions within structured aggregates but such packing is entropically disfavored since the rotation of alkyl chains is hindered by conformational restrictions imposed by packing. [52] For longer aliphatic chains, it has been suggested that exothermic enthalpic processes become predominant (close to 8—10 carbon atoms) and can outweigh the entropic penalties inherent from conformational restrictions that inhibit packing for shorter chain lengths.[52, 53] The exact details of the interplay between these parameters will of course also depend on the binding enthalpy of the ligands on the $PbBr_6$-terminated surface. While bending and bond rotations are likely still feasible on

the surfaces, the conformational degrees of freedom are greatly reduced upon aggregation of the ligand molecules on the surfaces that accompanies crystallization of the nanoplatelets. Consequently, longer chain ligands are expected to form better packed aggregates that can impede diffusion of monomeric species to the surfaces of the nanoplatelets. In other words, the low diffusion coefficient, higher steric footprint, and overall greater enthalpy of aggregation results in the formation of thinner nanoplatelets by restricting monomer addition along the vertical direction.

As a representative long chain RA cation with a diffusion constant deduced to be 0.78×10^{-9} m^2/s in the DMF—toluene mixture, the influence of C8 OA in modulating the extent of supersaturation and layer-by-layer growth is illustrated in **Figure II. 2** for concentrations ranging for MA:OA ratios of 1:0.5 to 1:8. **Figure II.2a** shows absorption spectra, whereas **Figure II. 2b** shows photoluminescence emission spectra acquired at these varying concentrations. At a MA:OA ratio of 1:8, a distinct excitonic absorption feature is observed at 427 nm (Figure II. 2a) and a single photoluminescence emission band is observed at 433 nm (Figure II. 2b) suggesting the stabilization of single-layered nanoplatelets. Halving the concentration yields bilayered nanoplatelets as the preponderant species but shoulders to the primary emission band in the photoluminescence spectra indicate the presence of $n = 1$, $n = 3$, and even highly agglomerated bulk nanoplatelets as minor products (Table A. 1). Halving the

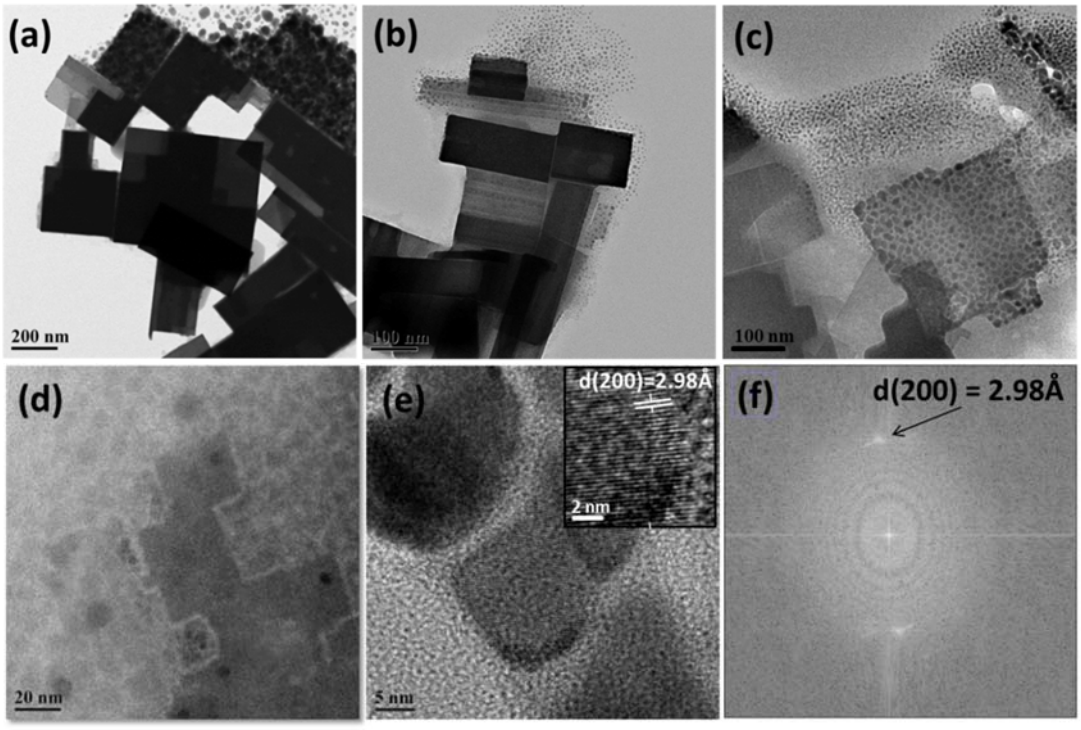

Figure II. 3 TEM images of 2D $MAPbBr_3$ nanoplatelets obtained at different ratios of the capping ligand C8 OA, MA:OA = 1:*x* where (a) *x* = 0.5, (b) *x* = 1, (c) *x* = 2, and (d) *x* = 4; (e) high-magnification image of $MAPbBr_3$ nanoplatelets obtained at a MA:OA ratio of 1:2 (the inset depicts a lattice spacing of 0.298 nm, which is attributed to the separation between 200 planes); and (f) fast Fourier transform of the high-resolution TEM image of (e).

concentration again yields trilayered nanoplatelets as the primary moieties in photoluminescence spectra with *n* = 2, *n* = 4, and highly agglomerated bulk nanoplatelets as minor moieties. At a concentration of MA:RA = 1:1, *n* = 6 nanoplatelets are stabilized, whereas upon further decreasing the OA concentration, the added ligands are unable to prevent vertical oligomerization of the nanoplatelets resulting in the formation of bulk crystallites. Figure 2c plots the peak position of the primary emission band as a function of the OA concentration, indicating a single-exponential fit with $y = 110e^{(-x/2.23)}+431.9$,

and suggesting that the RA groups buffer the extent of supersaturation and thus directly control the layer-by-layer growth of these materials. The inset to this figure indicates the pronounced blue-shifts engendered by confining the nanoplatelets to one or two unit cell dimensions,

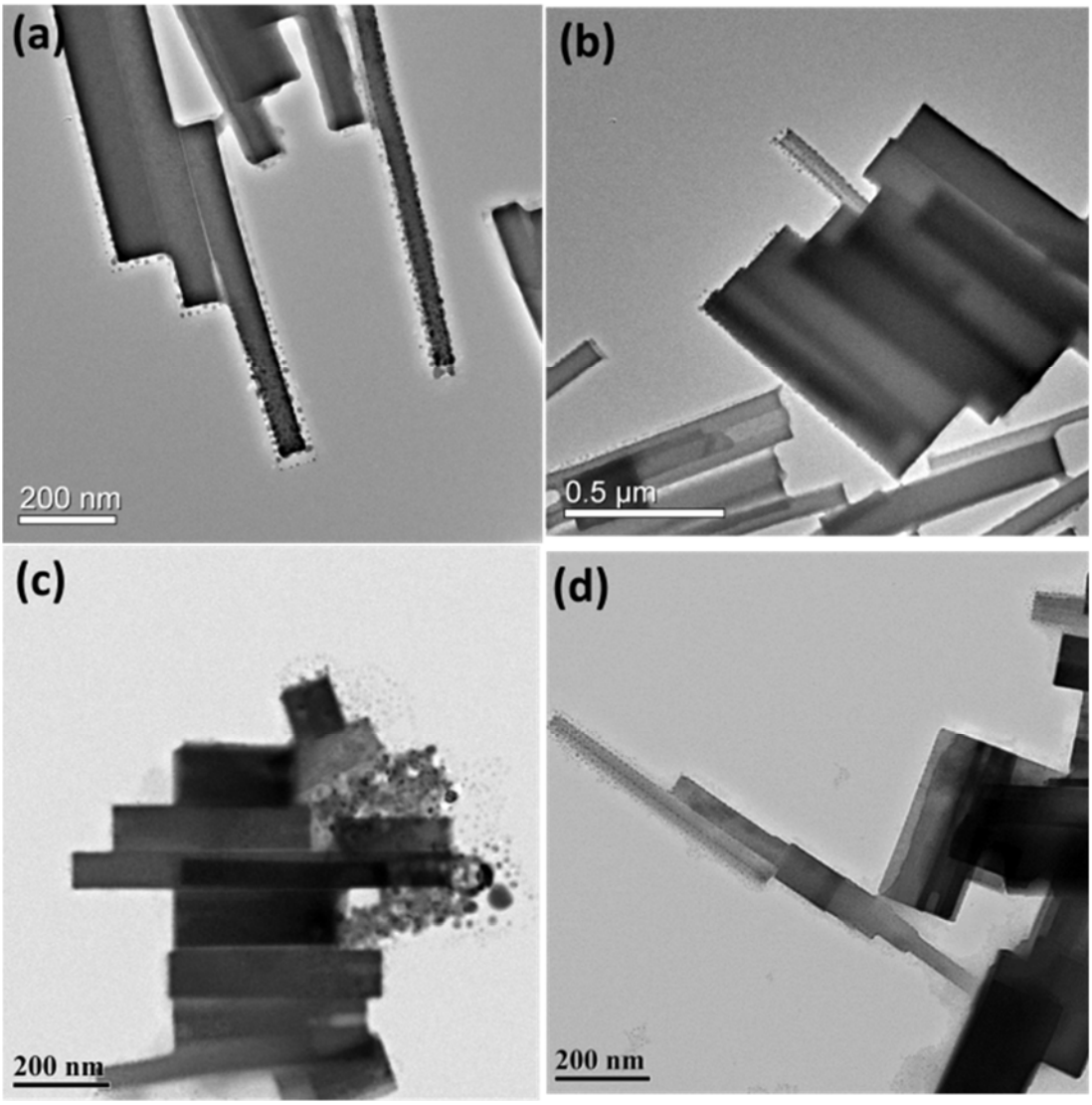

Figure II. 4 Tem images of face-to-face orientation of 2D perovskite nanoplatelets obtained at a, b) MA:BA ratio of 1:2; c) MA:OA ratio of 1:1; and d) and MA:OA ratio of 1:2.

which are in the strongly quantum confined regime.[18] $MAPbBr_3$ nanoplatelets are extremely sensitive under an electron beam and are rapidly disintegrated upon prolonged imaging.[18, 32]

Nevertheless, the transmission electron microscopy (TEM) images in Figure II. 3 and the scanning electron microscopy images in **Figure A. 3** are consistent with the concentration-dependent thickness variations deduced from the optical absorption and emission spectra. Large cubic crystals with sides on the order of 500±100 nm are observed for MA:RA ratios of 1:0.5 (Figures A. 3a and b). The particles are visibly thinner for MA:RA ratios of 1:1 (Figures A. 3c and d) and indeed upon further increasing the ratio to MA:RA of 1:2, ultrathin nanoplatelets are observed with relatively low electron density contrast. **Figure II. 3** indicates TEM images acquired for nanoplatelets grown at different MA:OA ratios. Again at low OA concentrations, relatively large nanoplatelets are observed that are ca. 100±20 nm in thickness and span ca. 400±100 nm in terms of their lateral dimensions (Figures II. 3a-b). At MA:OA ratio of 1:2 (Figure II. 3c) and 1:4 (Figure II. 3d), the nanoplatelets are extremely thin as well as smaller in terms of their lateral dimensions (ca. 30±10 nm). However, clear elucidation of size distributions by electron microscopy is precluded by beam damage since these thin nanosheets are extremely susceptible to degradation, forming 0D quantum dots.[26, 31] Figures II. 3e and f indicate lattice-resolved TEM images and a SAED pattern acquired for individual nanoplatelets estimated to span three or four layers in thickness. Given the electron beam sensitivity of the nanoplatelets, AFM has been deployed to corroborate the assigned layer thicknesses. **Figure A. 4** indicates AFM images and height profiles

obtained for nanoplatelets grown at different concentrations of C8 OA. The reduction in vertical dimensions is clearly visible as a function of the alkylamine concentration; at low concentrations of OA (MA:OA of 1:1), the nanoplatelets span few hundred nanometers in thickness. However, at high relative concentrations (above MA:OA of 1:4), nanoplatelets that are only 1.5 ± 0.3 nm in thickness are observed and can be assigned to $n = 1$ monolayers as also observed previously in the literature.[18] Intermediate relative concentrations yield finite numbers of layers ($n = 3$ and $n = 5$ at MA:RA concentrations of 1:2). The AFM results are thus consistent with the assignments derived from photoluminescence and optical absorption spectra. **Figure A. 5** indicates SAXS measurement for nanoplatelets prepared using different relative concentrations of OA (MA: OA 1:x, where x = 1-4). A reflection at $q = 0.176$ Å^{-1} is observed to increase in intensity with increasing concentration of OA. The reflection corresponds to a separation of 3.58 nm and is attributed to the separation between individual monolayer (n =1) nanoplatelets assembled within columnar aggregates.[53] The value of 3.58 nm corresponded to the thickness of a monolayer of $MAPbBr_3$ (ca. 1.5 nm) and a double layer of surface bound octylammonium cations (ca. 2.0 nm).

Figure A. 6 depicts absorption and photoluminescence spectra acquired for the C4, C6, C12, and C18 alkylammonium groups as a function of increasing concentration. A similar concentration-dependent blue-shift of absorption and emission features is observed with increasing concentration for all of the RA groups. However, as also illustrated by Figure 1a, the shorter chain groups need to be present at higher concentrations to be able to confine the nanoplatelets to thinner dimensions. The growth

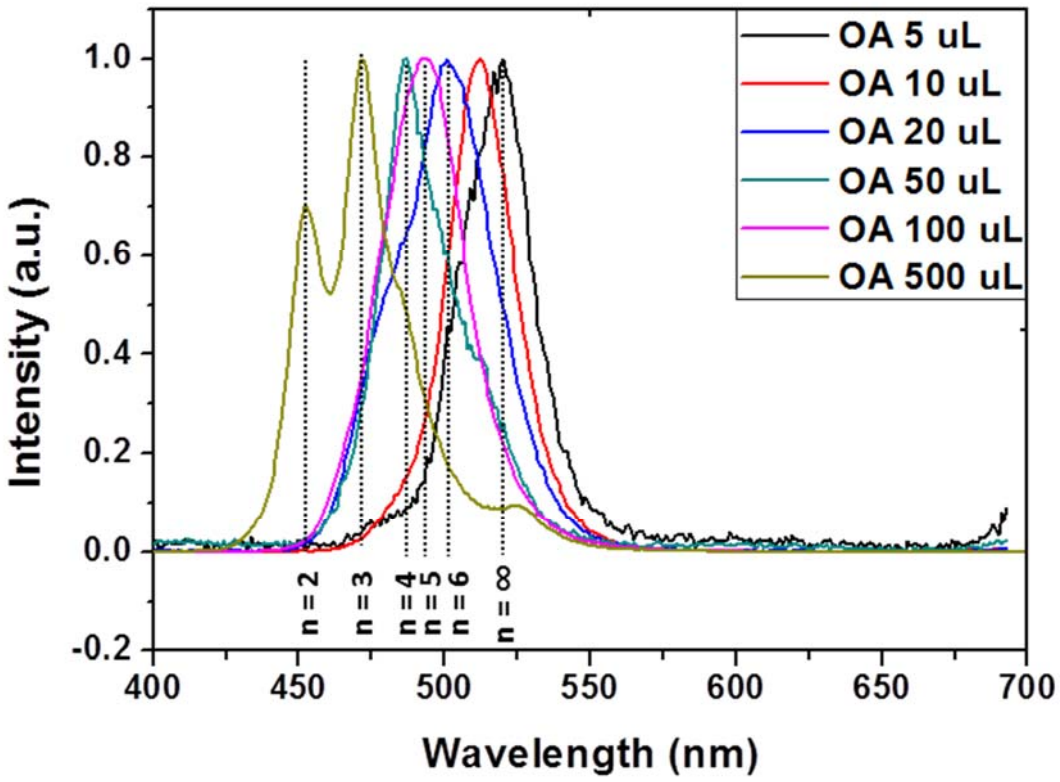

Figure II. 5 Photoluminescence emission spectra of synthesized 2D perovskite nanoplatelets as a function of the OAc concentration while keeping the same molar ratio of MA:OA at 1:2. The photoluminescence spectra have been normalized to a unitary intensity to exhibit variations of the peak maxima.

of the single-layered (n = 1) monomer units is easier along the edges since the long chain alkylammonium cations bind preferentially to the faces; vertical oligomerization can result from addition of monomeric units after displacement of the surface ligands or via oriented attachment along the faces.[44, 54, 55] Indeed, **Figure II. 4** indicates the face-to-face ordering of nanoplatelets that may precede oriented attachment.[28, 56, 57]

It is worth noting that long chain alkylamines are used in the reaction and are transformed to alkylammonium cations that bind electrostatically to the $PbBr_6$ sheets

upon protonation by the added large excess of oleic acid (RA:oleic acid = 1:93.75). Consequently, the solution-phase activities of the ligand species are expected to vary with the oleic acid concentration if it is not added in large excess. Indeed, **Figure II. 5** illustrates that with decreasing OA:oleic acid ratios, the photoluminescence emission bands are strongly red-shifted and indeed at a MA:oleic acid ratio of 1:0.94, the concentration of protonated alkylammonium cations is too low to effectively bind to the surfaces of the monomeric units yielding platelets approaching the bulk limit.

II.4 Conclusions

In summary, we have investigated the role of the chain-length-dependent diffusion coefficient and the concentration of alklylammonium ions in confining the crystal growth of $MAPbBr_3$ nanoplatelets. Longer chain alkylammonium cations and high concentrations of alkylammonium cations of intermediate chain length are strongly electrostatically bound to the faces of the perovskite crystals and confine crystal growth along the vertical direction yielding nanoplatelets of tunable thickness. This approach allows for precise modulation of layer thickness ranging from strongly quantum confined nanoplatelets that are single- or bilayered in thickness to nanoplatelets in the weakly confined regime that span three to six layers in thickness. The added alkylammonium cations induce a strong growth anisotropy as a result of preferential binding to the top and bottom $PbBr_6$ sheets. Vertical oligomerization is thought to be mediated by oriented attachment. The results here suggest the facile control of morphology and layer thickness that can be induced in this polar system by varying the steric footprint of added ligands.

Future work will focus on mixed ligand systems and "entropic ligands" to further exploit the interplay between enthalpic stabilization and entropic conformational restriction of the ligand shell in mediating crystal growth.

II.5 References

(1) Kojima, A.; Teshima, K.; Shirai, Y.; Miyasaka, T., Organometal Halide Perovskites as Visible-Light Sensitizers for Photovoltaic Cells. *J. Am. Chem. Soc.* **2009,** 131, 6050-6051.

(2) Lee, M. M.; Teuscher, J.; Miyasaka, T.; Murakami, T. N.; Snaith, H. J., Efficient Hybrid Solar Cells Based on Meso-Superstructured Organometal Halide Perovskites. *Science* **2012,** 338, 643-647.

(3) Zhou, H.; Chen, Q.; Li, G.; Luo, S.; Song, T.-b.; Duan, H.-S.; Hong, Z.; You, J.; Liu, Y.; Yang, Y., Interface engineering of highly efficient perovskite solar cells. *Science* **2014,** 345, 542-546.

(4) Park, N.-G., Organometal perovskite light absorbers toward a 20% efficiency low-cost solid-state mesoscopic solar cell. *J. Phys. Chem. Lett.* **2013,** 4, 2423-2429.

(5) Green, M. A.; Ho-Baillie, A.; Snaith, H. J., The emergence of perovskite solar cells. *Nat. Photonics* **2014,** 8, 506-514.

(6) Dong, Q.; Fang, Y.; Shao, Y.; Mulligan, P.; Qiu, J.; Cao, L.; Huang, J., Electron-hole diffusion lengths> 175 μm in solution-grown $CH_3NH_3PbI_3$ single crystals. *Science* **2015,** 347, 967-970.

(7) Shi, D.; Adinolfi, V.; Comin, R.; Yuan, M.; Alarousu, E.; Buin, A.; Chen, Y.; Hoogland, S.; Rothenberger, A.; Katsiev, K., Low trap-state density and long carrier diffusion in organolead trihalide perovskite single crystals. *Science* **2015,** 347, 519-522.

(8) Wang, H.; Whittaker-Brooks, L.; Fleming, G. R., Exciton and Free Charge Dynamics of Methylammonium Lead Iodide Perovskites Are Different in the Tetragonal and Orthorhombic Phases. *J. Phys. Chem. C* **2015,** 119, 19590-19595.

(9) Kim, Y.-H.; Cho, H.; Heo, J. H.; Kim, T.-S.; Myoung, N.; Lee, C.-L.; Im, S. H.; Lee, T.-W., Multicolored Organic/Inorganic Hybrid Perovskite Light-Emitting Diodes. *Adv. Mater.* **2015,** 27, 1248-1254.

(10) Ling, Y.; Yuan, Z.; Tian, Y.; Wang, X.; Wang, J. C.; Xin, Y.; Hanson, K.; Ma, B.; Gao, H., Bright Light-Emitting Diodes Based on Organometal Halide Perovskite Nanoplatelets. *Adv. Mater.* **2016,** 28, 305-311.

(11) Stoumpos, C. C.; Malliakas, C. D.; Kanatzidis, M. G., Semiconducting Tin and Lead Iodide Perovskites with Organic Cations: Phase Transitions, High Mobilities, and Near-Infrared Photoluminescent Properties. *Inorg. Chem.* **2013,** 52, 9019-9038.

(12) Boix, P. P.; Agarwala, S.; Koh, T. M.; Mathews, N.; Mhaisalkar, S. G., Perovskite Solar Cells: Beyond Methylammonium Lead Iodide. *J. Phys. Chem. Lett.* **2015,** 6, 898-907.

(13) Akkerman, Q. A.; D'Innocenzo, V.; Accornero, S.; Scarpellini, A.; Petrozza, A.; Prato, M.; Manna, L., Tuning the Optical Properties of Cesium Lead Halide Perovskite Nanocrystals by Anion Exchange Reactions. *J. Am. Chem. Soc.* **2015,** 137, 10276-10281.

(14) Jang, D. M.; Park, K.; Kim, D. H.; Park, J.; Shojaei, F.; Kang, H. S.; Ahn, J.-P.; Lee, J. W.; Song, J. K., Reversible Halide Exchange Reaction of Organometal Trihalide Perovskite Colloidal Nanocrystals for Full-Range Band Gap Tuning. *Nano Lett.* **2015,** 15, 5191-5199.

(15) Stoumpos, C. C.; Kanatzidis, M. G., The Renaissance of Halide Perovskites and Their Evolution as Emerging Semiconductors. *Acc. Chem. Res.* **2015,** 48, 2791-2802.

(16) Im, J.-H.; Chung, J.; Kim, S.-J.; Park, N.-G., Synthesis, structure, and photovoltaic property of a nanocrystalline 2H perovskite-type novel sensitizer ($CH_3CH_2NH_3$)PbI_3. *Nanoscale Res. Lett.* **2012,** 7, 1-7.

(17) Ren, Y.; Oswald, I. W. H.; Wang, X.; McCandless, G. T.; Chan, J. Y., Orientation of Organic Cations in Hybrid Inorganic–Organic Perovskite CH3NH3PbI3 from Subatomic Resolution Single Crystal Neutron Diffraction Structural Studies. *Cryst. Growth Des.* **2016,** 16, 2945-2951.

(18) Sichert, J. A.; Tong, Y.; Mutz, N.; Vollmer, M.; Fischer, S.; Milowska, K. Z.; García Cortadella, R.; Nickel, B.; Cardenas-Daw, C.; Stolarczyk, J. K., Quantum size effect in organometal halide perovskite nanoplatelets. *Nano Lett.* **2015,** 15, 6521-6527.

(19) Tanaka, K.; Takahashi, T.; Ban, T.; Kondo, T.; Uchida, K.; Miura, N., Comparative study on the excitons in lead-halide-based perovskite-type crystals $CH_3NH_3PbBr_3$ $CH_3NH_3PbI_3$. *Solid State Commun.* **2003,** 127, 619-623.

(20) Koutselas, I. B.; Ducasse, L.; Papavassiliou, G. C., Electronic properties of three- and low-dimensional semiconducting materials with Pb halide and Sn halide units. *J. Phys. Condens. Matter* **1996,** 8, 1217.

(21) Manser, J. S.; Saidaminov, M. I.; Christians, J. A.; Bakr, O. M.; Kamat, P. V., Making and Breaking of Lead Halide Perovskites. *Acc. Chem. Res.* **2016,** 49, 330-338.

(22) Murray, C. B.; Kagan, C.; Bawendi, M., Synthesis and characterization of monodisperse nanocrystals and close-packed nanocrystal assemblies. *Annu. Rev. Mater. Sci.* **2000,** 30, 545-610.

(23) Alvarado, S. R.; Guo, Y.; Ruberu, T. P. A.; Tavasoli, E.; Vela, J., Inorganic chemistry solutions to semiconductor nanocrystal problems. *Coord. Chem. Rev.* **2014,** 263, 182-196.

(24) Wang, W.; Banerjee, S.; Jia, S.; Steigerwald, M. L.; Herman, I. P., Ligand control of growth, morphology, and capping structure of colloidal CdSe nanorods. *Chem. Mater.* **2007,** 19, 2573-2580.

(25) Gonzalez-Carrero, S.; Galian, R. E.; Pérez-Prieto, J., Maximizing the emissive properties of $CH_3NH_3PbBr_3$ perovskite nanoparticles. *J. Mater. Chem. A* **2015,** 3, 9187-9193.

(26) Schmidt, L. C.; Pertegás, A.; González-Carrero, S.; Malinkiewicz, O.; Agouram, S.; Mínguez Espallargas, G.; Bolink, H. J.; Galian, R. E.; Pérez-Prieto, J., Nontemplate Synthesis of $CH_3NH_3PbBr_3$ Perovskite Nanoparticles. *J. Am. Chem. Soc.* **2014,** 136, 850-853.

(27) Neve, F.; Francescangeli, O.; Crispini, A.; Charmant, J., $A_2[MX_4]$ Copper(II) Pyridinium Salts. From Ionic Liquids to Layered Solids to Liquid Crystals. *Chem. Mater.* **2001,** 13, 2032-2041.

(28) Tyagi, P.; Arveson, S. M.; Tisdale, W. A., Colloidal Organohalide Perovskite Nanoplatelets Exhibiting Quantum Confinement. *J. Phys. Chem. Lett.* **2015,** 6, 1911-1916.

(29) Ishihara, T.; Takahashi, J.; Goto, T., Exciton state in two-dimensional perovskite semiconductor $(C_{10}H_{21}NH_3)_2PbI_4$. *Solid State Commun.* **1989,** 69, 933-936.

(30) Huang, H.; Susha, A. S.; Kershaw, S. V.; Hung, T. F.; Rogach, A. L., Control of Emission Color of High Quantum Yield $CH_3NH_3PbBr_3$ Perovskite Quantum Dots by Precipitation Temperature. *Adv. Sci* **2015,** 2, 1500194.

(31) Zhang, F.; Zhong, H.; Chen, C.; Wu, X.-g.; Hu, X.; Huang, H.; Han, J.; Zou, B.; Dong, Y., Brightly Luminescent and Color-Tunable Colloidal $CH_3NH_3PbX_3$ (X = Br, I, Cl) Quantum Dots: Potential Alternatives for Display Technology. *ACS Nano* **2015,** 9, 4533-4542.

(32) Zhu, F.; Men, L.; Guo, Y.; Zhu, Q.; Bhattacharjee, U.; Goodwin, P. M.; Petrich, J. W.; Smith, E. A.; Vela, J., Shape Evolution and Single Particle Luminescence of Organometal Halide Perovskite Nanocrystals. *ACS Nano* **2015,** 9, 2948-2959.

(33) Yuan, Z.; Shu, Y.; Tian, Y.; Xin, Y.; Ma, B., A facile one-pot synthesis of deep blue luminescent lead bromide perovskite microdisks. *Chem. Commun.* **2015,** 51, 16385-16388.

(34) Yuan, Z.; Shu, Y.; Xin, Y.; Ma, B., Highly luminescent nanoscale quasi-2D layered lead bromide perovskites with tunable emissions. *Chem. Commun.* **2016,** 52, 3887-3890.

(35) Dou, L.; Wong, A. B.; Yu, Y.; Lai, M.; Kornienko, N.; Eaton, S. W.; Fu, A.; Bischak, C. G.; Ma, J.; Ding, T.; Ginsberg, N. S.; Wang, L.-W.; Alivisatos, A. P.; Yang,

P., Atomically thin two-dimensional organic-inorganic hybrid perovskites. *Science* **2015,** 349, 1518-1521.

(36) Di, D.; Musselman, K. P.; Li, G.; Sadhanala, A.; Ievskaya, Y.; Song, Q.; Tan, Z.-K.; Lai, M. L.; MacManus-Driscoll, J. L.; Greenham, N. C.; Friend, R. H., Size-Dependent Photon Emission from Organometal Halide Perovskite Nanocrystals Embedded in an Organic Matrix. *J. Phys. Chem. Lett.* **2015,** 6, 446-450.

(37) Sichert, J. A.; Tong, Y.; Mutz, N.; Vollmer, M.; Fischer, S.; Milowska, K. Z.; García Cortadella, R.; Nickel, B.; Cardenas-Daw, C.; Stolarczyk, J. K.; Urban, A. S.; Feldmann, J., Quantum Size Effect in Organometal Halide Perovskite Nanoplatelets. *Nano Letters* **2015,** 15, 6521-6527.

(38) Sapori, D.; Kepenekian, M.; Pedesseau, L.; Katan, C.; Even, J., Quantum confinement and dielectric profiles of colloidal nanoplatelets of halide inorganic and hybrid organic–inorganic perovskites. *Nanoscale* **2016,** 8, 6369-6378.

(39) De Nolf, K.; Capek, R. K.; Abe, S.; Sluydts, M.; Jang, Y.; Martins, J. C.; Cottenier, S.; Lifshitz, E.; Hens, Z., Controlling the Size of Hot Injection Made Nanocrystals by Manipulating the Diffusion Coefficient of the Solute. *J. Am. Chem. Soc.* **2015,** 137, 2495-2505.

(40) Hanwell, M. D.; Curtis, D. E.; Lonie, D. C.; Vandermeersch, T.; Zurek, E.; Hutchison, G. R., Avogadro: an advanced semantic chemical editor, visualization, and analysis platform. *J. Cheminformatics.* **2012,** 4, 1-17.

(41) Lignos, I.; Stavrakis, S.; Nedelcu, G.; Protesescu, L.; deMello, A. J.; Kovalenko, M. V., Synthesis of Cesium Lead Halide Perovskite Nanocrystals in a Droplet-Based Microfluidic Platform: Fast Parametric Space Mapping. *Nano Lett.* **2016,** 16, 1869-1877.

(42) Protesescu, L.; Yakunin, S.; Bodnarchuk, M. I.; Krieg, F.; Caputo, R.; Hendon, C. H.; Yang, R. X.; Walsh, A.; Kovalenko, M. V., Nanocrystals of Cesium Lead Halide Perovskites ($CsPbX_3$, X = Cl, Br, and I): Novel Optoelectronic Materials Showing Bright Emission with Wide Color Gamut. *Nano Lett.* **2015,** 15, 3692-3696.

(43) Noh, J. H.; Im, S. H.; Heo, J. H.; Mandal, T. N.; Seok, S. I., Chemical management for colorful, efficient, and stable inorganic–organic hybrid nanostructured solar cells. *Nano Lett.* **2013,** 13, 1764-1769.

(44) Kort, K. R.; Banerjee, S., Ligand-Mediated Control of Dislocation Dynamics and Resulting Particle Morphology of GdOCl Nanocrystals. *Small* **2015,** 11, 329-334.

(45) Zhang, D.; Eaton, S. W.; Yu, Y.; Dou, L.; Yang, P., Solution-phase synthesis of cesium lead halide perovskite nanowires. *J. Am. Chem. Soc.* **2015,** 137, 9230-9233.

(46) Kort, K. R.; Banerjee, S., Shape-Controlled Synthesis of Well-Defined Matlockite LnOCl (Ln: La, Ce, Gd, Dy) Nanocrystals by a Novel Non-Hydrolytic Approach. *Inorg. Chem.* **2011,** 50, 5539-5544.

(47) Drum, C., Twist and axial imperfections in filamentary crystals of aluminum nitride. II. *J. Appl. Phys.* **1965,** 36, 824-829.

(48) Li, Y.; Wu, Y., Critical role of screw dislocation in the growth of Co (OH) 2 nanowires as intermediates for Co3O4 nanowire growth. *Chem. Mater.* **2010,** 22, 5537-5542.

(49) Morin, S. A.; Bierman, M. J.; Tong, J.; Jin, S., Mechanism and kinetics of spontaneous nanotube growth driven by screw dislocations. *Science* **2010,** 328, 476-480.

(50) Papavassiliou, G. C.; Koutselas, I. B.; Lagouvardos, D. J.; Kapoutsis, J.; Terzis, A.; Papaioannou, G. J., Optical and Related Properties of Some Natural Three and Lower Dimensional Semiconductor Systems. *Molecular Crystals and Liquid Crystals Science and Technology. Section A. Molecular Crystals and Liquid Crystals* **1994,** 253, 103-112.

(51) Matulis, D.; Bloomfield, V. A., Thermodynamics of the hydrophobic effect. II. Calorimetric measurement of enthalpy, entropy, and heat capacity of aggregation of alkylamines and long aliphatic chains. *Biophys. Chem.* **2001,** 93, 53-65.

(52) Yang, Y.; Qin, H.; Jiang, M.; Lin, L.; Fu, T.; Dai, X.; Zhang, Z.; Niu, Y.; Cao, H.; Jin, Y., Entropic Ligands for Nanocrystals: From Unexpected Solution Properties to Outstanding Processability. *Nano Lett.* **2016,** 16, 2133-2138.

(53) Bekenstein, Y.; Koscher, B. A.; Eaton, S. W.; Yang, P.; Alivisatos, A. P., Highly luminescent colloidal nanoplates of perovskite cesium lead halide and their oriented assemblies. *J. Am. Chem. Soc.* **2015,** 137, 16008-16011.

(54) Lhuillier, E.; Pedetti, S.; Ithurria, S.; Nadal, B.; Heuclin, H.; Dubertret, B., Two-Dimensional Colloidal Metal Chalcogenides Semiconductors: Synthesis, Spectroscopy, and Applications. *Acc. Chem. Res.* **2015,** 48, 22-30.

(55) Ithurria, S.; Bousquet, G.; Dubertret, B., Continuous transition from 3D to 1D confinement observed during the formation of CdSe nanoplatelets. *J. Am. Chem. Soc.* **2011,** 133, 3070-3077.

(56) Son, J. S.; Wen, X. D.; Joo, J.; Chae, J.; Baek, S. i.; Park, K.; Kim, J. H.; An, K.; Yu, J. H.; Kwon, S. G., Large-Scale Soft Colloidal Template Synthesis of 1.4 nm Thick CdSe Nanosheets. *Angew. Chem.* **2009,** 121, 6993-6996.

(57) Quan, L. N.; Yuan, M.; Comin, R.; Voznyy, O.; Beauregard, E. M.; Hoogland, S.; Buin, A.; Kirmani, A. R.; Zhao, K.; Amassian, A., Ligand-Stabilized Reduced-Dimensionality Perovskites. *J. Am. Chem. Soc.* **2016,** 138, 2649-2655.

CHAPTER III

INFLUENCE OF LIGAND SHELL ORDERING ON DIMENSIONAL CONFINEMENT OF CESIUM LEAD BROMIDE ($CsPbBr_3$) PEROVSKITE NANOPLATELETS*

III.1 Introduction

The colloidal synthesis of ultrathin two-dimensional materials, particularly semiconductors, has inspired tremendous recent research interest owing to the ability to induce directional dimensional confinement within these structures. Directional elimination of structural coherence allows for selective modulation of the electronic structure along specific directions of the Brillouin zone and gives rise to thickness-dependent optical, electronic, and magnetic properties.[1-5] Much recent interest has focused on perovskite halide semiconductors with the composition ABX_3 (where A = Cs^+, methylammonium, formadimium; B= Pb^{2+}, Sn^{2+}, Ge^{2+}; and X = Cl^-, Br^-, I^- or some mixture therein), which are characterized by tunable exciton binding energies, high absorption cross-sections, narrow emission bands, and high photoluminescence (PL) quantum yields.[6-11] Such properties are particularly desirable for light-emitting diodes (LEDs) and electroluminescent (EL) devices.[12-14] The perovskite structure affords some degree of compositional flexibility, and thus tunability of photophysical properties,

*Reprinted with permission from "Influence of ligand shell ordering on dimensional confinement of cesium lead bromide ($CsPbBr_3$) perovskite nanoplatelets" J. Cho, H. Jin, D. G. Sellers, D. F. Watson, D. H. Son, and S. Banerjee, *J. Mater. Chem. C*, **2017**, 5, 8810-8818. Reproduced with permission of © 2017 Royal Society of Chemistry. All rights reserved.

based on substitution of the constituent A, B, and X ions within a parameter space constrained primarily by the perovskite tolerance factor;[15] layered Ruddleson-Popper phases are stabilized to accommodate ions that induce larger distortions.[16] While much of the interest in perovskite semiconductors grew out of the remarkable properties of organic—inorganic hybrid methylammonium lead halide perovskites, their susceptibility to degradation has focused attention on the more stable all-inorganic analogue, $CsPbX_3$.[17-21]

Dimensional reduction provides a means to access the quantum confined regime and modulate the excitonic binding energies and diffusion lengths of such materials beyond the scope of compositional modulation.[22] The synthesis of colloidal 2D $CsPbBr_3$ perovskite nanoplatelets with a high PL quantum yield (>70%) as a result of reduction of trap states has been reported by several research groups.[15, 18, 19, 21] Such syntheses typically deploy surface capping ligands that afford a high degree of control over the thickness of the obtained nanoplatelets. For instance, Akkerman *et al.* have demonstrated tunability of morphology from nanoplatelets to nanocubes for $CsPbBr_3$ using a reprecipitation method by adjusting the amount of bromic acid.[18] The extent of protonation of oleylamine added as a ligand can effectively control the nucleation and growth of nanoplatelets since the surfactant alkylammonium cation competes with the cesium cation to electrostatically bind the BX_2 layers. The surface ligands are electrostatically bound to the basal planes of corner-sharing $PbBr_6$ octahedra; their reversible adsorption and desorption mediates further addition of monomeric

species, which determines the eventual thickness of the nanoplatelets. Bekenstein *et al.* have examined the influence of reaction temperature and observe wide variations of the shape, morphology, and band gap emission of stacked columnar perovskite structures as a function of temperature; high reaction temperatures (150°C) induce the growth of symmetric nanocubes, whereas anisotropic nanoplatelets are obtained at lower reaction temperatures (90°C).[19] In recent work, Pan *et al.* have examined the role of surface-capping ligands at different temperatures to elucidate the influence of these parameters on the size and shape of the obtained nanocrystals.[23] However, detailed mechanistic understanding of the influence of alkylammonium chain length and branching as well as the interplay between thermodynamics and kinetics as it affects nucleation and growth remains to be elucidated. The highly ionic nature of perovskite halides poses somewhat of a synthetic challenge in that growth rates are high and thus discretization of a growth focusing step to obtain monodisperse nanoplatelets can be difficult.[24] As a practical consequence, the PL spectra of as-prepared perovskite nanoplatelets often comprise multiple PL emission peaks corresponding to different octahedral layer thicknesses (n).[18, 19] A post-synthesis treatment with a polar solvent has been developed to obtain quasi-monodisperse nanoplatelets, but the treatment degrades crystal quality by disrupting the ligand shell.[18, 19,23]

Alkylammonium cations are commonly used as surface-capping ligands for the synthesis of perovskite nanoplatelets, and can stabilize nanostructures

spanning only a few unit cells in thickness by dint of electrostatic interactions with negatively charged PbX_2 layers.[20] The intermolecular interactions amongst capping ligands on nanocrystal surfaces are expected to strongly influence the further addition of monomer species. Consequently, the crystallinity or ordering of the ligand shell is of paramount importance, particularly in systems where monomer diffusion is rapid. In essence, the structure of the ligand shell reflects the trade-off between enthalpic gains from surface adsorption (ligand—surface interactions) and dispersive interactions (ligand—ligand interactions) and the entropic penalty imposed by conformational restrictions (as compared to a freely rotating ligand molecule in solution). However, to the best of our knowledge, the correlation between ligand packing and the nucleation and growth rate has not been studied. In this article, we evaluate the influence of chain length, branching, and temperature on the dimensional modulation of 2D perovskite nanoplatelets. A clear correlation is observed between crystallinity of the ligand shell and dimensional confinement of the perovskite nanoplatelets and is rationalized based on distinct thermodynamic and kinetic regimes.[25]

III.2 Experimental

Synthesis of 2D $CsPbBr_3$ nanoplatelets. In a typical reaction, cesium oleate (Cs-OA) was prepared by adapting a previously reported method wherein 0.032 g Cs_2CO_3 and 10 mL OLAc were loaded in a 50 mL three-neck round-bottomed flask, degassed under vacuum at 120°C, and heated to 150°C under Ar flow to ensure complete dissolution of

the solids.[21] In parallel, 0.015 g of $PbBr_2$ was dissolved in 5 mL ODE and 0.250 mL of OLAc; the lead oleate thus formed was mixed with a desired stoichiometric ratio of alkylamine (RA:C4—C18) in a three-neck round-bottomed flask and degassed under vacuum for 20 min at 100°C; for C4 mixture was heated at 80—90°C because of low boiling point of C4 (78°C). The alkylamine (RA) concentration (x) was systematically varied. After complete dissolution of $PbBr_2$, the temperature of the flask was set at the desired temperature (which was varied from 50–150°C). Next, 1 mL of the as-prepared Cs-OA solution was rapidly injected under Ar flow. The reaction mixture was maintained for 10 s and immediately quenched with 15 mL of cool hexanes to 30—40 °C). The pale yellow-colored precipitate was collected by centrifugation at 12,000 rpm for 10 min and then resuspended to form a colloidal dispersion in hexanes. The colloidal dispersion of the nanoplatelets in hexanes was used for further characterization. It is worth noting that thinner perovskite nanoplatelets tend to grow into thicker crystals in solution if the reaction is not quenched. The PL emission spectra of nanoplatelets capped with C4 and C14 obtained after 24 h are red-shifted in comparison to spectra obtained immediately after synthesis. The nanoplatelet populations corresponding to n = 2 disappear for C14; the n = 3–4 are also substantially decreased for C4, (**Figure A. 15**). The attachment of nanoplatelets likely underpins the observed increase of thickness.

Characterization. Single-particle PL emission spectra from individual perovskite nanoplatelets were measured with a home-built wide-field microscope equipped with an imaging spectrograph (Princeton Instruments, Acton SpectraPro SP-2300) and an electron multiplying charge-coupled device (EMCCD) (Princeton Instruments, ProEM

16002). A Xe-lamp (Oriel Instrument, 300 W) in conjunction with a monochromator (Newport, Oriel Cornerstone 130) was used as the excitation light source. The nanoplatelets were excited via an attenuated total reflection scheme using a quartz prism to minimize the interference from the excitation light during the PL measurement. A dilute dispersion of colloidal nanoplatelets was cast onto a thin quartz plate to deposit well-separated individual nanoplatelets. Next, the plate was placed on top of the prism using an index matching liquid (hexanes). The PL from individual nanoplatelets was collected using an objective lens (Olympus, PLanFL N 40×) and was focused onto the EMCCD either as an image or as a spectrum using a tube lens (Nikon) through the imaging spectrograph. High-resolution transmission electron microscopy (TEM) images were obtained using a FEI Tecnai G2 F20 ST instrument at accelerating voltage 200 kV. Powder X-ray diffraction (XRD) measurements were performed using a Bruker D8-Focus Bragg-Brentano X-ray Powder Diffractometer with a Cu Kα radiation source (λ = 1.5418 Å) in the range of 10—60°. Small angle X-ray scattering (SAXS) measurements were performed using a Rigaku S-Max3000 Pinhole SAXS Camera in the range of 0.02 – 0.30 $Å^{-1}$. UV-Vis absorption spectra were obtained using a Hitachi U-4100 UV-Vis-NIR spectrophotometer. PL emission spectra were acquired using a Horiba PTI Quanta-Master series spectrofluorometer with a Xenon arc lamp as the light source and a photomultiplier tube (PMT) as the light detector. Fourier transform infrared (FTIR) spectra were obtained using Bruker VERTEX 70 in the range of 4000—400 cm^{-1} with a spatial resolution of 4 cm^{-1}.

Calculation of the average octahedra layer thickness (*n*) of nanoplatelets. The average octahedral layer thickness of nanoplatelets is reported as per the following equation.

$$n_{avg} = \sum_{i=1}^{\infty}(a_i \times n_i) \cdots\cdots \text{(III. 1)}$$

$$a_i = \frac{Integrated\ area\ of\ n_i\ in\ PL\ spectra}{Totally\ integrated\ area\ in\ PL\ spectra} \cdots\cdots \text{(III. 2)}$$

where n_{avg} is average octahedral layer thickness for a specific sample, a_i (i = 1—6 and bulk) is the weighting factor representing the population of a specific layer thickness, and n_i (i = 1—6 and bulk) is the number of octahedral; layers of few-layered nanoplatelets. For nanoplatelets thicker than n = 6 in the bulk limit, a value of n = 30 has been approximated, based on TEM measurement for thick perovskite approaching to bulk limit. In order to calculate the relative proportion of each population, the integrated area of individual nanoplatelets at a specific PL maximum emission wavelength is obtained and then divided by the total integrated area in the PL spectrum.

III.3 Results and Discussion

Nanocrystals of $CsPbBr_3$ have been obtained by the hot injection of cesium-oleate (Cs-OA) to an octadecene (ODE) solution of lead-oleate (Pb-OA) precursors in the presence of oleic acid and alkylamine (RA) based on adaptation of a previously reported method.[21] The chain length of the alkylamine is varied from R = C4—C18; linear as well as branched alklyamines are contrasted for their ability to induce dimensional confinement. The injection is performed at varying

reaction temperatures ranging from 50–150°C. The synthetic procedures are described in further detail in the Experimental section. Prior to injection, the solution contains alkylammonium cations protonated by reaction with excess oleic acid; the cations are thought to associate with bromide ions to form alkylammonium bromide.[20, 26]

The large molar excess of oleic acid ensures rapid protonation of the added alkylamines at the stoichiometric ratios examined here. The oleic acid concentration strongly affects the growth rate, likely as a result of chain-length-dependent protonation rates, at lower oleic acid:RA molar ratios, as observed in previous work. [20] Indeed, the explicit addition of hydrogen bromide has been shown to yield thinner nanoplatelets owing to faster capping by ligands that now have an increased binding affinity and can thereby efficiently compete with Cs^+ ions and confine growth along the vertical direction.[18, 20] In this study, the oleic acid concentration is held constant at 3.895 mmols of oleic acid to 0.019 mmols of Cs-OA in order to specifically examine the influence of ligand aggregation on crystal growth. The injection of Cs-OA initiates rapid crystallization of the ionic perovskite and the reaction is quenched immediately after injection by the addition of hexanes.[24] The rapid nucleation and growth kinetics of perovskite nanoplatelets render precise dimensional control somewhat more challenging as compared, for instance, to II-VI chalcogenide quantum dots. Nevertheless, the alkylammonium cations acting as surface-capping ligands strongly influence the

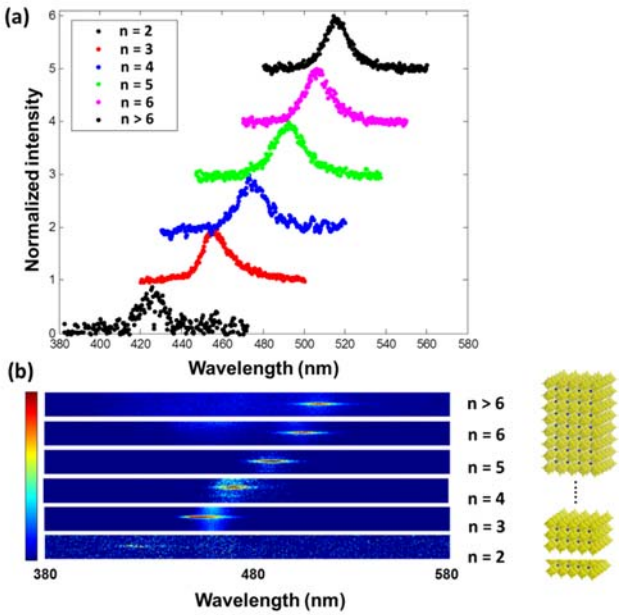

Figure III. 1 (a) Single-particle PL emission spectra acquired for $CsPbBr_3$ nanoplatelets spanning the range from 2—6 octahedral layers in thickness. The spectra are compared to spectra acquired for bulk (n > 6) $CsPbBr_3$, which is beyond the quantum confined regime. (b) Intensity map acquired for single particles depicting the shift of emission maximum with increasing layer thickness.

morphology and dimensions of the resulting nanoplatelets by controlling the monomer supersaturation, monomer addition to incipient nuclei, and the diffusion rate.[20, 27] In this article, we have sought to correlate the nature of the ligand shell to the specific dimensions of the obtained $CsPbBr_3$ nanoplatelets and to develop mechanistic understanding of ligand-directed crystal growth.

Figure A. 7 and **Table A. 2** shows the result of a Rietveld refinement to the powder X-ray diffraction of $CsPbBr_3$ nanoplatelets obtained using C8 amine as the ligand at 150°C. Unlike in the bulk wherein the cubic phase is the thermodynamically stable polymorph, colloidal nanocrystals prepared at these

temperatures have been seen to have a preference for a lower symmetry orthorhombic phase.[21, 28] Indeed, the refinement suggests the stabilization of a distorted orthorhombic structure with space group *Pnma* and lattice parameters of a = 8.29 Å, b = 11.79 Å, and c = 8.23 Å (Table 1). The vertical dimensions of the nanoplatelets are thus expressed in terms of the number of $PbBr_6$ octahedral layers.

Evaluation of the dimensional confinement of the nanoplatelets is facilitated by the thickness-dependent spectral signatures induced as a result of quantum confinement along the vertical direction. A Bohr exciton diameter of ca. 7.0 nm has been deduced for this material suggesting substantial scope for tunability of the bandgap as a function of $PbBr_6$ octahedral layer thickness (in both cubic and orthorhombic crystal structures, the thickness of a single octahedral layer is 0.584 nm).[18-21, 27] Single-particle spectroscopy enables us to unequivocally assign the spectral signatures of individual nanoplatelets with varying thickness based on the peak positions of the PL emission maxima, which correspond to band-edge emission.[29] **Figure III. 1** indicates single-particle PL emission spectra with distinctive spectral signatures for bilayer (λ_{em} = 427 nm), trilayer (λ_{em} = 456 nm), four-layer (λ_{em} = 475 nm), five-layer (λ_{em} = 490 nm), six-layer (λ_{em} = 505 nm), and bulk (n > 6, λ_{em} = 515 nm) $CsPbBr_3$ nanoplatelets**.**[18, 19] [30] The samples shown in Figure III.1 correspond to different synthetic conditions in each instance. The PL emission spectra for individual nanoplatelets depicted in Figure III. 1 correspond to the following synthetic conditions with a fixed ligand concentration of 0.760 mmol of RA: n = 2 nanoplatelets have been obtained using

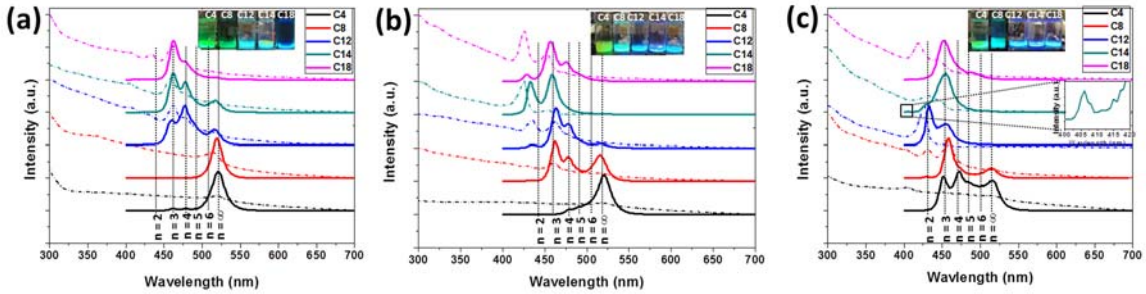

Figure III.2 Photoluminescence emission (solid line) and UV-vis absorption spectra (dotted line) obtained for $CsPbBr_3$ nanoplatelets prepared using different chain lengths of alkylamines (C4—C18) at (a) 150°C, (b) 100°C, and (c) 50°C. The insets of (a-c) depict digital photographs of colloidal dispersions of the nanoplatelets in hexanes under UV illumination. The bottom inset to (c) depicts a magnified view of the spectra in the range from 400—420 nm indicating stabilization of monolayer nanoplatelets for the C14 alkylamine.

the C12 amine at 50°C; n = 3 nanoplatelets have been isolated from dispersions prepared with the C12 amine at 100 °C; n =4 and n = 5 nanoplatelets have been imaged from dispersions prepared using C12 amine at 150°C (the latter is a minority species); and n = 6 and particles in the bulk regime have been imaged from samples prepared using the C8 amine at 100°C (the former is a minority species). The PL excitation spectra for these samples are depicted as **Figure A. 8**. The PL emission maxima are red-shifted with increasing layer thickness as a result of reduced extent of quantum confinement. In contrast to II-VI semiconductor quantum dots where in principle the particle size, and thus extent of quantum confinement can be varied continuously, for $CsPbBr_3$, discrete quantized values of bandgaps are accessible based on the number of octahedral layers stacked along the confined dimension. Single-layered nanoplatelets have not been isolated under these conditions but a contribution from such species is

discernible in ensemble PL spectra (λ_{em} = 406 nm) and can be attributed to a minority population of such species (Figure III. 2c, inset).

The measured PL emission maxima wavelengths and assignments to layer thicknesses in terms of numbers of octahedral layers are listed in **Table A. 3**. The thickness-dependent spectral signatures allow for mapping of the influence of reaction conditions on the extent of dimensional confinement and thereby facilitate development of a rich picture of the thermodynamics and kinetics of crystal growth.

Figures III. 2a-c plots the evolution of PL emission spectra as a function of the alkylamine chain length at different temperatures (Pb-OA:RA ratio has been kept constant at 1:20). The insets depict digital photographs of colloidal dispersions of the nanoplatelets in hexanes under UV excitation. The rapid crystallization of the ionic perovskite halides yields a distribution of layer thicknesses[24] for several of the reaction conditions, which are manifested as multiple PL emission peaks. The average layer thickness for a specific set of reaction conditions (temperature and alkylamine chain length) is deduced by fitting the ensemble PL emission spectra to multiple Gaussian peaks, each corresponding to the emission of $CsPbBr_3$ nanoplatelets of a certain layer thickness as depicted in **Figure A. 9**. Figure A.9 and **Table A. 4** depict the fitting results for all of the samples prepared here along with the assignments to the number of octahedral layers. The relative intensity of each fitted curve is calculated as described in the Experimental section and provides a measure of the

average layer thickness. The corresponding optical absorption spectra are depicted in Figure III.2a-c. The absorption spectra in Figure III. 2b depicts a consistent blue shift of optical absorption feature, which corroborate the progression seen in Figure III. 2a. While the photoluminescent quantum yield is thickness-, excitation-wavelength, and ligand-dependent, the high quantum yield (>40%) of these materials allows for a reasonable evaluation of the layer thickness.[21, 30, 31] The trends observed in PL emission along with absorption spectra have been further verified by electron microscopy (*vide infra*).

Figure III. 3 plots the average thickness of the nanoplatelets expressed in terms of the number of octahedral layers stacked along the vertical dimension as a function of the temperature and alkyl chain length of the alkylamine ligands, clearly demonstrating the strong influence of these parameters on the extent of dimensional confinement. For a reaction temperature of 150°C, increasing the chain length of the alkylamine results in a monotonic decrease of the thickness of the nanoplatelets, which is manifested as an overall blue-shift of the PL emission (Figure III. 2a). Using C4 and C8 capping ligands results in a PL emission peak centered at 520 nm, which suggests that the nanocrystals grow beyond the quantum confined regime to the bulk limit as these ligands are unable to substantially constrain crystal growth. The C12 moiety primarily yields four-layered platelets with a PL emission peak of 475 nm and minority populations at 456, 490, and 520 nm corresponding to n = 3, 5, and bulk, respectively. Further increasing the chain length to C14 yields a primary product of tri-layered

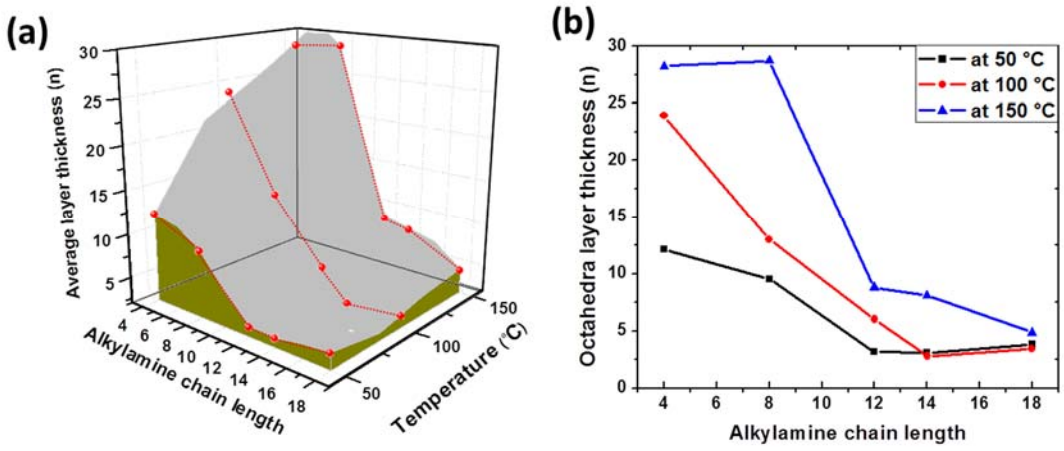

Figure III. 3 (a) 3D correlation and (b) 2D mapping of the nanoplatelet thickness expressed in terms of the number of octahedra layers as a function of the alkyl chain length at different reaction temperatures

nanoplatelets with a blue-shifted characteristic PL emission band at 456 nm with minor contributions from n = 4, 5, and bulk species. As the chain-length is further increased, the C18 ligand yields tri-layered nanoplatelets with minor contributions from n = 4, 5 species. A prominent blue-shift of the emission with increasing chain length is clearly discernible in the digital photograph shown as the inset of Figure III. 2a. A similar blue-shift is evidenced for the absorption features in the spectra depicted in Figure III. 2a. An analogous correlation with increasing chain length is also observed for reaction temperatures of 100 and 50°C for alkylamine chain lengths ranging from C4 to C12.

Once precursors are decomposed resulting in the formation of monomeric species, the nucleation and growth of the crystals will be influenced by the monomer supersaturation, which in turn is influenced by the ligand chain length. The diffusion rate of the monomers is further dependent on the length of the

ligands and thus it is clear that with increasing ligand chain length, the electrostatically bound alkylammonium monolayer is increasingly able to restrict monomer addition, thereby limiting the vertical growth of the nanoplatelets.[20, 32-35] In other words, longer chain alkylammonium cations are able to inhibit access of incoming monomers to the incipient crystallite and the monomers themselves are likely to be sterically more encumbered and thus slower to diffuse with the net effect of longer chain species being able to substantially retard crystal growth, allowing for stabilization of ultra-thin nanoplatelets.

The kinetics of crystal growth being proportional to the diffusion coefficient of monomers is expected to be accelerated at higher temperatures and indeed for C4-C12 ligands, the thickness of the layers increases with increasing reaction temperature.[20, 32, 36] **Figure A. 10** depicts the PL emission spectra for each alkylammonium chain length examined here as a function of temperature. Interestingly, Figure III. 3 and A. 10 indicate several departures from the correlations noted above for longer chain alkylammonium cations C14 and C18. At 50°C, despite their greater steric footprint and sluggish diffusion, the layer thicknesses are increased as compared to C12. Indeed, the thinnest nanoplatelets at 50°C are obtained for C12, at 100°C for C14, and at 150°C for C18. Figure A.10 indicates that for C14 ligands, decreasing temperature from 150 to 100°C results in the nanoplatelets becoming thinner but further decreasing the temperature to 50°C induces a red-shift of the emission suggesting the stabilization of thicker nanoplatelets.

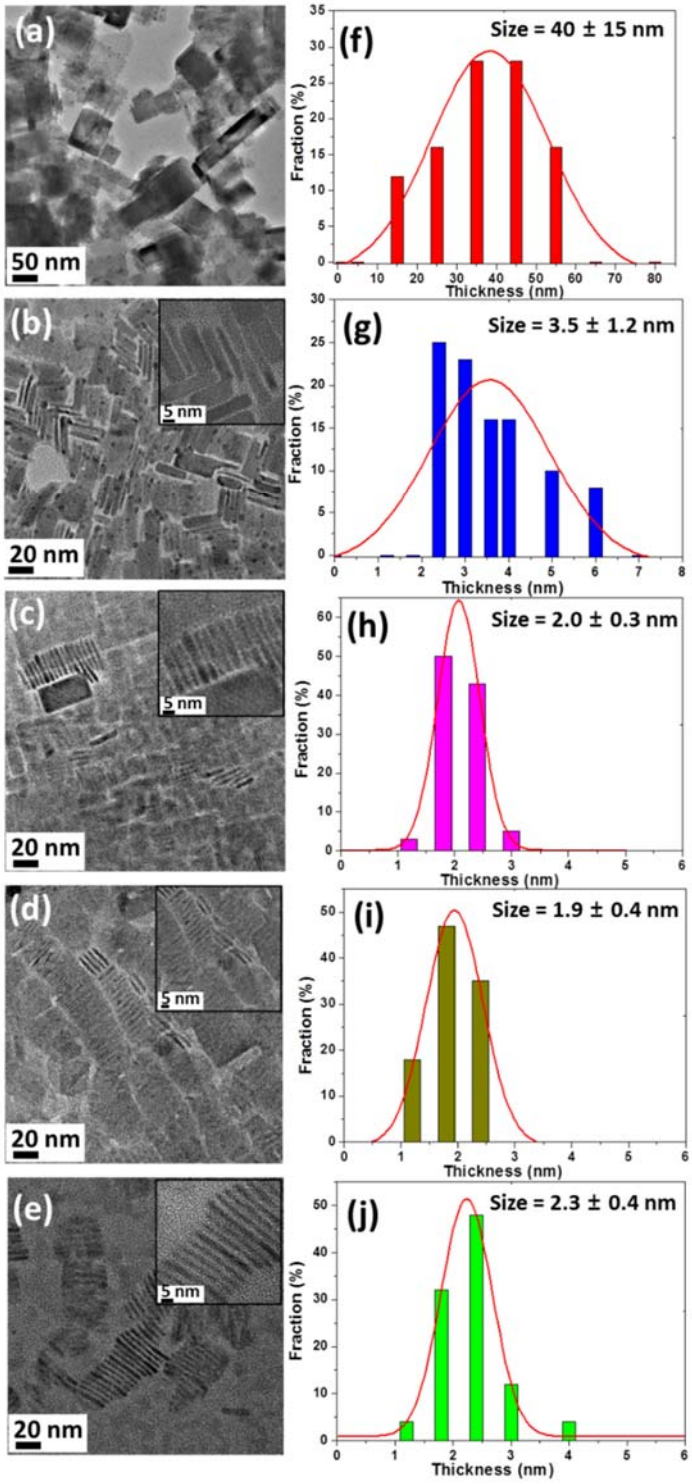

Figure III. 4 TEM images and size distribution histograms acquired for nanoplatelets prepared by injection at 100°C using alkylamines with different chain-lengths: a,f) C4; b,g) C8; c,h) C12; d,i) C14; and e,j) C18.

Further evaluation of the extent of dimensional confinement has been derived from transmission electron microscopy (TEM) data depicted in **Figure III. 4** The relative stability of these materials under an electron beam (methylammonium lead halides in contrast are rapidly disintegrated) and their predilection to form columnar stacks (e.g., inset to Figure III.4c) arrayed in a face-to-face manner allows for direct measurement of the thickness of the prepared nanoplatelets. Figure III. 4 contrasts the nanocrystals obtained as a function of varying alklyamine chain length at temperature of 100°C. Additional TEM images acquired for $CsPbBr_3$ nanoplatelets prepared as a function of varying alkylamine chain lengths, illustrating top views of the extended basal planes of the nanoplatelets, are shown in **Figure A. 11**. The shorter-chain ligands yield cubic morphologies or relatively thicker rectangular platelets that are strongly modified to anisotropic thin nanoplatelets for longer chain alkylamines. The selected area electron diffraction (SAED) pattern depicted in Figure A.11f attests to the single-crystalline nature of individual nanoplatelets, which is further verified by the lattice-resolved HRTEM images depicted in **Figure A. 12a and b**. The C4 amine yields large rectangular nanocrystals with lateral dimensions of 100±50 nm and vertical dimensions of 40±15 nm. The smallest dimension is well above the Böhr radius, consistent with the observation of bulk band-edge emission in PL emission spectra of these nanoplatelets (Figure III. 2). Increasing the chain-length of the alkylamine to C8 renders the growth strongly anisotropic, resulting in the stabilization of thin nanoplatelets, indicative of selective dimensional confinement

along the vertical direction (Figure A. 12b).[37] A relatively broad size distribution of nanoplatelets is observed under these conditions as illustrated by the size distribution histograms in Figure III. 4f,g. Figure A. 12c provides a high-magnification view of the columnar stacks; such images allow for precise thickness measurements and assignment to discrete numbers of octahedral layers. The nanoplatelets prepared using C8 alkylamine are 30±5 nm in terms of lateral dimensions. In terms of vertical dimensions, two discrete populations are discernible, thin nanoplatelets with vertical dimensions of 3±1 nm and thicker nanoplatelets with vertical dimensions of 6±2 nm. The former distribution corresponds to stacks of 3–6 octahedral layers, whereas the latter is beyond the quantum confined regime. The observed distribution of vertical dimensions in histograms deduced from the TEM images is consistent with the multiple emission bands observed in the PL spectra (Figure III. 2). The anisotropic growth induced by the alkylammonium ligands corresponds to their selective binding

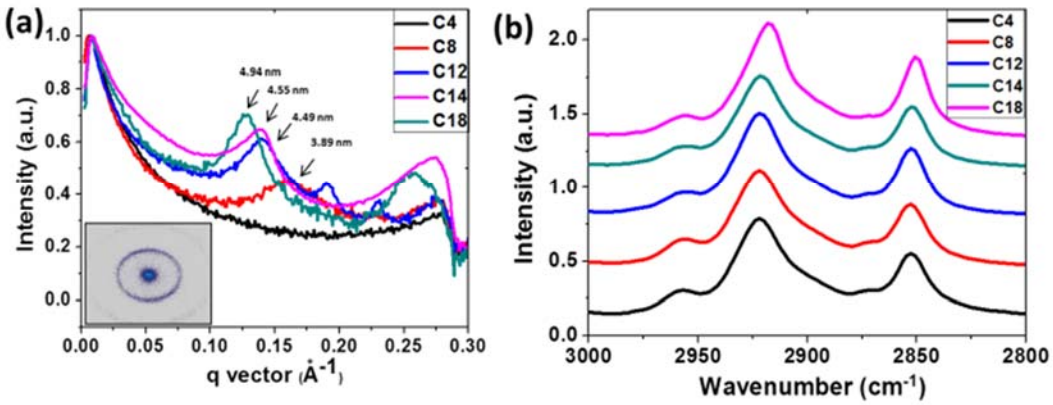

Figure III. 5 (a) SAXS and (b) IR spectra of few-layered perovskite nanoplatelets prepared using various alkylamine chain lengths at 100 °C. The insets (a) depict SAXS pattern of nanoplatelets using C18.

along the basal planes of the nanoplatelets wherein they are able to selectively regulate monomer addition along the vertical direction.[20, 37] In contrast, monomers can continue to be added to the uncapped edges enabling the lateral growth of the nanoplatelets along the *ab* plane.[25, 38] The relatively greater thickness of the C8 monolayer as compared to C4 alkylammonium monolayer formed on the nanoplatelet faces retards vertical oligomerization, yielding thinner nanoplatelets. For longer-chain C12 alkylamines, extremely thin nanoplatelets are stabilized that range 25±5 nm in lateral dimensions but are only 2.0±0.3 nm in terms of vertical dimensions. The corresponding values for C14 alkylamines are 20±5 nm in terms of lateral dimensions and 1.9±0.4 nm for vertical dimensions. As also illustrated by Figure III. 3, C18 alkylamines appear to be less adept at confining crystal growth as compared to their C14 counterparts at 100°C. Indeed, these ligands yield $CsPbBr_3$ nanoplatelets with lateral dimensions of 35±5 nm and vertical dimensions of 2.3±0.4 nm.

Figure III. 4 and A. 12 indicate the tendency, particularly of the thinner nanoplatelets, to form columnar stacks. Such columnar stacks comprising ligand-capped nanoplatelets spaced at quasi-regular intervals suggests a high degree of ordering of alkylammonium groups assembled on the basal planes of the nanoplatelets, essentially forming bilayers. Small angle X-ray scattering (SAXS) has been used to characterize the vertical stacking and long-range ordering of the nanoplatelets **(Figure III. 5a)**. [19] The nanoplatelets prepared using C4 do not exhibit any characteristic reflections in SAXS patterns; this is consistent with the

stabilization of larger cubes that do not further show a pronounced degree of ordering. For the longer-chain alklyamines, a distinctive reflection is evidenced and is shifted to a lower angular momentum vector value with increasing chain-length; the reflection is ascribed to a quasi-regular periodicity established between the nanoplatelets and is shifted from q = 0.164 $Å^{-1}$, corresponding to a separation of 3.89 nm for C8, to q = 0.140 $Å^{-1}$ (separation of 4.49 nm) for C12, to q = 0.138 $Å^{-1}$ (separation of 4.55 nm) for C14, and q = 0.128 $Å^{-1}$ (separation of 4.94 nm) for C18 (Figure III.5a). The repeat distance corresponds to the bilayer of the self-assembled alklyammonium monolayers on the basal planes of the platelets in addition to the thickness of the few-layered nanoplatelets.[20] With an increase of the chain length of the alkylamines, the interlayer separation is monotonically increased as a result of the double layer of surface passivating ligands. The sharpening of the feature with increasing chain length corresponds to an increase in cumulative van der Waals' interactions, which define a more rigid ligand shell and yield a more consistent spacing. The increased ordering of the ligand shell is also reflected in the FTIR spectra contrasted in **Figure III. 5b**. The ν_a (CH_2) asymmetric stretching frequency and ν_s (CH_2) symmetric stretching frequency of the alkylamine is shifted to slightly lower wavenumbers with increasing chain length (ν_a (CH_2) from 2920 cm^{-1} for nanoplatelets capped with the C4 alkylamine to 2918 cm^{-1} for C18 as the capping ligand; ν_s (CH_2) from 2852 cm^{-1} for nanoplatelets capped with the C4 alkylamine to 2850 cm^{-1} for C18 as the capping ligand. These results suggest a higher number of dispersive interactions with

increasing chain length.[39] The intermolecular interactions reduce electron density in C—H bonds, slightly softening this mode.

The TEM, SAXS, and FTIR data presented in Figure III. 4, III. 5, and A. 12 provide strong *post facto* evidence for the presence of highly ordered monolayers of alkylammonium cations assembled on the basal planes of the $CsPbBr_3$ nanoplatelets. The correlation between chain length of the alkylamine capping ligands and the dimensional confinement induced within these systems can be attributed to the characteristics of such monolayers. Upon initial rapid nucleation of highly ionic crystallites, the alkylammonium cations are electrostatically bound to negatively charged planes of $PbBr_6$ octahedra. Their preferential binding to these surface planes restricts monomer addition along the *c* direction, whereas growth along the *ab* plane is less hindered, enforcing planar growth anisotropy. The spontaneous binding of the alkylammonium cations onto the $CsPbBr_3$ nanocrystals is mediated by two specific interactions with distinguishable free energy contributions:

$$\Delta G_{\text{binding}} = \Delta G_{\text{electrostatic}} + \Delta G_{\text{aggregation}} \quad \text{…(III. 3)}$$

The first term corresponds to the attractive interactions between the quaternary ammonium ions and the negatively charged surfaces, whereas the second term ($\Delta G_{\text{aggregation}}$) corresponds to the interactions between alkylammonium cations on the $CsPbBr_3$ surface. The electrostatic interactions between the alkylammonium cations and the surfaces are likely not a strong function of the alkylamine chain length for the C4—C18 moieties examined here

(given the strong enthalpic component of the electrostatic interaction, the loss of entropy at room temperature is relatively small). The latter term can further be separated into enthalpic and entropic components as per:

$$\Delta G_{\text{aggregation}} = \Delta H_{\text{aggregation}} - T\Delta S_{\text{aggregation}} \ldots \text{(III. 4)}$$

where T is the absolute temperature. In comparison to a freely diffusing molecule in solution, an amine molecule adsorbed onto a surface within a crystalline monolayer is enthalpically stabilized by dispersive interactions with adjacent molecules;[26, 40] the magnitude of the dispersive interactions increase with the number of carbon atoms. In contrast, assembly within a monolayer incurs an entropic penalty as a result of loss of conformational degrees of freedom and is also chain-length dependent.

The Gibbs free energy of aggregation of linear primary amines varies as a function of alkyl chain length as per:

$$\Delta G_{aggregation}(n) = -RT(nln\Delta w + lnw_0) \ldots \text{(III. 5)}$$

where n is the alkyl chain length, Δw has been empirically determined based on regression fits to aggregation data and is 4.241 for each methylene group.[41, 42]

The value of w_0 has been empirically determined to be 4.16×10^{-4} for alkylamines.[43] $\Delta G_{aggregation}$ of the alkylamines used here at the different reaction temperatures are plotted in **Figure A. 13**.[42] Figure A. 13 suggests that beyond C6 alkylamines, the formation of well-ordered monolayers of long *n*-alkyl chains is strongly favored simply taking into account aggregational parameters.[42, 44] If incipient nuclei are capped immediately with alkylammonium cations, their

growth will depend fundamentally on the rate of monomer addition. From a kinetic perspective, the rate of monomer addition will scale as

$$Rate_{\text{growth}} \propto \frac{d^2}{D} \quad \ldots(\text{III. 6})$$

where d is the diffusion path length that the monomer needs to traverse to the nuclei and D is the diffusion coefficient. Two distinct diffusion regimes can be distinguished, diffusion of monomers in solution to a growing nanocrystal and diffusion of the monomer through the ordered ligand shell following Fickian kinetics.[45] The diffusion coefficient can be expressed as:

$$D = \frac{kT}{6\pi\eta a}\ln(\frac{2a}{b})\ldots(\text{III. 7})$$

where D is the diffusion coefficient, k_B is Boltzmann's constant, T is the absolute temperature, η is the viscosity of the medium, a represents the radius of the long axis, and b is the radius of the short axis of prolate ellipsoids of the alkylamine.[34] In the two regimes, the viscosity of the medium will differ substantially with diffusion through the ligand-shell being subject to a substantially greater retarding force as compared to diffusion across the solution.

These correlations allow for mechanistic understanding of the observed chain-length and temperature-dependence of the extent of dimensional confinement. The diffusion coefficient of monomers both in solution as well as across the alkylammonium bilayer is proportionally increased with decrease of the chain-length, resulting in relatively rapid growth of nanocubes approaching the bulk limit.[20, 26, 34] As per Equation III. 4, the quasi-solid-state diffusion path length

through the ligand shell is further relatively small for shorter chain lengths. In contrast, thinner nanoplatelets are stabilized for longer ligand chain lengths owing to the larger interfacial diffusion path lengths and the slower diffusion of monomers in solution and across the ligand shell (Figures. III. 2-4).[40, 46] Increasing temperature imparts greater kinetic energy and increases the diffusion coefficient as per Equation III. 7 resulting in easier monomer addition and the stabilization of relatively thicker nanoplatelets (Figure III. 3).

Figure III. 6 plots $\Delta G_{\text{aggregation}}$ at different temperatures *versus* the thickness of the nanoplatelets expressed in terms of octahedral layer thickness, suggesting that ligand shell crystallinity is generally well correlated with dimensional confinement. This is especially true at 150°C, which suggests that the interplay between aggregational enthalpic gain and entropic cost of forming ordered ligand shells governs the overall rate of monomer addition and determines the specific octahedral layer thickness stabilized at a given temperature for a capping ligand of a specific chain length.[20 44, 46] Considering that the attachment and aggregation of alkylammonium cations is part of a dynamic equilibrium also characterized by ligand desorption, increasing the concentration of the amine ought to favor formation of the ligand shell. **Figure A. 14** demonstrates the influence of concentration of C4, C14, and C18 amines at 100 °C. For the short-chain amine, even high concentrations do not substantially suppress growth along the vertical direction given the high solution-phase and interfacial diffusion coefficients and the short diffusion path length across the monolayer. In contrast,

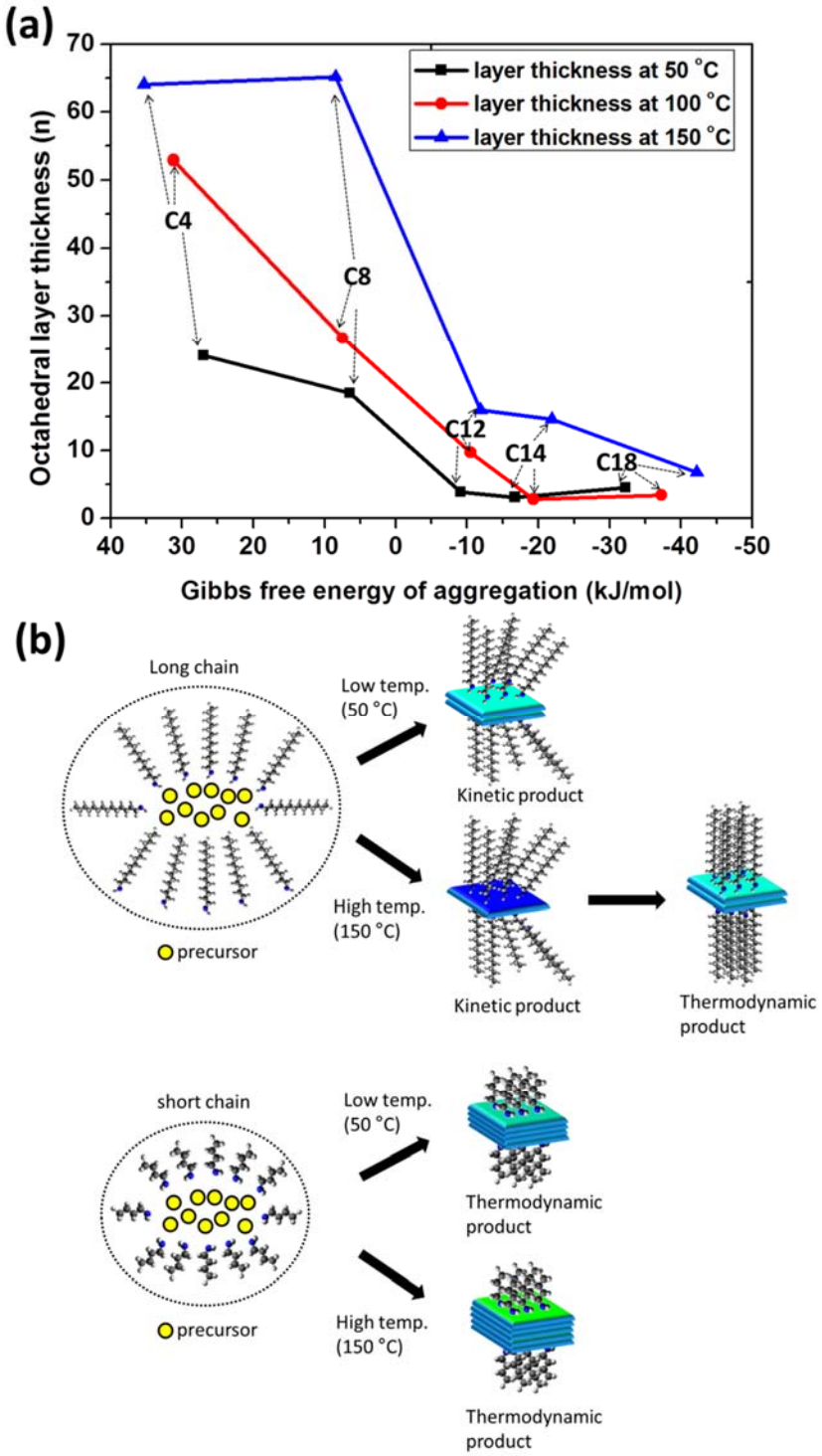

Figure III. 6 (a) Aggregational Gibbs free energy of ligand packing as a function of chain-length of ligands at various temperature and (b) schematic illustration of ligand shell packing and rearrangement at low and high temperatures.

for both long-chain amines of C14 and C18, increasing the alkylamine concentration strongly limits vertical growth. Specifically, the dimensional confinement along vertical direction as a function of concentration of C14 can be clearly discernible for C14 that the octahedral layer thickness change from bulk limit to bilayer upon increasing the ligand concentration. As noted above, longer chain ligands (C14 and C18) at lower temperatures exhibit a pronounced departure from this correlation at 50 and 100°C. Despite their longer chain lengths and expected sluggish monomer diffusion, Figures. III. 2-4 indicate the stabilization of relatively thicker nanoplatelets. Adsorption of ligand molecules likely initially happens in a somewhat stochastic manner with subsequent desorption/adsorption equilibria facilitating ligand shell rearrangement from a disordered to an ordered structure.[47 48] The thermal energy required to facilitate this ordering is furthermore dependent on chain length. It is thus posited that the longer-chain alkylamines form relatively less ordered (metastable) ligand-shell assemblies at low temperatures; the relatively lower packing density make such ligand shells more permeable to monomers, resulting in the growth of thicker nanoplatelets (Figure III. 6b).[47] The up-turn in Figure III. 3 can thus be ascribed to kinetic stabilization of less ordered ligand shells on the basal planes.

Indeed, to examine the influence of relatively poor ligand shell crystallinity, primary (*n*-octylamine), secondary (di-*n*-octylamine), and tertiary (tri-*n*-octylamine) amines have been used in the synthesis of $CsPbBr_3$ nanoplatelets.[35, 49] **Figure III. 7** depicts a strong red-shift of the PL emission

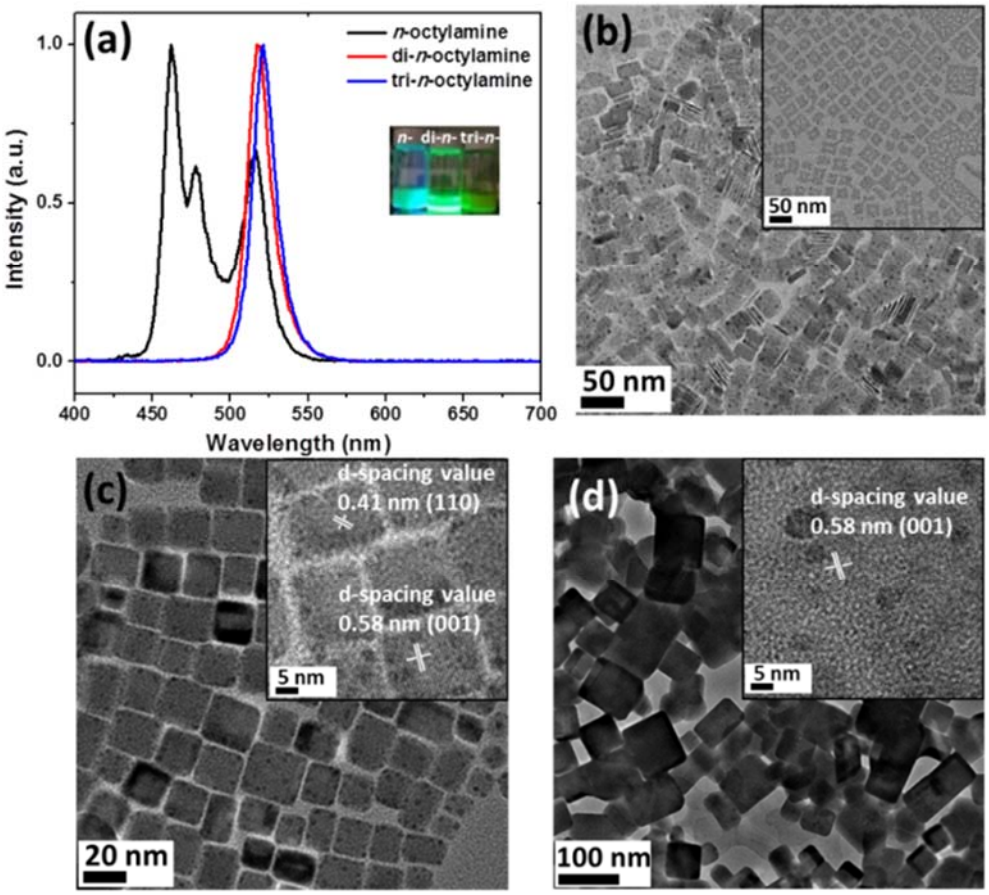

Figure III. 7 (a) PL emission spectra of $CsPbBr_3$ nanocrystals prepared using *n*-octylamine, di-*n*-octylamine, and tri-*n*-octylamine. Corresponding TEM images for (b) *n*-octylamine, (c) di-*n*-octylamine, and (d) tri-*n*-octylamine.

spectra to the bulk limit of 515 nm with increasing branching of the alkylamine, suggesting that reducing the crystallinity of the ligand shell results in stabilization of thicker nanoplatelets. The corresponding TEM images further confirm thicker vertical dimensions of 20±5 nm for $CsPbBr_3$ nanoplatelets prepared using di-*n*-octylamine and 80±20 nm for $CsPbBr_3$ nanoplatelets prepared using tri-*n*-octylamine as compared to 3±1 nm for the nanoplatelets prepared using the primary amine. The branched amines have a stronger entropic penalty and lower

enthalpic gain upon surface adsorption yielding a less ordered ligand shell. The reduced ordering and lower packing density of the ligand shell for the secondary and tertiary amines facilitates easier monomer addition yielding thicker nanoplatelets.[49]

III.4 Conclusions

In summary, the influence of ligand chain length, branching, concentration, and temperature on the dimensional confinement of $CsPbBr_3$ nanoplatelets has been mapped. Alkylammonium capping groups induce anisotropic growth by selectively binding to the basal planes of $CsPbBr_3$ nanoplatelets. The ability of the ligands to induce dimensional confinement is found to depend on the crystallinity of the ligand shell; a high degree of ordering correlates to a higher degree of dimensional confinement primarily by limiting monomer addition. The degree of ordering is chain-length dependent and depends on the balance between enthalpic gain from increased dispersive interactions and entropic loss arising from conformational restrictions. In general, at high temperatures longer-chain primary alkylamines yield better ordering of monolayers and restrict monomer diffusion while also providing a longer interfacial diffusion path length. However, at lower temperatures, disordered monolayers represent metastable assemblies that are less effective at constraining growth along the vertical dimensions. These results provide a mechanistic basis for developing syntheses to precisely modulate the dimensions of perovskite halide nanoplatelets.

III.5 References

(1) Andrews, J. L.; De Jesus, L. R.; Tolhurst, T. M.; Marley, P. M.; Moewes, A.; Banerjee, S., Intercalation-induced Exfoliation and Thickness-modulated Electronic Structure of a Layered Ternary Vanadium Oxide. *Chem. Mater.* **2017,** 29, 3285-3294.

(2) Chhowalla, M.; Shin, H. S.; Eda, G.; Li, L.-J.; Loh, K. P.; Zhang, H., The chemistry of two-dimensional layered transition metal dichalcogenide nanosheets. *Nat. Chem.* **2013,** 5, 263-275.

(3) Ithurria, S.; Tessier, M.; Mahler, B.; Lobo, R.; Dubertret, B.; Efros, A. L., Colloidal nanoplatelets with two-dimensional electronic structure. *Nat. Chem.* **2011,** 10, 936-941.

(4) Lhuillier, E.; Pedetti, S.; Ithurria, S.; Nadal, B.; Heuclin, H.; Dubertret, B., Two-dimensional colloidal metal chalcogenides semiconductors: synthesis, spectroscopy, and applications. *Acc. Chem. Res.* **2015,** 48, 22-30.

(5) Wang, Q. H.; Kalantar-Zadeh, K.; Kis, A.; Coleman, J. N.; Strano, M. S., Electronics and optoelectronics of two-dimensional transition metal dichalcogenides. *Nat. Nanotechnol.* **2012,** 7, 699-712.

(6) Di, D.; Musselman, K. P.; Li, G.; Sadhanala, A.; Ievskaya, Y.; Song, Q.; Tan, Z.-K.; Lai, M. L.; MacManus-Driscoll, J. L.; Greenham, N. C., Size-dependent photon emission from organometal halide perovskite nanocrystals embedded in an organic matrix. *J. Phys. Chem. Lett* **2015,** 6, 446-450.

(7) Dong, Q.; Fang, Y.; Shao, Y.; Mulligan, P.; Qiu, J.; Cao, L.; Huang, J., Electron-hole diffusion lengths> 175 μm in solution-grown $CH_3NH_3PbI_3$ single crystals. *Science* **2015,** 347, 967-970.

(8) Shi, D.; Adinolfi, V.; Comin, R.; Yuan, M.; Alarousu, E.; Buin, A.; Chen, Y.; Hoogland, S.; Rothenberger, A.; Katsiev, K., Low trap-state density and long carrier diffusion in organolead trihalide perovskite single crystals. *Science* **2015,** 347, 519-522.

(9) Swarnkar, A.; Chulliyil, R.; Ravi, V. K.; Irfanullah, M.; Chowdhury, A.; Nag, A., Colloidal CsPbBr3 perovskite nanocrystals: Luminescence beyond traditional quantum dots. *Angew. Chem.* **2015,** 127, 15644-15648.

(10) Tyagi, P.; Arveson, S. M.; Tisdale, W. A., Colloidal organohalide perovskite nanoplatelets exhibiting quantum confinement. *J. Phys. Chem. Lett* **2015,** 6, 1911-1916.

(11) Wang, H.; Whittaker-Brooks, L.; Fleming, G. R., Exciton and Free Charge Dynamics of Methylammonium Lead Iodide Perovskites Are Different in the Tetragonal and Orthorhombic Phases. *J. Phys. Chem. C* **2015,** 119, 19590-19595.

(12) Kim, Y.-H.; Cho, H.; Heo, J. H.; Kim, T.-S.; Myoung, N.; Lee, C.-L.; Im, S. H.; Lee, T.-W., Multicolored Organic/Inorganic Hybrid Perovskite Light-Emitting Diodes. *Adv. Mater.* **2015,** 27, 1248-1254.

(13) Ling, Y.; Yuan, Z.; Tian, Y.; Wang, X.; Wang, J. C.; Xin, Y.; Hanson, K.; Ma, B.; Gao, H., Bright Light-Emitting Diodes Based on Organometal Halide Perovskite Nanoplatelets. *Adv. Mater.* **2016,** 28, 305-311.

(14) Yantara, N.; Bhaumik, S.; Yan, F.; Sabba, D.; Dewi, H. A.; Mathews, N.; Boix, P. P.; Demir, H. V.; Mhaisalkar, S., Inorganic halide perovskites for efficient light-emitting diodes. *J. Phys. Chem. Lett* **2015,** 6, 4360-4364.

(15) Protesescu, L.; Yakunin, S.; Bodnarchuk, M. I.; Krieg, F.; Caputo, R.; Hendon, C. H.; Yang, R. X.; Walsh, A.; Kovalenko, M. V., Nanocrystals of cesium lead halide

perovskites ($CsPbX_3$, X= Cl, Br, and I): novel optoelectronic materials showing bright emission with wide color gamut. *Nano Lett.* **2015,** 15, 3692-3696.

(16) Tsai, H.; Nie, W.; Blancon, J.-C.; Stoumpos, C. C.; Asadpour, R.; Harutyunyan, B.; Neukirch, A. J.; Verduzco, R.; Crochet, J. J.; Tretiak, S., High-efficiency two-dimensional Ruddlesden–Popper perovskite solar cells. *Nature* **2016,** 536, 312-316.

(17) Schmidt, L. C.; Pertegás, A.; González-Carrero, S.; Malinkiewicz, O.; Agouram, S.; Minguez Espallargas, G.; Bolink, H. J.; Galian, R. E.; Pérez-Prieto, J., Nontemplate synthesis of $CH_3NH_3PbBr_3$ perovskite nanoparticles. *J. Am. Chem. Soc.* **2014,** 136, 850-853.

(18) Akkerman, Q. A.; Motti, S. G.; Kandada, A. R. S.; Mosconi, E.; D'Innocenzo, V.; Bertoni, G.; Marras, S.; Kamino, B. A.; Miranda, L.; De Angelis, F., Solution synthesis approach to colloidal cesium lead halide perovskite nanoplatelets with monolayer-level thickness control. *J. Am. Chem. Soc.* **2016,** 138, 1010-1016.

(19) Bekenstein, Y.; Koscher, B. A.; Eaton, S. W.; Yang, P.; Alivisatos, A. P., Highly luminescent colloidal nanoplates of perovskite cesium lead halide and their oriented assemblies. *J. Am. Chem. Soc.* **2015,** 137, 16008-16011.

(20) Cho, J.; Choi, Y.-H.; O'Loughlin, T. E.; De Jesus, L.; Banerjee, S., Ligand-Mediated Modulation of Layer Thicknesses of Perovskite Methylammonium Lead Bromide Nanoplatelets. *Chem. Mater.* **2016,** 28, 6909-6916.

(21) Shamsi, J.; Dang, Z.; Bianchini, P.; Canale, C.; Stasio, F. D.; Brescia, R.; Prato, M.; Manna, L., Colloidal synthesis of quantum confined single crystal $CsPbBr_3$ nanosheets

with lateral size control up to the micrometer range. *J. Am. Chem. Soc.* **2016,** 138, 7240-7243.

(22) Cottingham, P.; Brutchey, R. L., Compositionally Dependent Phase Identity of Colloidal CsPbBr3–x I x Quantum Dots. *Chem. Mater.* **2016,** 28, 7574-7577.

(23) Pan, A.; He, B.; Fan, X.; Liu, Z.; Urban, J. J.; Alivisatos, A. P.; He, L.; Liu, Y., Insight into the Ligand-Mediated Synthesis of Colloidal $CsPbBr_3$ Perovskite Nanocrystals: The Role of Organic Acid, Base, and Cesium Precursors. *ACS Nano* **2016,** 10, 7943-7954.

(24) Lignos, I.; Stavrakis, S.; Nedelcu, G.; Protesescu, L.; deMello, A. J.; Kovalenko, M. V., Synthesis of cesium lead halide perovskite nanocrystals in a droplet-based microfluidic platform: fast parametric space mapping. *Nano Lett.* **2016,** 16, 1869-1877.

(25) Kort, K. R.; Banerjee, S., Ligand-Mediated Control of Dislocation Dynamics and Resulting Particle Morphology of GdOCl Nanocrystals. *Small* **2015,** 11, 329-334.

(26) De Roo, J.; Ibanez, M.; Geiregat, P.; Nedelcu, G.; Walravens, W.; Maes, J.; Martins, J. C.; Van Driessche, I.; Kovalenko, M. V.; Hens, Z., Highly dynamic ligand binding and light absorption coefficient of cesium lead bromide perovskite nanocrystals. *ACS Nano* **2016,** 10, 2071-2081.

(27) Sichert, J. A.; Tong, Y.; Mutz, N.; Vollmer, M.; Fischer, S.; Milowska, K. Z.; García Cortadella, R.; Nickel, B.; Cardenas-Daw, C.; Stolarczyk, J. K., Quantum size effect in organometal halide perovskite nanoplatelets. *Nano Lett.* **2015,** 15, 6521-6527.

(28) Cottingham, P.; Brutchey, R. L., On the crystal structure of colloidally prepared CsPbBr 3 quantum dots. *Chem. Commun.* **2016,** 52, 5246-5249.

(29) Jin, H.; Ahn, M.; Jeong, S.; Han, J. H.; Yoo, D.; Son, D. H.; Cheon, J., Colloidal Single-Layer Quantum Dots with Lateral Confinement Effects on 2D Exciton. *J. Am. Chem. Soc.* **2016,** 138, 13253-13259.

(30) Liang, Z.; Zhao, S.; Xu, Z.; Qiao, B.; Song, P.; Gao, D.; Xu, X., Shape-Controlled Synthesis of All-Inorganic CsPbBr3 Perovskite Nanocrystals with Bright Blue Emission. *ACS. Appl. Mater. Interfaces* **2016,** 8, 28824-28830.

(31) Du, X.; Wu, G.; Cheng, J.; Dang, H.; Ma, K.; Zhang, Y.-W.; Tan, P.-F.; Chen, S., High-quality CsPbBr 3 perovskite nanocrystals for quantum dot light-emitting diodes. *RSC Adv.* **2017,** 7, 10391-10396.

(32) Wang, W.; Banerjee, S.; Jia, S.; Steigerwald, M. L.; Herman, I. P., Ligand control of growth, morphology, and capping structure of colloidal CdSe nanorods. *Chem. Mater.* **2007,** 19, 2573-2580.

(33) Ji, X.; Copenhaver, D.; Sichmeller, C.; Peng, X., Ligand bonding and dynamics on colloidal nanocrystals at room temperature: the case of alkylamines on CdSe nanocrystals. *J. Am. Chem. Soc.* **2008,** 130, 5726-5735.

(34) De Nolf, K.; Capek, R. K.; Abe, S.; Sluydts, M.; Jang, Y.; Martins, J. C.; Cottenier, S.; Lifshitz, E.; Hens, Z., Controlling the Size of Hot Injection Made Nanocrystals by Manipulating the Diffusion Coefficient of the Solute. *J. Am. Chem. Soc.* **2015,** 137, 2495-2505.

(35) Foos, E. E.; Wilkinson, J.; Mäkinen, A. J.; Watkins, N. J.; Kafafi, Z. H.; Long, J. P., Synthesis and surface composition study of CdSe nanoclusters prepared using solvent

systems containing primary, secondary, and tertiary amines. *Chem. Mater.* **2006,** 18, 2886-2894.

(36) Li, Z.; Peng, X., Size/shape-controlled synthesis of colloidal CdSe quantum disks: ligand and temperature effects. *J. Am. Chem. Soc.* **2011,** 133, 6578-6586.

(37) Ithurria, S.; Bousquet, G.; Dubertret, B., Continuous transition from 3D to 1D confinement observed during the formation of CdSe nanoplatelets. *J. Am. Chem. Soc.* **2011,** 133, 3070-3077.

(38) Kort, K. R.; Banerjee, S., Shape-controlled synthesis of well-defined matlockite LnOCl (Ln: La, Ce, Gd, Dy) nanocrystals by a novel non-hydrolytic approach. *Inorg. Chem.* **2011,** 50, 5539-5544.

(39) Kern, M. E.; Watson, D. F., Influence of Dispersion Forces and Ordering on the Compositions of Mixed Monolayers of Alkanoic Acids on Nanocrystalline TiO_2 Films. *Langmuir* **2013,** 29, 13797-13807.

(40) Pradhan, N.; Reifsnyder, D.; Xie, R.; Aldana, J.; Peng, X., Surface ligand dynamics in growth of nanocrystals. *J. Am. Chem. Soc.* **2007,** 129, 9500-9509.

(41) Tanford, C., *The Hydrophobic Effect: Formation of Micelles and Biological Membranes 2d Ed*. John Wiley and Sons: 1980.

(42) Matulis, D.; Bloomfield, V. A., Thermodynamics of the hydrophobic effect. I. Coupling of aggregation and pK a shifts in solutions of aliphatic amines. *Biophys. Chem.* **2001,** 93, 37-51.

(43) Matulis, D., Thermodynamics of the hydrophobic effect. III. Condensation and aggregation of alkanes, alcohols, and alkylamines. *Biophys. Chem.* **2001,** 93, 67-82.

(44) Yang, Y.; Qin, H.; Jiang, M.; Lin, L.; Fu, T.; Dai, X.; Zhang, Z.; Niu, Y.; Cao, H.; Jin, Y., Entropic ligands for nanocrystals: From unexpected solution properties to outstanding processability. *Nano Lett.* **2016,** 16, 2133-2138.

(45) Chen, C.-F.; Mukherjee, P. P., Probing the morphological influence on solid electrolyte interphase and impedance response in intercalation electrodes. *PCCP* **2015,** 17, 9812-9827.

(46) Schessler, H.; Karpovich, D.; Blanchard, G., Quantitating the balance between enthalpic and entropic forces in alkanethiol/gold monolayer self assembly. *J. Am. Chem. Soc.* **1996,** 118, 9645-9651.

(47) Silberzan, P.; Leger, L.; Ausserre, D.; Benattar, J., Silanation of silica surfaces. A new method of constructing pure or mixed monolayers. *Langmuir* **1991,** 7, 1647-1651.

(48) Ulman, A., Formation and structure of self-assembled monolayers. *Chem. Rev.* **1996,** 96, 1533-1554.

(49) Luo, B.; Pu, Y. C.; Lindley, S. A.; Yang, Y.; Lu, L.; Li, Y.; Li, X.; Zhang, J. Z., Organolead halide perovskite nanocrystals: branched capping ligands control crystal size and stability. *Angew. Chem.* **2016,** 128, 9010-9014.

CHAPTER IV

LIGAND-ASSISTED NAVIATION OF A TERNARY PHASE DIAGRAM: ESTABLISHING SYNTHETIC CONTROL OF STRUCTURAL DIMENSIONALITY IN SOLUTION-GROWN CESIUM LEAD BROMIDE NANOCRYSTALS*

IV.1 Introduction

Lead halide perovksites have in short order emerged as promising next-generation candidates for photovoltaics, light-emitting displays, and other optoelectronic applications owing to their excellent electronic and optical properties such as tunable exciton binding energies, high absorption cross-sections, long carrier diffusion lengths, and near unitary photoluminescence quantum yields.[1-7] Hybrid organic—inorganic and all-inorganic ABX_3 perovksites (where A = Cs^+, $CH_3NH_3^+$, $CH_2(NH_2)^+$; B = Sn^{2+}, Pb^{2+}; X = Cl^-, Br^-, I^-) have been extensively investigated over the last several years.[8, 9] The phase space of ternary ABX_3 perovskites has been systematically mapped in terms of compositional variations; for instance, solid-solution mixed-halide perovskites have been stabilized through topochemical ion-exchange reactions;[10-12] similarly, a variety of transition metal dopants have been incorporated on the A- and B-cation sublattices.[13-15] Beyond substitutional variations, considerable progress has been achieved in terms of controlling particle dimensionality (below the Böhr exciton radius, estimated to be ca. 3.5 nm for $CsPbBr_3$)[16] and morphology (0D quantum dots and 2D nanosheets) through

the use of passivating ligands and templates.[17-19] Other ternary halide perovskites with reduced structural dimensionality and more anisotropic crystal structures have started to attract increasing attention such as the A_2PbX_4 Ruddlesden—Popper phases,[20, 21] tetragonal phases,[22, 23] and hexagonal Cs_4PbX_6.[24, 25] These ternary lead halides are characterized by structural motifs that are quite distinct from the ABX_3 phase. In contrast to the 3D network of corner-sharing $[PbBr_6]^{4-}$ octahedra in the 3D perovskite, the A_2PbX_4 Ruddlesden—Popper phase is constituted from 2D sheets of corner-sharing $[PbX_6]^{4-}$ octahedral layers alternated by layers of bulkier A ligands.[26 27] In this structure, the connectivity of $[PbX_6]^{4-}$ octahedra is constrained to being only along the 2D plane; the resulting 2D confinement of photogenerated excitons results in a strong blue-shift of the excitonic absorption feature as compared to analogous 3D perovskite compositions, which reflects the electronic decoupling of $[PbX_6]^{4-}$ octahedra along the crystallographic *c*-axis. Distinctive from these two motifs, the Pb-deficient Cs_4PbBr_6 phase has isolated $[PbBr_6]^{4-}$ octahedra surrounded by Cs-ions, crystallizing in a 0D structure characterized by highly localized excitations. The reduction in dimensionality is reflected in a pronounced increase of the bandgap; 3D $CsPbBr_3$ has a bulk bandgap of 2.36 eV (tunable in the 2.36—3.2 eV range as a result of confinement below the Böhr radius),[28] whereas in Cs_4PbBr_6 the bandgap is ca. 3.95 eV as a result of the electronic decoupling of $[PbBr_6]^{4-}$ octahedra.[24, 29] In this article, we demonstrate that the concentration, steric bulk, and denticity of ligands used in synthesis allows for remarkable tunability of structural dimensionality from 3D $CsPbBr_3$ to 0D Cs_4PbBr_6. In other words, coordinating

ligands allow for navigation of the Cs—Pb—Br phase diagram and provide simultaneous control over both structural and particulate dimensionality.

Akkerman *et al.* have developed a colloidal synthesis route for the preparation of 0D Cs_4PbBr_6 quantum dots with dimensions tunable in the range between 8.8—34.0 nm.[24] The obtained Cs_4PbBr_6 nanocrystals are transformed to $CsPbBr_3$ nanocrystals upon titrating with excess $PbBr_2$. Liu *et al.* have reported a post-synthetic modification route to access Cs_4PbBr_6 nanocrystals from $CsPbBr_3$ nanocrystals.[25] The addition of excess alkylamine or thiol ligands results in leaching of $PbBr_2$ and exfoliation of the 3D perovskite nanocrystals to Cs_4PbBr_6 nanocrystals.[30] However, the fundamental role of ligands in mediating the transformation between $CsPbBr_3$ and the lead-deficient Cs_4PbBr_6 phase remains to be understood. Two distinct mechanisms have been advanced to explain the observed ligand-induced structural transformations: (1) the reversible topochemical transformation of $CsPbBr_3$ to Cs_4PbBr_6 by the addition/elimination of $PbBr_2$ with complete retention of morphology; and (2) a dissolution—recrystallization process wherein the $CsPbBr_3$ phase is dissolved and subsequently precipitated as Cs_4PbBr_6. The latter mechanism is expected to allow for greater tunability of the particle dimensions and morphology, which in the case of the former is dictated by the dimensions and morphology of the initial nanocrystals.

Previous work by our group and others has demonstrated that for highly polar $CsPbBr_3$ nanocrystals, the diffusion coefficients, extent of aggregation, and the degree of ordering within self-assembled ligand monolayers determines the kinetics of crystal growth, yielding precise control over particle size and dimensionality.[31-34] Herein, we

evaluate the influence of added ligands in mediating the stabilization of 3D $CsPbBr_3$ and 0D Cs_4PbBr_6 structures based on variation of concentration, denticity, and steric bulk of alkylamine ligands.

IV.2 Experimental

Preparation of cesium oleate. A 0.4M solution of cesium oleate was prepared by dissolving Cs_2CO_3 with excess OLAc in ODE. Briefly, 2.5 mmol of Cs_2CO_3 was placed in a round-bottom flask with 10 mL of ODE and 2.5 mL of OLAc; the reaction mixture was heated to temperatures in the range of 150–200°C in an Ar ambient under Schlenk conditions until the solid inside the flask was completely dissolved to yield a transparent homogenous yellow liquid.

Ligand-Mediated Synthesis of $CsPbBr_3$ and Cs_4PbBr_6 Nanocrystals. Cesium lead bromide nanocrystals were synthesized by modifying a previously published ligand-mediated reprecipitation process.[1] A precursor solution containing Cs-oleate and $PbBr_2$ was prepared by dissolving 37.5 μL of 0.4M Cs-oleate (in ODE) and 0.030 mmol of $PbBr_2$ in 0.2 mL OLAc and 0.6 mL DMF (a polar solvent that dissolves all of the precursors) with the appropriate amount of the amine (RA). The molar ratio of Cs/Pb precursors was held constant at 0.5:1, whereas the Pb:RA molar ratio (1:*x*) was systematically varied for *x* between 0.5 and 8. Alkylamines with different denticity, steric bulk, and varying alkyl chain lengths were evaluated for their role in directing crystal growth. It is worth noting that for chelating ligands such as ODA, DDA, and TAA, the precursor solution was heated to 100–150°C in order to facilitate the dissolution of the

amine. In all of the syntheses, the prepared precursor solution containing the dissolved salts and ligands were rapidly added to 10 mL of toluene under vigorous stirring, thereby inducing the reaction of the polar precursors and crystallization (directed by the added ligands) at room temperature. The resulting precipitate was collected by centrifugation at 12,000—15,000 rpm for 10 min and then resuspended in 5 mL of toluene for further characterization.

Reversible phase transformation from $CsPbBr_3$ to Cs_4PbBr_6. A compositional transformation from Cs_4PbBr_6 to $CsPbBr_3$ was observed upon reacting the as-synthesized Cs_4PbBr_6 hexagonal platelets with excess $PbBr_2$ solution. In a typical transformation reaction, 2 mL of the Cs_4PbBr_6 dispersion in toluene was mixed with 0.2 mL $PbBr_2$ solution; the $PbBr_2$ solution was prepared separately by mixing 0.2 mmol of $PbBr_2$ with 0.25 mL of OLAc and 0.25 mL of OLAm in 0.5 mL of toluene. Upon addition of the $PbBr_2$ solution, the reaction mixture was heated at 120°C until its color changed to yellowish-green. Phase transformation from $CsPbBr_3$ to Cs_4PbBr_6 was accomplished by treating an as-prepared 2 mL colloidal dispersion of $CsPbBr_3$ with 0.2 mL of an ODA solution at 120°C until it turned cloudy; the ODA solution was prepared separately by mixing 0.2 mmol ODA with 0.25 mL OLAc in 0.75 mL toluene.

Characterization. Powder XRD measurements were performed using a Bruker D8-Focus Bragg-Brentano diffractometer with a Cu Kα radiation source (λ = 1.5418 Å) in the 2θ range of 10—60°. High-resolution transmission electron microscopy images were obtained using a FEI Tecnai G2 F20 ST instrument operated at an accelerating voltage of 200 kV. Energy dispersive X-ray spectroscopy (EDS) data were acquired using an

EDAX Instruments EDS detector. UV-Vis absorption spectra were obtained using a Hitachi U-4100 UV-Vis-NIR spectrophotometer in the range of 300—700 nm. Photoluminescence (PL) emission and excitation spectra were acquired using a Horiba PTI Quanta-Master series spectrofluorometer with a Xenon arc lamp as the source and a photomultiplier tube (PMT) as the detector. For $CsPbBr_3$ nanoplatelets, an excitation wavelength of 360 nm was used to acquire PL emission spectra and an emission wavelength of 515 nm was used to acquire PL excitation spectra. For Cs_4PbBr_6 hexagonal platelets, an excitation wavelength of 300 nm was used to acquire PL emission spectra and an emission wavelength of 360 nm was used to acquire PL excitation spectra. FTIR spectra were obtained using a Bruker VERTEX 70 instrument in the energy range of 3500—500 cm^{-1} with a spatial resolution of 4 cm^{-1}. The signal was averaged over 64 scans. NMR spectra were recorded on an Inova NMR spectrometer equipped with a Quad probe operating at a ^1H frequency of 300 MHz.

^1H NMR Characterization: *n*-octylamine (OA; 300 MHz; $CDCl_3$): δ 2.60—2.55 ppm (t, 2H), 1.33—1.12 ppm (10H), and 0.78 ppm (t; 3H); 1,8-octyldiamine (ODA; 300 MHz; $CDCl_3$) δ: 2.66—2.61 ppm (t, 4H) and 1.41—1.26 ppm (12H); oleic acid (OLAc; 300 MHz; $CDCl_3$) δ: 5.36 ppm (t, 2H), 2.38—2.33 ppm (t, 2H), 2.04—2.02 ppm (t, 4H), 1.67—1.62 (t, 2H), 1.32—1.28 ppm (18H), and 0.89 ppm (t, 3H)

IV.3 Results and Discussion

Tuning Structural Dimensionality Based on Ligand Denticity and Steric Bulk

Nanocrystals of the 3D $CsPbBr_3$ perovskite and the 0D hexagonal Cs_4PbBr_6 phases have been prepared using a ligand-mediated reprecipitation reaction at room temperature. In this reaction, a soluble mixture of cesium oleate, lead bromide, and alkylamines is prepared in DMF and rapidly added to toluene under vigorous stirring. The large resulting change in polarity and concomitant decrease in solubility induces rapid nucleation and growth of the ionic cesium lead bromide perovskite lattice in nanocrystalline form.[18, 33] The reaction mixture changes appearance from colorless to green or pale blue upon formation of $CsPbBr_3$ (depending on the extent of quantum confinement, as dictated by the added ligands) and to a turbid cloudy coloration upon stabilization of Cs_4PbBr_6. The stabilization of 0D or 3D ternary cesium lead bromide nanocrystals is observed to be dictated by the concentration, steric bulk, and denticity of the added alkylamine ligand. Figures IV. 1 and 2 present characterization data obtained for nanocrystals stabilized using varying concentrations of monodentate *n*-octylamine (OA) as the ligand. Figure IV. 3 presents analogous data acquired for nanocrystals stabilized using secondary and tertiary monodentate amines, whereas Figures IV. 4 and 5 present characterization data for nanocrystals stabilized using various concentrations of bidentate 1,8-octyldiamine (ODA) as the ligand. For the monodentate and bidentate C_8 ligands, the molar ratio of the $PbBr_2$ precursor to the added ligand has been varied in the range of 1:0.5 to 1:8. Notably, in the absence of any added ligand (x = 0) to induce

dimensional confinement, submicron-sized particles of $CsPbBr_3$ are stabilized (Figure A. 16).

Figure IV. 1A plots UV-vis absorption spectra of ternary lead halide perovskites stabilized as a function of increasing OA concentration (x); a pronounced blue-shift of the first excitonic absorption characteristic of $CsPbBr_3$ is observed from 515 nm (x = 0.5) to 450 nm (x = 4); however, the excitonic feature is completely eliminated at the highest OA concentration (x = 8) suggesting that the 3D perovskite is no longer stabilized at this concentration. At an OA concentration of x = 2, several features are observed, which can be reasonably attributed to the different layer thicknesses (n) of nanoplatelets: the band centered at 475 nm to n =4; the band at 450 nm to n = 3; the band at 400 nm to n = 1; and the band at 375 nm is characteristic of $PbBr_2$ complexed to OA (**Figure A. 17** shows UV-vis absorption and PL emission spectra acquired for this complex in DMF solution).[34]

The inset to Figure IV. 1A displays digital photographs of the colloidal dispersions of the nanocrystals under ambient laboratory light and 365 nm UV excitation; the bottom inset indicates a change in coloration from green to blue and to violet-blue with increasing concentration of OA, suggestive of the increased dimensional confinement of the obtained nanocrystals up to x = 4. PL emission and excitation spectra have further recorded for these materials. Based on previous single-particle PL emission spectroscopy measurements, the observed spectral features can be correlated with the specific layer thickness (n) of $CsPbBr_3$ nanoplatelets.[34] Indeed, a continuous blue-shift of the emission maximum is observed from 518 nm (corresponding to n = bulk limit) for x = 0.5 to 475 nm (n = 4) with a minority population at 455 nm (n = 3) at x = 2 (**Figure IV. 1B**). In past

work, we have demonstrated that for a fixed alkyl chain length, increasing the concentration of alkylamine ligands brings about the pronounced dimensional confinement of $CsPbBr_3$ nanoplatelets by enabling the stabilization of a well-ordered ligand shell that limits monomer addition.[33] Specifically, the equilibrium between bound and free ligands is shifted towards the former, which results in the stabilization of a well-

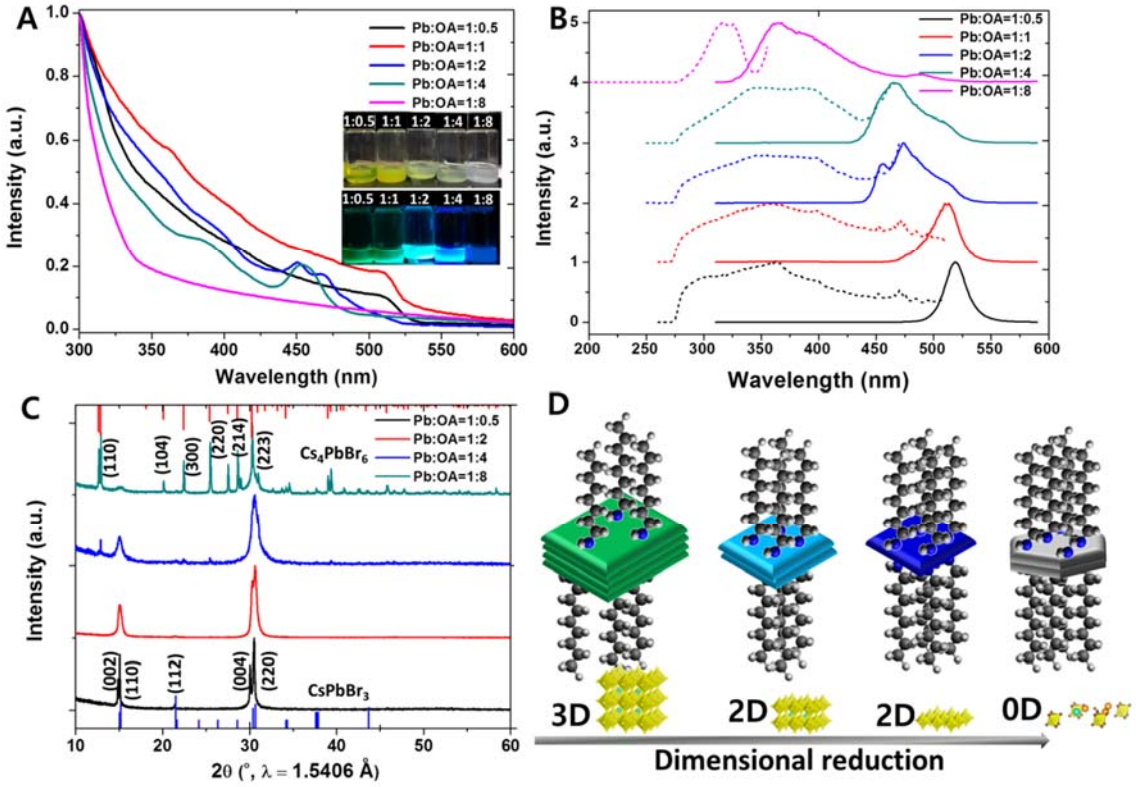

Figure IV. 1 Ligand-mediated dimensionality control of cesium lead bromide using *n*-octylamine as a ligand. (A) UV-vis absorption spectra acquired at different molar ratios of the Pb precursor to OA, 1:x where x = 0.5—8 (the top and bottom insets display digital photographs of the obtained samples under laboratory ambient light and 360 nm UV excitation, respectively); (B) PL emission (solid lines) and excitation spectra (dotted lines); and (C) XRD patterns of the obtained perovskite nanocrystals at different concentrations of OA (x = 0.5—8). The blue and red ticks on the bottom and top horizontal axes denote reflections of $CsPbBr_3$ (PDF# 01-072-7929) and Cs_4PbBr_6 (PDF# 01-073-2478), respectively. (D) Schematic depiction of quantum confinement and the reduction of dimensionality with increasing concentration of OA from 3D $CsPbBr_3$ to 0D Cs_4PbBr_6.

ordered ligand shell at high ligand concentrations. The ligand-induced dimensional confinement close to the Böhr radius (3.5 nm for $CsPbBr_3$) brings about the pronounced observed modulation of optical properties in this concentration regime.[35] Notably, the relatively thin ligand shell formed by OA is unable to constrain growth to monolayer or bilayer dimensions, which typically necessitates longer-chain alkylamines.[18, 36, 37] Interestingly, still further increasing the OA concentration to x = 8, brings about a pronounced discontinuous shift of the PL emission maximum to 360 nm; a cloudy appearance is furthermore noted in the digital photographs shown in Figure IV. 1A. The observed emission spectrum is concordant with the stabilization of the wide bandgap 0D Cs_4PbBr_6 phase, as further verified by powder X-ray diffraction (XRD, *vide infra*).[24, 38] The PL excitation spectrum acquired for the x = 8 sample provides additional evidence for the stabilization of 0D Cs_4PbBr_6 nanocrystals. Two distinct excitation bands are observed centered at 320 nm, respectively, which can be assigned to localized $6s_{1/2}$—$6p_{1/2}$ optical transitions of Pb^{2+} cations of individual $[PbBr_6]^{4-}$ octahedra.[25, 39, 40]

Structural characterization of the products obtained at different molar ratios of the Pb precursor to OA has been performed using power XRD as shown in **Figure IV. 1C**. In the Pb-precursor:OA range of 1:0.5—1:2, the products can be unequivocally assigned to the orthorhombic phase of $CsPbBr_3$ (PDF# 01-072-7929).[41] Bulk $CsPbBr_3$ adopts different crystal structures depending upon the temperature (orthorhombic at room temperature, tetragonal above 88°C, and cubic above 130°C);[42] colloidal nanoplatelets adopt the lower symmetry orthorhombic structure as a result of a distortion of $[PbBr_6]^{4-}$ octahedra that is stabilized upon dimensional confinement.[43, 44] A pronounced Scherrer

broadening of the Bragg reflections is observed with increasing OA concentration, indicative of greater dimensional confinement, as also suggested by the optical spectroscopy results in Figures IV. 1A and B.[33] At an OA concentration of $x = 4$, several additional reflections are observed that can be indexed to the rhombohedral Cs_4PbBr_6 phase (PDF# 01-073-2478). At the highest OA concentration of $x = 8$, the rhombohedral Cs_4PbBr_6 phase is the primary product with some residual reflections from $CsPbBr_3$. Indeed, at this concentration, elongated reaction times of up to 24 h induces complete transformation to the lead-deficient Cs_4PbBr_6 phase within the limits of detection (Figure A. 18).[45] As discussed below, $CsPbBr_3$ is the kinetic product that transforms to the thermodynamically favored Cs_4PbBr_6 phase (and complexed $PbBr_2$) upon prolonged reaction. **Figure IV. 1D** schematically illustrates the dimensional confinement of ternary cesium lead bromide nanoplatelets induced as a function of increasing ligand concentration; high ligand concentrations initially result in stabilization of strongly quantum confined three- or four-layered $CsPbBr_3$ nanoplatelets; further increasing the OA concentration brings about a reduction of the intrinsic dimensionality of the structure and the stabilization of the Pb-deficient Cs_4PbBr_6 phase.

Coordinating ligands can fundamentally alter the extent of supersaturation of monomers available for addition to incipient nuclei.[46] Monodentate *n*-alkylamines bind Pb^{2+} cations strongly with a complexation constant (log K) of 1.55±0.1 under aqueous conditions.[47] High concentrations of ligands that sequester $PbBr_2$ and decrease the activity of the monomeric lead species promote stabilization of the Pb-deficient phase. Indeed, at higher ligand concentrations, given the reduced availability of the Pb

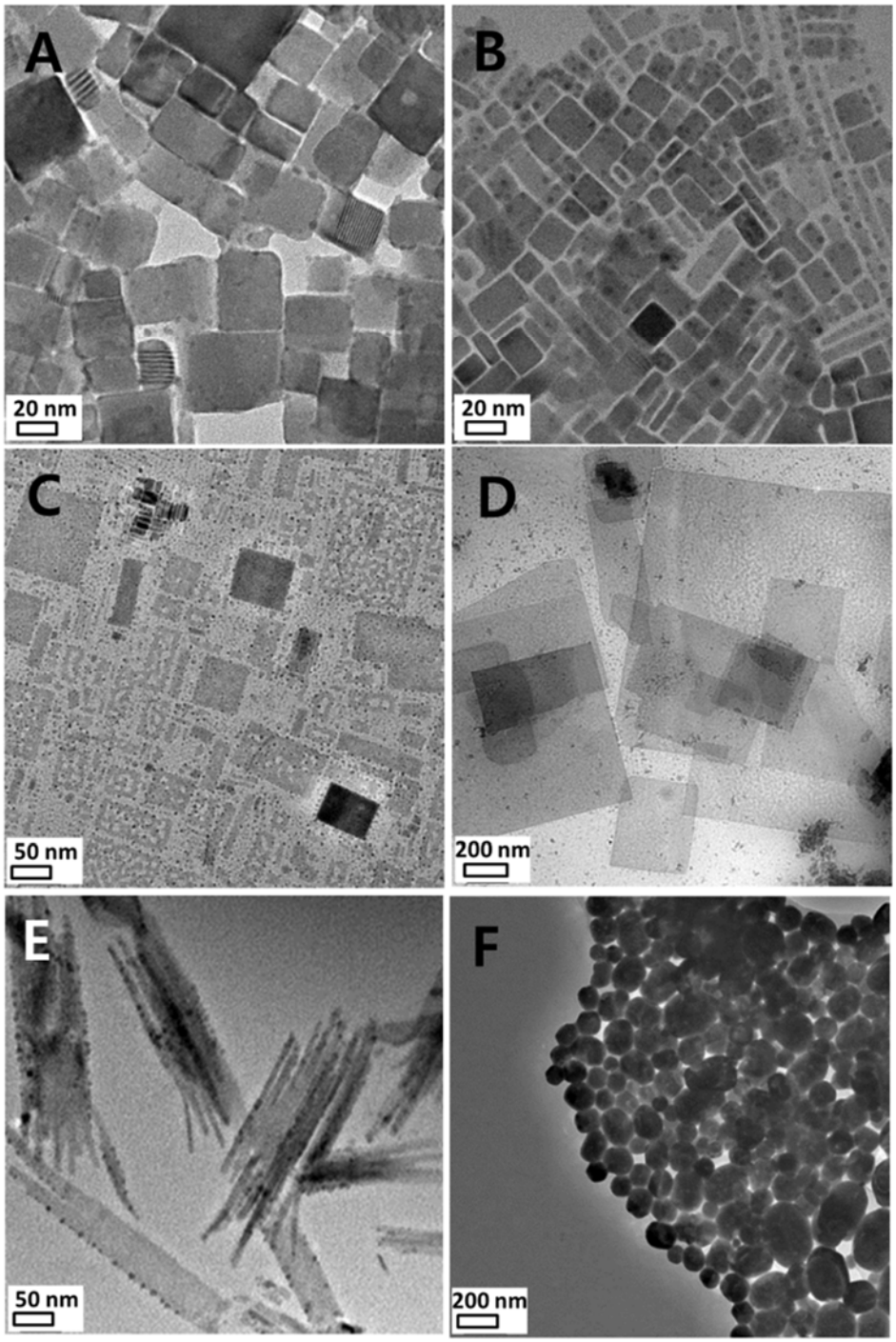

Figure IV. 2 Evolution of the size and morphology of cesium lead bromide nanocrystals as a function of the OA concentration. TEM images of cesium lead perovskite nanocrystals obtained as a function of increasing OA concentration (x): (A) $x = 0.5$; (B) $x = 1$; (C) $x = 2$; (D) $x = 4$; (E) $x = 6$; and (F) $x = 8$.

monomer as well as the potential leaching of $PbBr_2$ from incipient $CsPbBr_3$ nanoplatelets,[11,24] the 0D Cs_4PbBr_6 phase with discrete lead-centered octahedra emerges as the thermodynamically favored species, as further evidenced by the observation of time-dependent transformation of $CsPbBr_3$ to Cs_4PbBr_6 indicated in Figure A. 19 and discussed at further length below.[48]

Figure A. 19 provides further mechanistic insight into the ligand-induced modulation of dimensionality. At an intermediate OA concentration of $x = 6$, the PL emission and excitation spectra are strongly modified as a function of time. Under 365 nm UV excitation, the initial color of the solution immediately upon mixing (at ca. 10 s) is bright blue, suggestive of the formation of strongly quantum confined $CsPbBr_3$ nanoplatelets; however, over a period of time the color of the solution changes to deep violet, indicative of the stabilization of Cs_4PbBr_6. The emission spectrum immediately upon mixing is characterized by a strong emission band at 458 nm corresponding to trilayer $CsPbBr_3$ nanoplatelets along with a minority population of Cs_4PbBr_6 nanoplatelets with a characteristic emission band at 365 nm.[34, 49] The latter band progressively grows in intensity as a function of time. In other words, under these conditions, the $CsPbBr_3$ nanoplatelets represent kinetically trapped metastable species and are transformed to the thermodynamic equilibrium comprising Pb-deficient Cs_4PbBr_6 nanocrystals and OA-coordinated $PbBr_2$ species.

Figure IV. 2 shows TEM images acquired for cesium lead bromide nanoplatelets grown at various OA concentrations ($x = 0.5$—8). The electron micrographs allow for direct visualization of dimensional confinement induced in the x range from 0.5 to 4. The

shape and morphology of the nanocrystals are significantly changed from rectangular crystals in the bulk limit (Figure IV. 2A) to ultra-thin nanoplatelets and subsequently to quasi-hexagonal nanoplatelets as a function of increasing ligand concentration. At an OA concentration of x = 0.5, the obtained $CsPbBr_3$ nanoplatelets have lateral dimensions of 70±10 nm and vertical dimensions of 50±10 nm (**Figures IV. 2A and A. 20A**). The inset to Figure A. 20A shows an indexed SAED pattern; the diffraction spots illustrate the single-crystalline nature of the nanoplatelets. Increasing the OA concentration to x = 1 brings about pronounced dimensional confinement down to the quantum confined regime; two discrete populations are observed, nanocubes with lateral dimensions of 20±5 nm and vertical dimensions of 15±5 nm and nanoplatelets with lateral dimensions of 30±5 nm and vertical dimensions of 5±2 nm (**Figures IV. 2B and A. 20B**). Still more pronounced dimensional confinement of nanoplatelets is observed at an OA concentration of x = 2; ultrathin nanoplatelets with vertical dimensions of 3±1 nm are stabilized (**Figures IV. 2C and A. 20C**). At a still higher OA concentration of x = 4, even larger nanosheets spanning a few micrometers in terms of their lateral dimensions are stabilized with vertical dimensions of three or four-layers. (**Figures IV. 2D and A. 20D**). The crystal growth of nanoplatelets is strongly confined along the crystallographic *c*-direction and indeed ordered ligand shells are constituted on the basal planes. As a result of the self-assembled monolayers that inhibit monomer addition along the vertical direction,[34] growth is strongly preferred along the unpassivated lateral edges. Notably, the higher concentration of OA is unable to induce further dimensional confinement owing to the facile diffusion of monomeric species across the relatively thin ligand shell.

Intriguingly, some degradation of the nanoplatelets and a speckled appearance is noted in **Figures IV. 2E and A. 20E** when the OA concentration is increased to $x = 6$, which can likely be attributed to leaching of $PbBr_2$ or surficial Pb-species by the excess alkylamine at these concentrations; the speckled appearance may also result from degradation of the nanoplatelets to either quantum dots[50] or extrusion of Pb nanoparticles under electron beam irradiation as noted previously in the literature.[51, 52] Further characterization of the speckles has been attempted but is precluded by their instability under the electron beam. However, the increase in the density of degraded particles appears to be correlated with high amine concentrations providing indirect evidence of greater instability of the $CsPbBr_3$ nanoplatelets under these conditions. The observed exfoliation and dissolution appears to be consistent with the observations of Figure A. 19 suggesting the preferential stabilization of Cs_4PbBr_6 as a function of time.[11, 25, 53] At the highest OA concentration of $x = 8$, self-assembled hexagonal platelets of Cs_4PbBr_6 are stabilized as depicted in **Figures IV. 2F and A. 20F**. The platelets have diameters of 120 ± 30 nm and indeed $CsPbBr_3$ nanoplatelets are no longer observed from SAED patterns (Figure A. 20F).

In order to examine the influence of the steric bulk of the ligands on the Cs—Pb—Br ternary phase diagram for ligand-assisted reprecipitation, di-*n*-octylamine (DOA) and tertiary tri-*n*-octylamine (TOA) amines have further been investigated as passivating ligands. **Figures IV. 3A and B** show PL excitation and emission spectra acquired for the obtained cesium lead bromide nanocrystals prepared using different concentrations of DOA and TOA, respectively. DOA yields submicron-sized $CsPbBr_3$ nanoplatelets

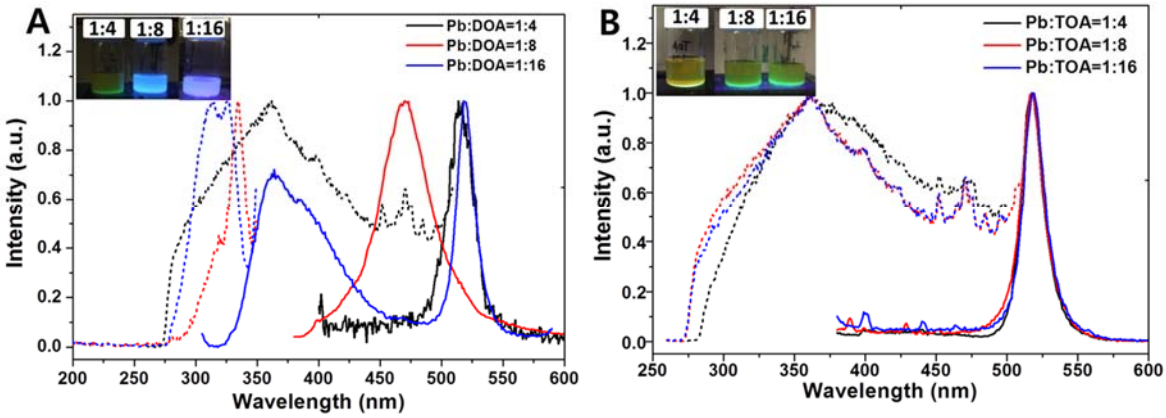

Figure IV. 3 Influence of the steric bulk of added ligands on the Cs—Pb—Br ternary phase diagram. PL emission (solid lines) and PL excitation (dotted lines) spectra of cesium lead bromide nanocrystals acquired at different ligand concentrations (x = 4—16) using (A) DOA and (B) TOA. The insets to Figures 3A and 3B show digital photographs acquired under 365 nm UV illumination.

(approaching the bulk limit in terms of their optical properties) at low concentrations; only at a value of x = 8 is a blue-shift to 460 nm observed suggesting quantum confinement of the $CsPbBr_3$ nanocrystals (down to approximately trilayer thicknesses).

Indeed, for the secondary amine, a high ligand concentration approaching x = 16 (twice as high as in the case of the monodentate C8 amine) is required to stabilize the Pb-deficient Cs_4PbBr_6 phase, albeit even at this concentration a significant population of $CsPbBr_3$ nanocrystals is present, as suggested by the distinctive emission band at 519 nm in Figure IV. 3A. In contrast, for TOA, even at a high ligand concentration of x = 16, only $CsPbBr_3$ nanocrystals at the bulk limit are observed. In other words, increasing steric bulk of passivating ligands strongly shifts the synthetic landscape to stabilization of the 3D $CsPbBr_3$ phase. The increased steric bulk of these ligands diminishes their ability to form an ordered ligand shell and passivate the nanocrystal surfaces.[34] As a

result, rapid monomer diffusion and growth immediately after nucleation (with minimal temporal separation of nucleation and growth steps) results in the formation of large $CsPbBr_3$ crystals.[34] It is notable that the 1°, 2°, and 3° amines evaluated here furthermore have different pKb values, which has been shown to affect crystal growth[54]. However, notably the pKb values for amines used in this study are 3.35 for the primary amine (OA), 2.99 for the secondary amine (DOA), and 3.92 for the tertiary amine (TOA), respectively, at room temperature[55], which does not correlate directly with the observed control of structural dimensionality. This suggests that the sterics and resulting entropic losses for the branched amines[34], which result in a less ordered ligand shell, play a greater role as compared to the pKb values. In other words, sterically bulky ligands have a much more modest impact on determining the effective monomer concentration at the surface of the incipient nuclei and thereby have only a limited influence on controlling nanocrystal growth.

A bidentate C_8 ligand, ODA, has further been evaluated for its influence on controlling the dimensionality of cesium lead bromide nanocrystals as shown in Figures IV. 4 and 5. **Figure IV. 4A** plots UV-vis absorption spectra as a function of the ODA concentration. For an ODA concentration of x = 0.5, the characteristic first excitonic peak of $CsPbBr_3$ is observed at 520 nm; successively increasing the ODA concentration to x = 1, 2, 4, and 8 yields distinctly different absorption bands centered at 324, 322, 318, and 317 nm, respectively, which can be ascribed to the absorption of Cs_4PbBr_6

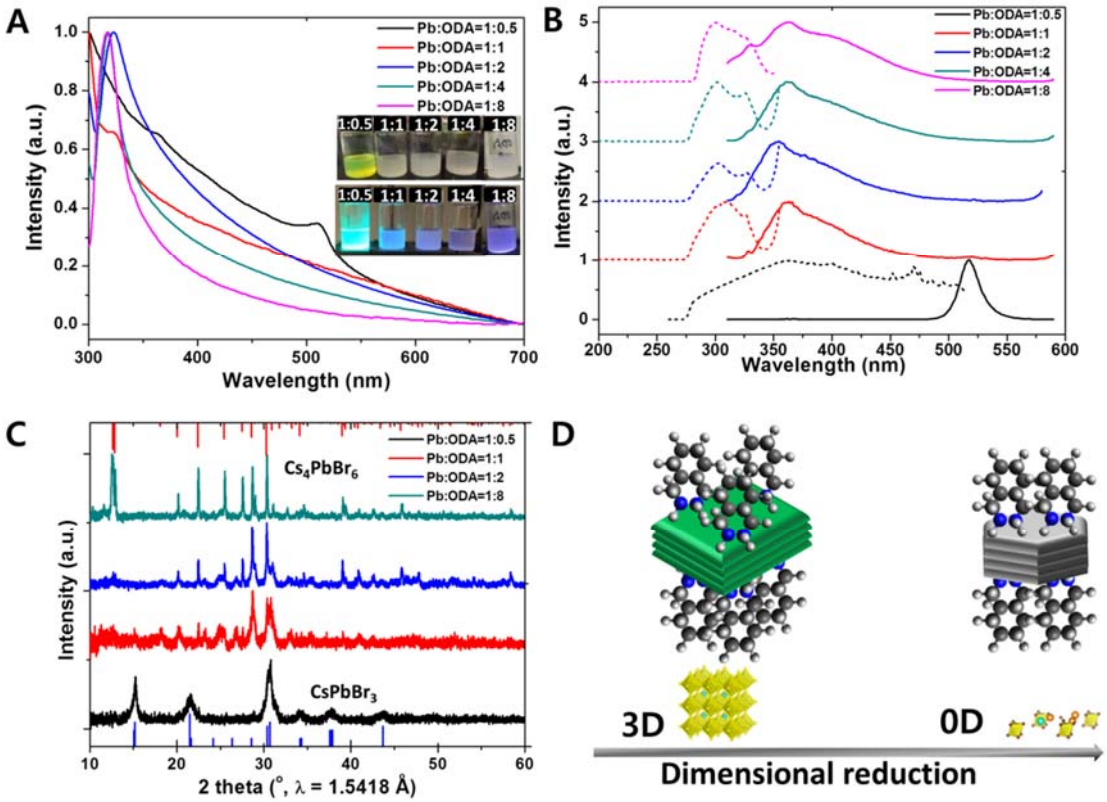

Figure IV. 4 Ligand-mediated dimensionality control of cesium lead bromide; 1,8-octyldiamine as a ligand. (A) UV-vis absorption spectra (the inset shows digital photographs acquired under ambient laboratory light (top) and 365 nm UV illumination (bottom)); (B) PL emission (solid lines) and excitation spectra (dotted lines); and (C) XRD patterns of the obtained cesium lead bromide perovskite nanocrystals at different concentrations of ODA (x = 0.5—8). (D) Schematic depiction of quantum confinement and phase transformation with increasing concentration of ODA from 3D $CsPbBr_3$ to 0D Cs_4PbBr_6.

nanocrystals. The pronounced blue-shift of the absorption maxima of Cs_4PbBr_6 can be rationalized based on electronic decoupling of $[PbBr_6]^{4-}$ octahedra within the 0D Cs_4PbBr_6 structure.[24, 56] Consistent with the absorption spectra, the PL emission and excitation spectra depicted in **Figure IV. 4B** show a pronounced blue shift with increasing ODA concentration. At an ODA concentration of x = 1, two distinct emission bands are observed at 370 nm and 520 nm (**Figure A. 21**); the bands arise from the

presence of two disparate populations, a majority population of Cs_4PbBr_6 and a minority species of $CsPbBr_3$. Further increasing the ODA concentration yields only the characteristic emission band of Cs_4PbBr_6. The XRD patterns plotted in **Figure IV. 4C** reflect a clear evolution from orthorhombic $CsPbBr_3$ to rhombohedral Cs_4PbBr_6 with increasing concentration of ODA. At an ODA concentration of x = 0.5, phase-pure $CsPbBr_3$ nanoplatelets are stabilized; at an intermediate ODA concentration of x = 1, a biphasic mixture of $CsPbBr_3$ and Cs_4PbBr_6 is discernible. At higher ODA concentrations of x = 2—8, phase-pure Cs_4PbBr_6 is stabilized within limits of detection (Figure IV. 4C).

The nanocrystals obtained using ODA have further been characterized by TEM. At an ODA concentration of x = 0.5, aggregated $CsPbBr_3$ nanocubes are observed (**Figure IV. 5A**); increasing the ODA concentration to x = 1 yields well-defined hexagonal platelets of Cs_4PbBr_6 with a diameter of 200±40 nm along with debris of somewhat degraded $CsPbBr_3$ nanoplatelets, suggesting that at this concentration, the ODA is beginning to leach $PbBr_2$ layers from the incipient $CsPbBr_3$ nanoplatelets (**Figure IV. 5B**), consistent with previous reports in the literature.[57] At an ODA concentration of x = 2, well-defined hexagonally close packed superlattices of Cs_4PbBr_6 hexagonal nanoplatelets are stabilized with each platelet having a side of 80±10 nm (**Figures IV. 5D and A. 22**). EDS analysis of the hexagonal nanoplatelets indicates an elemental ratio of Cs:Pb:Br = 4.1:1.18:6, which is concordant with the expected Cs_4PbBr_6 stoichiometry with the excess Pb likely arising from surficial $PbBr_2$ layers stabilized by ODA (**Figure A. 21B**).

The chelating nature of the bidentate ligand induces a much more facile transformation to the lead-deficient Cs_4PbBr_6 phase, at a significantly lower concentration of x = 1 as

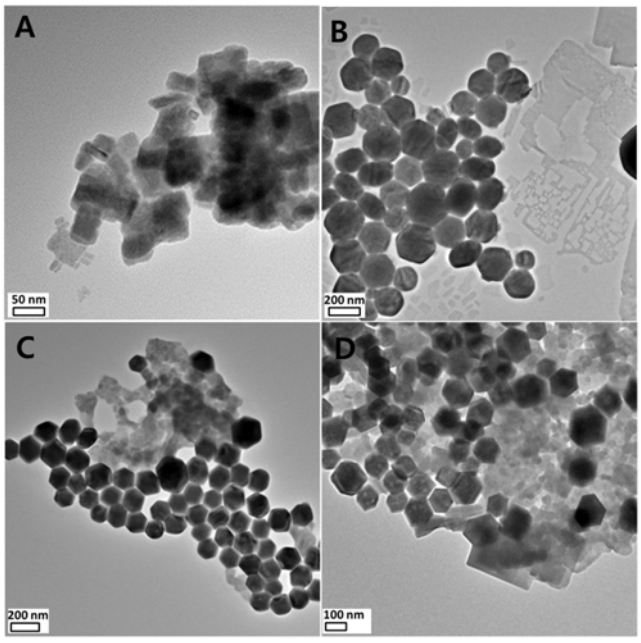

Figure IV. 5 Evolution of size, morphology, and crystal structure of cesium lead bromide nanocrystals as a function of the ODA concentration. TEM images of cesium lead perovskite nanocrystals obtained as a function of increasing ODA concentration (x): (A) $x = 0.5$; (B) $x = 1$; and (C,D) $x = 2$.

compared to OA (where the crossover is achieved at $x = 6$) as a result of the strong binding of these ligands to $PbBr_2$ species (**Figure IV. 4D**). The strong binding of amines reduces the availability of the Pb monomer, and the leaching of $PbBr_2$ from incipient $CsPbBr_3$ nuclei brings about a rapid phase transformation to Cs_4PbBr_6. Depending upon the denticity of the surface-passivating ligands, the binding affinity (or complexation constant) of the amines to $PbBr_2$ is strongly altered, which in turn modifies the monomer supersaturation and resulting crystal growth kinetics. In comparison to monodentate amines, bidentate amines bind $PbBr_2$ more strongly and thus have a stronger influence on dimensional confinement and phase transformation as compared to their monodentate counterparts.

Diamines of different chain lengths, specifically, ethylenediamine (EDA) and dodecyldiamine (DDA)) have also been examined as structure-directing ligands at two different concentrations of x = 1—2. Based on absorption and PL emission spectra shown in Figure A. 23, both diamine species stabilize Cs_4PbBr_6 nanocrystals at these ligand concentrations. For EDA, the sharp absorption peak at 316 nm can be attributed to $6s_{1/2}$—$6p_{1/2}$ transitions within electronically decoupled $[PbBr_6]^{4-}$ octahedra[25, 58] (**Figure A. 23**); sharp excitation bands are observed at 310 nm and 330 nm along with a broad emission at 360 nm (**Figure A. 23B**), corroborating the stabilization of Cs_4PbBr_6 nanocrystals. Similarly, the utilization of DDA stabilizes stabilizes Cs_4PbBr_6 nanocrystals at these concentrations (**Figure A. 23C,D**). It is worth noting that relatively low concentration (x < 1) of both bidentate ligands can stabilize $CsPbBr_3$ as majority populations. To further evaluate the influence of ligand denticity on the stabilization of cesium lead bromide nanoplatelets, a tridentate amine, *tris*(2-aminoethyl)amine (TAA), has been evaluated as a ligand. However, the strongly chelating nature of tridentate ligands results in the formation of the lead-deficient Cs_4PbBr_6 as well as unidentified molecular lead complexes coordinated even at concentrations as low as x = 0.5.

Figure IV. 6 schematically illustrates the synthetic phase space of ternary cesium lead bromide stabilized using monodentate OA and bidentate ODA. With increasing denticity of the ligand, the Pb-deficient Cs_4PbBr_6 phase is stabilized at successively lower ligand concentrations. The results can be rationalized considering the complexation constants (log K) for binding of Pb^{2+} by monodentate, bidentate, tridentate, and tetradendate amines. Considering ethyl groups where a consistent dataset is available

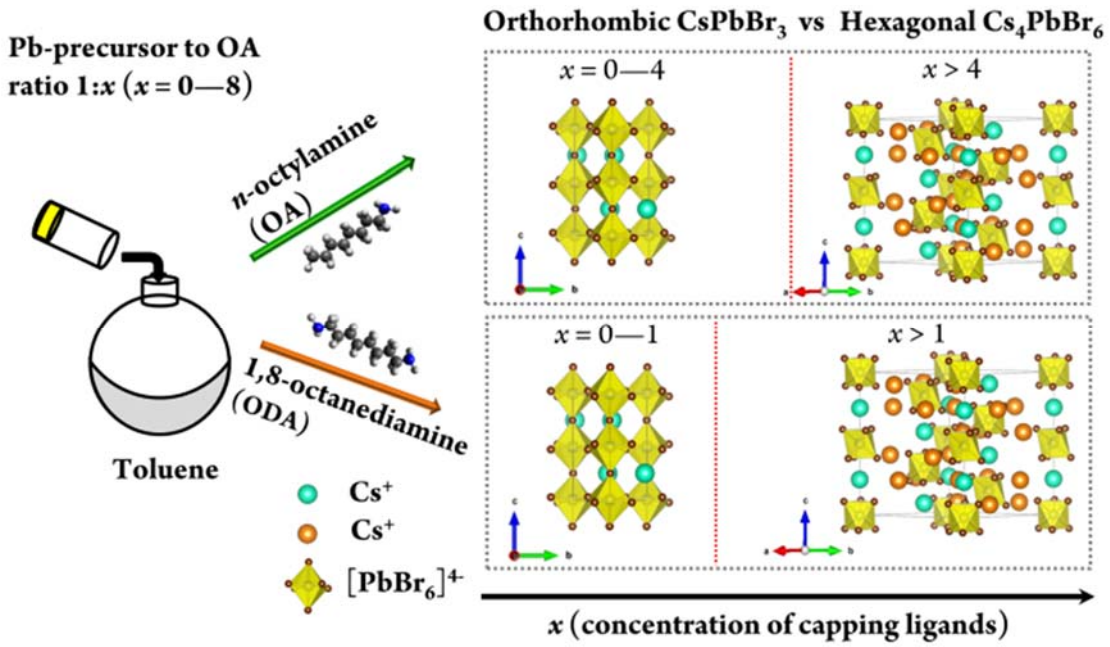

Figure IV. 6 Synthetic phase diagram of ternary cesium lead bromide stabilized using monodentate OA and bidentate ODA as a surface capping ligands. The ligand concentrations have been varied in the range of x = 0—8. Cs atoms with different local coordination environments are depicted in cyan and orange.

(albeit under aqueous conditions), the log K values scale with ligand denticity from one to four as 1.55±0.1, 5.04±0.05, 7.56±0.05, and 10.35±0.04, respectively.[47, 59] While these values have been measured under aqueous conditions, the trends attest to the much stronger ability of multidentate ligands to sequester divalent lead cations as a result of the chelate effect[60] reflective of both enthalpic and entropic stabilization of the amine-$PbBr_2$ complexes. Lower concentrations of the ligand, correlated to a higher supersaturation of monomeric $PbBr_2$, stabilize the orthorhombic $CsPbBr_3$ phase, whereas at higher ligand concentrations, the Pb-deficient rhombohedral Cs_4PbBr_6 phase is stabilized consistent with a greater sequestration of the lead precursor (and a correspondingly lower extent of supersaturation of active lead monomers).[61] In other

words, the added amine ligands appear to buffer the extent of supersaturation of the lead monomer and thereby allow for stabilization of a Pb-rich or Pb-deficient phase. At null or low concentrations of the ligands or in the presence of sterically bulky ligands that do not yield well-ordered ligand shells, the $CsPbBr_3$ phase is stabilized, reflecting rapid nucleation and growth of this phase driven by strong electrostatic interactions between the Cs-oleate and $PbBr_2$ precursors, both of which are present at higher supersaturation upon reversal of polarity by the addition of toluene. Low concentrations of ligands bind to the surfaces of incipient nanocrystals but as a result of sub-monolayer coverage are unable to preclude rapid addition of monomeric species, resulting in stabilization of relatively large crystals spanning several hundred nanometers in dimensions (Figure A. 16). With increasing ligand concentration and resulting greater sequestration of Pb^{2+} precursors, the supersaturation of Pb precursors is decreased, slowing crystal growth and allowing for dimensional confinement down to the quantum confined regime (Figure IV. 1D). Further decrease in the available Pb concentration, induced at relatively low concentrations of multidentate ligands, results in preferential stabilization of the Cs_4PbBr_6 phase. Still further decreases in Pb concentration induced by addition of tridentate ligands altogether precludes the precipitation of cesium lead bromide nanocrystals.

It is worth noting that initial nucleation processes are driven by local supersaturation (burst nucleation)[62] and thus at intermediate ligand concentrations, a significant population of $CsPbBr_3$ nuclei are formed as a kinetically stabilized phase; however, such nuclei are unstable with respect to the Pb-deficient Cs_4PbBr_6 and are

transformed over the course of time as observed in Figure A. 19. In other words, owing to sequestration of Pb-species by the ligands, Cs_4PbBr_6 is the thermodynamically favored polymorph within the low-Pb composition regime; as a result, diffusion—recrystallization processes result in transformation of the initially nucleated $CsPbBr_3$ nanocrystals to Cs_4PbBr_6 (with leaching of solution-phase complexes of amines and $PbBr_2$). Indeed, Palazon *et al*. have studied the phase transformation of $CsPbBr_3$ to Cs_4PbBr_6 upon the addition of butylamine and tetramethylethylenediamine; the diamine species is observed to immediately induce the stabilization of a white precipitate of Cs_4PbBr_6.[38]

Surface Passivation of Cesium Lead Bromide Nanocrystals

In order to verify the role of the added amines as passivating ligands bound to the nanocrystal surfaces, Fourier transform infrared (FTIR) spectroscopy measurements have been performed for materials obtained at a ligand concentration of $x = 2$ for OA and ODA (corresponding to $CsPbBr_3$ for OA and Cs_4PbBr_6 for ODA). The passivating nature of the ligands is verified based on comparison with FTIR spectra of the uncomplexed amines. Assignments of the FTIR bands for the amines and amine-passivated nanocrystals are indicated in **Figure A. 24**.[63,64] The aliphatic amine vibrational modes are considerably weakened for the colloidal dispersions of nanocrystals given that they are only present as surficial layers; however, the N-H stretching mode at 3300— 300 cm^{-1} and N-H bending mode at 1600—1700 cm^{-1} are observed for both $CsPbBr_3$ and Cs_4PbBr_6 nanocrystals. The relative intensity of the N-H wagging mode is considerably

weakened as a result of conformational restrictions arising from binding of the ligands to the nanocrystal surfaces. ^{1}H nuclear magnetic resonance (NMR) spectroscopy has further been used to characterize the ligand shells as shown in **Figure A. 25**.

NMR spectra have been acquired for the ligands as well as ligand-capped nanocrystals in $CDCl_3$. For OA, after coordination to perovskite nanocrystals, the proton signal from the aliphatic linear chain is shifted downfield from 0.78 to 0.94 ppm for the terminal CH_3 protons 1 (as labeled in Figure A. 25) and from 1.12–1.18 to 1.32–1.38 for intermediate CH_2 protons 2-7[65]; the α-CH_2 proton 8 depicted in Figure A. 25 is no longer observed, likely as a result of broadening from the conformational restrictions at the nanocrystal surface. The reduced shielding arises from coordination of the Lewis basic amine ligands to the cation-terminated surfaces and provides strong evidence for the formation of the amine ligand shell along the lines of the schematic depiction in Figures IV. 1D and 4D. Taken together, the FTIR and NMR data along with the observations noted above from varying amine denticity, sterics, and concentration point to the pivotal role of the amine ligands in controlling both particle size and defining the range of the Cs—Pb—Br ternary phase diagram reached by the system (thereby controlling the structural dimensionality).

Ligand-Induced Leaching and Recrystallization of $CsPbBr_3$ to Cs_4PbBr_6

Figure A. 19 illustrates the remarkable change in visible coloration and absorption/emission spectra of $CsPbBr_3$ as a function of time. The reversal of polarity

upon the addition of polar precursors to toluene and the resulting sharp increase in precursor supersaturation induces burst nucleation of $CsPbBr_3$ nanocrystals. However, at

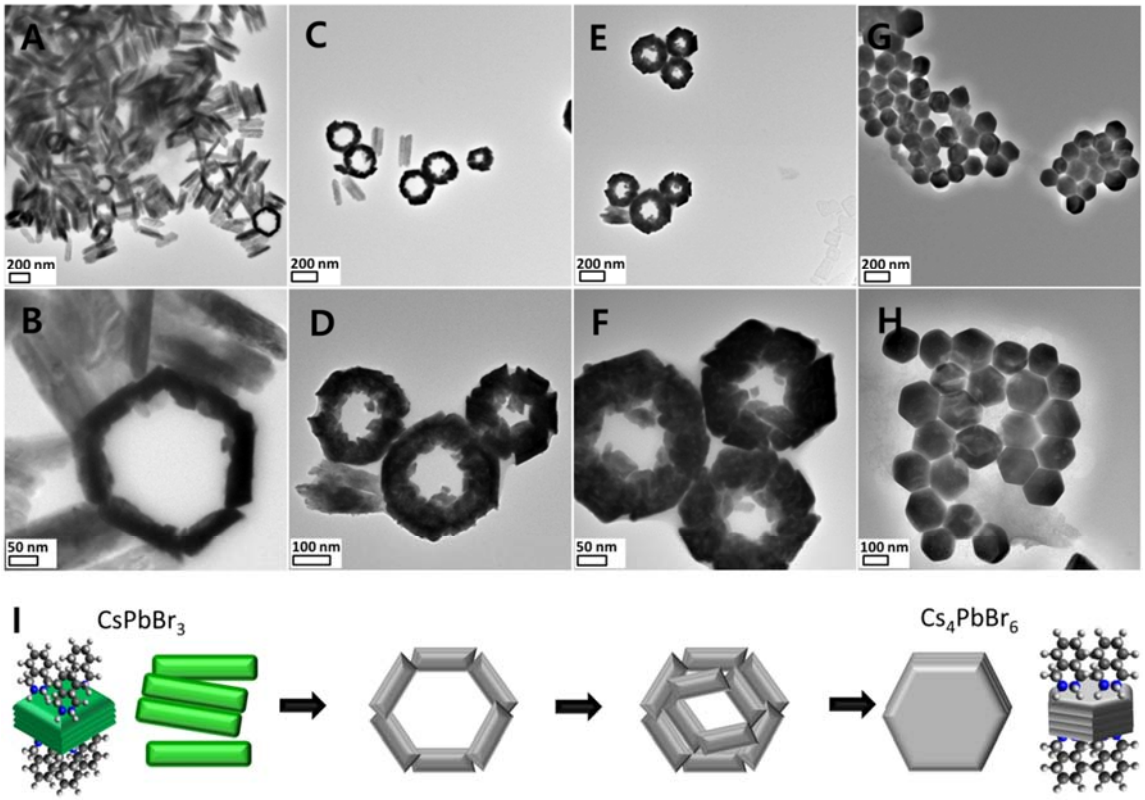

Figure VI.7 Ligand-induced leaching and phase transformation from $CsPbBr_3$ to Cs_4PbBr_6 occurring through dissolution—recrystallization processes. TEM images of cesium lead bromide nanocrystals obtained using bidentate ODA at a concentration of (A,F) $x = 1$ and (G—H) $x = 2$. (I) Schematic illustration of the phase transformation of $CsPbBr_3$ nanoplatelets to Cs_4PbBr_6 hexagonal nanoplatelets. precludes the precipitation of cesium lead bromide nanocrystals.

high ligand concentrations, thermodynamic equilibria favor a Pb-deficient region of the ternary phase diagram, and consequently Cs_4PbBr_6 nanocrystals are formed as the equilibrium solid-phase product with excess $PbBr_2$ complexed to the amine ligand remaining in solution. Subsequent to nucleation of 3D perovskite nanocrystals, the system approaches quasi-equilibrium conditions through diffusion and leaching of $PbBr_2$

facilitated by the amine ligands. TEM images obtained for cesium lead bromide nanocrystals synthesized at an ODA concentrations of x = 1 and 2 provide intriguing snapshots of the transformation process. In **Figure IV. 7A**, stacked lamellar $CsPbBr_3$ nanoplatelets assembled within columnar aggregates can be distinguished from a few hollow hexagonal Cs_4PbBr_6 platelets. The nanoplatelets are thought to be agglomerated as a result of the formation of self-assembled ligand monolayers. However, the edges of the nanoplatelets are not passivated and it is posited that ODA-mediated leaching of $PbBr_2$ is accommodated through fusion of nanoplatelets to form hexagonal templates. Lattice-resolved TEM images, fast Fourier transforms, and selected-area electron diffraction patterns acquired for the columnar aggregates and hexagonal nanoplatelets (**Figure A. 26**) allows for their differentiation as orthorhombic $CsPbBr_3$ and rhombohedral Cs_4PbBr_6, respectively. **Figures IV. 7C and D** demonstrate the growth of the initially hollow Cs_4PbBr_6 nuclei as the inner core of the hollow hexagonal platelets gets filled, resulting eventually in the formation of solid single-crystalline Cs_4PbBr_6 platelets (**Figures IV. 7G and H**). The uniform hexagonal morphologies, reflective of energy-minimized Wulff constructions, are further suggestive of the Cs_4PbBr_6 nanocrystals being the thermodynamic product under these conditions. While *in situ* monitoring of the recrystallization process is required to obtain unambiguous evidence, the TEM images in Figures IV. 7 and A. 26 suggest an inverse Kirkendall effect[66] subsequent to the oriented attachment of rhomboidal nuclei.[36, 49] Rhombohedral Cs_4PbBr_6 nuclei obtained upon ODA-induced $PbBr_2$ leaching have an increased surface area with multiple high-surface-energy exposed facets; the nuclei are condensed to form

hollow hexagonal rings through an oriented attachment mechanism, which enables minimization of surface free energy. The empty voids are subsequently filled as a result of the diffusion of monomeric ionic species (**Figure IV. 7I**). Solid hexagonal Cs_4PbBr_6 nanoplatelets are stabilized at the end of this process and self-assembled within hexagonal superlattices.

The reversibility of the transformation along the Cs—Pb—Br phase diagram from 0D Cs_4PbBr_6 to 3D $CsPbBr_3$ has been investigated as shown in Figures A. 27 and 28. **Figure A. 27** shows that treating as-synthesized Cs_4PbBr_6 hexagonal nanoplatelets recovered using OA at a concentration of x = 8 for an extended period of time with excess $PbBr_2$ dissolved in oleylamine and oleic acid in toluene brings about a pronounced change in coloration of the solution and the PL emission spectra indicating reversion to the $CsPbBr_3$ phase; the emission band at 465 nm observed upon addition of $PbBr_2$ is attributed to n = 3 nanoplatelets. Similarly, **Figure A. 28** shows a change in coloration from cloudy to greenish yellow within ca. 30 min. Consistent with this change of color, the UV-vis absorption band in Figure A. 28 is shifted from 325 nm to 460 nm reflecting the stabilization of trilayered $CsPbBr_3$ nanoplatelets in the presence of excess OLAm and OLAc. Conversely, upon treatment of $CsPbBr_3$ nanocubes with excess ODA dissolved in OLAc under heating at 120°C, the solution changes appearance from a clear green to cloudy coloration within ca. 10 min. The excitonic absorption band at 515 nm is replaced by a new absorption at 320 nm. The PL emission spectra acquired for the $PbBr_2$ addition and ODA-leaching experiments corroborate the reversibility of the transformations between 0D Cs_4PbBr_6 to 3D $CsPbBr_3$ nanocrystals. The dynamic

equilibrium between lead-rich and –deficient phase and corresponding reversible phase transformation can thus be written as:

$$4CsPbBr_3 \leftrightarrows 3PbBr_2 + Cs_4PbBr_6 \qquad \text{(IV. 1)}$$

IV.4 Conclusions

In summary, we map the synthetic landscape of the ternary Cs—Pb—Br system with respect to structural and morphological dimensionality as dictated by the concentration, denticity, and steric bulk of added aliphatic amine ligands. In the ligand-assisted reprecipitation reaction, the reversal of polarity resulting from the addition of ionic precursors dissolved in polar solvents to toluene results in a sharp increase of monomer supersaturation, bringing about nucleation of 3D perovskite $CsPbBr_3$ nanocrystals. In the presence of high concentrations of amines with large complexation coefficients for binding $PbBr_2$, thermodynamic equilibrium favors the stabilization of the Pb-deficient 0D Cs_4PbBr_6 phase in the Cs—Pb—Br phase diagram and indeed this structure is rapidly stabilized as the solid-phase product with excess $PbBr_2$ complexed to the amine ligand remaining in solution. The predilection for stabilizing the Pb-deficient Cs_4PbBr_6 phase is observed to be directly correlated to the chelating ability of the amines, which reduces the local monomer supersaturation at the surfaces of incipient nuclei. The ability to stabilize this phase is inversely correlated to steric bulk since bulky ligands form disordered monolayers at the surfaces of nuclei and are unable to adequately separate nucleation and growth processes. The general trend with increasing concentration of ligands, correlated to lower monomer supersaturation, is initially

dimensional confinement of the nanoplatelets, followed subsequently by stabilization of the Pb-deficient Cs_4PbBr_6 phase as the monomer concentrations decreases below a critical value. Monodentate amines bring about a smooth progression from thicker nanoplatelets to few-layered nanoplatelets to nanoplatelets of the Pb-deficient phase as a function of the amine concentration (Figure IV. 1D). In contrast, the transformation across the phase diagram is more abrupt for bidentate ligands wherein the Pb-deficient regime is reached at a much lower amine concentration (Figure IV. 4D). The results presented here not only define a mechanism-based understanding of synthetic parameters but furthermore are expected to be widely generalizable to the navigation of synthetic landscapes for the growth of ternary and more complex nanocrystals.

IV.5 References

(1) Di, D.; Musselman, K. P.; Li, G.; Sadhanala, A.; Ievskaya, Y.; Song, Q.; Tan, Z.-K.; Lai, M. L.; MacManus-Driscoll, J. L.; Greenham, N. C., Size-dependent photon emission from organometal halide perovskite nanocrystals embedded in an organic matrix. *J. Phys. Chem. Lett* 2015, 6, 446-450.

(2) Dong, Q.; Fang, Y.; Shao, Y.; Mulligan, P.; Qiu, J.; Cao, L.; Huang, J., Electron-hole diffusion lengths> 175 μm in solution-grown $CH_3NH_3PbI_3$ single crystals. *Science* 2015, 347, 967-970.

(3) Shi, D.; Adinolfi, V.; Comin, R.; Yuan, M.; Alarousu, E.; Buin, A.; Chen, Y.; Hoogland, S.; Rothenberger, A.; Katsiev, K., Low trap-state density and long carrier diffusion in organolead trihalide perovskite single crystals. *Science* 2015, 347, 519-522.

(4) Swarnkar, A.; Chulliyil, R.; Ravi, V. K.; Irfanullah, M.; Chowdhury, A.; Nag, A., Colloidal $CsPbBr_3$ perovskite nanocrystals: Luminescence beyond traditional quantum dots. *Angew. Chem.* 2015, 127, 15644-15648.

(5) Tyagi, P.; Arveson, S. M.; Tisdale, W. A., Colloidal organohalide perovskite nanoplatelets exhibiting quantum confinement. *J. Phys. Chem. Lett* 2015, 6, 1911-1916.

(6) Wang, H.; Whittaker-Brooks, L.; Fleming, G. R., Exciton and Free Charge Dynamics of Methylammonium Lead Iodide Perovskites Are Different in the Tetragonal and Orthorhombic Phases. *J. Phys. Chem. C* 2015, 119, 19590-19595.

(7) Nimens, W. J.; Ogle, J.; Caruso, A.; Jonely, M.; Simon, C.; Smilgies, D.; Noriega, R.; Scarpulla, M.; Whittaker-Brooks, L., Morphology and Optoelectronic Variations Underlying the Nature of the Electron Transport Layer in Perovskite Solar Cells. *ACS Appl. Energy Mater.* 2018, 1, 602-615.

(8) Akkerman, Q. A.; Rainò, G.; Kovalenko, M. V.; Manna, L., Genesis, challenges and opportunities for colloidal lead halide perovskite nanocrystals. *Nat. Mater.* 2018, 17, 394–405.

(9) Kovalenko, M. V.; Protesescu, L.; Bodnarchuk, M. I., Properties and potential optoelectronic applications of lead halide perovskite nanocrystals. *Science* 2017, 358, 745-750.

(10) Akkerman, Q. A.; D'Innocenzo, V.; Accornero, S.; Scarpellini, A.; Petrozza, A.; Prato, M.; Manna, L., Tuning the Optical Properties of Cesium Lead Halide Perovskite Nanocrystals by Anion Exchange Reactions. *J. Am. Chem. Soc.* 2015, 137, 10276-10281.

(11) van der Stam, W.; Geuchies, J. J.; Altantzis, T.; van den Bos, K. H.; Meeldijk, J. D.; Van Aert, S.; Bals, S.; Vanmaekelbergh, D.; de Mello Donega, C., Highly Emissive Divalent-Ion-Doped Colloidal $CsPb_{1-x}M_xBr_3$ Perovskite Nanocrystals through Cation Exchange. *J. Am. Chem. Soc.* 2017, 139, 4087-4097.

(12) Parobek, D.; Dong, Y.; Qiao, T.; Rossi, D.; Son, D. H., Photoinduced Anion Exchange in Cesium Lead Halide Perovskite Nanocrystals. *J. Am. Chem. Soc.* 2017, 139, 4358-4361.

(13) Begum, R.; Parida, M. R.; Abdelhady, A. L.; Murali, B.; Alyami, N. M.; Ahmed, G. H.; Hedhili, M. N.; Bakr, O. M.; Mohammed, O. F., Engineering Interfacial Charge Transfer in $CsPbBr_3$ Perovskite Nanocrystals by Heterovalent Doping. *J. Am. Chem. Soc.* 2017, 139, 731-737.

(14) Zou, S.; Liu, Y.; Li, J.; Liu, C.; Feng, R.; Jiang, F.; Li, Y.; Song, J.; Zeng, H.; Hong, M.; Chen, X., Stabilizing Cesium Lead Halide Perovskite Lattice through Mn(II) Substitution for Air-Stable Light-Emitting Diodes. *J. Am. Chem. Soc.* 2017, 139, 11443-11450.

(15) Parobek, D.; Roman, B. J.; Dong, Y.; Jin, H.; Lee, E.; Sheldon, M.; Son, D. H., Exciton-to-Dopant Energy Transfer in Mn-Doped Cesium Lead Halide Perovskite Nanocrystals. *Nano Lett.* 2016, 16, 7376-7380.

(16) Protesescu, L.; Yakunin, S.; Bodnarchuk, M. I.; Krieg, F.; Caputo, R.; Hendon, C. H.; Yang, R. X.; Walsh, A.; Kovalenko, M. V., Nanocrystals of Cesium Lead Halide Perovskites ($CsPbX_3$, X = Cl, Br, and I): Novel Optoelectronic Materials Showing Bright Emission with Wide Color Gamut. *Nano Lett.* 2015, 15, 3692-3696.

(17) Zhu, F.; Men, L.; Guo, Y.; Zhu, Q.; Bhattacharjee, U.; Goodwin, P. M.; Petrich, J. W.; Smith, E. A.; Vela, J., Shape Evolution and Single Particle Luminescence of Organometal Halide Perovskite Nanocrystals. *ACS Nano* 2015, 9, 2948-2959.

(18) Sun, S.; Yuan, D.; Xu, Y.; Wang, A.; Deng, Z., Ligand-mediated synthesis of shape-controlled cesium lead halide perovskite nanocrystals via reprecipitation process at room temperature. *ACS Nano* 2016, 10, 3648-3657.

(19) Liang, Z.; Zhao, S.; Xu, Z.; Qiao, B.; Song, P.; Gao, D.; Xu, X., Shape-Controlled Synthesis of All-Inorganic $CsPbBr_3$ Perovskite Nanocrystals with Bright Blue Emission. *ACS Appl. Mater. Inter.* 2016, 8, 28824-28830.

(20) Tsai, H.; Nie, W.; Blancon, J.-C.; Stoumpos, C. C.; Asadpour, R.; Harutyunyan, B.; Neukirch, A. J.; Verduzco, R.; Crochet, J. J.; Tretiak, S., High-efficiency two-dimensional Ruddlesden–Popper perovskite solar cells. *Nature* 2016, 536, 312-316.

(21) Yu, Y.; Zhang, D.; Yang, P., Ruddlesden–Popper Phase in Two-Dimensional Inorganic Halide Perovskites: A Plausible Model and the Supporting Observations. *Nano Lett.* 2017, 17, 5489-5494.

(22) Ruan, L.; Shen, W.; Wang, A.; Xiang, A.; Deng, Z., Alkyl-Thiol Ligand-Induced Shape-and Crystalline Phase-Controlled Synthesis of Stable Perovskite-Related $CsPb_2Br_5$ Nanocrystals at Room Temperature. *J. Phys. Chem. Lett* 2017, 8, 3853-3860.

(23) Wang, K.-H.; Wu, L.; Li, L.; Yao, H.-B.; Qian, H.-S.; Yu, S.-H., Large-Scale Synthesis of Highly Luminescent Perovskite-Related $CsPb_2Br_5$ Nanoplatelets and Their Fast Anion Exchange. *Angew. Chem. Inter. Ed* 2016, 55, 8328-8332.

(24) Akkerman, Q. A.; Park, S.; Radicchi, E.; Nunzi, F.; Mosconi, E.; De Angelis, F.; Brescia, R.; Rastogi, P.; Prato, M.; Manna, L., Nearly Monodisperse Insulator Cs_4PbX_6 (X= Cl, Br, I) Nanocrystals, Their Mixed Halide Compositions, and Their Transformation into $CsPbX_3$ Nanocrystals. *Nano Lett.* 2017, 17, 1924-1930.

(25) Liu, Z.; Bekenstein, Y.; Ye, X.; Nguyen, S. C.; Swabeck, J.; Zhang, D.; Lee, S.-T.; Yang, P.; Ma, W.; Alivisatos, A. P., Ligand Mediated Transformation of Cesium Lead Bromide Perovskite Nanocrystals to Lead Depleted Cs_4PbBr_6 Nanocrystals. *J. Am. Chem. Soc* 2017, 139, 5309-5312.

(26) Dou, L.; Wong, A. B.; Yu, Y.; Lai, M.; Kornienko, N.; Eaton, S. W.; Fu, A.; Bischak, C. G.; Ma, J.; Ding, T., Atomically thin two-dimensional organic-inorganic hybrid perovskites. *Science* 2015, 349, 1518-1521.

(27) Quan, L. N.; Yuan, M.; Comin, R.; Voznyy, O.; Beauregard, E. M.; Hoogland, S.; Buin, A.; Kirmani, A. R.; Zhao, K.; Amassian, A., Ligand-Stabilized Reduced-Dimensionality Perovskites. *J. Am. Chem. Soc.* 2016, 138, 2649-2655.

(28) Huang, H.; Polavarapu, L.; Sichert, J. A.; Susha, A. S.; Urban, A. S.; Rogach, A. L., Colloidal lead halide perovskite nanocrystals: synthesis, optical properties and applications. *NPG Asia Mater.* 2016, 8, e328.

(29) Chen, X.; Chen, D.; Li, J.; Fang, G.; Sheng, H.; Zhong, J., Tunable CsPbBr3/Cs4PbBr6 phase transformation and their optical spectroscopic properties. *Dalton Trans.* 2018, 47, 5670-5678.

(30) Udayabhaskararao, T.; Houben, L.; Cohen, H.; Menahem, M.; Pinkas, I.; Avram, L.; Wolf, T.; Teitelboim, A.; Leskes, M.; Yaffe, O.; Oron, D.; Kazes, M., A Mechanistic

Study of Phase Transformation in Perovskite Nanocrystals Driven by Ligand Passivation. *Chem. Mater.* 2018, 30, 84-93.

(31) Kort, K. R.; Banerjee, S., Shape-Controlled Synthesis of Well-Defined Matlockite LnOCl (Ln: La, Ce, Gd, Dy) Nanocrystals by a Novel Non-Hydrolytic Approach. *Inorg. Chem.* 2011, 50, 5539-5544.

(32) Kort, K. R.; Banerjee, S., Ligand-Mediated Control of Dislocation Dynamics and Resulting Particle Morphology of GdOCl Nanocrystals. *Small* 2015, 11, 329-334.

(33) Cho, J.; Choi, Y.-H.; O'Loughlin, T. E.; De Jesus, L.; Banerjee, S., Ligand-Mediated Modulation of Layer Thicknesses of Perovskite Methylammonium Lead Bromide Nanoplatelets. *Chem. Mater.* 2016, 28, 6909-6916.

(34) Cho, J.; Jin, H.; Sellers, D. G.; Watson, D. F.; Son, D. H.; Banerjee, S., Influence of ligand shell ordering on dimensional confinement of cesium lead bromide ($CsPbBr_3$) perovskite nanoplatelets. *J. Mater. Chem. C* 2017, 5, 8810-8818.

(35) Sichert, J. A.; Tong, Y.; Mutz, N.; Vollmer, M.; Fischer, S.; Milowska, K. Z.; García Cortadella, R.; Nickel, B.; Cardenas-Daw, C.; Stolarczyk, J. K., Quantum size effect in organometal halide perovskite nanoplatelets. *Nano Lett.* 2015, 15, 6521-6527.

(36) Shamsi, J.; Dang, Z.; Bianchini, P.; Canale, C.; Stasio, F. D.; Brescia, R.; Prato, M.; Manna, L., Colloidal synthesis of quantum confined single crystal $CsPbBr_3$ nanosheets with lateral size control up to the micrometer range. *J. Am. Chem. Soc.* 2016, 138, 7240-7243.

(37) Pan, A.; He, B.; Fan, X.; Liu, Z.; Urban, J. J.; Alivisatos, A. P.; He, L.; Liu, Y., Insight into the Ligand-Mediated Synthesis of Colloidal $CsPbBr_3$ Perovskite

Nanocrystals: The Role of Organic Acid, Base, and Cesium Precursors. *ACS Nano* 2016, 10, 7943-7954.

(38) Palazon, F.; Almeida, G.; Akkerman, Q. A.; De Trizio, L.; Dang, Z.; Prato, M.; Manna, L., Changing the Dimensionality of Cesium Lead Bromide Nanocrystals by Reversible Postsynthesis Transformations with Amines. *Chem. Mater.* 2017, 29, 4167-4171.

(39) Nikl, M.; Mihokova, E.; Nitsch, K.; Somma, F.; Giampaolo, C.; Pazzi, G.; Fabeni, P.; Zazubovich, S., Photoluminescence of Cs_4PbBr_6 crystals and thin films. *Chem. Phys. Lett.* 1999, 306, 280-284.

(40) Nitsch, K.; Cihlář, A.; Dušek, M.; Hamplova, V.; Nikl, M.; Rodova, M.; Ryšavá, N., Growth and characterization of crystals of incongruently melting ternary alkali lead chlorides. *Phys. Status Solidi A* 1993, 135, 565-571.

(41) Miao, X.; Qiu, T.; Zhang, S.; Ma, H.; Hu, Y.; Bai, F.; Wu, Z., Air-stable $CsPb_{1-x}Bi_xBr_3$ ($0 \leq x < 1$) perovskite crystals: optoelectronic and photostriction properties. *J. Mater. Chem. C* 2017, 5, 4931-4939.

(42) Stoumpos, C. C.; Malliakas, C. D.; Peters, J. A.; Liu, Z.; Sebastian, M.; Im, J.; Chasapis, T. C.; Wibowo, A. C.; Chung, D. Y.; Freeman, A. J.; Wessels, B. W.; Kanatzidis, M. G., Crystal Growth of the Perovskite Semiconductor $CsPbBr_3$: A New Material for High-Energy Radiation Detection. *Crystal Growth & Design* 2013, 13, 2722-2727.

(43) Cottingham, P.; Brutchey, R. L., On the crystal structure of colloidally prepared $CsPbBr_3$ quantum dots. *Chem. Commun.* 2016, 52, 5246-5249.

(44) Cottingham, P.; Brutchey, R. L., Compositionally Dependent Phase Identity of Colloidal $CsPbBr_{3-x}I_x$ Quantum Dots. *Chem. Mater.* 2016, 28, 7574-7577.

(45) Chen, D.; Wan, Z.; Chen, X.; Yuan, Y.; Zhong, J., Large-scale room-temperature synthesis and optical properties of perovskite-related Cs_4PbBr_6 fluorophores. *J. Mater. Chem. C* 2016, 4, 10646-10653.

(46) Waetzig, G. R.; Horrocks, G. A.; Jude, J. W.; Villalpando, G. V.; Zuin, L.; Banerjee, S., Ligand-Mediated Control of Dopant Oxidation State and X-ray Excited Optical Luminescence in Eu-Doped LaOCl. *Inorg. Chem.* 2018, 57, 5842-5849.

(47) Mulla, F.; Marsicano, F.; Nakani, B. S.; Hancock, R. D., Stability of ammonia complexes that are unstable to hydrolysis in water. *Inorg. Chem.* 1985, 24, 3076-3080.

(48) Koscher, B. A.; Swabeck, J. K.; Bronstein, N. D.; Alivisatos, A. P., Essentially Trap-Free $CsPbBr_3$ Colloidal Nanocrystals by Postsynthetic Thiocyanate Surface Treatment. *J. Am. Chem. Soc.* 2017, 139, 6566-6569.

(49) Bekenstein, Y.; Koscher, B. A.; Eaton, S. W.; Yang, P.; Alivisatos, A. P., Highly luminescent colloidal nanoplates of perovskite cesium lead halide and their oriented assemblies. *J. Am. Chem. Soc.* 2015, 137, 16008-16011.

(50) Tong, Y.; Bladt, E.; Aygüler, M. F.; Manzi, A.; Milowska, K. Z.; Hintermayr, V. A.; Docampo, P.; Bals, S.; Urban, A. S.; Polavarapu, L.; Feldmann, J., Highly Luminescent Cesium Lead Halide Perovskite Nanocrystals with Tunable Composition and Thickness by Ultrasonication. *Angew. Chem. Inter. Ed* 2016, 55, 13887-13892.

(51) Polavarapu, L.; Nickel, B.; Feldmann, J.; Urban, A. S., Advances in Quantum-Confined Perovskite Nanocrystals for Optoelectronics. *Adv. Energy Mater.* 2017, 7, 1700267.

(52) Dang, Z.; Shamsi, J.; Palazon, F.; Imran, M.; Akkerman, Q. A.; Park, S.; Bertoni, G.; Prato, M.; Brescia, R.; Manna, L., *In Situ* Transmission Electron Microscopy Study of Electron Beam-Induced Transformations in Colloidal Cesium Lead Halide Perovskite Nanocrystals. *ACS Nano* 2017, 11, 2124-2132.

(53) Hintermayr, V. A.; Richter, A. F.; Ehrat, F.; Döblinger, M.; Vanderlinden, W.; Sichert, J. A.; Tong, Y.; Polavarapu, L.; Feldmann, J.; Urban, A. S., Tuning the Optical Properties of Perovskite Nanoplatelets through Composition and Thickness by Ligand-Assisted Exfoliation. *Adv. Mater.* 2016, 28, 9478-9485.

(54) Almeida, G.; Goldoni, L.; Akkerman, Q.; Dang, Z.; Khan, A. H.; Marras, S.; Moreels, I.; Manna, L., Role of Acid–Base Equilibria in the Size, Shape, and Phase Control of Cesium Lead Bromide Nanocrystals. *ACS Nano* 2018, 12, 1704-1711.

(55) Davis, M. M.; Schuhmann, P. J., Acid-base reactions in benzene and other organic solvents; behavior of bromphthalein magenta with different classes of organic bases. *J. Res. Natl. Bur. Stand.* 1947, 39, 221.

(56) Palazon, F.; Urso, C.; De Trizio, L.; Akkerman, Q. A.; Marras, S.; Locardi, F.; Nelli, I.; Ferretti, M.; Prato, M.; Manna, L., Post-Synthesis Transformation of Insulating Cs_4PbBr_6 Nanocrystals Into Bright Perovskite $CsPbBr_3$ Through Physical and Chemical Extraction of CsBr. *ACS Energy Lett.* 2017. 2, 2445-2448.

(57) de Weerd, C.; Lin, J.; Gomez, L.; Fujiwara, Y.; Suenaga, K.; Gregorkiewicz, T., Hybridization of Single Nanocrystals of Cs_4PbBr_6 and $CsPbBr_3$. *J. Phys. Chem. C* 2017, 121, 19490-19496.

(58) Velázquez, M.; Ferrier, A.; Péchev, S.; Gravereau, P.; Chaminade, J.-P.; Portier, X.; Moncorgé, R., Growth and characterization of pure and Pr^{3+}-doped Cs_4PbBr_6 crystals. *J. Cryst. Growth* 2008, 310, 5458-5463.

(59) Irving, H.; Williams, R., The stability of transition-metal complexes. *J. Chem. Soc.* 1953, 0, 3192-3210.

(60) Soja, G. R.; Mann, J. R.; Watson, D. F., Temporal Evolution of the Composition of Mixed Monolayers on TiO_2 Surfaces: Evidence for a Dimerization-Induced Chelate Effect. *Langmuir* 2008, 24, 5249-5252.

(61) Kort, K. R.; Banerjee, S., Ligand-Mediated Control of Dislocation Dynamics and Resulting Particle Morphology of GdOCl Nanocrystals. *Small* 2015, 11, 329-334.

(62) Baronov, A.; Bufkin, K.; Shaw, D. W.; Johnson, B. L.; Patrick, D. L., A simple model of burst nucleation. *Phys. Chem. Chem. Phys.* 2015, 17, 20846-20852.

(63) Al-Sabagh, A.; Nasser, N.; Khamis, E.; Mahmoud, T., Synthesis of non-ionic surfactants based on alkylene diamine and evaluation of their corrosion inhibition efficiency on carbon steel in formation water. *Egypt. J. Petrol* 2017, 26, 41-51.

(64) Tian, Y.; Yu, B.; Li, X.; Li, K., Facile solvothermal synthesis of monodisperse Fe_3O_4 nanocrystals with precise size control of one nanometre as potential MRI contrast agents. *J. Mater. Chem.* 2011, 21, 2476-2481.

(65) De Roo, J.; Ibanez, M.; Geiregat, P.; Nedelcu, G.; Walravens, W.; Maes, J.; Martins, J. C.; Van Driessche, I.; Kovalenko, M. V.; Hens, Z., Highly dynamic ligand binding and light absorption coefficient of cesium lead bromide perovskite nanocrystals. *ACS Nano* 2016, 10, 2071-2081.

(66) Gusak, A. M.; Tu, K. N., Interaction between the Kirkendall effect and the inverse Kirkendall effect in nanoscale particles. *Acta Mater.* 2009, 57, 3367-337

CHAPTER V

ULTRAFAST TRANSIENT ABSORPTION SPECTROSCOPY FOR TIME-RESOLVED CHARGE TRANSFER KINETICS WITHIN $M_xV_2O_5$/QDs HETEROSTRUCTURES*

V.1 Introduction

Nanoscale semiconductor heterostructures are of tremendous interest for solar energy conversion owing primarily to the tunability of the bandgaps and band-edge potentials of semiconductors as a function of composition and size.[1-4] In a typical heterostructure configuration used for solar energy conversion, a light-harvesting semiconductor nanoparticle (excited-state charge donor) is interfaced with a wide-bandgap semiconductor (charge acceptor), and photogenerated charge carriers are transferred across the interface.[5-7] To achieve efficient solar energy conversion, the separation of excited electrons and holes must occur more rapidly than excited-state relaxation; and subsequent charge-transport or redox photocatalytic steps must outcompete charge recombination. The kinetics of charge separation depend substantially on the thermodynamic driving force, which is dictated by interfacial energetic offsets of electron-donating and accepting states. Consequently, the design of nanoscale semiconductor heterostructures for charge transfer and solar energy conversion requires careful consideration of interfacial energetic offsets.[8-10] The

*Reprinted with permission from "Programming Interfacial Energetic Offsets and Charge Transfer in β-$Pb_{0.33}V_2O_5$/Quantum-Dot Heterostructures: Tuning Valence-Band Edges to Overlap with Midgap States" by K.E. Pelcher, C. C. Milleville, L. Wangoh, J. Cho, A. Sheng, S. Chauhan, M. Y. Sfeir, L. F. J. Piper, D. F. Watson, and S. Banerjee, *J. Phys. Chem. C* **2016**, 51, 28992-29001 Reproduced by permission of © 2016 American Chemical Society. All rights reserved.

tunability of electronic structure that is accessible in semiconductor quantum dots (QDs) provides a powerful adjustable parameter for achieving heterostructures with desired energetic offsets. [1, 11-12]

Recently, we demonstrated a promising tunable platform for light-harvesting and excited-state charge transfer derived from interfacing β-$Pb_{0.33}V_2O_5$ nanowires (NWs) with CdSe QDs.[13-14] This platform exploits a distinctive feature in the electronic structure of ternary vanadium oxide bronzes: the presence of intrinsic midgap states, derived from the intercalating cations, that are situated between the valence and conduction band edges.[15-16] In the case of β-$Pb_{0.33}V_2O_5$, midgap states are derived from Pb 6s-O 2p antibonding interactions.[17-18] The energies and occupancies of these midgap states are tunable through the choice of intercalating cation and the cation stoichiometry.[17, 19] Since the intercalating cations are homogeneously incorporated within the quasi-1D crystal structure, such states constitute an integral part of the electronic structure and are quite distinct from midgap states derived from defects or dopants. Hard X-ray photoemission spectroscopy measurements revealed substantial energetic overlap between the midgap states of β-$Pb_{0.33}V_2O_5$ and valence-band states of CdSe, suggesting that the transfer of photogenerated holes from the valence band of CdSe into the midgap states of β-$Pb_{0.33}V_2O_5$ is possible as also verified by transient absorption spectroscopy experiments.[13-14] However, the valence band edge of CdSe QDs was measured to lie ca. 0.7 eV higher in energy than the highest-energy midgap states of β-$Pb_{0.33}V_2O_5$ NWs. Therefore, the transfer of thermalized holes at the valence band edge

of CdSe QDs to the midgap states of β-$Pb_{0.33}V_2O_5$ NWs was thermodynamically unfavorable.[13]

The size- and composition-dependent electronic structure of QDs is advantageous when designing heterostructures with desirable interfacial energetic offsets and tunable driving forces for excited-state charge transfer.[2, 5] In this article, we demonstrate that an improved driving force for hole transfer in QD/NW heterostructures is obtained by replacing CdSe QDs with CdS QDs of the appropriate dimensionality as light-harvesters and excited-state hole donors. The valence band edge of bulk CdS is ca. 0.5 eV lower in energy than that of bulk CdSe,[20-21] which provides a means for improving the energetic overlap of the valence-band states of QDs with midgap states of β-$Pb_{0.33}V_2O_5$ NWs, thereby rendering such interfaces more suitable for excited-state charge separation and yielding heterostructures designed to optimally harvest solar radiation. Interfacial energetic offsets have been examined for heterostructures with distinctive sizes and modes of attachment of CdS and CdSe QDs. Transient absorption spectroscopy measurements have further been used to dynamically resolve hole and electron transfer processes in these heterostructures and suggest that the midgap states of β-$Pb_{0.33}V_2O_5$ NWs mediate hole transfer from photoexcited QDs at <1 ps timescales. The design concepts illustrated here underscore the programmability of charge transfer in heterostructures coupling QDs with NWs characterized by distinctive intercalative states.

V.2 Experimental

Synthesis of β-$Pb_{0.33}V_2O_5$ nanowires. β-$Pb_{0.33}V_2O_5$ NWs were prepared using a one-step hydrothermal reaction as previously reported.[18] In brief, stoichiometric amounts of $Pb(CH_3COO)_2 \cdot 3H_2O$ and V_2O_5 were placed in a polytetrafluoroethylene-lined acid digestion vessel (Parr) along with 16 mL of deionized (DI) water. The vessel was sealed in an autoclave and heated to 250ºC for 72 h. The product was isolated by vacuum filtration, washed with water, and allowed to dry in air.

Synthesis of Cysteinate-capped CdSe Quantum Dots. Cysteinate-capped CdSe QDs with average diameters less than 2 nm, hereafter referred to as Cys-CdSe(sm), were synthesized as previously reported.[22] The selenium precursor was prepared by refluxing an aqueous solution of Se powder and Na_2SO_3 overnight, and the cadmium precursor was an aqueous solution of $3CdSO_4 \cdot 8H_2O$ and cysteine. The pH of the cadmium precursor was titrated to 12.5—13.0 with solid NaOH. The hot selenium precursor was added to the cadmium precursor and allowed to stir for 30 min. The resulting dispersions of Cys-CdSe(sm) QDs were purified by solvent/non-solvent (H_2O/MeOH, 3:1) washing to remove excess reagents. Cysteinate-capped CdSe QDs with greater average diameters, hereafter referred to as Cys-CdSe(lg) QDs, were synthesized and purified by a similar procedure, differing only in that the cadmium precursor was heated to, and maintained at, 80ºC for the duration of the experiment (2 h)[23].

Synthesis of Cysteinate-capped CdS Quantum Dots. Cysteinate-capped CdS QDs were prepared using a modification of the synthesis of Cys-CdSe(sm) QDs. A sulfur precursor solution was prepared by adding sodium thiosulfate (1.17 g, 7.41 mmol) to 25

mL DI water in a 50 mL round bottom flask and heating to reflux for 30 min. For QDs with relatively smaller average particle size, hereafter referred to as Cys-CdS(sm) QDs, the cadmium precursor was an aqueous solution (10.5 mL) of cadmium sulfate octahydrate (0.433 g, 1.69 mmol) and cysteine (1.02 g, 8.44 mmol). The pH of the solution was titrated to 12.5—13.0 with solid NaOH. The hot sodium thiosulfate solution (4.5 mL) was added to the cadmium precursor with stirring. The reaction was allowed to stir overnight (12—16 h) resulting in the formation of a cloudy, white suspension of flocculated Cys-CdS(sm) QDs. For QDs with relatively larger average particle size, hereafter referred to as Cys-CdS(lg) QDs, the cadmium precursor was an aqueous solution (21 mL) of cadmium sulfate octahydrate (0.866g, 3.38 mmol) and cysteine (2.05 g, 16.88 mmol). The pH of the solution was titrated to 12.5—13.0 with solid NaOH. The cadmium precursor was then heated to 80^{o}C and the hot sodium thiosulfate solution (9 mL) was added with stirring. The reaction was allowed to continue heating for 4 h with stirring, resulting in the formation of a cloudy, yellow suspension of flocculated Cys-CdS(lg) QDs. Typical concentrations of cadmium, sulfur, and Cys in the reaction mixtures for both Cys-CdS(sm) and Cys-CdS(lg) were 113, 90, and 563 mM, respectively. Dispersions of both Cys-CdS(sm) and Cys-CdS(lg) QDs were purified by solvent/non-solvent washing to remove excess reagents. First, 5 mL of the flocculated QDs were centrifuged to isolate the QDs and the supernatant was discarded. The pellet of QDs was then fully dispersed into 10 mL DI water resulting in a clear dispersion. Then, 30 mL of methanol was added to the dispersion of QDs, resulting in the flocculation of QDs. The flocculate was then centrifuged again to isolate the QDs,

supernatant was discarded, and the QDs were redispersed into 10 mL DI water. This process was repeated once for a total of two purification cycles.

Successive Ionic Layer Adsorption and Reaction (SILAR) Assembly of β-$Pb_{0.33}V_2O_5$ /CdX (X = Se, S) Heterostructures. CdSe was deposited directly onto β-$Pb_{0.33}V_2O_5$ NWs via SILAR using a previously reported method.[13] In a single SILAR cycle, CdSe QDs were grown directly onto β-$Pb_{0.33}V_2O_5$ NWs by sequentially mixing the NWs with a cadmium precursor solution ($Cd(NO_3)_2$ in ethanol), followed by a selenium precursor (Na_2Se in ethanol). The NWs were washed with ethanol following each mixing step to remove excess ions. CdS/β-$Pb_{0.33}V_2O_5$ heterostuctures were prepared using a modification of this procedure. A 50 mM solution of Na_2S was prepared by dissolving $Na_2S{\cdot}9H_2O$ in ethanol. Meanwhile, β-$Pb_{0.33}V_2O_5$ NWs (50 mg) were dispersed in 15 mL of ethanol, and a 100 mM solution of $Cd(NO_3)_2{\cdot}4H_2O$ was prepared in ethanol. All solutions and dispersions were placed in a glovebag filled with Ar gas. To begin the SILAR cycle, the dispersion of NWs was mixed with the $Cd(NO_3)_2$ solution, thus bringing the concentration of $Cd(NO_3)_2$ to 50 mM. The solution was stirred for 30 s, and the NWs were then removed through centrifugation at 6500 rpm for 90 s. Subsequently, the NWs were washed with 10 mL of ethanol for 30 s and centrifuged. Next, the NWs were mixed with the Na_2S solution for 30 s, centrifuged and isolated, and washed again with 10 mL of ethanol. This final washing step concludes one SILAR cycle.

Linker-assisted Assembly of Cys-CdSe/β-$Pb_{0.33}V_2O_5$ Heterostructures. Cys-CdSe(sm)/β-$Pb_{0.33}V_2O_5$ and Cys-CdSe(lg)/β-$Pb_{0.33}V_2O_5$ heterostructures were prepared *via* LAA as reported previously.[13] An aqueous dispersion of β-$Pb_{0.33}V_2O_5$ NWs was

added to an aqueous dispersion of purified Cys-CdSe(sm) or Cys-CdSe(lg) QDs and allowed to equilibrate overnight (12—16 h). CdSe-functionalized NWs were recovered by centrifugation, rinsed with DI water to remove excess QDs, and dried at room temperature before characterization.

Linker-assisted Assembly of Cys-CdS/β-$Pb_{0.33}V_2O_5$ Heterostructures. Cys-CdS/β-$Pb_{0.33}V_2O_5$ heterostructures were prepared using a modification of the LAA method employed for formation of Cys-CdSe/β-$Pb_{0.33}V_2O_5$ heterostructures. β-$Pb_{0.33}V_2O_5$ NWs (10 mg) were dispersed in DI water (10 mL) in a 20 mL scintillation vial. The dispersion was sonicated for 20 min to maximize the amount of dispersed NWs. An aqueous dispersion of either purified Cys-CdS(sm) QDs or purified Cys-CdS(lg) QDs (1 mL) was added to the dispersion of β-$Pb_{0.33}V_2O_5$ NWs and allowed to equilibrate overnight (12—16 h). Cys-CdS(sm)/β-$Pb_{0.33}V_2O_5$ or Cys-CdS(lg)/β-$Pb_{0.33}V_2O_5$ heterostructures were recovered *via* centrifugation and then rinsed with DI water to remove excess QDs. The heterostructures were dried at room temperature prior to characterization.

Synthesis of β-$Sn_xV_2O_5$/CdX (X = Se, Te) QD Heterostructures. β-$Sn_xV_2O_5$ nanowires were interfaced with CdX QDs using the SILAR method in a glovebag under an argon atmosphere. In a typical SILAR process, as-prepared β-$Sn_xV_2O_5$ nanowires were first dispersed in an ethanol solution of the cadmium precursor ($Cd(NO_3)_2 \cdot H_2O$, Alfa Aesar, 98.5%) for 45 seconds under manual stirring, washed with ethanol, and recovered by centrifugation at 6000 rpm for 2 minutes. In a second step, the material was then immersed in an ethanol solution of the sodium chalcogenide precursor (Na_2X, Alfa Aesar, 99.8% in ethanol, X = Se, Te) for 45 seconds under manual stirring, washed

with ethanol, and finally recovered by centrifugation at 6000 rpm for 2 minutes. One SILAR cycle thus comprises immersion in the cadmium precursor solution and an ethanol washing step, followed immediately by immersion in the chalcogenide precursor and an ethanol washing step. Three complete SILAR cycles were performed to prepare the β-$Sn_xV_2O_5$/CdX heterostructures examined in this study. After three SILAR cycles, the heterostructures were washed with a large excess of ethanol to remove excess QDs not adhered to the nanowire surfaces and were then allowed to dry at room temperature under ambient conditions.

Time-resolved transient absorption spectroscopy. Transient absorption (TA) measurements were acquired using a commercial Ti:sapphire amplified laser system (SpectraPhysics Spitfire Pro, 800 nm, 1 kHZ repetition rate). Wavelength tunable pump pulses were generated in a commercial optical parametric amplifier (LightConversion). For femtosecond time delays, a supercontinuum probe beam (425—900 nm) was generated by focusing a fraction of the laser fundamental into a sapphire disc to generate supercontinnum probe light and was mechanically delayed (dynamic range of 3 ns) relative to the pump pulse. For longer probe times, a separate fiber-based supercontinuum laser was used to generate the probe beam and was electronically delayed (dynamic range of > 20 μs) relative to the pump pulse (Ultrafast Systems). TA decay traces were compiled by averaging ΔA values over a given range of probe wavelengths at each delay time.

V.3 Results and Discussion

1st Generation Photocatalytic Architectures of β-$Pb_xV_2O_5$/QD

The design of semiconductor heterostructures for solar energy conversion necessitates not just optimal thermodynamics for directional charge transfer but also requires that the photoinduced charge transfer processes occur more rapidly than competing charge recombination pathways. In order to evaluate the timescales of these competing pathways, excited state charge carrier dynamics were investigated for the CdS/β-$Pb_{0.33}V_2O_5$ heterostructures given that X-ray photoelectron spectroscopy (XPS) measurements indicate that the valence band of these QDs is better overlapped with the midgap states of the NWs. TA spectroscopy experiments at picosecond timescales allow for a clear mapping of charge transfer processes within these heterostructures. The pump excitation wavelength of 360 nm (3.4 eV) used in these experiments corresponds to an above-bandgap excitation for both the CdS QDs (bandgap of 2.8 eV) and β-$Pb_{0.33}V_2O_5$ NWs (bandgap of 2.4 eV). TA spectra have been acquired in the wavelength range of 450–750 nm and 425–750 nm for thin films of SILAR- and LAA-derived CdS QD/NW heterostructures, respectively.

Figure V. 1 contrasts the TA spectra of unfunctionalized β-$Pb_{0.33}V_2O_5$ NWs as well as SILAR- and LAA-derived CdS QD/β-$Pb_{0.33}V_2O_5$ NWs heterostructures. The spectra are extracted from the data matrix by averaging ΔA values at delay times between 1000 and 2500 ps. The following spectral features are distinguished in all three spectra: a transient bleach at 440—480 nm, an induced absorption band centered at 550—650 nm, and another lower energy induced absorption band at 650—750 nm. The

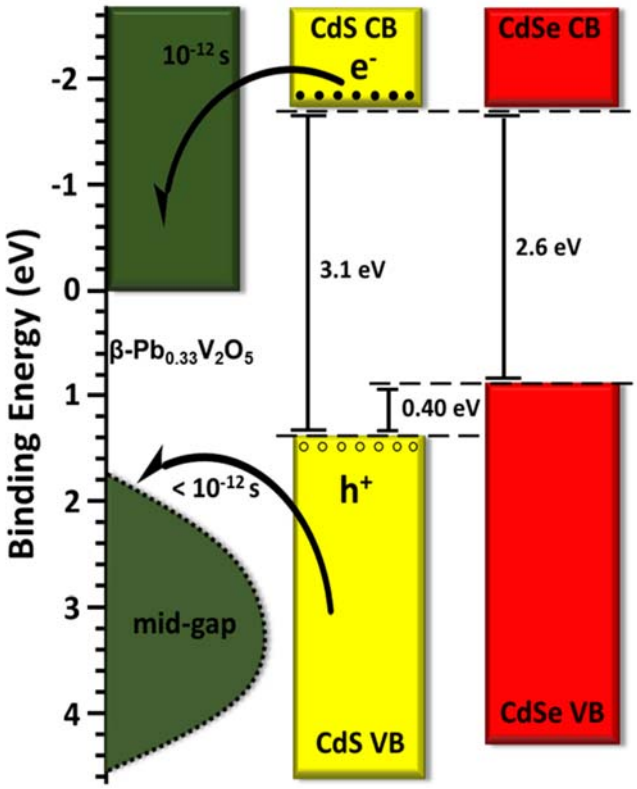

Figure V. 1 Schematic indicating the relative positioning of the valenceband and conduction-band edges of Cys-CdSe versus Cys-CdS as deduced from XPS measurements, as well as the time scales for electron and hole transfer from photoexcited CdS QDs into the midgap states and CB of β-$Pb_{0.33}V_2O_5$, respectively, as obtained from TA spectroscopy experiments.

spectral features have been assigned based on spectroelectrochemical studies of β-$Pb_{0.33}V_2O_5$ NWs,[14] which indicate that the TA spectrum for this material is captured well by a summation of spectra for electrochemically oxidized and reduced species. Considering unfunctionalized β-$Pb_{0.33}V_2O_5$,[14] the intense 550—650 nm induced absorption band can be ascribed to the excitation of electrons from the valence band to empty midgap states (and is thus characteristic of a hole situated on the β-$Pb_{0.33}V_2O_5$ framework).[14] The lower energy 650—750 nm band can be attributed to the excitation of

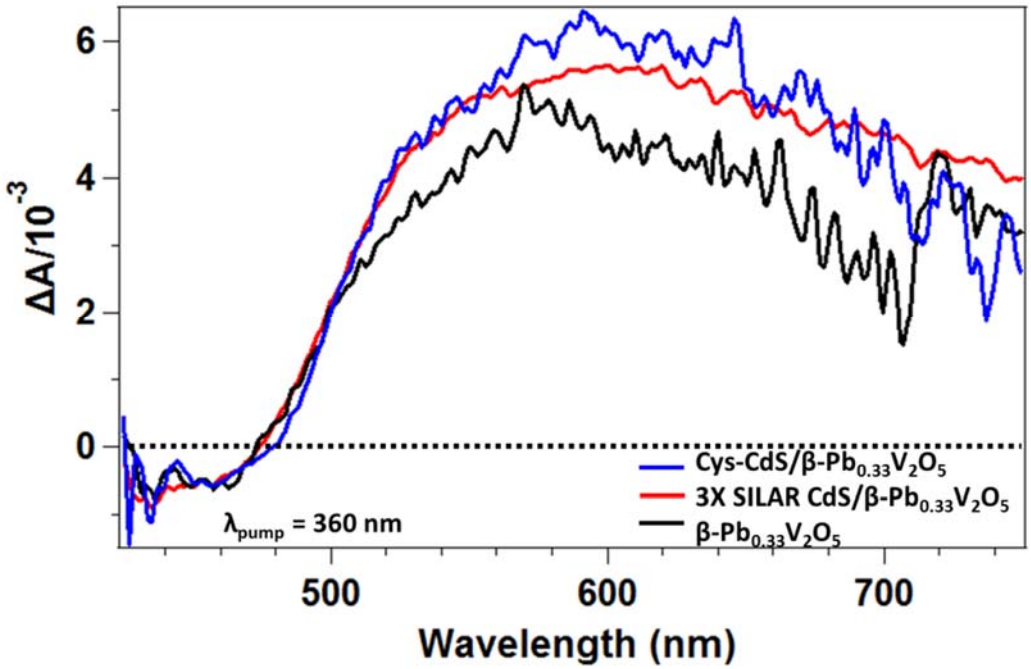

Figure V. 2 TA spectra of unfunctionalized β-$Pb_{0.33}V_2O_5$ NWs (black), 3× SILAR CdS/ β-$Pb_{0.33}V_2O_5$ heterostructures (blue), and Cys-CdS β-$Pb_{0.33}V_2O_5$ heterostructures (red) acquired at λ_{pump} = 360 nm. The spectra are averaged for delay times in the interval 1000–2500 ps.

electrons from the conduction band to higher energy states in the conduction band (and is thus characteristic of a free electron in β-$Pb_{0.33}V_2O_5$). The bleach in the differential absorption spectra reflects the reduced oscillator strength of the bandgap absorption once an electron has been excited into the conduction band (bleach of ground state absorption).

The spectra in Figure V.1 are normalized to the transient bleach of β-$Pb_{0.33}V_2O_5$ NWs in an attempt to contrast the spectral features of bare β-$Pb_{0.33}V_2O_5$ NWs with those of the CdS/β-$Pb_{0.33}V_2O_5$ heterostructures. Both the LAA- and SILAR-derived QD/NW heterostructures exhibit an increased population of electrons and holes (but an otherwise very similar spectral profile) as compared to the bare β-$Pb_{0.33}V_2O_5$ nanowires where the

carrier density derives entirely from direct photoexcitation. The increased population of holes and electrons is attributed to charge transfer from the photoexcited CdS as schematically illustrated in **Figure V. 2**, wherein electrons are transferred from the photoexcited QDs to the conduction band of the β-$Pb_{0.33}V_2O_5$ NWs, whereas holes are transferred to the midgap states of the β-$Pb_{0.33}V_2O_5$ NWs. This charge-transfer mechanism, and the transient absorption spectral features, are consistent with previously-reported results for CdSe/β-$Pb_{0.33}V_2O_5$ heterostructures.[14]

To resolve the dynamics of electron and hole transfer, ultrafast transient absorption measurements were acquired on picosecond time scales for the LAA- and SILAR-derived CdS/β-$Pb_{0.33}V_2O_5$ heterostructures and are shown in **Figure V. 3** Ultrafast measurements for β-$Pb_{0.33}V_2O_5$ NWs are shown in **Figure A. 29** and suggest that the transient absorption bands reach their maximum amplitude within the response time of the instrument, which is consistent with the assignment of these spectral features to electron—hole pairs generated by direct photoexcitation. The spectra for both the LAA and SILAR-derived samples evolve to the TA spectra observed in Figures V. 3. However, several additional features are discernible at earlier time scales and enable direct observation of interfacial charge transfer in these heterostructures. A pronounced bleach with a minimum at 455 nm is observed for LAA-derived Cys-CdS/β-$Pb_{0.33}V_2O_5$ heterostructures; a similar bleach centered at 485 nm is observed for SILAR-derived CdS/β-$Pb_{0.33}V_2O_5$ heterostructures. These features are attributed to the bleach of the first excitonic ground state absorption of the CdS QDs, consistent with the nanosecond-timescale TA spectrum of colloidal Cys-CdS QDs (**Figure A. 30**). The TA spectrum of

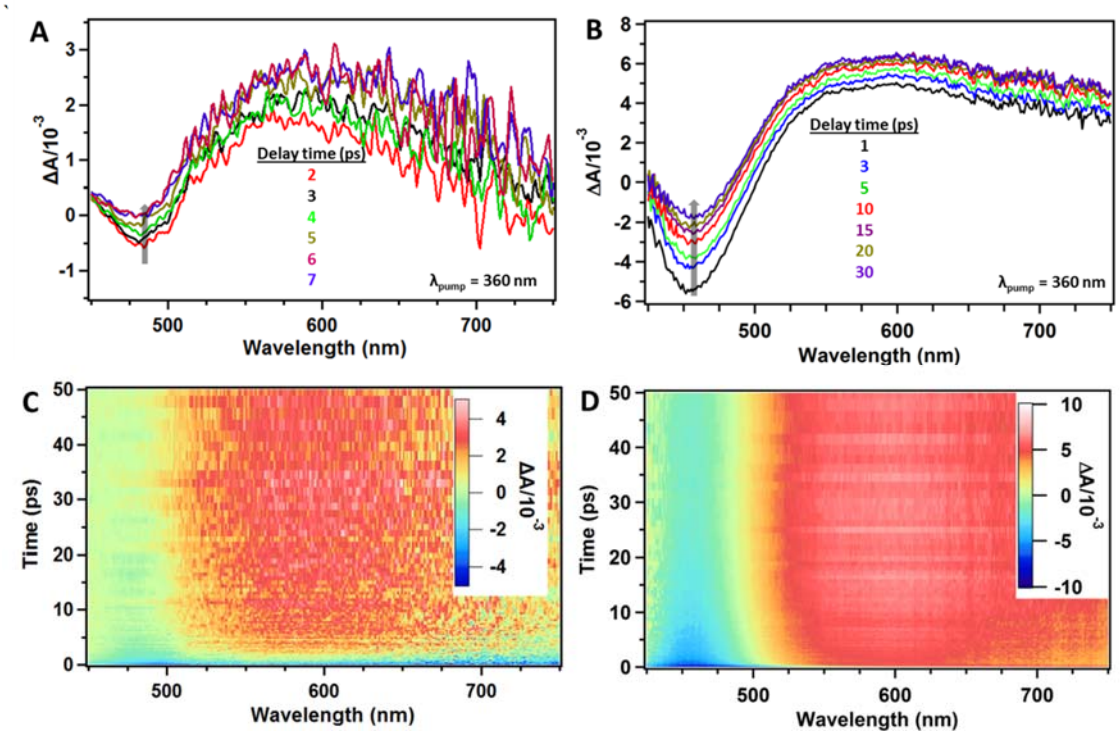

Figure V. 3 TA spectra of (A) 3× SILAR CdS/β-$Pb_{0.33}V_2O_5$ and (B) Cys-CdS β-$Pb_{0.33}V_2O_5$ and 3D TA color maps of (C) 3× SILAR CdS/β-$Pb_{0.33}V_2O_5$ and (D) Cys-CdS β-$Pb_{0.33}V_2O_5$, indicating ΔA in the 0–50 ps range for probe wavelengths in the range of 425–850 nm with λ_{pump} = 360 nm.

aqueous dispersions of Cys-CdS(lg) QDs exhibits a long-lived bleach with an average lifetime of 230±45 ns (**Table A. 5**) centered at 440 nm with an onset at 462 nm (Figure A. 30). Since both Cys-CdS QDs and β-$Pb_{0.33}V_2O_5$ NWs absorb at 360 nm, the TA spectra of the heterostructures can be reasonably assigned to the combination of the TA spectra of the individual components. The bleach derived from the CdS QDs recovers much more rapidly but at different timescales for the LAA- and SILAR-derived heterostructures until only the blue-shifted characteristic bleach of β-$Pb_{0.33}V_2O_5$ remains (**Figure V.3**). The bleach recovers with an average lifetime of 5.4±1.1 ps for the LAA-

derived Cys-CdS/β-$Pb_{0.33}V_2O_5$ heterostructure (**Table A. 6**). The characteristic red-shifted residual bleach of β-$Pb_{0.33}V_2O_5$ is fully recovered upon decay of the CdS bleach after ca. 30 ps. For the SILAR-derived CdS/β-$Pb_{0.33}V_2O_5$ heterostructure, the TA spectrum shows a bleach signal throughout the spectrum due to some contribution of instrument response to the TA signal, which precludes the reliable extraction of lifetimes. Nevertheless, it can be inferred from Figure V. 3C and 3D that the bleach corresponding to CdS QDs recovers to the blue-shifted bleach of β-$Pb_{0.33}V_2O_5$ NWs within approximately 5 ps. Since the bleach feature in TA spectra of QDs is dominated by the electron population in the excited state,[33-35] the much more rapid decay of the bleach observed in QD/NW heterostructures as compared to the aqueous dispersion of Cys-CdS QDs can be reasonably assigned to electron transfer from CdS QDs to β-$Pb_{0.33}V_2O_5$ NWs. The red-shifted bleach observed for the SILAR QD/NW heterostructures is attributed to the larger size of these QDs. The slower decay of the excitonic bleach of CdS for LAA-derived heterostructures (ca. 30 ps to completion) relative to SILAR-derived heterostructures (ca. 5 ps to completion) reveals that electron transfer is slower for the LAA-derived heterostructures. The greater barrier to electron injection observed for the LAA-derived heterostructures likely derives from the increased charge-transfer distance and relatively lower extent of electronic coupling (decreased overlap integrals) at these interfaces as compared to the directly coupled SILAR interfaces as also predicted by Marcus' kinetic theory.[31-32, 36-37] The induced absorption band centered at 550—650 nm in Figure V. 3 approaches its maximum amplitude within the instrument response suggesting that hole transfer proceeds much

faster, at <1 ps timescales, than electron transfer for both SILAR and LAA-derived heterostructures (completed within 5 and 30 ps, respectively, as noted above). Some modest growth of both the induced absorption bands is nevertheless still discernible over a few picoseconds in Figures V. 3A and B.

TA kinetic traces were extracted around the 440—470 nm bleach, the 550—650 nm absorption, and the 700—750 nm absorption band (Fig. 6). The decay of the bleach and the rises of the absorptions were fitted to multiexponential kinetics as per the following equation:

$$\Delta A = \Delta A_0 + \sum_i C_i e^{\left(-\frac{t}{\tau_i}\right)} \qquad \text{(V. 1)}$$

where ΔA is absorbance difference, ΔA_0 is the absorbance difference that the data approach at long timescales, C_i is a preexponential weighting factor, t is delay time, and τ_i is lifetime. The smallest number of individual lifetime components, τ_i, which resulted in the minimum χ^2, were used for each fit. The decay curves corresponding to bleach and induced absorption features for aqueous dispersion of cysteinate-capped CdS QDs, LAA-derived CdS/β-$Pb_{0.33}V_2O_5$ heterostructures, and SILAR-derived CdS/β-$Pb_{0.33}V_2O_5$ heterostructures were fitted to either monoexponential kinetics (i = 1) or biexponential kinetics (i = 2). Decay curves for SILAR-derived CdS/β-$Pb_{0.33}V_2O_5$ heterostructures could not be fitted accurately due to the highly variable bleach component observed at zero delay time, which is attributed to instrument response. The fitted parameters for the decay curves for various samples are tabulated in Tables A. 5 and A. 6. Amplitude-weighted average lifetimes (<τ>) were calculated using equation 2:

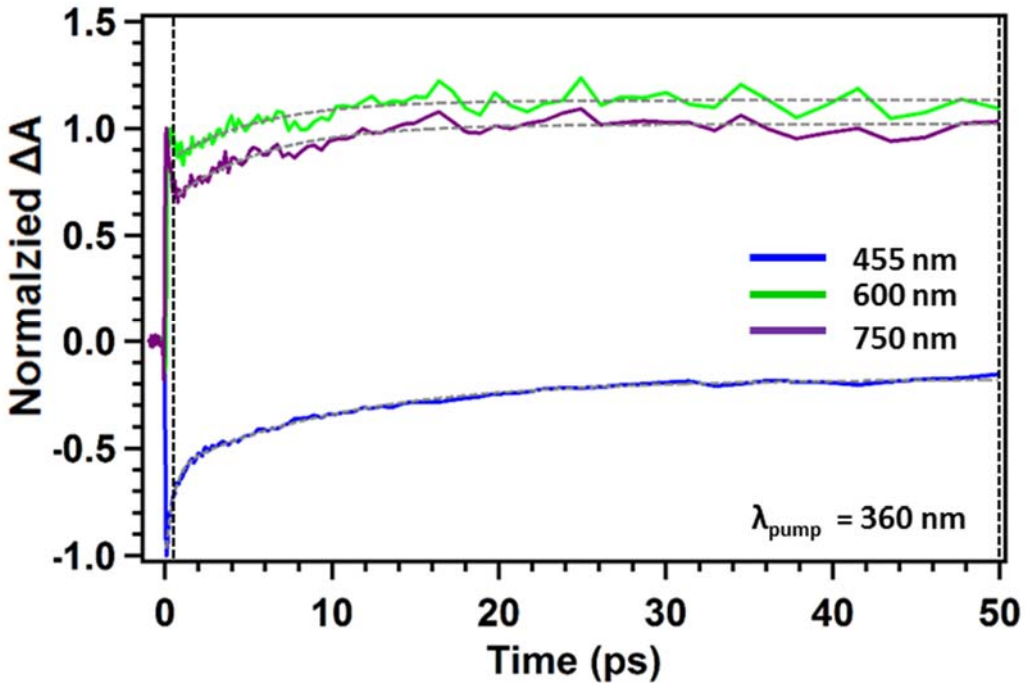

Figure V. 4 TA decay traces and multiple exponential fits measured for LAA-derived QD/NW heterostructures at different probe wavelengths of 455 (biexponential), 600 (monoexponential), and 740 nm (monoexponential) with λ_{pump} = 360 nm.

$$\langle \boldsymbol{\tau} \rangle = \frac{\sum_i \boldsymbol{C_i \tau_i}}{\sum_i \boldsymbol{C_i}} \qquad \text{(V. 2)}$$

The percentage of non-time-resolvable and time-resolvable growth of induced absorption bands, which provide indications of the percentages of hole-transfer events that occurred within our instrument response and on slower, resolvable, time scales, respectively, were estimated as $\Delta A_{non\text{-}resolvable}$ and $\Delta A_{resolvable}$:

$$\%\, \Delta A_{non-resolvable} = \frac{\Delta A_1}{\Delta A_2} \cdot 100 \qquad \text{(V. 3)}$$

$$\%\, \Delta A_{resolvable} = \frac{\Delta A_2 - \Delta A_1}{\Delta A_2} \cdot 100 = 100 - \%\, \Delta A_{non-resolvable} \qquad \text{(V. 4)}$$

where $\boldsymbol{\Delta A_1}$ and $\boldsymbol{\Delta A_2}$ are the absorbance differences at delay times of 0.8 ps (immediately after the initial sharp increase of apparent absorption attributable to instrument response)

and 50 ps, respectively, for a given bleach or induced absorption band. The relevant delay times are indicated by dashed lines in **Figure V. 4**.

For the Cys-CdS(lg)/β-$Pb_{0.33}V_2O_5$ heterostructures, values of $\%\Delta A_{\text{non-resolvable}}$ for the 600 and 740 nm absorption bands were estimated to be 76.3% and 68.3%, respectively. This difference suggests that more holes were injected into the midgap states of β-$Pb_{0.33}V_2O_5$ NWs (the 550—650 nm induced absorption band is the characteristic signature of holes) from the photoexcited CdS QDs as compared to electrons into the conduction band of the NWs (the 740 nm induced absorption band is the characteristic spectral signature of electrons) within the instrument response time. This observation is further consistent with the timescales for electron and hole transfer deduced above. The relative ease with which holes are transferred in these heterostructures and the ability to enhance the differential in the timescales of hole and electron transfer by insertion of molecular linkers suggests that the QD/NW heterostructures exploiting midgap states constitute a viable architecture for excited-state charge separation and photocatalysis

2nd Generation Photocatalytic Architectures of β-$Sn_xV_2O_5$/QD

The central advance of 2nd generation photocatalytic architectures is illustrated by the improved alignment of the Sn-derived midgap state (blue) with the VB of the CdSe QDs (green), leading to a diminished thermodynamic barrier (Φ_h) for hole transfer from the photoexcited QD to the semiconducting nanowire as shown in the energy offset diagram (Figure I. 5). We next turn our attention to determining whether such initially

Table V. 1 Experimentally determined valence band onsets for CdSe/β-$Pb_{0.33}V_2O_5$ heterostructures

Sample	Valence Band Edge (eV)
LAA Cys-CdS/β-$Pb_{0.33}V_2O_5$	1.33±0.02
SILAR CdS/β-$Pb_{0.33}V_2O_5$	1.32±0.02
LAA Cys-CdSe/β-$Pb_{0.33}V_2O_5$	0.92±0.01
SILAR CdSe/β-$Pb_{0.33}V_2O_5$	0.94±0.02

predicted and now experimentally realized midgap states give rise to efficacious or rapid hole extraction from the VB of photoexcited QDs using transient absorption (TA) spectroscopy measurements.[14,38] **Figure V. 5** depicts 3D TA color maps ranging between 0—5 ps and TA spectra acquired at various delay times (from 0.5—20 ps) for β-$Sn_xV_2O_5$ nanowires and β-$Sn_xV_2O_5$/CdSe heterostructures. The 3D color maps clearly elucidate the rise of transient induced absorption features (indicated in red) and the recovery of the transient bleaches (indicated in blue) as a function of delay time. The bare β-$Sn_xV_2O_5$ nanowires (**Figure V. 5A and C**) are characterized by two broad induced absorption bands at 500—600 nm and 650—750 nm as well as a bleach centered at ca. 465 nm. Based on spectroelectrochemical measurements and TA spectra measured for β-$Pb_xV_2O_5$ nanowires, the short-wavelength induced absorption feature observed for β-$Sn_{0.23}V_2O_5$ can be ascribed to transitions from deep VB states into the midgap states after photoexcitation of electrons from the midgap states (and thus corresponds to oxidation of the nanowires). The longer-wavelength induced absorption band can be assigned to excitation of electrons in the conduction band of β-$Sn_{0.23}V_2O_5$ to higher energy states (corresponding to the reduction of the nanowires).[14,38] In other words, the shorter wavelength (500—600 nm) and longer wavelength (650—750 nm) induced absorption

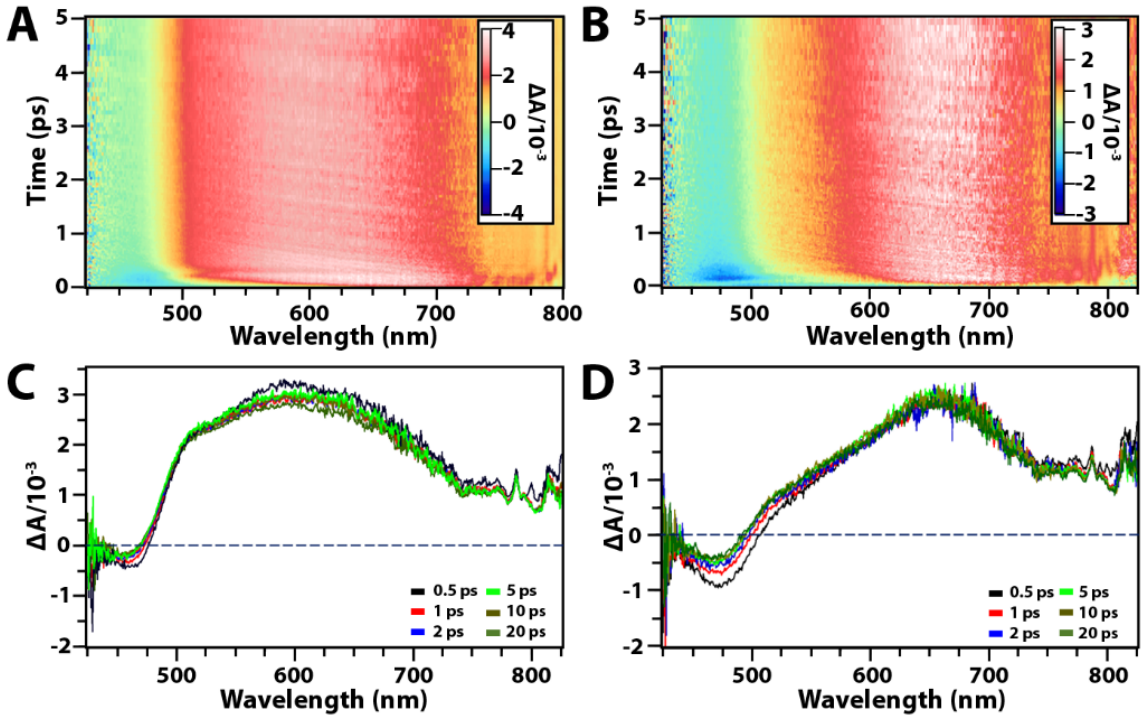

Figure V. 5 Evidence of fast hole transfer dynamics from photoexcited Cd*Se* QDs to occupied midgap states of β-$Sn_xV_2O_5$. TA intensity maps acquired for **(A)** β-$Sn_xV_2O_5$ nanowires and **(B)** β-$Sn_xV_2O_5$/CdSe heterostructures in the delay time range of 0—5 ps across a probe wavelength range of 425—825 nm at an excitation wavelength of 360 nm. TA spectra collected within the same time range for **(C)** β-$Sn_xV_2O_5$ nanowires and D) β-$Sn_xV_2O_5$/CdSe heterostructures. Each individual spectrum in (C) and **(D)** is taken as a horizontal 'slice' of the 3D maps in (A) and (B) at specific delay times (integrated across: a ±0.1 ps time window for the 0.5 ps decay; a ±0.5 ps time window for 1, 2.5, and 5 ps decay traces; and a ±2.5 ps time window for 10, 20 ps decay traces). TA decay and recovery traces as well as multiexponential fits are shown in Figure A. 31.

features can be assigned to excited-state holes in the midgap gap state and electrons situated in the conduction bands of β-$Sn_xV_2O_5$ nanowires, respectively. Upon direct photoexcitation at 360 nm both bands are presented within the instrument response time corresponding to the creation of holes in the midgap states and excited electrons in the conduction band. The TA spectra of β-$Sn_xV_2O_5$/CdSe heterostructures (**Figure V. 5B and D**) show some stark differences from spectra acquired for the bare β-$Sn_xV_2O_5$ nanowires.

A significant reduction in the induced absorption band at 500—600 nm is clearly discernible, which is a result of overlap with the characteristic excitonic bleach of CdSe QDs.[14,38] The bleach of the ground-state absorption of CdSe QDs, combining both first and second excitonic transitions, gives rise to an initial broad bleach feature in the ΔA spectra.[14,39] A pronounced rise of the $Sn_xV_2O_5$ induced absorption bands and the recovery of the CdSe bleach (to the blue-shifted bleach of β-$Sn_xV_2O_5$) is clearly distinguishable in the differential absorption spectra (ΔA) well within 5 ps. The recovery of the CdSe excitonic bleach at picosecond timescales is attributed to electron transfer from the conduction band of the QDs to the CB of β-$Sn_xV_2O_5$ nanowires (bleaches observed in excited QDs primarily reflect electron dynamics).[34,40] Note that this process occurs in binary heterostructures in the absence of an electron acceptor that would spatially separate the hole and electron as achieved in the photocatalytic architectures described above. Consequently, the hole transfer dynamics from photoexcited CdSe QDs to the midgap states of β-$Sn_xV_2O_5$ occurs within the instrument response time, reflecting ultrafast sub-picosecond timescales, whereas the electron transfer process can be resolved within the first few picoseconds.

TA recovery traces have been extracted and fitted for the exciton bleach feature attributed solely to QDs (centered at 485 nm); similarly, TA decay traces have been analyzed for an induced absorption band coupled to the QD bleach centered at 525 nm (**Figure A. 31**). The TA recovery and decay traces have been fitted using multiexponential functions since multiple relaxation pathways are operational including multiple trap-state-mediated recombination processes.[14,38] The fitting parameters used to

describe the decay and recovery kinetics are listed in **Table A. 7**. Decay traces obtained for the β-$Sn_xV_2O_5$/CdSe heterostructures are well described using biexponential decay functions (i = 2). As noted above, the hole transfer kinetics cannot be resolved within the instrument response time; however, the multiexponential fits suggest complete recovery of the CdSe excitonic bleach and growth of the corresponding induced absorption band at 525 nm, both corresponding to electron transfer processes, occurs within 1—2 ps. The deduced average lifetimes <τ> at probe wavelengths of 485 and 525 nm are calculated to be 0.4±0.1 ps and 0.3±0.1 ps, respectively (**Table A. 7**).

Analogous TA data for β-$Sn_xV_2O_5$/CdTe heterostructures is shown in **Figure. A. 32A and B**. The 3D TA color maps and time-resolved TA spectra are again consistent with ultrafast sub-picosecond hole transfer (which cannot be resolved within the instrument response time) but electron transfer (observed as recovery of the excitonic bleach of CdTe QDs)[41] is demonstrably slower as compared to the CdSe heterostructures. The pronounced rise of ΔA over time corresponds to increased injection of electrons from the CB of CdTe QDs to the CB of β-$Sn_xV_2O_5$. **Figure A. 32C** illustrates the TA decay and recovery traces and their corresponding multiexponential fits measured for β-$Sn_xV_2O_5$/CdTe heterostructures at 485 nm and 675 nm. The former corresponds to excitonic bleach CdTe QDs, whereas the latter corresponds to the first excitonic feature of CdTe QDs coupled with the induced absorption feature of β-$Sn_xV_2O_5$. The deduced average lifetimes <τ> at 485 and 675 nm are 4.3±0.3 and 3.5±0.8 ps, respectively, which suggest a considerably slower electron transfer process as compared to the β-$Sn_xV_2O_5$/CdSe heterostructures. The slower electron transfer

dynamics can be directly attributed to the decreased thermodynamic driving force for charge transfer relative to β-$Sn_xV_2O_5$/CdSe (Figure V. 5).[31,36,37] In summary, the TA results attest to the ultra-fast hole extraction mediated by Sn-derived midgap states within β-$Sn_xV_2O_5$/CdX heterostructures with notably improved offsets for charge transfer for CdSe as compared to CdTe.

V.4 Conclusions

We have synthesized CdS QD/β-$Pb_{0.33}V_2O_5$ NW heterostructures through both SILAR and LAA methods. TEM and SEM images revealed a continuous shell of CdS QDs on the surface of β-$Pb_{0.33}V_2O_5$ NWs. SAED and Raman spectroscopy confirmed the wurtzite crystal structure of the CdS. XPS valence band measurements on CdS/β-$Pb_{0.33}V_2O_5$ and CdSe/β-$Pb_{0.33}V_2O_5$ have demonstrated that the valence band edge of CdS QDs is lower in energy relative to CdSe QDs, suggesting a ca. 0.4 eV decrease in the thermodynamic barrier for hole injection from the valence band edge of the QDs and a significant increase of the fraction of valence band states that can inject holes into the NWs. Charge transfer within these heterostructures has been examined by TA spectroscopy, which provides direct evidence of hole transfer from photoexcited CdS QDs to the midgap states of β-$Pb_{0.33}V_2O_5$ NWs along with electron transfer into the conduction band of the β-$Pb_{0.33}V_2O_5$ NWs. Hole transfer is substantially faster, with the majority occurring at <1 ps timescales, whereas completion of electron transfer requires ca. 5 ps for the SILAR-derived heterostructures and ca. 30 ps for the LAA-derived heterostructures. The disparate timescales of electron and hole transfer, and the tunability of the relative timescales as a function of the mode of attachment, which is

explicable based on the variation of electronic coupling in these systems as per Marcus' theory of electron transfer, provides a vital design tool for designing photocatalytic architectures to promote interfacial charge separation. The approach demonstrated here suggests that semiconductor QD/midgap-state NW architectures are a versatile platform wherein thermodynamics and kinetics of charge transfer can be systematically modulated to improve charge separation across interfaces.

The theory-guided design and topochemical synthesis of metastable β-$Sn_xV_2O_5$ paves the way to development of 2nd generation β-$Sn_xV_2O_5$/CdSe heterostructures wherein Sn 5s-derived midgap states are ideally positioned to extract photogenerated holes from CdSe QDs. The energetic offsets have been verified by XPS and HAXPES measurements and <0.5 ps hole transfer kinetics have been observed within these heterostructures. The reconfiguration of ζ-V_2O_5 to precisely position states derived from stereoactive lone pairs of p-block cations, achieved through development of a novel and highly versatile topochemical synthesis route, represents a major advance and suggest a versatile strategy for optimizing energetic offsets. The β-$Sn_xV_2O_5$/CdSe is shown to be viable light-harvesting and charge-separating photocatalytic architectures capable of water splitting. Future work will focus on the preparation of ternary heterostructures with the further addition of an electron acceptor to enhance charge separation.

V.5 References

(1) Selinsky, R. S.; Ding, Q.; Faber, M. S.; Wright, J. C.; Jin, S., Quantum Dot Nanoscale Heterostructures for Solar Energy Conversion. *Chem. Soc. Rev.* **2013**, *42*, 2963-2985.

(2) Dalpian, G. M.; Chelikowsky, J. R., Self-Purification in Semiconductor Nanocrystals. *Phys. Rev. Lett.* **2006**, *96*, 226802/1-226802/4.

(3) Li, X.; Yu, J.; Low, J.; Fang, Y.; Xiao, J.; Chen, X., Engineering Heterogeneous Semiconductors for Solar Water Splitting. *J. Mater. Chem. A* **2015**, *3*, 2485-2534.

(4) Osterloh, F. E., Inorganic Nanostructures for Photoelectrochemical and Photocatalytic Water Splitting. *Chem. Soc. Rev.* **2013**, *42*, 2294-2320.

(5) Kamat, P. V., Quantum Dot Solar Cells. The Next Big Thing in Photovoltaics. *J. Phys. Chem. Lett.* **2013**, *4*, 908-918.

(6) Li, W.; Zhong, X., Capping Ligand-Induced Self-Assembly for Quantum Dot Sensitized Solar Cells. *J. Phys. Chem. Lett.* **2015**, *6*, 796-806.

(7) Semonin, O. E.; Luther, J. M.; Beard, M. C., Quantum Dots for Next-Generation Photovoltaics. *Mater. Today* **2012**, *15*, 508-515.

(8) Bridewell, V. L.; Alam, R.; Karwacki, C. J.; Kamat, P. V., Cdse/Cds Nanorod Photocatalysts: Tuning the Interfacial Charge Transfer Process through Shell Length. *Chem. Mater.* **2015**, *27*, 5064-5071.

(9) Goodman, S. M.; Singh, V.; Ribot, J. C.; Chatterjee, A.; Nagpal, P., Multiple Energy Exciton Shelves in Quantum-Dot-DNA Nanobioelectronics. *J. Phys. Chem. Lett.* **2014**, *5*, 3909-3913.

(10) Nagpal, P.; Klimov, V. I., Role of Mid-Gap States in Charge Transport and Photoconductivity in Semiconductor Nanocrystal Films. *Nat. Commun.* **2011**, *2*, 1492/1-1492/7.

(11) Kamat, P. V., Quantum Dot Solar Cells. Semiconductor Nanocrystals as Light Harvesters. *J. Phys. Chem. C* **2008**, *112*, 18737-18753.

(12) Tvrdy, K.; Frantsuzov, P. A.; Kamat, P. V., Photoinduced Electron Transfer from Semiconductor Quantum Dots to Metal Oxide Nanoparticles. *Proc. Natl. Acad. Sci. U. S. A.* **2011**, *108*, 29-34, S29/1-S29/6.

(13) Pelcher, K. E.; Milleville, C. C.; Wangoh, L.; Chauhan, S.; Crawley, M. R.; Marley, P. M.; Piper, L. F. J.; Watson, D. F.; Banerjee, S., Integrating B-Pb0.33v2o5 Nanowires with Cdse Quantum Dots: Toward Nanoscale Heterostructures with Tunable Interfacial Energetic Offsets for Charge Transfer. *Chem. Mater.* **2015**, *27*, 2468-2479.

(14) Milleville, C. C.; Pelcher, K. E.; Sfeir, M. Y.; Banerjee, S.; Watson, D. F., Directional Charge Transfer Mediated by Mid-Gap States: A Transient Absorption Spectroscopy Study of Cdse Quantum Dot/B-Pb0.33v2o5 Heterostructures. *J. Phys. Chem. C* **2016**, *120*, 5221-5232.

(15) Yamauchi, T.; Ueda, H.; Ueda, Y.; Kikuchi, J., Rich Phase Transitions under Pressure in B-A0.33v2o5 (a=Ca and Pb). *Phys. C* **2007**, *460-462*, 532-533.

(16) Marley, P. M.; Singh, S.; Abtew, T. A.; Jaye, C.; Fischer, D. A.; Zhang, P.; Sambandamurthy, G.; Banerjee, S., Electronic Phase Transitions of Δ-Agxv2o5 Nanowires: Interplay between Geometric and Electronic Structures. *J. Phys. Chem. C* **2014**, *118*, 21235-21243.

(17) Wangoh, L.; Marley, P. M.; Quackenbush, N. F.; Sallis, S.; Fischer, D. A.; Woicik, J. C.; Banerjee, S.; Piper, L. F. J., Electron Lone Pair Distortion Facilitated Metal-

Insulator Transition in B-Pb0.33v2o5 Nanowires. *Appl. Phys. Lett.* **2014**, *104*, 182108/1-182108/4.

(18) Marley, P. M.; Stabile, A. A.; Kwan, C. P.; Singh, S.; Zhang, P.; Sambandamurthy, G.; Banerjee, S., Charge Disproportionation and Voltage-Induced Metal-Insulator Transitions Evidenced in B-Pbxv2o5 Nanowires. *Adv. Funct. Mater.* **2013**, *23*, 153-160.

(19) Marley, P. M.; Abtew, T. A.; Farley, K. E.; Horrocks, G. A.; Dennis, R. V.; Zhang, P.; Banerjee, S., Emptying and Filling a Tunnel Bronze. *Chem. Sci.* **2015**, *6*, 1712-1718.

(20) Tian, J.; Cao, G., Control of Nanostructures and Interfaces of Metal Oxide Semiconductors for Quantum-Dots-Sensitized Solar Cells. *J. Phys. Chem. Lett.* **2015**, *6*, 1859-1869.

(21) Xu, Y.; Schoonen, M. A. A., The Absolute Energy Positions of Conduction and Valence Bands of Selected Semiconducting Minerals. *Am. Mineral.* **2000**, *85*, 543-556.

(22) Nevins, J. S.; Coughlin, K. M.; Watson, D. F., Attachment of Cdse Nanoparticles to Tio2 Via Aqueous Linker-Assisted Assembly: Influence of Molecular Linkers on Electronic Properties and Interfacial Electron Transfer. *ACS Appl. Mater. Interfaces* **2011**, *3*, 4242-4253.

(23) Coughlin, K. M.; Nevins, J. S.; Watson, D. F., Aqueous-Phase Linker-Assisted Attachment of Cysteinate(2-)-Capped Cdse Quantum Dots to Tio2 for Quantum Dot-Sensitized Solar Cells. *ACS Appl. Mater. Interfaces* **2013**, *5*, 8649-8654.

(24) Hung, P.; O'Loughlin, T. E.; Lewis, A.; Dechter, R.; Samayoa, M.; Banerjee, S.; Wood, E. L.; Walker, A. R. H. In *Potential Application of Tip-Enhanced Raman*

Spectroscopy (Ters) in Semiconductor Manufacturing, SPIE Advanced Lithography, International Society for Optics and Photonics: 2015; pp 94241S-94241S-13.

(25) Yu, W. W.; Qu, L.; Guo, W.; Peng, X., Experimental Determination of the Extinction Coefficient of Cdte, Cdse, and Cds Nanocrystals. *Chem. Mater.* **2003**, *15*, 2854-2860.

(26) Han, K.; Im, W. B.; Heo, J.; Chung, W. J., A Complete Inorganic Color Converter Based on Quantum-Dot-Embedded Silicate Glasses for White Light-Emitting-Diodes. *Chem. Commun.* **2016**, *52*, 3564-3567.

(27) Scofield, J. H. *Theoretical Photoionization Cross Sections from 1 to 1500 Kev*; California University, Livermore, Lawrence Livermore Lab., : 1973.

(28) Wong, J.; Lytle, F. W.; Messmer, R. P.; Maylotte, D. H., K-Edge Absorption Spectra of Selected Vanadium Compounds. *Phys. Rev. B: Condens. Matter* **1984**, *30*, 5596-610.

(29) Jasieniak, J.; Califano, M.; Watkins, S. E., Size-Dependent Valence and Conduction Band-Edge Energies of Semiconductor Nanocrystals. *ACS Nano* **2011**, *5*, 5888-5902.

(30) Lee, J. R. I.; Meulenberg, R. W.; Hanif, K. M.; Mattoussi, H.; Klepeis, J. E.; Terminello, L. J.; Van Buuren, T., Experimental Observation of Quantum Confinement in the Conduction Band of Cdse Quantum Dots. *Phys. Rev. Lett.* **2007**, *98*, 146803/1-146803/4.

(31) Marcus, R. A., On the Theory of Oxidation-Reduction Reactions Involving Electron Transfer. I. *J. Chem. Phys.* **1956**, *24*, 966-978.

(32) Marcus, R. A., Electron Transfer Reactions in Chemistry: Theory and Experiment (Nobel Lecture). *Angew. Chem. Int. Ed.* **1993**, *32*, 1111-1121.

(33) Malko, A. V.; Mikhailovsky, A. A.; Petruska, M. A.; Hollingsworth, J. A.; Klimov, V. I., Interplay between Optical Gain and Photoinduced Absorption in Cdse Nanocrystals. *J. Phys. Chem. B* **2004**, *108*, 5250-5255.

(34) Klimov, V. I., Spectral and Dynamical Properties of Multiexcitons in Semiconductor Nanocrystals. *Annu. Rev. Phys. Chem.* **2007**, *58*, 635-673.

(35) Abdellah, M.; Marschan, R.; Zidek, K.; Messing, M. E.; Abdelwahab, A.; Chabera, P.; Zheng, K.; Pullerits, T., Hole Trapping: The Critical Factor for Quantum Dot Sensitized Solar Cell Performance. *J. Phys. Chem. C* **2014**, *118*, 25802-25808.

(36) Dibbell, R. S.; Watson, D. F., Distance-Dependent Electron Transfer in Tethered Assemblies of Cds Quantum Dots and TiO_2 Nanoparticles. *J. Phys. Chem. C* **2009**, *113*, 3139-3149.

(37) Guijarro, N.; Shen, Q.; Gimenez, S.; Mora-Sero, I.; Bisquert, J.; Lana-Villarreal, T.; Toyoda, T.; Gomez, R., Direct Correlation between Ultrafast Injection and Photoanode Performance in Quantum Dot Sensitized Solar Cells. *J. Phys. Chem. C* **2010**, *114*, 22352-22360.

(38) Pelcher, K. E.; Milleville, C. C.; Wangoh, L.; Cho, J.; Sheng, A.; Chauhan, S.; Sfeir, M. Y.; Piper, L. F. J.; Watson, D. F.; Banerjee, S., Programming Interfacial Energetic Offsets and Charge Transfer in β-$Pb_{0.33}V_2O_5$/Quantum-Dot Heterostructures: Tuning Valence-Band Edges to Overlap with Midgap States. *J. Phys. Chem. C* **2016**, 120, 28992-29001.

(39) Bawendi, M. G.; Wilson, W. L.; Rothberg, L.; Carroll, P. J.; Jedju, T. M.; Steigerwald, M. L.; Brus, L. E., Electronic structure and photoexcited-carrier dynamics in nanometer-size CdSe clusters. *Phys. Rev. Lett.* **1990**, 65, 1623-1626.

(40) Klimov, V. I. Optical nonlinearities and ultrafast carrier dynamics in semiconductor nanocrystals. *J. Phys. Chem. B* **2000**, 104, 6112–6123.

(41) Smith, A. M., Lane, L. A. & Nie, S. Mapping the spatial distribution of charge carriers in quantum-confined heterostructure. *Nat. Commun*.**2014**, 5, 4506 (2014).

CHAPTER VI

POLYMORPHYSM OF V_2O_5 AS A MEANS OF TUNING ENERGETIC OFFSETS IN TYPE II V_2O_5/CdSe QUANTUM DOT HETEROSTRUCTURES: IMPLICATIONS FOR CHARGE SEPARATION AND PHOTOCATALYTIC PERFORMANCE

VI.1 Introduction

Harnessing solar energy is imperative to mitigate the catastrophic environmental consequences of global reliance on fossil fuels as the primary energy source underpinning electrical grids and the transportation infrastructure. Solar energy can be converted directly to electrical energy by photovoltaic devices or to energy-dense chemical fuels in photoelectrochemical cells.[1-4] In solar photocatalysis, absorbed sunlight is used to mediate an enthalpically disfavorable reaction, thereby yielding a solar fuel. The fuel is stored and subsequently combusted along a thermodynamically favored pathway to recover the energy at the point of use, yielding water as a by-product.[1, 5-7] Nanoscale semiconductors are oftentimes used to harvest solar energy given the typically high oscillator strengths of band-edge absorption features in direct-bandgap semiconductors and the potential to tune their overlap with the solar spectrum through compositional modulation and dimensional confinement.[8, 9] Solar photocatalysis necessitates a sequential cascade of events initiated by the absorption of sunlight and ensuing creation of an electron—hole pair, involving separation of the charges and their transport to sites where redox catalysis steps can be separately mediated. In practice, effective charge separation is often achieved by utilizing binary or ternary

semiconductor heterostructures such that photogenerated electrons or holes or both are rapidly transferred across interfaces, thereby diminishing their non-productive recombination.[10-12] In other words, interfacial charge transfer processes must outcompete multiple undesirable processes such as carrier cooling as well as non-radiative and radiative recombination pathways in order to be used to catalyze redox processes.[13-15]

As per Marcus' kinetic theory of charge transfer extrapolated to semiconductor interfaces with a continuum of donor or acceptor states, the rate constants of interfacial charge-transfer processes are dependent on the thermodynamic driving force, the reorganization energy at the heterojunction, the extent of electronic coupling between the donor and the acceptor, and the density of charge-accepting states.[14, 16] The relative band alignment (or interfacial energetic offsets) within semiconductor heterostructures determine the thermodynamic driving forces for interfacial charge transfer.[10, 12, 17, 18] Staggered Type-II interfaces are quite effective for engendering charge separation,[19-21] and indeed light-absorbing II-VI semiconductor quantum dots are often paired with wider bandgap transition metal oxides to define such heterojunctions. In such heterojunctions, the valence band edges of II-VI semiconductor quantum dots are tunable as a function of composition as per Fajan's rules regarding covalency and ionicity down the chalcogenide series[10]; similarly, the conduction band edges of quantum dots are tunable as a function of size in the quantum confined regime below the Bohr radius.[22] In contrast, the valence and conduction band edges of transition metal oxides are generally considered to be immutable. Remarkably, in the case of V_2O_5, the rich accessible energy landscape makes available a variety of metastable polymorphs

with varying extents of ionicity and covalency, and thus allows for considerable tunability of the energy positioning of valence and conduction band edges as a function of structure for the same chemical composition.[23-28] In this article, we examine energetic offsets in V_2O_5-nanowire/CdSe-quantum dot heterostructures for three different polymorphs of V_2O_5 illustrating a pronounced alteration of energetic offsets, which thereby alters the extent of charge separation and photocatalytic activity.

The thermodynamically stable α-phase of V_2O_5 has a layered orthorhombic crystal structure wherein [VO_5] square pyramids are connected through corner- and edge-sharing (**Figure VI. 1**).[26] Several metastable phases of V_2O_5 are accessible through topochemical deintercalation of ternary vanadium bronzes, $M_xV_2O_5$ where M is metal and x is stoichiometry; the "emptied" open framework structures represent kinetically trapped polymorphs that are unable to revert to the thermodynamic sink, the layered α-phase, at the low temperatures at which soft-chemical de-intercalation is performed.[24-27, 29, 30] The γ′-phase of V_2O_5 with puckered single layers is stabilized by leaching of Li-ions from γ-$Li_xV_2O_5$ ($x \sim 1.0$), whereas the tunnel-structured ζ-phase of V_2O_5 is obtained by extracting Ag-ions from β-$Ag_xV_2O_5$ (Figure VI. 1).[25] The three polymorphs exhibit vastly different extents of V—O hybridization, allowing for considerable tunability of energetic offsets in their heterojunctions with CdSe quantum dots.[31, 32] In this article, we evaluate semiconductor heterostructures comprising nanowires of the three V_2O_5 polymorphs functionalized with II-VI QDs, which represent intriguing new reconfigurable platforms for solar energy conversion. The nanowires of the V_2O_5 polymorphs have been interfaced with CdSe quantum dots by two distinctive

approaches, linker-assisted assembly (LAA)[33] and successive ionic layer adsorption and reaction (SILAR).[34] Transient absorption spectroscopy measurements suggest that the V_2O_5/CdSe heterostructures form long-lived charge-separated states with lifetimes extending to a few microseconds, allowing for their effective utilization as photocatalysts for the hydrogen evolution reaction.

VI.2 Experimental

Synthesis of V_2O_5 nanowires of different polymorphs. α-V_2O_5 nanowires were prepared using a two-step reaction according to previously reported methods.[26] Briefly, micron-sized powders of V_2O_5 were hydrothermally reduced to $V_3O_7{\cdot}xH_2O$ nanowires using oxalic acid ($C_2H_2O_4$) as a reducing agent; the $V_3O_7{\cdot}xH_2O$ nanowires were annealed in air at 350°C for 72 h to obtain phase-pure α-V_2O_5 nanowires.

γ′-V_2O_5 nanowires were prepared by a procedure adapted from a previously reported synthesis.[50, 51] Briefly, α-V_2O_5 nanowires prepared as described above were in a LiI solution in dry acetonitrile in a 3:1 molar excess of the lithium precursor at 22°C under an argon atmosphere within a round bottom flask adapted to a Schlenk-line for 72 h. The nanowire powders were dispersed in the LiI/acetonitrile solution by sonication for 5min every 6 h to promote phase purity. The yellow α-V_2O_5 nanowires turned dark green, reflecting the reduction of pentavalent vanadium to tetravalent vanadium upon insertion of Li-ions; the acetonitrile supernatant acquired a brown/purple coloration, which is characteristic of the formation of dissolved I_2. The resulting suspension was isolated by vacuum filtration and washed with acetonitrile and 2-propanol to obtain δ-

$Li_xV_2O_5$ nanowires ($x \sim 1.0$). The dried powder was placed in an alumina crucible and annealed in a tube furnace under a combination of vacuum and flowing Ar atmosphere (100 ml·min^{-1}) at 250°C for 4 h to obtain phase-pure γ-$Li_xV_2O_5$ nanowires ($x \sim 1.0$). A small amount of the metastable ε′-LiV_2O_5 phase sometimes observed as a secondary phase upon lithiation of V_2O_5 also anneals to the γ-$Li_xV_2O_5$ phase.[52] Upon cooling, the γ-$Li_xV_2O_5$ nanowires were resuspended in a 0.1 M solution of $NOBF_4$ in dry acetonitrile under an argon atmosphere within a glovebox and gently stirred for 24 h. The resulting γ′-phase V_2O_5 nanowires were washed with copious amounts of acetonitrile.

ζ-V_2O_5 nanowires were obtained from parent β-$Ag_xV_2O_5$ nanowires as described in previous work.[25, 36] Briefly, Ag-ions were topochemically extracted from hydrothermally prepared β-$Ag_xV_2O_5$ nanowires by hydrothermal treatment of 300 mg of β-$Ag_xV_2O_5$ nanowires with 16 mL of an aqueous solution of 0.51 M HCl at 210°C for 24 h. The topochemcial extraction was performed within a PTFE-lined stainless steel autoclave with a capacity of 23 mL. The resulting brown powders were washed with copious amounts of water and 2-propanol and allowed to dry in air overnight. The insoluble AgCl precipitate was removed from the resulting sample by suspending the powders in a 5 wt.% aqueous solution of sodium thiosulfate as described in previous work.[25] The suspension was separated by vacuum filtration and further washed with copious amounts of water to remove adsorbed ionic species.

Synthesis of Cysteinate-capped CdSe QDs. Cysteinate-capped CdSe QDs with average diameters less than 2 nm were prepared as per previously reported methods.[4, 53] The selenium precursor was prepared by refluxing an aqueous solution of Se powder and

Na_2SO_3 overnight; the cadmium precursor was an aqueous solution of $3CdSO_4 \cdot 8H_2O$ and cysteine. The pH of the cadmium precursor was titrated to 12.5—13.0 with solid NaOH. The hot selenium precursor solution was transferred to the cadmium precursor solution and allowed to stir for 30 min. The resulting dispersions of cysteinate-capped CdSe QDs were purified by solvent/non-solvent precipitation/redispersion (H_2O/MeOH, 3:1 (v/v)) to remove excess reagents.

Surface functionalization of V_2O_5 nanowires with CdSe QDs using SILAR and LAA. CdSe QDs were attached to nanowires of different polymorphs of V_2O_5 using SILAR and LAA procedures, which were performed as per previously reported methods.[4] The SILAR-derived V_2O_5/CdSe heterostructures correspond to three sequential cycles of immersion of V_2O_5 nanowires in Cd and Se precursor solutions. $Cd(NO_3)_2 \cdot 4H_2O$ in ethanol was used as the Cd precursor, whereas Na_2Se in ethanol was used as the Se precursor. The powders were washed extensively with ethanol following each immersion step to remove weakly bound ions.

In LAA-derived V_2O_5/CdSe heterostructures, the two components were tethered together using cysteine. Briefly, an aqueous dispersion of V_2O_5 nanowires was transferred to an aqueous dispersion of purified cysteinate-capped CdSe QDs in a flask and allowed to equilibrate overnight (12—16 h) at room temperature under vigorous stirring. CdSe-functionalized V_2O_5 nanowires were isolated by centrifugation, washed with copious amount of deionized water to remove excess, weakly adsorbed quantum dots, and allowed to dry at room temperature.

Structural characterization. Scanning electron microscopy (SEM) imaging was performed using a FEI Quanta 600 FE-SEM operated at an accelerating voltage of 10 kV. The instrument was equipped with an IR-CCD chamber camera and an Oxford system for energy dispersive X-ray spectroscopy (EDS) measurements. Samples for SEM measurements were prepared by dispersing powders recovered from synthesis onto carbon tape adhered onto machined stubs. High-resolution transmission electron microscopy (HRTEM) and selected area electron diffraction (SAED) measurements were performed using a FEI Tecnai G2 F20 microscope operated at an accelerating voltage of 200 kV. Samples for TEM measurements were prepared by drop-casting heterostructrure dispersions in ethanol onto Formvar/carbon support films on 400 mesh Cu grids.

Determination of optical energy bandgap by diffuse reflectance measurements. Diffuse reflectance measurements were performed using the Praying Mantis accessory in a Hitachi U-4100 UV-vis-NIR spectrophotometer. Diffuse reflectance spectra were obtained in the range of 200–800 nm for all samples at a scan rate of 600 nm/min. Samples for diffuse reflectance spectroscopy were prepared by finely crushing the powders recovered from synthesis with a mortar and pestle; the fine-grained powders were next placed within a sampling cup from the Praying Mantis diffuse reflectance accessory.

The optical bandgaps of the V_2O_5 polymorphs were determined by extrapolating the linear region of the diffuse reflectance spectrum to the abscissa and utilization of Kubelka-Munk theory, as per:

$$F(R) = \frac{(1-R)^2}{2R} \quad \text{(VI. 1)}$$

where R is the measured diffuse reflectance and $F(R)$ is the Kubelka-Munk function, which is proportional to the extinction coefficient.[42] By plotting $F(R)$ versus energy (eV), the optical bandgap was deduced for each V_2O_5 polymorph by extrapolation of the best-fit to the linear section of the curve.

Transient absorption spectroscopy. Nanosecond transient absorption spectroscopy measurements were carried out using 800 nm pump pulses with a subnanosecond pulse duration and an electronically delayed supercontinuum light source as the probe. An EOS spectrometer (Ultrafast System) was used to acquire the TA spectra. TA decay traces were compiled by averaging ΔA values over a given range of probe wavelengths at each delay time. Averaged TA spectra were obtained by averaging the absorption differential (ΔA) at delay times in the range of 1.5—10 ns from the 3D data matrix plotting in 425—900 nm as a function of pump-probe delay time (t), exemplified in Figure VI. 5. TA measurements were performed on thin films of V2O5 nanowires and V_2O_5/CdSe heterostructures, which were prepared by spray-coating a 5 mL ethanol dispersion at a concentration of 1 mg/mL onto glass microscope slides.

Photocatalytic H_2 generation. An aqueous dispersion of V_2O_5 polymorphs (50 mg) nanowires was added to an aqueous dispersion of purified Cys-CdSe quantum dots and allowed to equilibrate for 1 h. The photocatalysts (V_2O_5 nanowires functionalized with CdSe quantum dots) were recovered by centrifugation, rinsed with deionized water to remove excess quantum dots, and subsequently dried at room temperature before further use. Photocatalytic H_2 generation was performed in a 100 mL Pyrex flask at ambient

temperature and atmospheric pressure. The flask was sealed with a silicone rubber septum. The light source was a 100 W Xe arc lamp (Oriel 133 Photomax); a cut-off filter transmitting 400 to 720 nm (visible) light was used to modulate the irradiance. The focused intensity on the flask, measured using a power meter (Gentec solo PE laser power meter with sensor), was 120 mW/cm^2. The catalyst (50 mg) was suspended in a 50 mL mixed solution of lactic acid (20 vol.%) and water under vigorous stirring. The co-catalyst used was Ni-(3-MPA) (0.1 M Ni^{2+} and 0.2 M 3-mercaptopropionic acid). Before irradiation, the suspensions were bubbled with Ar for 30 min to remove dissolved oxygen. Magnetic stirring was used in order to maintain a colloidal dispersion of the photocatalyst particles. A total of 3 mL of headspace vapors were collected through the septum after 1 h and analyzed using a gas chromatograph (Perkin Elmer Clarus 580) equipped with a thermal conductivity detector (TCD) using Ar as the carrier gas.

VI.3 Results and Discussion

Electronic Structure of V_2O_5 Polymorphs and Implications for Energetic Offsets

Polymorphs of V_2O_5 differ substantially in the connectivity of V—O bonds and arrangement of vanadium-centered polyhedra.[30] Alteration of V—O connectivity strongly influences the electronic structure as well as energy dispersion and separation between the valence and conduction bands. **Figure VI. 1A—C** illustrate the three different polymorphs of V_2O_5 examined here as components of Type-II heterostructures.[26, 27] Layered α-V_2O_5 is the thermodynamically stable phase and has been directly prepared in the form of nanowires based on hydrothermal reduction of

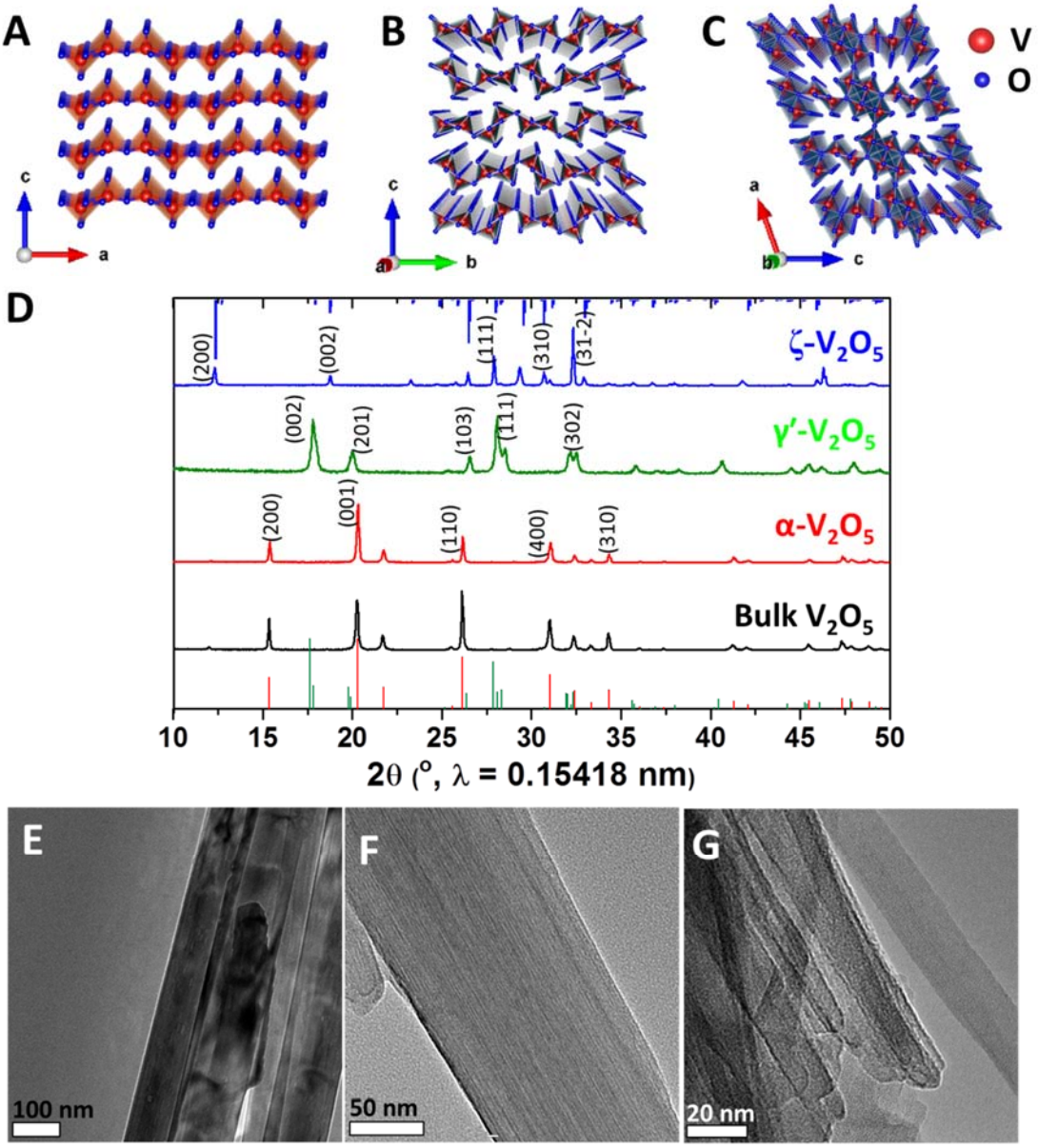

Figure VI. 1 (A-C) Crystal structures of V_2O_5 polymorphs: (A) α-phase, (B) γ′-phase, and (C) ζ-phase; (D) X-ray diffraction patterns for V_2O_5 polymorphs and a bulk counterpart; and (E-G) TEM images of corresponding V_2O_5 polymorphs: (D) α-phase, (E) γ′-phase, and (F) ζ-phase. In Figure VI. 1A-C, V atoms and O atoms are correspondent to the red and blue sphere, respectively.

micron-sized V_2O_5 to $V_3O_7{\cdot}H_2O$ followed by oxidation to V_2O_5 nanowires (as detailed further in the Methods section).[26] This polymorph comprises [VO_5] square pyramids connected by alternating edge-sharing and corner-sharing (**Figure VI. 1A**) with a defined van der Waals' gap along the crystallographic c direction. Figure VI. VI. 1D shows a XRD pattern of the α-V_2O_5 nanowires with reflections indexed to PDF# 41-1426,[26] establishing the phase purity of the structures. **Figure VI. 1E** shows a transmission electron microscopy (TEM) image; the prepared nanowires have lateral dimensions of 200±50 nm and are tens of microns in length.

V_2O_5 is characterized by a "rugged" energy landscape with numerous metastable polymorphs in relatively close proximity to the thermodynamic phase.[30] The single-layered γ′-V_2O_5 polymorph, shown in **Figure VI. 1B**, comprises puckered sheets of V_2O_5 and is accessed by topochemical de-intercalation of Li-ions from a distorted γ-$Li_xV_2O_5$ structure. The ternary γ-$Li_xV_2O_5$ phase in turn is derived from an irreversible intercalation-induced transition upon lithiation of α-V_2O_5 that allows for accommodation of a higher concentration of Li-ions above x >1 through an increase in the interlayer separation and puckering of $[V_2O_5]_n$ sheets as well as a shear distortion with respect to adjacent sheets. Figure VI. 1D plots a powder XRD pattern acquired for the γ′-phase V_2O_5, which can be indexed to PDF# 85-2422, attesting to the phase purity of the topochemically stabilized γ'-V_2O_5 phase.[35] **Figure VI. 1F** shows TEM images acquired for the prepared nanowires, which have lateral dimensions of 150±20 nm and vertical dimensions of several microns in length.

The metastable ζ-V_2O_5 structure pictured in **Figure VI. 1C** is stabilized by topochemical leaching of Ag-ions from a β-$Ag_xV_2O_5$ Wadsley bronze as described in the methods section; the structure is characterized by a quasi-1D tunnel-structured framework constituted from corner- and edge-sharing [VO_6] octahedra and edge-sharing [VO_5] square pyramids.[23, 36] Figure VI. 1D plots a powder XRD pattern acquired for the topochemically stabilized material, which can be indexed as per a previous Rietveld refinement performed for this crystal structure.[25] **Figure VI. 1G** shows TEM images of ζ-V_2O_5 nanowires, which have lateral dimensions of 150±5 nm and are several microns in length.

In V_2O_5 polymorphs, states at the top of the valence band are typically O 2p in origin, whereas states at the bottom of the conduction band are typically V 3d in origin[30]; α-V_2O_5 is notably characterized by a narrow split-off conduction band that is V $3d_{xy}$ in origin.[37-39] The valence band edge potential of α-phase V_2O_5 nanowires (as well as CdSe QDs) has been determined based on hard X-ray photoemission spectroscopy (HAXPES) and is schematically shown in **Figure VI. 2**.[4] Density functional theory (DFT) calculations and HAXPES measurements indicate that the valence band edge potentials, which are derived primarily from non-bonding O 2p states, are relatively unaltered in different V_2O_5 polymorphs. In contrast, the energy positioning of the V 3d—O 2p conduction band edge is strongly sensitive to the extent of hybridization.[24, 40] The conduction band edge of V_2O_5 has been deduced based on delineation of the optical bandgap, as measured for the different polymorphs by diffuse reflectance spectroscopy (Figure VI. 2A). Different absorption profiles are observed for V_2O_5 polymorphs. The

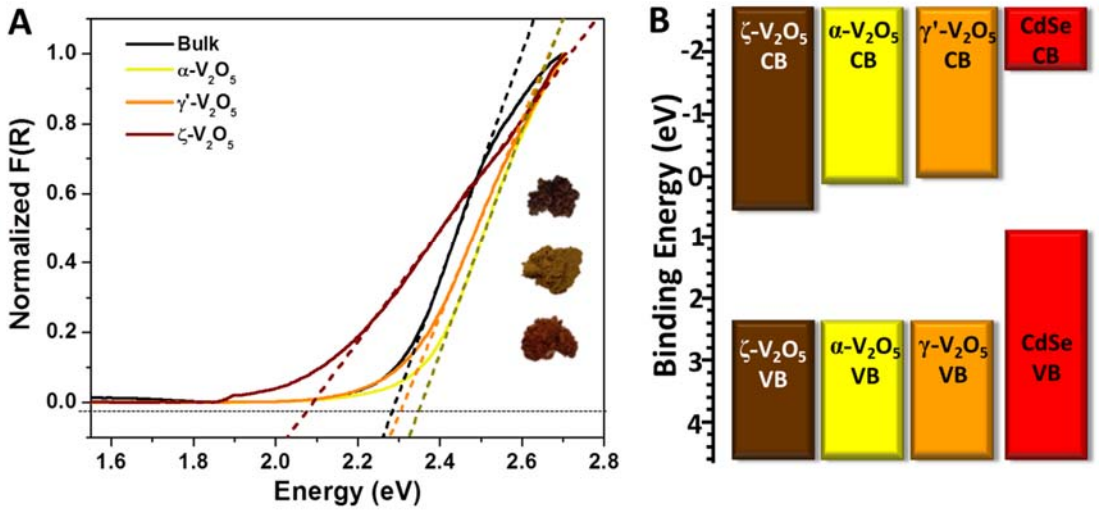

Figure VI. 2 (A) Diffuse reflectance spectra of V_2O_5 polymorphs and bulk V_2O_5 counterpart and (B) relative energy positioning of the valence and conduction bands edges of polymorph V_2O_5 nanowires versus CdSe QD.

optical bandgaps have been determined by the Kubelka—Munk method[41, 42] as detailed in the experimental section. The bandgaps are determined to be 2.36 eV for γ′-V_2O_5, 2.31 eV for α-V_2O_5 (concordant with the 2.29 eV value measured for bulk V_2O_5), and 2.09 eV for ζ-V_2O_5. The inset to **Figure VI. 2A** displays a change in visible coloration from light brown for the γ′-phase to yellow for the α–phase, and dark brown for ζ-V_2O_5.

The energetic offsets expected in heterostructures comprising V_2O_5 polymorphs interfaced with CdSe quantum dots is plotted in Figure VI. 2B. The relative energy positioning suggest a type II interface for heterostructures of all three V_2O_5 polymorphs functionalized with CdSe quantum dots, which should result in interfacial charge separation upon photoexcitation. Photoexcitation of either component of the heterostructures is expected to bring about confinement of holes at the valence band edges of the quantum dots and electrons at the conduction band edges of V_2O_5. The

driving forces for hole transfer are seen to be essentially constant, whereas the driving force for electron transfer varies as a function of the covalency of the V_2O_5 framework (**Figure VI. 2B**).

Surface Functionalization of V_2O_5 Nanowires with CdSe Quantum Dots

As per Marcus theory, the nature of the interface between the donor and the acceptor dictates the overlap integrals that determine the charge transfer kinetics.[43, 44] V_2O_5 nanowires of the different polymorphs have been functionalized with CdSe quantum dots using SILAR and LAA methods as described in the Methods section. SILAR-derived heterostructures are characterized by a direct interface with the nanocrystals grown directly onto the nanowire surfaces, whereas in the LAA-derived heterostructures, a trifunctional molecule, cysteine, is used to tether the two components. Under the weak basic reaction condition (pH 8.5—9), the deprotonated thiol group of linker molecules is preferentially coordinated to Cd^{2+} surface site on QD whereas the protonated amine group of cysteine is predominantly attached to surficial hydroxyl groups of V_2O_5 nanowires as per hard-soft Lewis acid-base theory.[4] **Figures A. 33** and **34** show scanning electron microscopy (SEM) and energy dispersive X-ray spectroscopy (EDS) characterization of the prepared heterostructures, respectively.

Figure A. 33 displays SEM images of pristine V_2O_5 nanowires, LAA-derived V_2O_5/CdSe heterostructures, and SILAR-derived V_2O_5/CdSe heterostructures for all three polymorphs of V_2O_5. The surfaces of the V_2O_5 nanowires are initially smooth but

take on a speckled appearance upon functionalization with CdSe quantum dots. **Figure VI. 3A—F** depicts bright-field TEM images of the obtained LAA and SILAR

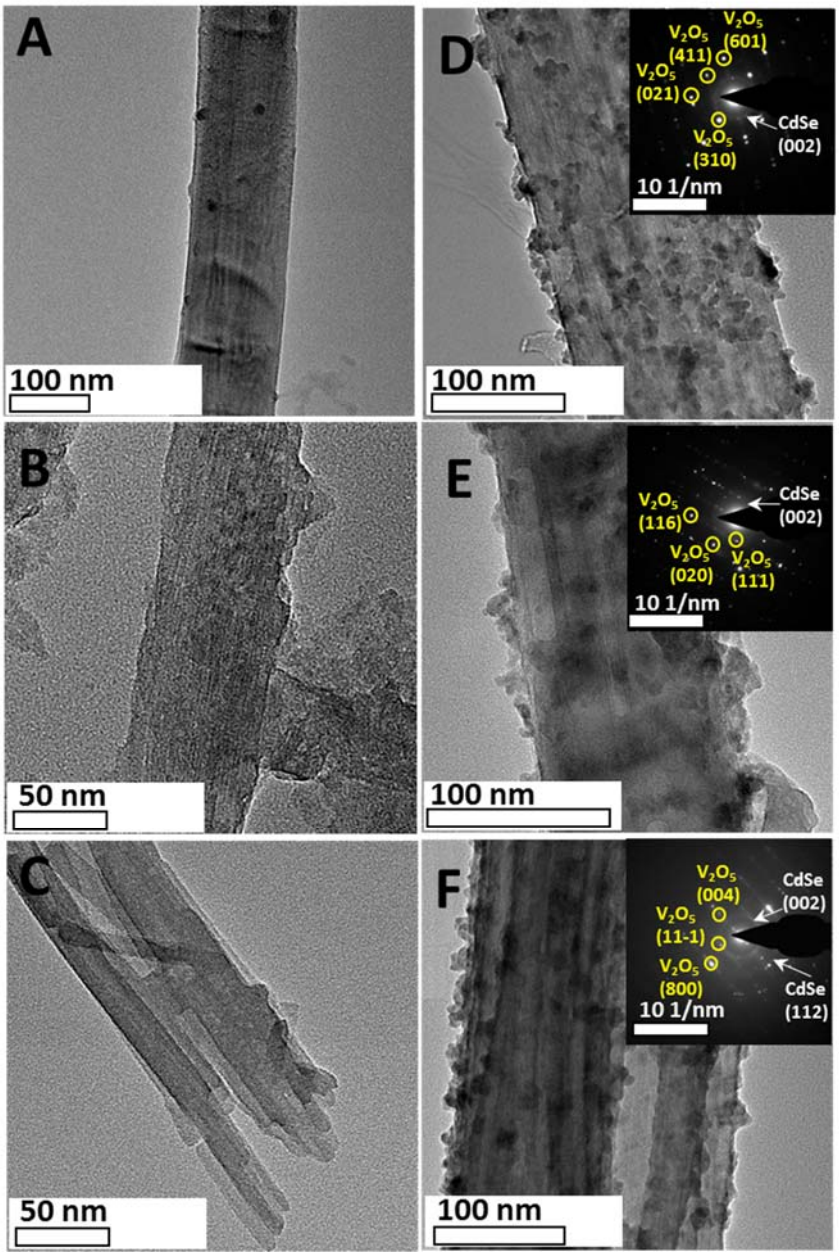

Figure VI. 3 TEM images of (A—C) LAA-derived V_2O_5/CdSe heterostructures and (D—F) SILAR-derived V_2O_5/CdSe heterostructures: (A,D) α-V_2O_5; (B,E) γ′-V_2O_5; and (C,F) ζ-V_2O_5. Insets to D-F show indexed SAED patterns acquired for SILAR-derived heterostructures.

heterostructures for all three polymorphs of V_2O_5. In stark contrast to the smooth surfaces of pristine nanowires (shown in Figure VI. 1E-F), protuberant specks and dots are discernible on the surfaces of both SILAR- and LAA-derived heterostructures. Relatively high extents of surface coverage with quantum dots are noted for SILAR-derived heterostructures corresponding to three cycles of immersion in Cd and Se precursor solutions. The indexed SAED patterns shown in **Figure VI. 3D—F** provide additional corroboration of the growth of wurtzite-structured CdSe quantum dots on the nanowire surfaces. The diffraction spots have been indexed to the lattice planes of the different polymorphs of V_2O_5, whereas the diffuse rings are indexed to (002) and (112) reflections of wurtzite CdSe quantum dots.[4, 10] **Figure VI. 4** shows high-resolution TEM images of heterostructures; lattice-resolved images shown as insets provide further corroboration of the growth of crystalline wurtzite CdSe nanocrystals on the surfaces of the V_2O_5 nanowires (for all three polymorphs). The measured separation between the lattice planes of ca. 3.47Å can be indexed as the separation between the (002) planes of wurtzite CdSe.[45, 46] Diffraction contrast images in Figure VI. 4 provide an intensity profile corresponding to the concentration of quantum dots on the surfaces of the V_2O_5 nanowires. Fast Fourier transform (FFT) patterns acquired across the lattice-resolved regions corroborate the hexagonal symmetry of wurtzite CdSe quantum dots grown onto the nanowire surfaces.[46] **Figure A. 34** plots EDS spectra measured for LAA- and SILAR-derived V_2O_5/CdSe heterostructures. The loading of CdSe quantum dots is approximately 5—20 at.% for the SILAR heterostructures and 3—10 at.% for LAA heterostructures based on the relative atomic ratios of Cd and V.

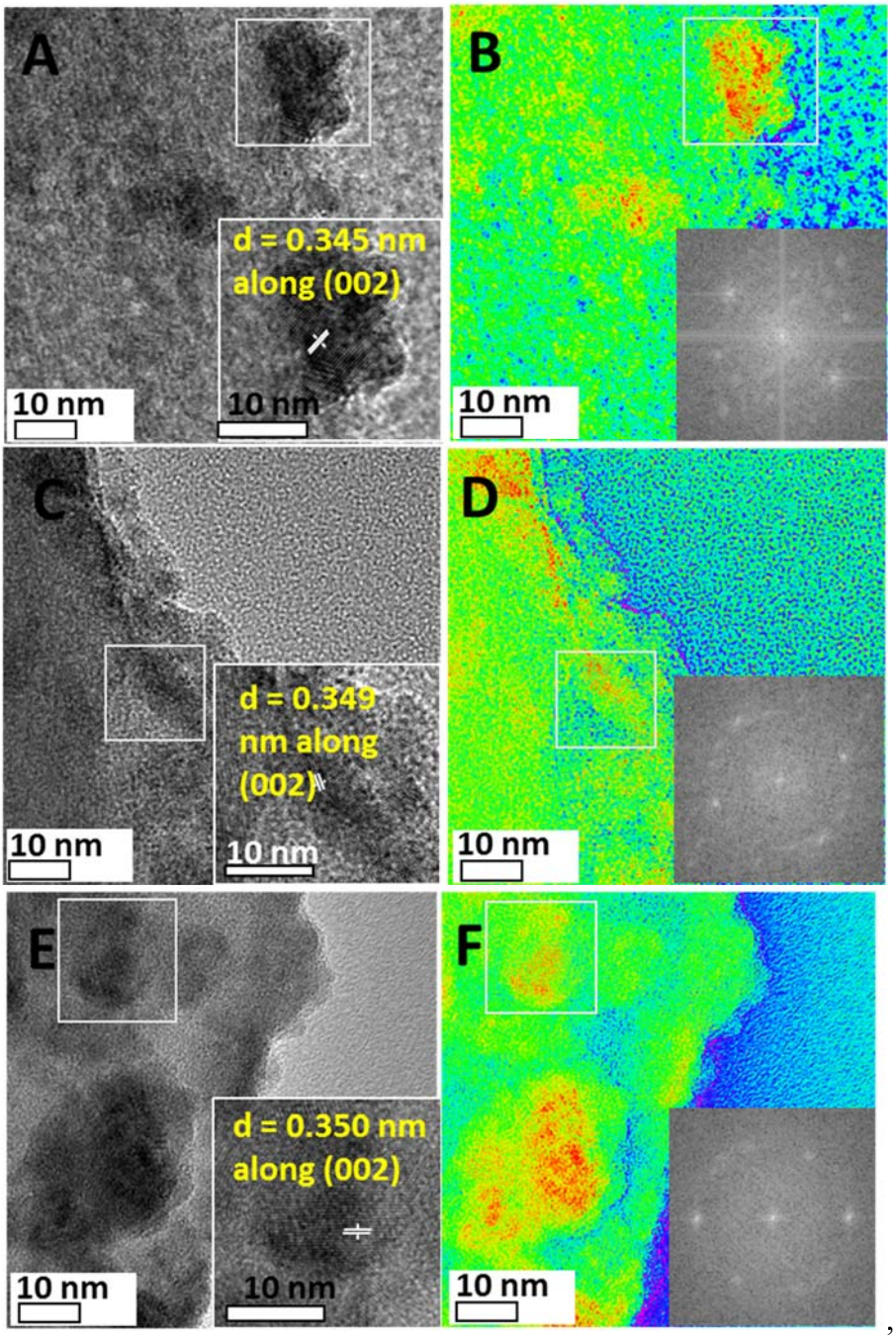

Figure VI. 4 High-resolution TEM images (left) and false-color diffraction contrast images (right) for (A,B) SILAR-derived α-V_2O_5/CdSe, (C,D) SILAR-derived γ'-V_2O_5/CdSe, and (E,F) SILAR-derived ζ-V_2O_5/CdSe. Insets to panels A,C,E show magnified lattice-resolved views of the regions denoted by a white square in the panels. The observed fringes can be indexed to separation between the (002) planes of wurtzite CdSe quantum dots. The insets to panels B,D, and F correspond to fast Fourier transforms acquired for the same region.

Charge Separation within V_2O_5/CdSe Heterostructures

Polymorphism of V_2O_5 along with compositional and dimensional tunability of II-VI quantum dots makes V_2O_5/II-VI quantum dot heterostructures a versatile and programmable platform for tuning thermodynamic driving forces for charge transfer. As shown in Figure VI. 2, the energetic offsets across all three V_2O_5 polymorphs and CdSe quantum dots has a staggered type II alignment. Such interfaces are particularly desirable for solar energy conversion as a result of the potential for obtaining long-lived charge separated states upon photoexcitation. Type-II interfaces separate charges in space through interfacial charge transfer, allowing for their further utilization to generate a photocurrent or for catalyzing redox processes.[19, 21] The charge carrier relaxation dynamics of V_2O_5/CdSe heterostructures constituted from different V_2O_5 polymorphs have been resolved using transient absorption (TA) spectroscopy upon photoexcitation at an excitation wavelength of 360 nm.

In previous work, we have measured TA spectra for pristine α-V_2O_5 nanowires and their heterostructures with CdSe quantum dots QD.[11] In the TA spectra of V_2O_5 nanowires, an induced absorption band observed at 450—600 nm is assigned to excited-state holes (corresponding to excitation of electrons from the deep valence band to the valence band edge), whereas an induced absorption band in the range of 600—750 nm can be attributed to excited-state electrons (being promoted to still higher lying conduction band states). **Figure A. 35** plots TA spectra of V_2O_5 polymorphs acquired on the nanosecond timescale. In accordance with previous assignments, TA spectra of V_2O_5 polymorphs are characterized by a transient bleach (centered at 440 nm for α- and 425

nm for γ'-V_2O_5 and 490 nm for ζ-V_2O_5) and two induced absorption bands (high energy band from 475—600 nm and a low energy band from 600—750 nm).[11] The transient bleach in the differential absorption spectra is ascribed to carrier depletion from the ground-state upon band edge excitation, which results in a bleach of the ground-state absorption.[47] The ground-state bleach is centered at 425—450 nm for γ′-V_2O_5, 440—510 nm for α-V_2O_5, and 480—520 nm for ζ-V_2O_5. The relative trend of the ground state bleach values is indeed consistent with the optical bandgap values deduced from the diffuse reflectance measurements (Figure VI. 2A).

Intense, broad induced absorption features are observed at 550—600 nm for α-V_2O_5, 510—550 nm for γ′-V_2O_5, and 560—620 nm for ζ-V_2O_5, and can be assigned to the photogenerated excited-state holes situated at the valence band edge of the V_2O_5 polymorphs, which correspond to the excitation of electrons from the deep valence band to valence band edge states.[11] In contrast, low-energy induced absorption bands are observed at 650—750 nm for α-V_2O_5, 550—620 nm for γ′-V_2O_5, and 650—750 nm for ζ- V_2O_5, and can be assigned to excited-state electrons located in the conduction bands of the V_2O_5 polymorphs, which can be ascribed to the state-filling of electrons in the conduction band of V_2O_5 and further excitation of electrons from the conduction band edge to higher energy states in the conduction band that become accessible upon photoexcitation.[11]

Figure VI. 5A—C plot TA spectra acquired for pristine V_2O_5 polymorphs, SILAR-derived V_2O_5/CdSe heterostructures, and LAA-derived V_2O_5/CdSe heterostructures. Spectra acquired for unfunctionalized V_2O_5 nanowires are contrasted

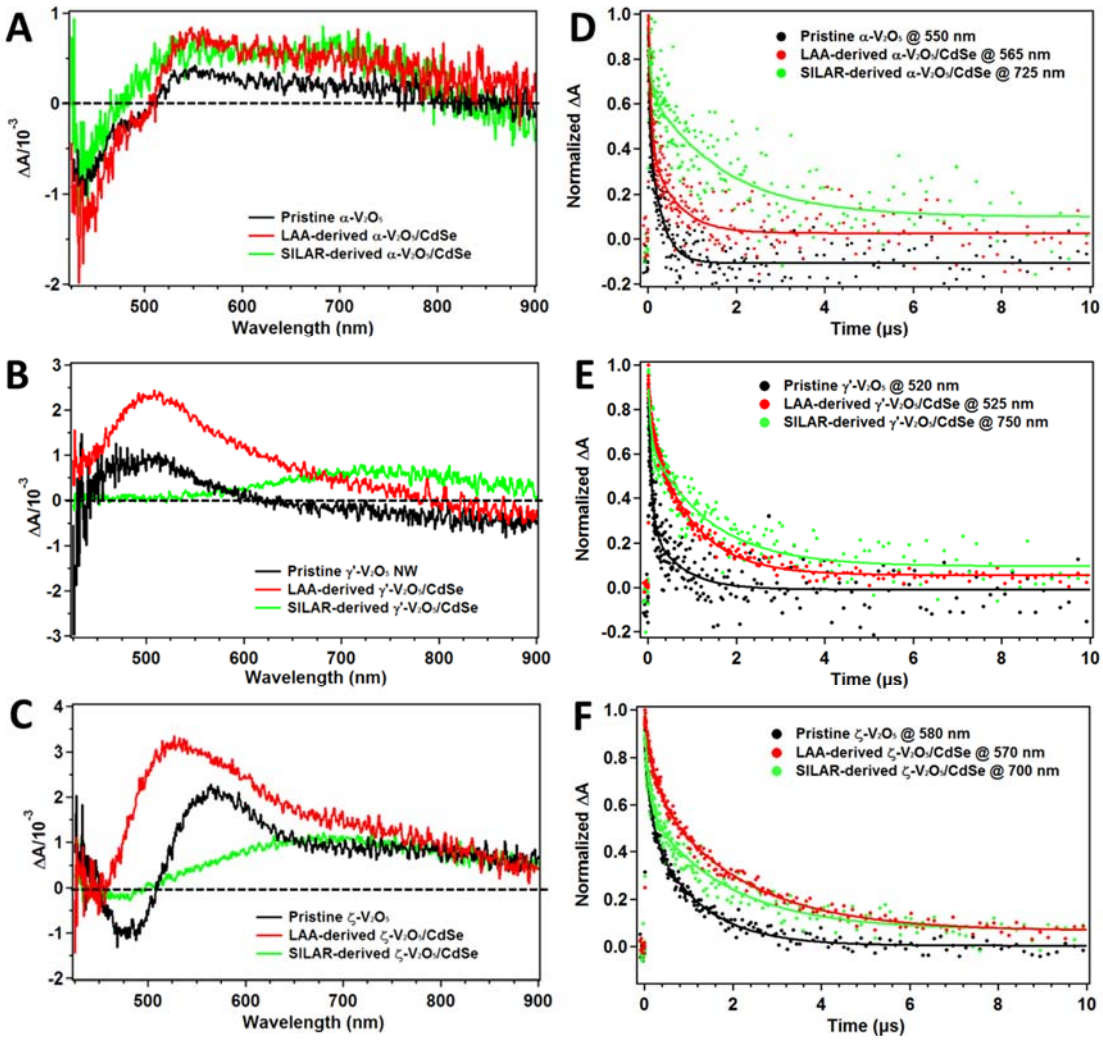

Figure VI. 5 (A-C) TA spectra of unfunctionalized V_2O_5 nanowires, LAA-derived V_2O_5/CdSe heterostructures, and SILAR-derived V_2O_5/CdSe heterostructures: (A) α-V_2O_5, (B) γ′-V_2O_5, and (C) ζ-V_2O_5. (D-F) Decay traces and multiexponential kinetic fitting for pristine V_2O_5 nanowire, LAA-derived V_2O_5/CdSe heterostructures, and SILAR-derived V_2O_5/CdSe heterostructures at the induced absorption band maximum: (D) α-V_2O_5 nanowires and their heterostructures, (E) γ′-V_2O_5 nanowires and their heterostructures, and (F) ζ-V_2O_5 nanowires and their heterostructures.

with spectra measured for SILAR-derived and LAA-derived heterostructures for each of the polymorphs. Notably, spectra acquired for three SILAR-derived V_2O_5/CdSe heterostructures are characterized by a pronounced induced absorption band at longer

wavelengths 650—800 nm, whereas all three LAA-derived V_2O_5/CdSe heterostructures exhibit excited-state spectral features rather similar to that of unfunctionalized V_2O_5 nanowires with an amplification of the measured intensity. For the three SILAR samples, a broad induced absorption band is discernible, centered at 650—800 nm for α-V_2O_5/CdSe, 600—800 nm for γ′-V_2O_5/CdSe, and 500—800 nm for ζ-V_2O_5/CdSe, which is not observed for the pristine V_2O_5 nanowires, and is ascribed to formation of a charge separated state (*vide infra*). Additionally, the high energy (425—520 nm) induced absorption band corresponding to excited-state holes present in V_2O_5 nanowires is significantly diminished in intensity in spectra measured for SILAR-derived γ′- and ζ-V_2O_5/CdSe heterostructures, but is still observable for SILAR-prepared α-V_2O_5/CdSe. This observation suggests that the excited-state hole populations within SILAR-derived γ′- and ζ-V_2O_5/CdSe heterostructures are significantly decreased owing to hole transfer to the CdSe quantum dots in these constructs. In contrast, the TA spectrum of SILAR-derived α-V_2O_5/CdSe heterostructures corresponds to a combination of excited-state spectral features of pristine α-V_2O_5 nanowires and a charge-separated state.

In the case of the LAA-derived heterostructures, the excited-state spectral features of pristine V_2O_5 nanowires (characterized by a transient bleach and two induced absorption bands) are still discernible. The amplified TA intensity as compared to pristine V_2O_5 nanowires reflects an increase of the carrier concentrations but the charge separated state is not readily resolved given the relatively lower concentration of quantum dots. Photoexcitation at 360 nm corresponds to above-bandgap excitation for both V_2O_5 nanowires and CdSe quantum dots, which are simultaneously excited within

SILAR- and LAA-derived heterostructures (V_2O_5 nanowires have bandgaps in the range of 2.0—2.4 eV as noted in Figure VI. 2 and Table VI. 1,[24] whereas CdSe quantum dots have bandgaps in the range of 1.8—2.4 eV).[48] As per the energetic offsets plotted in Figure VI. 2, excited electrons are expected to be localized in the conduction band of V_2O_5 nanowires, whereas photogenerated holes are localized in the valence band of quantum dots upon direct photoexcitation of either component (corresponding to electron transfer from the conduction band of photoexcited quantum dots to the conduction band of V_2O_5 and hole transfer from the valence band of photoexcited V_2O_5 nanowires to valence band of CdSe quantum dots). As a result, the characteristic induced absorption band associated with excited-state holes in V_2O_5 nanowires is diminished as a result of a decreased hole population in V_2O_5 nanowires. Hole transfer further brings about an induced absorption band at long wavelengths (650—800 nm) derived from trapped-holes situated in the valence band of CdSe quantum dots.[11, 49] The excited-state electrons in V_2O_5 nanowires derived from both direct excitation and electron transfer give rise to a low energy band (650—800 nm). The broad spectral features characteristic of the charge-separated state observed for SILAR-derived heterostructures thus represent a summation of induced absorption bands derived from excited holes confined in CdSe quantum dots and electrons confined in V_2O_5 nanowires. In contrast, for the LAA heterostructures the excited-state spectral feature of pristine nanowires are intensified as a result of increased carrier concentrations but the charge separated state is not clearly discernible owing to the relatively low loading of quantum dots.

Figure VI. 5D—F plot decay traces for the long-wavelength induced absorption band for pristine V_2O_5 nanowires as well as their SILAR- and LAA-derived heterostructures, which are shown alongside multiexponential fits. The decay traces have been fitted to multiple exponential decay functions to resolve the excited-state relaxation dynamics as per equation (VI. 2) using the least number of components:

$$\Delta A = \Delta A_0 + \sum_i A_i e^{\left(-\frac{t}{\tau_i}\right)} \qquad \text{(VI. 2)}^{2,11}$$

where ΔA is differential absorbance, ΔA_0 is the differential absorbance at the longest timescales, A_i is a pre-exponential weighting factor, t is pump-probe delay time, and τ_i is lifetime of individual component. The extracted fitting parameters are tabulated in **Table A. 8**. The average carrier lifetime is computed by dividing the amplitude-weighted lifetime with the pre-exponential weight factor (A_i) as per:

$$\langle \tau \rangle = \frac{\sum_i A_i \tau_i}{\sum_i A_i} \qquad \text{(VI. 3)}$$

All the decay traces are well fitted using biexponential decay kinetics ($i = 2$) (*vide infra*). The pristine V_2O_5 nanowires exhibit well-defined multiexponential decay kinetics on the microsecond timescale, resulting from two main recombination processes: charge trapping by surface defect states and electron—hole radiative recombination. 3D color maps are plotted in **Figure A. 36—38**. The multiexponential fits as well as the 3D color maps indicate significantly increased carrier lifetimes for excited states of both SILAR- and LAA-derived heterostructures (Figures VI. 5D-F and Figures A.36—38). Average lifetimes <τ> are summarized in **Table VI. 1** to contrast carrier lifetimes between pristine V_2O_5 nanowires and their SILAR- and LAA-derived heterostructures as well as

Table VI. 1 Average carrier lifetimes derived from TA decay trace and kinetic fitting for nanowires of different polymorphs of V_2O_5, LAA-derived V_2O_5/CdSe heterostructures, and SILAR-derived V_2O_5/CdSe heterostructures.

Average carrier lifetimes for each sample (τ_{ave}; μs)	α-V_2O_5	γ′-V_2O_5	ζ- V_2O_5
Pristine nanowires	0.15 ± 0.01	0.28 ± 0.01	0.70 ± 0.01
LAA-derived V_2O_5/CdSe	0.27 ± 0.01	0.76 ± 0.01	1.5 ± 0.1
SILAR-derived V_2O_5/CdSe	1.2 ± 0.2	0.95 ± 0.1	1.2 ± 0.1
Energy band gap (eV)	2.31	2.36	2.09

the energy bandgap of V_2O_5 polymophs. Notably, the average lifetimes of SILAR or LAA heterostructures are substantially increased, by up to one order of magnitude, as compared to pristine V_2O_5 nanowires. The 3D TA color maps that both SILAR- and LAA-derived heterostructures have more intense and longer-lived induced absorption bands at their induced absorption maxima persisting up to 1—2 μs (**Figure A. 36—38**). The separation of charge in real space across V_2O_5/CdSe interfaces yields substantially longer-lived carriers within both heterostructures as compared to single component nanowires. The increased carrier lifetime can also partly be attributed to the surface passivation of V_2O_5 nanowires with CdSe quantum dots, which decreases the density of surface trap states and thereby suppresses trap-mediated recombination pathways. The SILAR-derived heterostructures have relatively thicker CdSe shells as compared to their LAA-derived counterparts (Figures VI. 3 and 4), resulting in relatively better surface passivation and longer-lived charge carriers.[4]

Photocatalytic hydrogen evolution

Photocatalytic H_2 production with the prepared type II heterostructures has been evaluated under visible light irradiation (400-720 nm) using lactic acid as a sacrificial proton donor and Ni-(3-MPA) as a co-catalyst (**Figure VI. 6**). **Figure VI. 6B** illustrates

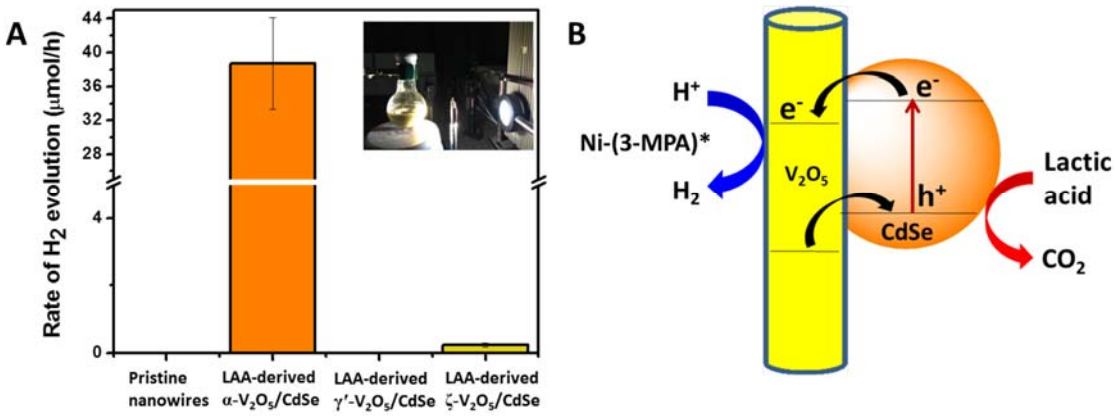

Figure VI. 6 (A) Comparison of the photocatalytic H_2 evolution rates of pristine V_2O_5 nanowires LAA-derived V_2O_5/CdSe heterostructures in a 20 vol. % aqueous solution of lactic acid under visible light irradiation in the presence of Ni-(3-MPA) co-catalyst. (B) Schematic illustration of catalytic scheme.

Table VI. 2 Rates of H_2 generation for LAA-derived V_2O_5/CdSe heterostructures with approximately similar loadings of QDs.

Photocatalyst (LAA)	Amount H_2(μmol h^{-1})
α-V_2O_5/$Cd_{0.23}Se_{0.17}$	38.7±5.4
γ'-V_2O_5/$Cd_{0.28}Se_{0.21}$	~ 0
ζ-V_2O_5/$Cd_{0.23}Se_{0.23}$	0.25±0.06

the mechanism of proton reduction reaction sought to be mediated by photogenerated electrons transferred to V_2O_5 nanowires along with oxidation of lactic acid using photogenerated holes at the quantum dot surfaces. The catalytic conditions are described in further detail in the experimental section. Control experiments performed in the absence of either the photocatalyst or light irradiation indicates the complete absence of hydrogen evolution. **Figure VI. 6A** shows a comparison of visible-light-driven photocatalytic H_2 evolution rates of pristine V_2O_5 polymorphs and LAA-derived V_2O_5/CdSe heterostructures. Notably, no H_2 gas evolution is detected for any of the three polymorphs of V_2O_5 prior to functionalization, whereas LAA-derived α- and ζ-

V_2O_5/CdSe heterostructures are seen to be excellent unassisted dispersed photocatalysts. For similar amounts of CdSe quantum dots, the LAA-derived α-V_2O_5/CdSe heterostructures show the highest rate of H_2 generation at 38.7±5.4 μmol/h, whereas LAA-derived ζ-V_2O_5/CdSe heterostructures exhibit H_2 generation at a rate of 0.3±0.1 μmol/h, almost two orders of magnitude slower; negligible H_2 evolution is observed using LAA-derived γ′-V_2O_5/CdSe heterostructures. The relatively poor performance of the metastable phases upon visible light irradiation is perhaps a function of their relative instability under acidic conditions. Ongoing experiments are focused on examining the structural stability of their heterostructures under operational conditions.

SILAR-derived heterostructures do not show any H_2 gas evolution upon visible light irradiation. Considering that proton reduction reactions occurs at the surfaces of V_2O_5 nanowires owing to electron localization in the conduction band of V_2O_5, the encapsulation of the nanowires by relatively thick CdSe quantum dot shells likely precludes adsorption of the Ni co-catalyst to the nanowire surfaces and establishes diffusion restrictions limiting hydrogen evolution. In contrast, SILAR heterostructures are likely to be promising oxidation catalysts given the localization and ready accessibility of trapped holes in CdSe shells enrobing the V_2O_5 nanowires.

VI.4 Conclusions

Well-defined V_2O_5/CdSe quantum dot heterostructures with a type II configuration have been prepared for nanowires of three different polymorphs of V_2O_5. The thermodynamically stable α-V_2O_5 phase as well as metastable ζ- and γ' V_2O_5

polymorphs have been interfaced with CdSe quantum dots. LAA- and SILAR methods have been used to assemble the heterostructures with the latter yielding relatively higher surface coverage. Nanosecond TA spectroscopy studies indicate that SILAR-derived heterostructures exhibit charge-separated states with electrons localized in V_2O_5 nanowires and holes localized in CdSe quantum dots. The states are long-lived with lifetimes of ca. 1—2 μs, increased by about two orders of magnitude as compared to the excited state features observed for unfunctionalized V_2O_5 nanowires. In TA spectra of LAA-derived heterostructures, increased concentrations of electrons and holes are evidenced as compared to pristine nanowires. Promising photocatalytic activity towards hydrogen evolution is observed for colloidal dispersions of LAA-derived heterostructures, whereas SILAR-derived heterostructures are expected to serve as oxidation catalysts owing to hole localization in the thicker CdSe shells enrobing the V_2O_5 nanowires. The polymorphism of V_2O_5 provides an interesting means of tuning energetic offsets of V_2O_5/CdSe type II interfaces providing an additional degree of freedom to the programmability inherent from compositional and dimensional modulation of the quantum dot components.

VI.5 References

(1) Nocera, D. G., The artificial leaf. *Acc. Chem. Res.* **2012,** 45, 767-776.

(2) Kamat, P. V.; Christians, J. A., Solar cells versus solar fuels: two different outcomes. *J. Phys. Chem. Lett.* **2015,** 6, 1917-1918.

(3) Kamat, P. V., Quantum dot solar cells. The next big thing in photovoltaics. *J. Phys. Chem. Lett.* **2013,** 4, 908-918.

(4) Pelcher, K. E.; Milleville, C. C.; Wangoh, L.; Chauhan, S.; Crawley, M. R.; Marley, P. M.; Piper, L. F.; Watson, D. F.; Banerjee, S., Integrating β-$Pb_{0.33}V_2O_5$ Nanowires with CdSe Quantum Dots: Toward Nanoscale Heterostructures with Tunable Interfacial Energetic Offsets for Charge Transfer. *Chem. Mater.* **2015,** 27, 2468-2479.

(5) Grätzel, M., The artificial leaf, molecular photovoltaics achieve efficient generation of electricity from sunlight. *Comments Inorg. Chem.* **1991,** 12, 93-111.

(6) Gust, D.; Moore, T. A.; Moore, A. L., Realizing artificial photosynthesis. *Faraday Discuss.* **2012,** 155, 9-26.

(7) Barber, J.; Tran, P. D., From natural to artificial photosynthesis. *J. R. Soc. Interface.* **2013,** 10, 20120984.

(8) Osterloh, F. E., Inorganic nanostructures for photoelectrochemical and photocatalytic water splitting. *Chem. Soc. Rev.* **2013,** 42, 2294-2320.

(9) Selinsky, R. S.; Ding, Q.; Faber, M. S.; Wright, J. C.; Jin, S., Quantum dot nanoscale heterostructures for solar energy conversion. *Chem. Soc. Rev.* **2013,** 42, 2963-2985.

(10) Pelcher, K. E.; Milleville, C. C.; Wangoh, L. W.; Cho, J.; Sheng, A.; Chauhan, S.; Sfeir, M. Y.; Piper, L. F.; Watson, D. F.; Banerjee, S., Programming Interfacial Energetic Offsets and Charge Transfer in β-$Pb_{0.33}V_2O_5$/Quantum-Dot Heterostructures: Tuning Valence Band Edges to Overlap with Midgap States. *J. Phys. Chem. C* **2016**, 28992-29001.

(11) Milleville, C. C.; Pelcher, K. E.; Sfeir, M. Y.; Banerjee, S.; Watson, D. F., Directional Charge Transfer Mediated by Mid-Gap States: A Transient Absorption Spectroscopy Study of CdSe Quantum Dot/β-Pb0. 33V2O5 Heterostructures. *J. Phys. Chem. C* **2016,** 120, 5221-5232.

(12) Bridewell, V. L.; Alam, R.; Karwacki, C. J.; Kamat, P. V., CdSe/CdS Nanorod Photocatalysts: Tuning the Interfacial Charge Transfer Process through Shell Length. *Chem. Mater.* **2015,** 27, 5064-5071.

(13) Carneiro, L. M.; Cushing, S. K.; Liu, C.; Su, Y.; Yang, P.; Alivisatos, A. P.; Leone, S. R., Excitation-wavelength-dependent small polaron trapping of photoexcited carriers in α-Fe_2O_3. *Nat. Mater.* **2017,** 16, 819.

(14) Tvrdy, K.; Frantsuzov, P. A.; Kamat, P. V., Photoinduced electron transfer from semiconductor quantum dots to metal oxide nanoparticles. *Proc. Natl. Acad. Sci.* **2011,** 108, 29-34.

(15) Hetsch, F.; Xu, X.; Wang, H.; Kershaw, S. V.; Rogach, A. L., Semiconductor nanocrystal quantum dots as solar cell components and photosensitizers: material, charge transfer, and separation aspects of some device topologies. *J. Phys. Chem. Lett.* **2011,** 2, 1879-1887.

(16) Marcus, R. A., Electron transfer reactions in chemistry. Theory and experiment. *Rev. Mod. Phys.* **1993,** 65, 599.

(17) Nagpal, P.; Klimov, V. I., Role of mid-gap states in charge transport and photoconductivity in semiconductor nanocrystal films. *Nat. Commun.* **2011,** 2, 486.

(18) Goodman, S. M.; Singh, V.; Ribot, J. C.; Chatterjee, A.; Nagpal, P., Multiple Energy Exciton Shelves in Quantum-Dot–DNA Nanobioelectronics. *J. Phys. Chem. Lett.* **2014,** 5, 3909-3913.

(19) Nishikawa, K.; Takeda, Y.; Motohiro, T.; Sato, D.; Ota, J.; Miyashita, N.; Okada, Y., Extremely long carrier lifetime over 200 ns in GaAs wall-inserted type II InAs quantum dots. *Appl. Phys. Lett.* **2012,** 100, 113105.

(20) Hatami, F.; Grundmann, M.; Ledentsov, N.; Heinrichsdorff, F.; Heitz, R.; Böhrer, J.; Bimberg, D.; Ruvimov, S.; Werner, P.; Ustinov, V., Carrier dynamics in type-II GaSb/GaAs quantum dots. *Phys. Rev. B* **1998,** 57, 4635.

(21) Kim, S.; Fisher, B.; Eisler, H.-J.; Bawendi, M., Type-II quantum dots: CdTe/CdSe (core/shell) and CdSe/ZnTe (core/shell) heterostructures. *J. Am. Chem. Soc.* **2003,** 125, 11466-11467.

(22) Pietryga, J. M.; Park, Y.-S.; Lim, J.; Fidler, A. F.; Bae, W. K.; Brovelli, S.; Klimov, V. I., Spectroscopic and device aspects of nanocrystal quantum dots. *Chem. Rev.* **2016,** 116, 10513-10622.

(23) Marley, P. M.; Horrocks, G. A.; Pelcher, K. E.; Banerjee, S., Transformers: the changing phases of low-dimensional vanadium oxide bronzes. *Chem. Commun.* **2015,** 51, 5181-5198.

(24) Tolhurst, T. M.; Leedahl, B.; Andrews, J. L.; Marley, P. M.; Banerjee, S.; Moewes, A., Contrasting 1D tunnel-structured and 2D layered polymorphs of V_2O_5: relating crystal structure and bonding to band gaps and electronic structure. *Phys. Chem. Chem. Phys.* **2016,** 18, 15798-15806.

(25) Andrews, J. L.; Mukherjee, A.; Yoo, H. D.; Parija, A.; Marley, P. M.; Fakra, S.; Prendergast, D.; Cabana, J.; Klie, R. F.; Banerjee, S., Reversible Mg-Ion Insertion in a Metastable One-Dimensional Polymorph of V_2O_5. *Chem* **2018**.

(26) Horrocks, G. A.; Likely, M. F.; Velazquez, J. M.; Banerjee, S., Finite size effects on the structural progression induced by lithiation of V_2O_5: a combined diffraction and Raman spectroscopy study. *J. Mater. Chem. A* **2013,** 1, 15265-15277.

(27) Horrocks, G. A.; Parija, A.; De Jesus, L. R.; Wangoh, L.; Sallis, S.; Luo, Y.; Andrews, J. L.; Jude, J.; Jaye, C.; Fischer, D. A., Mitigating Cation Diffusion Limitations and Intercalation-Induced Framework Transitions in a 1D Tunnel-Structured Polymorph of V_2O_5. *Chem. Mater.* **2017**.

(28) Parija, A.; Liang, Y.; Andrews, J. L.; De Jesus, L. R.; Prendergast, D.; Banerjee, S., Topochemically De-Intercalated Phases of V2O5 as Cathode Materials for Multivalent Intercalation Batteries: A First-Principles Evaluation. *Chem. Mater.* **2016,** 28, 5611-5620.

(29) De Jesus, L. R.; Andrews, J. L.; Parija, A.; Banerjee, S., Defining Diffusion Pathways in Intercalation Cathode Materials: Some Lessons from V_2O_5 on Directing Cation Traffic. *ACS Energy Lett.* **2018,** 3, 915-931.

(30) Parija, A.; Waetzig, G. R.; Andrews, J. L.; Banerjee, S., Traversing Energy Landscapes Away from Equilibrium: Strategies for Accessing and Utilizing Metastable Phase Space. *J. Phys. Chem. C* **2018**.

(31) Yu, W. W.; Qu, L.; Guo, W.; Peng, X., Experimental determination of the extinction coefficient of CdTe, CdSe, and CdS nanocrystals. *Chem. Mater.* **2003,** 15, 2854-2860.

(32) Murray, C.; Norris, D. J.; Bawendi, M. G., Synthesis and characterization of nearly monodisperse CdE (E= sulfur, selenium, tellurium) semiconductor nanocrystallites. *J. Am. Chem. Soc.* **1993,** 115, 8706-8715.

(33) Watson, D. F., Linker-assisted assembly and interfacial electron-transfer reactivity of quantum dot− substrate architectures. *J. Phys. Chem. Lett.* **2010,** 1, 2299-2309.

(34) Lee, H.; Wang, M.; Chen, P.; Gamelin, D. R.; Zakeeruddin, S. M.; Gratzel, M.; Nazeeruddin, M. K., Efficient CdSe quantum dot-sensitized solar cells prepared by an improved successive ionic layer adsorption and reaction process. *Nano Lett.* **2009,** 9, 4221-4227.

(35) Xu, H.; Chen, J.; Zhang, H.; Zhang, Y.; Li, W.; Wang, Y., Fabricating SiO 2-coated V 2 O 5 nanoflake arrays for high-performance lithium-ion batteries with enhanced cycling capability. *J. Mater. Chem. A* **2016,** 4, 4098-4106.

(36) Marley, P. M.; Abtew, T. A.; Farley, K. E.; Horrocks, G. A.; Dennis, R. V.; Zhang, P.; Banerjee, S., Emptying and filling a tunnel bronze. *Chem. Sci.* **2015,** 6, 1712-1718.

(37) Šipr, O.; Šimůnek, A.; Bocharov, S.; Kirchner, T.; Dräger, G., Geometric and electronic structure effects in polarized V K-edge absorption near-edge structure spectra of V_2O_5. *Phys. Rev. B* **1999,** 60, 14115.

(38) Velazquez, J. M.; Jaye, C.; Fischer, D. A.; Banerjee, S., Near edge X-ray absorption fine structure spectroscopy studies of single-crystalline V_2O_5 nanowire arrays. *J. Phys. Chem. C* **2009,** 113, 7639-7645.

(39) Maganas, D.; Roemelt, M.; Hävecker, M.; Trunschke, A.; Knop-Gericke, A.; Schlögl, R.; Neese, F., First principles calculations of the structure and V L-edge X-ray absorption spectra of V_2O_5 using local pair natural orbital coupled cluster theory and spin–orbit coupled configuration interaction approaches. *Phys. Chem. Chem. Phys.* **2013,** 15, 7260-7276.

(40) Tolhurst, T. M.; Leedahl, B.; Andrews, J. L.; Banerjee, S.; Moewes, A., The electronic structure of ε′-V 2 O 5: an expanded band gap in a double-layered polymorph with increased interlayer separation. *J. Mater. Chem. A* **2017,** 5, 23694-23703.

(41) Vargas, W. E.; Niklasson, G. A., Applicability conditions of the Kubelka–Munk theory. *Appl. Opt.* **1997,** 36, 5580-5586.

(42) Yang, L.; Kruse, B., Revised Kubelka–Munk theory. I. Theory and application. *J. Opt. Soc. Am. A* **2004,** 21, 1933-1941.

(43) Marcus, R. A., Electron transfer reactions in chemistry: theory and experiment *Angew. Chem. Int. Ed.* **1993,** 32, 1111-1121.

(44) Marcus, R. A., On the theory of oxidation-reduction reactions involving electron transfer. I. *J. Chem. Phys.* **1956,** 24, 966-978.

(45) Manna, L.; Scher, E. C.; Li, L.-S.; Alivisatos, A. P., Epitaxial growth and photochemical annealing of graded CdS/ZnS shells on colloidal CdSe nanorods. *J. Am. Chem. Soc.* **2002,** 124, 7136-7145.

(46) Rice, K. P.; Saunders, A. E.; Stoykovich, M. P., Seed-mediated growth of shape-controlled wurtzite CdSe nanocrystals: Platelets, cubes, and rods. *J. Am. Chem. Soc.* **2013,** 135, 6669-6676.

(47) Klimov, V.; Mikhailovsky, A.; Xu, S.; Malko, A.; Hollingsworth, J.; Leatherdale, C.; Eisler, H.-J.; Bawendi, M., Optical gain and stimulated emission in nanocrystal quantum dots. *Science* **2000,** 290, 314-317.

(48) Li, L.-s.; Hu, J.; Yang, W.; Alivisatos, A. P., Band gap variation of size-and shape-controlled colloidal CdSe quantum rods. *Nano Lett.* **2001,** 1, 349-351.

(49) Radich, J. G.; Peeples, N. R.; Santra, P. K.; Kamat, P. V., Charge transfer mediation through Cu_xS. The hole story of CdSe in polysulfide. *J. Phys. Chem. C* **2014,** 118, 16463-16471.

(50) Galy, J.; Satto, C.; Sciau, P.; Millet, P., Atomic Modeling of the δ↔ε LiV_2O_5 Phase Transition and Simulation of the XRD Powder Pattern Evolution. *J. Solid State Chem.* **1999,** 146, 129-136.

(51) Cocciantelli, J.; Gravereau, P.; Doumerc, J.; Pouchard, M.; Hagenmuller, P., On the Preparation and Characterization of a New Polymorph of V_2O_5. *J. Solid State Chem.* **1991,** 93, 497-502.

(52) Satto, C.; Sciau, P.; Dooryhee, E.; Galy, J.; Millet, P., The δ⟶ ε⟶ γ LiV_2O_5 "High Temperature" Phase Transitions Evidenced by Synchrotron X-Ray Powder Diffraction Analysis. *J. Solid State Chem.* **1999,** 146, 103-109.

(53) Nevins, J. S.; Coughlin, K. M.; Watson, D. F., Attachment of CdSe nanoparticles to TiO2 via aqueous linker-assisted assembly: Influence of molecular linkers on electronic

properties and interfacial electron transfer. *ACS. Appl. Mater. Interfaces.* **2011,** 3, 4242-4253.

CHAPTER VII

INCORPORATION OF HYDROXYETHYLCELLULOSE-FUNCTIONALIZED HALLOYSITES AS A MEANS OF DECREASING THE THERMAL CONDUCTIVITY OF OILWELL CEMENT

VII.1 Introduction

Well cementing, the pumping and solidification of cement within the annulus between the inserted casing and its surrounding rock formation, represents a critically important step in the completion of oil wells.[1] The oilwell cement provides zonal isolation, protects surrounding groundwater from contamination, structurally bolsters the casing, and substantially mitigates corrosion of the casing. The choice of cement and the method of cementing are determined by the specifics of the geological formation and the nature of the extraction process. Enhanced oil recovery methods that are increasingly being used to meet global energy needs often have specific requirements for well cementing,[2] which adds considerable cost and complexity to the myriad challenges of accessing unconventional deposits. In recent times, the steam-assisted gravity drainage (SAGD) process has emerged as one of the pre-eminent means of extracting viscous oil in the Canadian Oil Sands spread across Northern Alberta and Saskatchewan.[3, 4] In this process, steam is injected down a wellbore through an injection well creating a steam chamber that increases the temperature of the viscous oil deposits, thereby reducing the viscosity of the oil and allowing it to drain down to a lower production well (under the influence

of gravity) from which it is extracted using powerful pumps as an emulsified mixture of water and oil.[5, 6] Apart from load-bearing characteristics, the cement components deployed in SAGD wellbores also have to endure the severe thermal cycling inherent in the SAGD process; the oilwell cement must further be flexible and yet dense in order to avoid microannulus formation, adhere conformally to metal tubing, and provide zonal isolation.[7-9] Given the considerable temperature differential inevitable between the casing and the environment during the SAGD process, there is substantial interest in reducing the thermal conductivity of the oilwell cement in order to reduce heat loss and improve the energy efficiency of the SAGD process. Needless to say, a reduction in thermal conductivity needs to be accomplished without deleteriously impacting critically important mechanical properties such as ultimate compressive strength. In this article, we report a pronounced reduction in the thermal conductivity of oilwell cement upon inclusion of polymer-functionalized halloysite nanotubes (HNTs). The hollow interiors of the HNTs and the scattering of phonons at multiple interfaces yields cement with a substantially decreased thermal conductivity without degrading the mechanical properties of the cement.

Concrete cement is a mixture of silicates and oxides of calcium, aluminum, and iron, primarily comprising various phases of calcium and aluminum silicates. Upon the addition of water, hydraulic cement can be quickly gelled through the hydration reaction of various metal silicates.[10-13] Several thermal cements incorporating polymeric and polysulfide additives have been developed in order to provide enhanced elastic deformability and thermal insulation.[14] Increasing the flexibility (by decreasing the

Young's modulus) of the cementitious matrix helps prevent delamination at the metal tubing interface and further prevents buildup of strain gradients (derived in large measure from thermal gradients) that could bring about fracture and compromise well integrity.[14] Polymer-derived cements incorporate cross-linkable polymeric chains that are oftentimes covalently bonded to the cement matrix giving rise to a dense load-bearing framework. The ability to unravel polymeric chains and the intrinsic stretchability of polymeric backbones can substantially enhance the elastic properties of the matrix. As a result of their "softer" more deformable characteristics, the Young's modulus is decreased for such materials, albeit oftentimes with an accompanying reduction of compressive strength. Polymer-derived cements further serve to reduce water sorption, allow for enhanced corrosion resistance, and provide a means for improved adhesion to metal tubing. Polymeric inclusions further bring about some diminution of thermal conductivity as a result of the dissimilar nature of polymers and silicates, which results in considerable phonon scattering at their interfaces, thereby diminishing the thermal conductivity of the framework. Considerable efforts have also been directed at the inclusion of fibrous additives such as carbon nanotubes (CNTs) or plant fibers within cementitious matrices as a means of simultaneously enhancing deformability as well as fracture toughness.[8, 14-16] A major challenge in the preparation of cement nanocomposites, which is imperative to fully harness the functional benefits of the inclusions, is to ensure homogeneous dispersion of the inclusions within the cementitious matrix whilst precluding the entrainment of air.

While macroscopic porosity is most certainly deleterious to cement strength and well integrity, the incorporation of closed nanoscopic voids represents an intriguing means of embedding a low-thermal-conductivity medium. Naturally occurring hollow clay nanotubes provide a means of introducing nanoscopic voids if they can be incorporated within cementitious matrices in an appropriate manner but such an approach to modulate thermal conductivity has not hitherto been explored to the best of our knowledge. HNTs have a rather similar chemical composition ($Al_2Si_2O_5(OH)_4$) to cement but have not been extensively explored as cement additives.[17-19] Their porous tubular nature and deformability are promising for structural applications that require low thermal conductivity and high elastic modulus (estimated to be ca. 140 GPa). As a result of their high aspect ratios, they can effectively bridge multiple domains and thereby preclude crack formation even at low loadings of additives. In this work, we have contrasted the modulation of thermal conductivity induced upon inclusion of different fibrous additives, CNTs, HNTs, and jute fibers. Based on the superior modulation of thermal properties accessible using HNTs, we have further explored the evolution of the thermal conductivity and mechanical properties of nanocomposite cement as a function of the HNT/polymer loading within cement and the HNT:polymer ratio. An unprecedented decrease of thermal conductivity is engineered without deleterious modification of mechanical properties, suggesting an entirely new approach to oilwell cementing.

VII.2 Experimental

Materials & Methods. Portland cements with Class G employed in this study were sourced from Cenovus Energy, Inc. Classification of cement from Class A through H is defined by American Petroleum Institute (API).

$CaCl_2$ (Sanjel), SiO_2 flour (Sanjel), Multi-walled CNTs (CheapTubes), HNT nanoclays (Aldrich), twisted jute twine (SecureLine), hydroxyethylcellulose (Natrosol^{TM} 250H4Br PA; Ashland Chemicals), polyacrylic acid (Carbopol^{TM}; Acros Organics), poly(vinyl alcohol) (PVA; Aldrich), poly(acrylic acid) (Acrylsol^{TM}; Dow Chemicals), were obtained and used without additional purification.

Preparation of colloidal dispersion of polymer-functionalized fillers. The polymer-functionalized fillers were obtained by mechanically mixing fibrous fillers and the polymer in water. Several types of fibrous fillers were examined for their ability to facilitate modulation of the thermal properties of the cement: (a) CNTs (b) HNTs, and (c) cellulosic jute fibers. Several polymers were further investigated that can grafted to the cement matrix: (a) hydroxyethylcellulose (Natrosol^{TM}); (b) polyacrylic acid (Carbopol^{TM}), (c) PVA, and (d) poly(acrylic acid) (Acrysol^{TM}). Initially, 2 g of the fibrous filler was placed within a plastic container and next a dispersion comprising 0.5 g of polymer blended in 10 mL of water was added. The obtained dispersion was ultrasonicated for 10 min using a bath sonicator to ensure homogenization of the mixture. The relative mass ratios of the filler and polymer was varied from 8:1 to 1:1 while keeping the total mass at 2.5 g.

Preparation of cement nanocomposites incorporating polymer-functionalized fillers. Unmodified cement specimens were constituted by mixing and drying the cementitious slurry, which was prepared by mechanically stirring 223.62 g of G-class cement, 89.58 g of silica flour, and 6.26 g of $CaCl_2$ in 133 mL of de-ionized water for 10 min. The well-mixed cementitious slurry was immediately transferred to a plastic mold with a diameter of 52 cm and height of 104 cm and cured for 7 days. The preparation of modified cement nanocomposites followed exactly the same procedure with the addition of pre-prepared polymer-functionalized fillers during the mixing step. After drying for 7 days, the cement slurry was extracted from the mold for further characterization. The obtained cement slab typically had a diameter of 50 cm and a height of 100 cm.

Structural and Morphological Characterization. The morphological characteristics of the cement samples, with and without inclusion of polymer-enrobed fillers, were evaluated using a Leica EZ4 stereomicroscope equipped with a KL 1500 LCD detector and a FEI Quanta 600 field emission scanning electron microscope (FE-SEM) equipped with a conventional Everhart-Thornley detector, back-scattered electron detector, and IR-CCD chamber camera operated at an accelerating voltage of 10–20 kV. The chemical composition of cement samples was analyzed by EDS using an Oxford Instruments silicon drift detector. The samples for SEM/EDS characterizations were prepared by fracturing the cured large cement slab with a mechanical clamp; ultra-thin sections with a smooth surface were selected, which were adhered to the SEM sample holder with carbon tape.

High-resolution transmission electron microscopy (TEM) images were acquired using a FEI-Tecnai G2 F20 ST instrument at an accelerating voltage of 200 kV. The samples for TEM characterization were prepared by mechanically fracturing with a mechanical clamp and grinding by mortar and pestle to get the powered cement sample, which was further dispersed in ethanol. Next, a few drops of the dispersion were transferred to a carbon-supported Cu TEM grid. Fourier transform infrared (FT-IR) spectra were obtained using a Bruker VERTEX 70 instrument in the range of 4000—500 cm^{-1} with a spectral resolution of 4 cm^{-1}. Powder X-ray diffraction (XRD) measurements were performed using a Bruker D8-Focus Bragg-Brentano X-ray Powder Diffractometer with a Cu Kα radiation source (λ = 1.5418 Å) in the 2θ range from 10—60°.

Thermal Conductivity Measurements. Thermal conductivity measurements were performed with a hot point sensor on a Linseis Transient Hot Bridge (THB) 100 – Thermal Conductivity Meter. The sample setup was performed by placing one cylinder flat on a table; next, the hot point sensor was placed at a desired measuring spot, and finally a second cylinder of the same exact composition was placed directly atop the first cylinder, thereby sandwiching the sensor and minimizing exposure to the open air. The measurements were performed using 10 mA of current and 40 mW of power over a period of 8 s and were performed in triplicate for each configuration with a wait time of 100 s in between measurements.

Compressibility Testing. The compressive strength of the cement nanocomposite specimens were measured on an Instron 5982 Mechanical Testing Device using a servo-

controlled 100 kN load capacity at a displacement rate of 5 mm/min. The dimensions of the cement specimens measured 5.1 cm in diameter and 6.1 cm in height.

VII.3 Results and Discussion

As a result of their covalently bonded -M-O-M- (M = Ca, Al, Fe) as well as silicate frameworks, cementitious materials are typically characterized by a high compressive strength and a high Young's modulus but have a relatively low tensile strength.[20] The incorporation of nanometer-sized inclusions provides a means of modulating properties of cement as a result of the structural reinforcement provided by typically harder or more elastic additives or as a result of the altered ratios of different crystalline silicates nucleated at the interfaces with the additives.[21-23] As with other hybrid nanocomposites, in order to fully realize the benefits of the nanoscopic filers, it is imperative to ensure optimal dispersion of the additives within the host matrix and to further ensure interfacial compatibility of the host matrix and the added fillers.[24]

Figure VII. 1 presents a schematic depiction of the design and preparation of the nanocomposite thermal cement incorporating various polymer-encapsulated fibrous fillers. The initial step corresponds to blending of the fillers within the polymer matrix to obtain a dispersion of polymer-functionalized fillers. Polymers with polar functional groups are used to ensure aqueous dispersibility. Colloidal dispersions are obtained as a result of non-covalent binding of the polymers around the anisotropic fibrous additives.[25] The as-prepared dispersion is immediately transferred to the cement slurry and

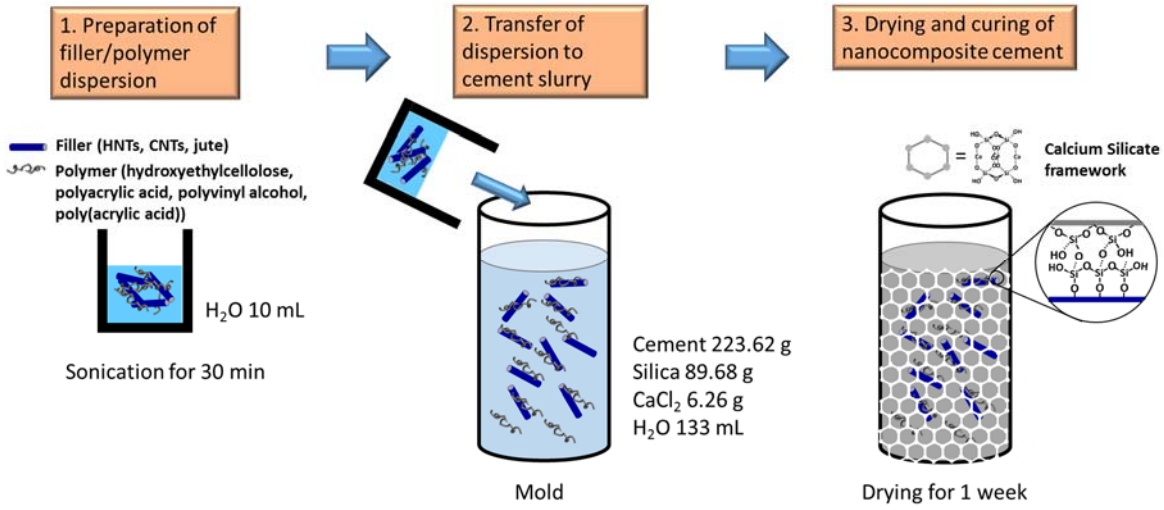

Figure VII. 1 Schematic illustration of the preparation of nanocomposite thermal cements based on the incorporation of polymer-functionalized fillers within cementitous matrices. An as-prepared dispersion of polymer-functionalized fibrous additives is added and vigorously mixed within a cement slurry, which is subsequently allowed to dry for 7 days resulting in solidification of the composite matrix.

homogeneously mixed with the help of a mechanical stirrer to prepare a slurry incorporating the polymer-encapsulated fibers. The slurry is allowed to cure within a mold for 7 days to allow for cross-linking and stabilization of a rigid framework. As delineated in Figure VII. 1, three distinct types of fillers have been incorporated within the nanocomposite cements, CNTs, HNTs, and cellulosic jute fibers. The relative ratio of the filler and the polymer and the overall loading of the filler within the cement matrix have been systematically varied.

A preliminary screening of thermal conductivity has been performed for three different types of fillers and four distinct polymers at a fixed filler loading of 2 wt.% with a 4:1 ratio of filler/polymer (CNTs, HNTs, jute fibers as fillers; hydroxyethylcellulose, polyacrylic acid (Carbopol^{TM}), poly(vinyl alcohol) (PVA),

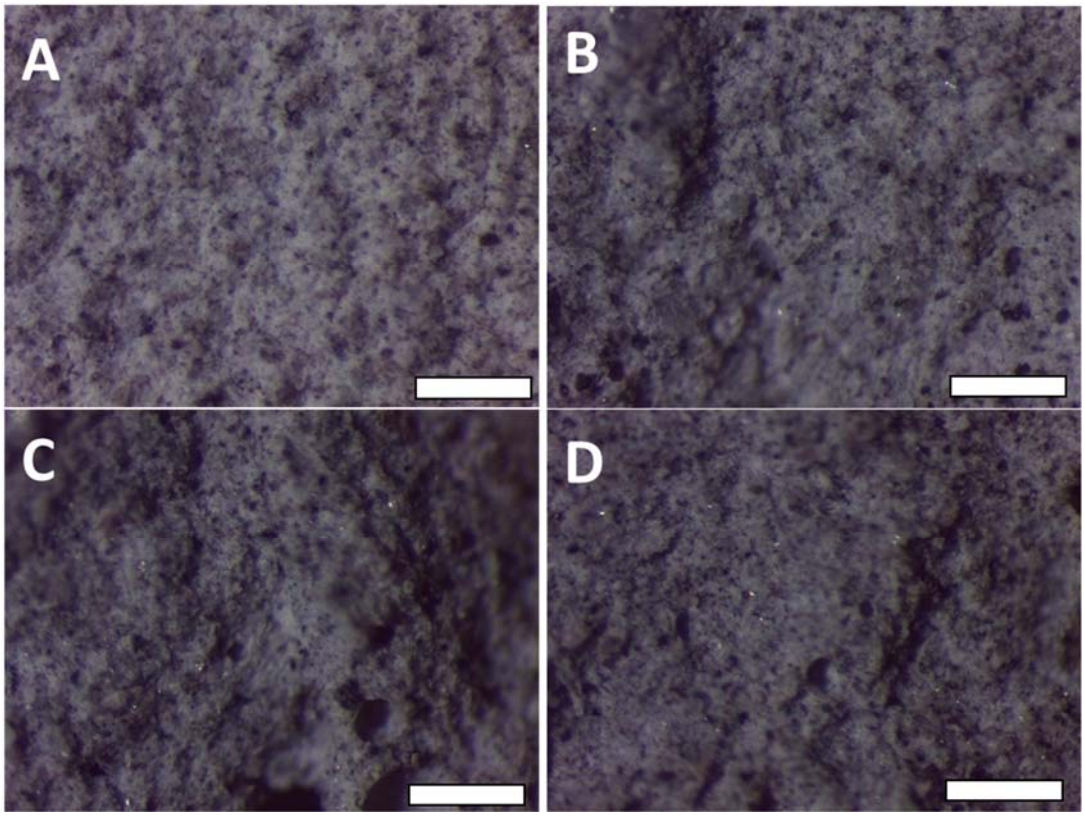

Figure VII. 2 Stereomicroscopy Observations of Modified Cement Specimens. Stereomicroscopy images of (A) an unmodified cement specimen and modified cement nanocomposite incorporating 2 wt.% of polymer—fibrous additive inclusions: (B) HNTs dispersed with the aid of hydroxyethylcellulose; (C) jute fibers dispersed using hydroxyethylcellulose; and (D) CNTs dispersed using hydroxyethylcellulose. The fiber:hydroxyethylcellulose ratio is 4:1 in each case. Scale bar = 1 mm.

poly(acrylic acid) (Acrylsol^{TM}), as the polymers). The inclusion of polyacrylic acid within the cement matrix induces rapid gelling and segregation of the polymeric media from the cementitious matrix and furthermore is seen to be accompanied by considerable entrainment of air bubbles by stereomicroscopy (**Figure A. 39**). The presence of macroscopic voids is discernible and thus this polymer has not been further considered as an additive. The hydroxyethylcellulose nanocomposites showed considerably greater diminution of thermal conductivity for test specimens as compared to the polyacrylic

acid and PVA blends (for all of the fibrous inclusions) and has thus been used as the polymeric dispersant in subsequent studies seeking to examine the evolution of thermal conductivity across a multidimensional compositional space.

Figure A. 40 illustrates digital photographs of colloidal dispersions of HNTs suspended in aqueous media using hydroxyethylcellulose as a dispersant at various particle loadings. The added amount of HNTs is varied from 0.1—2 g while keeping the mass of hydroxyethylcellulose constant at 0.5 g hydroxyethylcellulose in 10 mL water. Notably, even the highest loading of 2 g of HNT fillers shows excellent dispersion within the gelled hydroxyethylcellulose matrix 24 h after mixing. Similar stable dispersions are obtained for jute fibers and CNTs.

Figure VII. 2 exhibits cross-sectional stereomicroscopy images of modified cement composites with 2 wt.% loading of various fillers (HNTs, CNTs, and jute fibers) functionalized with hydroxyethylcellulose; the unmodified cement specimen has also been imaged as a control. The unmodified cement shows a homogeneous distribution of particles at this magnification; similarly the modified cement nanocomposites are microscopically homogeneous suggesting the absence of phase segregation of filler particles from the host cement matrix; no evidence for microannuli (as observed for poly(acrylic acid) nanocomposites in Figure A. 39), which are severely detrimental to the cementing process,[8] is observed in any of the images. Microannulus formation has been strongly implicated in failures of well cementing in casing applications and thus it is notable that the fibrous inclusions at 2 wt.% loading do not give rise to microannuli detectable by stereomicroscopy.[8, 9]

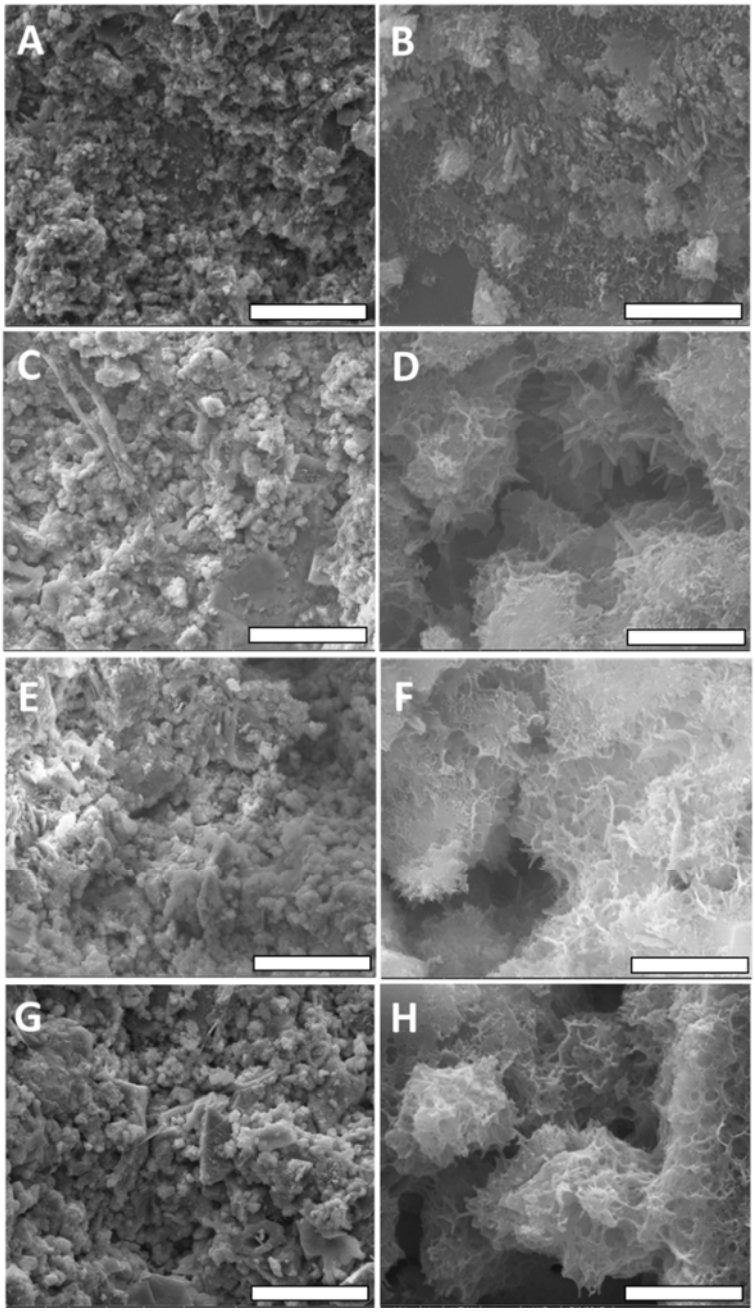

Figure VII. 3 Microstructure of Cement Specimens with and without Fibrous Additives. SEM images of A,B) unmodified cement; C,D) modified cement nanocomposite incorporating a 2 wt.% loading of HNT and hydroxyethylcellulose; E,F) modified cement nanocomposite incorporating a 2 wt.% loading of jute fibers and hydroxyethylcellulose; and G,H) modified cement nanocomposite incorporating a 2 wt.% loading of CNTs and hydroxyethylcellulose. The fiber:hydroxyethylcellulose ratio is 4:1 in each case. Scale bar = 40 μm for the left column and 4 μm for the right column.

The microstructures of the modified cement composites prepared using various fillers with hydroxyethylcellose have been investigated by scanning electron microscopy (SEM) (**Figure VII. 3**). Low-magnification SEM images display the presence of micron-sized primary particles. Similar micron-sized aggregates are observed in SEM aggregates of images of the modified composites. High-resolution SEM images demonstrate that at the nanoscale level, the modified cement nanocomposites exhibit a distinctive hierarchical microstructure that is quite different from that of the unmodified cement specimen (**Figures. VII. 3B,D,F,H**). A hierarchical porous microstructure is observed and is thought to derive from the shrinkage of the polymer-cross-linked cement particles upon drying (a similar microstructure is observed for all three fillers and thus appears to be primarily derived from the common hydroxyethylcellulose matrix). The stabilization of hierarchical nanoporous primary particles suggests an increased thermal contact resistance not observed in unmodified cement (which in contrast exhibits a characteristic 3D interconnected microstructure), resulting in an increased resistance to phonon transport across macroscopic cement specimens in the former.[26]

Figure VII. 4 contrasts the thermal conductivity profiles measured for unmodified and modified cement nanocomposites incorporating various filler/polymer additives (HNTs, CNTs, and jute fibers along with hydroxyethylcellulose) at a fixed loading of 2 wt.% using the transient hot bridge method. The temperature *versus* time plot demonstrates that the temperature of a cement composite with HNTs rises faster than that of the other cement composites upon resistive heating of the thermal source attesting to the relatively poor ability of this sample to dissipate heat (the increase in

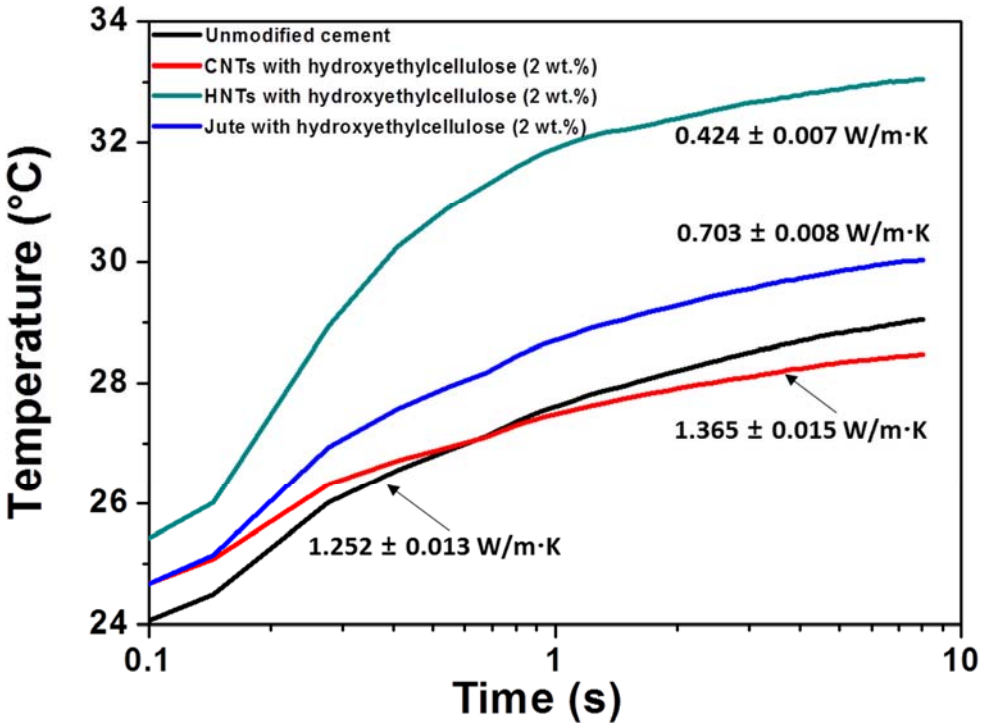

Figure VII. 4 Thermal Conductivity of Cement Specimens with and without Fibrous Additives. Plots showing the evolution of temperature as a function of time for unmodified cement and modified cement composites containing 2 wt.% loadings of various fillers (HNTs, CNTs, and jute fibers) dispersed using hydroxyethylcellulose. The fiber:hydroxyethylcellulose ratio is 4:1 in each case.

temperature can be ranked in the following order depending on the inclusion of fillers: HNTs > jute fibers > control specimen (no fillers) > CNTs). The deduced thermal conductivity values are 1.252 ± 0.013 W/m·K for unmodified cement; 0.424 ± 0.007 W/m·K for HNTs; 0.703 ± 0.008 W/m·K for jute fibers; and 1.365 ± 0.015 W/m·K for CNTs. The observed trend of thermal conductivity values is intriguing given the microstructure observed in Figure VII.3. A hierarchically porous structure, derived from the use of the hydroxyethylcellulose, enhances the thermal contact resistance for all three

types of fibrous additives, yet considerable differences are observed in the thermal conductivity values suggesting a pronounced dependence of thermal conductivity of the nanocomposites on the specific composition and structure of the fibrous fillers.

CNTs are excellent thermal conductors with thermal conductivity values approaching 3500 W/m·K along their length for individual single-walled carbon nanotubes [27] and approaching 1500 W/m·K for aligned fibers.[28] Their high aspect ratios imply that they can readily form a quasi-percolative network across the 3D cement matrix, thereby yielding a higher thermal conductivity matrix despite the stabilization of the porous microstructure as a result of dispersion using hydroxyethylcellulose. In stark contrast, the diminution of thermal conductivity upon incorporation of HNTs is stark and can be attributed to the nanoscopic voids within such materials, which provides a low-thermal-conductivity medium. The inherent low thermal conductivity of HNTs (0.1 W/m·K) thereby brings about a pronounced decrease in the thermal conductivity of nanocomposites that include these materials. A decrease of thermal conductivity of phase-change materials when HNTs are used as storage media and an increase in thermal conductivity for carbon-based materials has been observed in a different context for phase change materials used for latent heat storage.[29, 30] Jute fibers do not have the hollow voids characteristic of HNTs but being cellulosic in nature have low thermal conductivities (estimated to be 0.43 W/m·K)[31] and also bring about a diminution of thermal conductivity of the cement specimens although not to the same extent as HNTs. In other words, the HNT/hydroxyethylcellulose inclusions offer an abundance of

disparate interfaces and void space that can effectively scatter phonons, thereby reducing the thermal conductivity.[17-19]

To investigate the crystallographic phases present within the cement composites, powder X-ray diffraction (XRD) patterns have been acquired for the modified cement

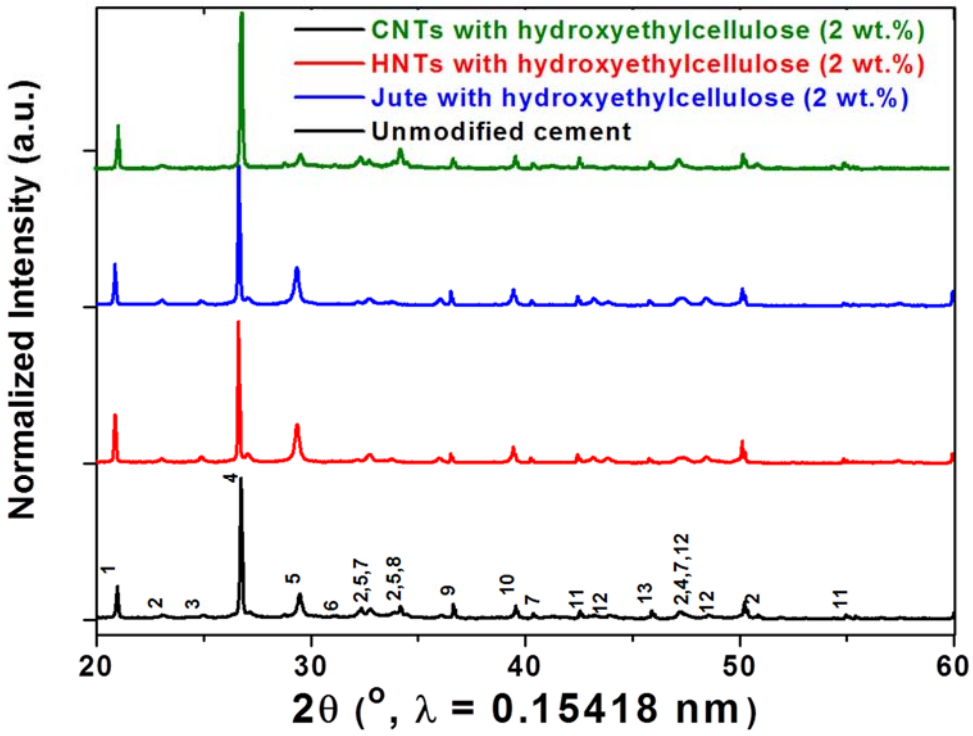

Figure VII. 5 XRD Patterns of Cement with and without Inclusion of Hydroxyethylcellulose-Modified HNTs. XRD patterns of unmodified cement (black) and modified cement nanocomposite incorporating 2 wt.% loadings of fibrous additives with hydroxyethylcellulose: HNT (red), Jute (blue), and CNT (green). The observed reflections are assigned to the following crystalline phases with the corresponding JCPDS number quoted in parenthesis in each case: **1**. $Ca_3Al_2O_6$ (32-0150); **2**. γ-C_2S ($2CaO{\cdot}SiO_2$; 31-0297); **3**. Anhydrite ($CaSO_4$; 37-1496); **4**. $CaCO_3$ (33-0268); **5**. C_3S ($3CaO{\cdot}SiO_2$; M1: 13-0272, M3: 42-0551); **6**. α-C_2S ($2CaO{\cdot}SiO_2$; 23-1042); **7**. TCA ($3CaO{\cdot}Al_2O_3$; 38-1429); **8**. $Ca_3Al_2O_6$ (32-0150); **9**. Arcanite (05-0613); **10**. $Na_{2x}Ca_{3-x}Al_2O_6$ (26-0957); **11**. a'-C2S (20-0237); **12**. C4AF ($4CaO{\cdot}Al_2O_3{\cdot}Fe_2O_3$); 30-0226); **13**. Sodium sulfate ($NaSO_4$; 37-1465,24-1132)

composites at 2 wt.% loading of various fillers and are compared to the pattern of unmodified cement (**Figure VII. 5**). The XRD pattern for unmodified cement verifies the presence of the major crystalline phases of Portland cement: 1) dicalcium silicate (belite; C_2S; $2CaO{\cdot}SiO_2$); 2) tricalcium silicate (alite; C_3S; $3CaO{\cdot}SiO_2$); 3) tricalcium aluminate (celite; C_3A; $3CaO{\cdot}Al_2O_3$); and 4) tetracalcium aluminoferrate (ferrite; C_4AF; $4CaO{\cdot}Al_2O_3{\cdot}Fe_2O_3$).[11, 32, 33] **Figure A. 41** shows a magnified view of the powder XRD pattern acquired for unmodified cement indicating characteristic reflections of the C_3S, C_2S, and C_3A phases in the 2θ range between 29—35°. The highest intensity reflection at a 2θ value of ca. 26° can be indexed to the (112) reflection of the vaterite phase of $CaCO_3$ which is a major component of cement. It is worth noting that the powder XRD pattern remains essentially the same upon the inclusion and crosslinking of hydroxyethylcellulose-functionalized HNT, CNT, and jute fiber fillers. Indeed, this observation suggests that the crystallinity and compositional ratio of the cementitious matrix remains largely unaltered upon inclusion of 2 wt.% of the fillers even as the microstructure of individual particles is strongly modified. The diminution of thermal conductivity can thus be attributed to microstructural modifications and the specific role of the fillers themselves and not to a compositional or structural modification of the host matrix.

Given the relatively higher diminution of thermal conductivity upon inclusion of HNTs, a detailed evaluation of HNT/hydroxyethylcellulose-modified cement has been performed at varying filler loadings. **Figure VII. 6** shows Fourier transform infrared (FTIR) spectroscopy data acquired for modified cement composites prepared with

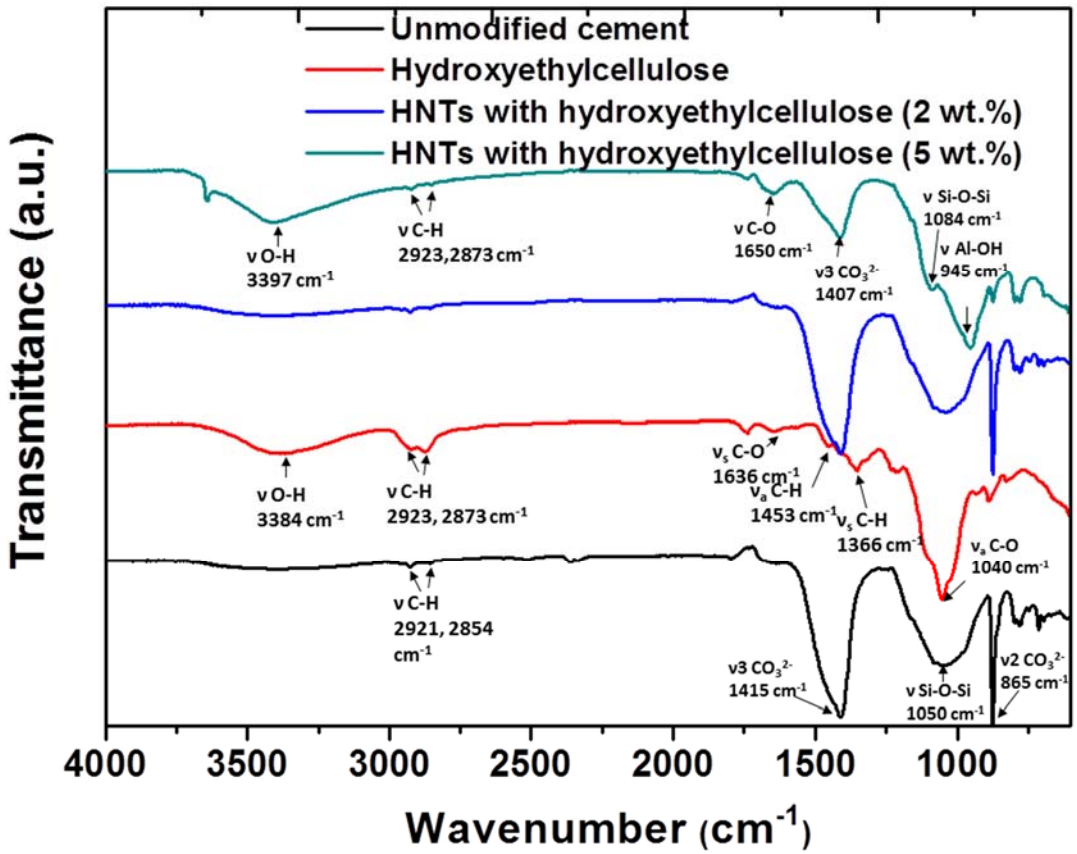

Figure VII. 6 FTIR Spectra of Cement Specimens with and without Inclusion of Hydroxyethylcellulose-Modified HNTs. FTIR spectra measured for unmodified cement, hydroxyethylcellulose, and modified cement composites incorporating 2 and 5 wt.% loadings of hydroxyethylcellulose-modified HNTs.

hydroxyethylcellulose-modified HNTs. The unmodified cement specimen displays prominent vibrational modes at 865, 1050, and 1415 cm^{-1}, respectively, which can be assigned to ν2 CO_3^{2-} stretching, Si-O-Si stretching, and ν3 CO_3^{2-} stretching modes, respectively; [34, 35] less intense modes are discernible at 2854^{-1} and 2921 cm^{-1} and can be assigned to CH_2 stretching modes. The modes arise from the $CaCO_3$ and calcium silicate (C_3S and C_2S) phases that are the primary constituents of cement. The modified cement composites with 2 and 5 wt.% loading of HNTs added with hydroxyethylcellulose show

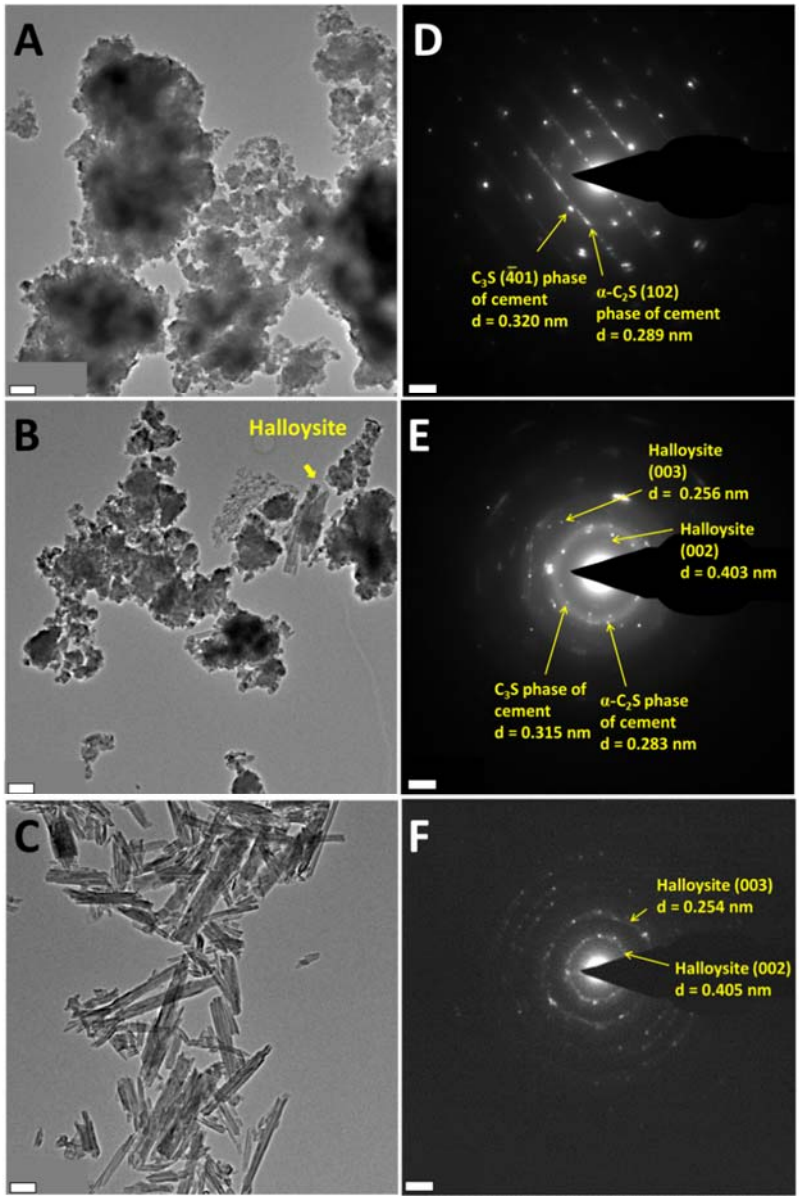

Figure VII. 7 TEM Images of Cement with and without Inclusion of Hydroxyethylcellulose-Modified HNTs. TEM images of (A) unmodified cement, (B) modified cement composite incorporating 2 wt.% of hydroxyethylcellulose-modified HNTs; and (C) HNT precursors. The corresponding SAED patterns are shown in (D)—(F); (D) the observed rings are indexed to the (-401) planes of C_3S and (102) plane of C_2S phase with d-spacings of 0.320 nm and 0.289 nm, respectively; (E) diffraction rings are indexed to C_3S and C_2S phases of cement and the (002) and (003) plane of HNTs; (F) diffraction rings are indexed to the (002) and (003) planes of HNTs with interplanar separations of 0.405 nm and 0.254 nm, respectively. Scale bar = 200 nm for TEM images and 2 nm^{-1} for SAED patterns.

intense IR bands centered around 1050—1100 cm^{-1} and 1400—1500 cm^{-1}, which again can be assigned to Si-O-Si and CO_3^{2-} stretching modes, respectively (as also observed for the unmodified cement specimen). The similarity in the vibrational spectra of the modified and unmodified cement specimens further attests to preservation of the primary phases. At a relatively high loading of 5 wt.% hydroxyethylcellulose-modified HNTs, a new vibrational mode at 945 cm^{-1} is observed and can be ascribed to the Al-OH stretch of the $Al_2Si_2O_5(OH)_4$ HNTs. A distinctive C—O stretching mode at 1650 cm^{-1} associated with elongation of the C-O vibration of cellulose rings is also observed for the modified cement specimens and derives from the incorporation of hydroxyethylcellulose within the cementitious matrix.[36-38]

Figure VII. 7 shows TEM images of unmodified cement and cement composites containing 2 wt.% of hydroxyethylcellulose-modified HNTs, contrasted with TEM images of the HNT precursors. Higher magnification images are shown in **Figure A. 42**. The HNTs are 40—50 nm in a diameter and span several micrometers in a length (Figure VII.7C and Figure A. 42E,F). The hollow nature of the HNTs is clearly discernible in the TEM images. The TEM images directly evidence the inclusion of HNTs within the cement matrix and further establish that the HNTs retain their structural integrity and void space upon inclusion within the matrix. The unmodified cement sample depicts dense aggregates of the silicate and carbonate particles comprising stacked thin sheets and aggregated microparticles (Figure VII. 7A and Figure A. 42). The SAED pattern in Figure VII.7B can be indexed to reflections from (-401) crystallographic planes of the C_3S phase and (102) planes of α-C_2S phase from

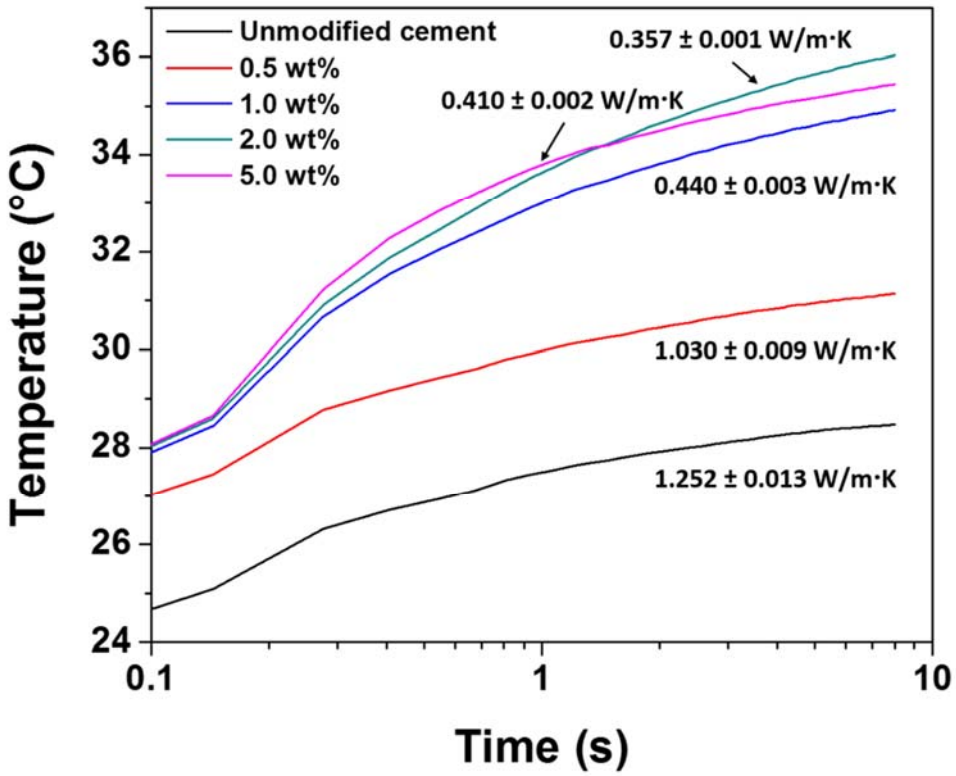

Figure VII.8 Thermal Conductivity of Nanocomposite Cement Specimens as a Function of Filler Loading. Plots showing the evolution of temperature as a function of time measured using a hot bridge analyzer for unmodified cement and modified cement composites with varying loadings of HNTs. The HNT to hydroxyethylcellulose ratio is held constant at 4:1.

unmodified cement.[39] Composite samples imaged after mechanical fracturing clearly show the presence of embedded HNTs (Figure VII.7B and Figure A. 42C,D). Indeed, the high-aspect-ratio HNTs appear to connect primary particles in several instances, perhaps as a result of covalent tethering of the hydroxyethylcellulose to cement. The SAED pattern in Figure VII. 7D attests to the retention of crystallinity of the HNTs; the observed diffraction rings can be indexed to diffraction spots from (002) and (003) planes of HNTs along with reflections from the primary cement phases. These images

thus provide direct evidence both of the nanoscopic voids and the multiple interfaces that result in the boundary scattering of phonons, thereby diminishing the thermal conductivity of cement.

The chemical homogeneity of cement samples before and after inclusion of hydroxyethylcellulose-modofied HNTs has been further been mapped using energy dispersive X-ray spectroscopy (EDS). **Figure A. 43** shows EDS spectra, whereas **Figure A. 44** shows micron-scale elemental maps. Based on EDS mapping, the unmodified cement shows a homogenous distribution of Si (ca. 7.0 at.%), and Ca (ca. 10.4 at.%), O (ca. 54.1 at.%) across the entire area of the specimen, which suggests that the various calcium silicate phases are well-dispersed without compositional segregation or formation of large voids. Some minor contributions from other elements such as Al (ca. 0.4 at.%), S (ca. 0.6 at.%), K (0.4 at.%), Fe (ca. 0.3 at.%), Zr (ca. 0.6 at.%) are also identified. After inclusion of hydroxyethylcellulose-modified HNTs, the relative concentration of Si and Al is found to increase (Figure A. 43). However, EDS mapping suggests that the compositional homogeneity is maintained (Figure A. 44) confirming the homogeneous distribution of HNTs within the cementitious matrix as also discernible from the TEM images in Figure VII. 7.

The HNT: polymer ratio and the overall loading of fillers have been systematically varied in the cement matrix. **Figure VII. 8** plots the temperature *versus* time profiles measured using a transient hot bridge analyzer for varying overall loadings of hydroxyethylcellulose-modified HNTs maintaining a constant polymer:HNT ratio of 4:1. The thermal conductivity values deduced from these measurements are 1.252 ±

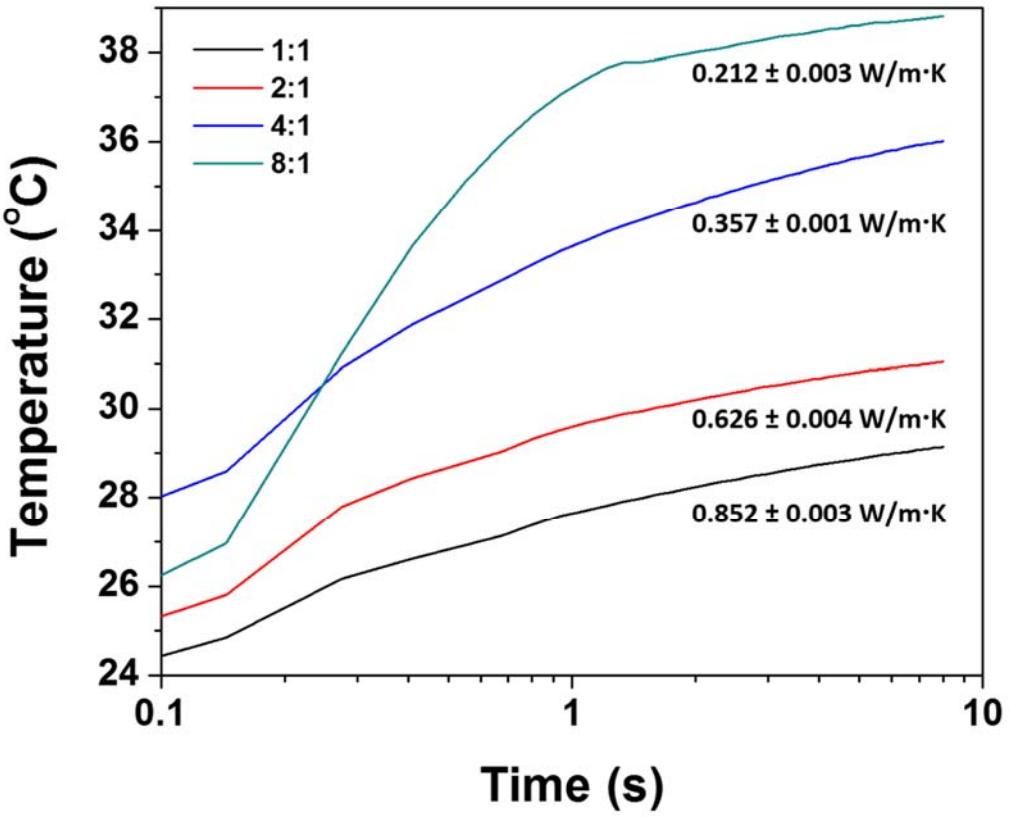

Figure VII. 9 Thermal Conductivity of Nanocomposite Cement Specimens as a Function of HNT:Hydroxyethycellulose Ratio. Plots of the evolution of temperature as a function of time measured using a hot bridge analyzer for unmodified cement and modified cement composites with varying ratios of HNT to hydroxyethylcellulose. The overall loading of hydroxyethylcellulose-modified HNTs is held constant at 2.0 wt.%.

0.013 W/m·K for unmodified cement, 1.030 ± 0.009 W/m·K for 0.5 wt.% hydroxyethylcellulose-HNT; 0.440 ± 0.003 W/m·K for 1.0 wt.% hydroxyethylcellulose-HNT; and 0.357 ± 0.001 W/m·K for 2.0 wt.% hydroxyethylcellulose-HNT. However, at 5.0 wt.% loading the thermal conductivity increases slightly to 0.410 ± 0.002 W/m·K. At relative high loadings of HNTs in the range of 2—5 wt.%, **Figure A. 45** indicates that flakes of cement are bridged by HNTs. Such a bridging function can mitigate crack

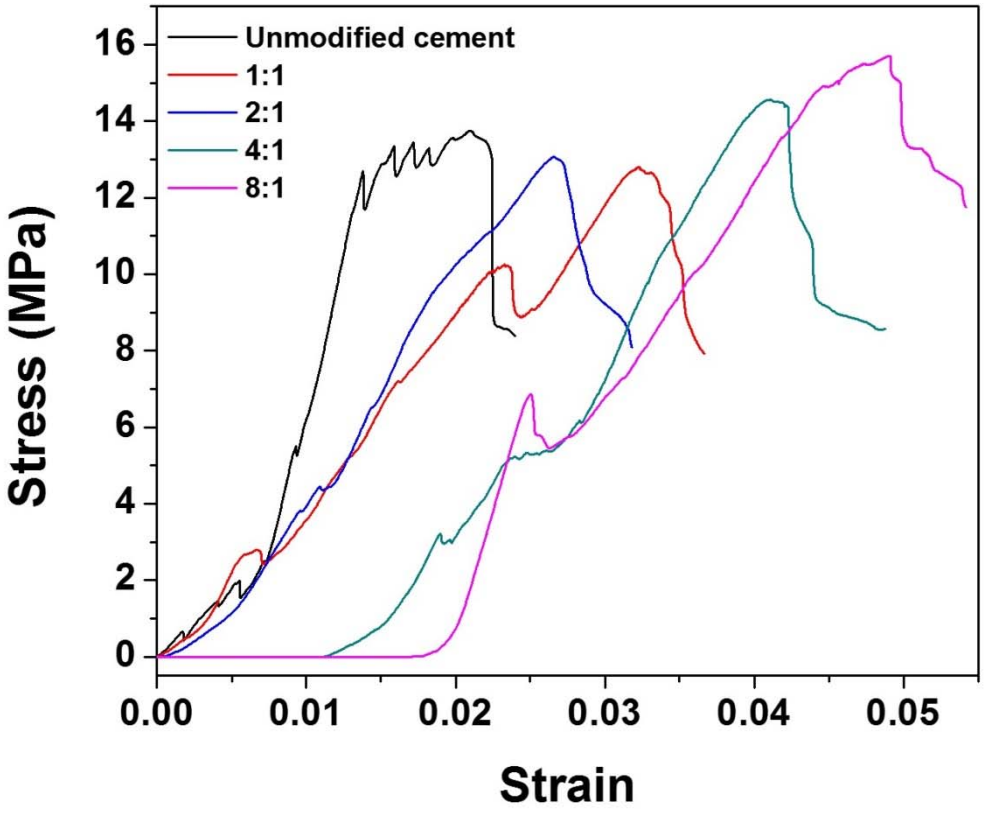

Figure VII. 10 Mechanical Testing of Cement Nanocomposites. Stress versus strain curves measured for unmodified and modified cement samples embedded with 2.0 wt.% of hydroxyethylcellulose-functionalized HNTs for different ratios of HNT:hydroxyethylcellulose.

formation. However, at high loadings, it is likely that the high-aspect ratio HNTs begin to form a percolative network that makes available a new pathway for phonon transport along their crystalline walls thereby increasing the measured thermal conductivity. In other words, the benefits of the nanoscopic voids and multiple interfaces are best realized below the threshold for stabilization of extended percolative networks.

The overall loading of hydroxyethylcellulose-modified HNTs has further been held constant at 2.0 wt.% and the relative ratio of HNT:hydroxyethylcellulose has been varied. The measured thermal profiles are plotted in **Figure VII. 9**. The deduced thermal conductivity values decrease with increased HNT:hydroxyethylcellulose loading; a 1:1 sample exhibits a thermal conductivity of 0.852 ± 0.003 W/m·K; a 2:1 sample exhibits a value of 0.626 ± 0.004 W/m·K; a 4:1 sample exhibits a value of 0.357 ± 0.001 W/m·K, and a 8:1 sample yields the lowest thermal conductivity value of this set of samples at 0.212 ± 0.003 W/m·K. The greater volumetric incorporation of nanoscopic voids and the increased number of interfaces likely contribute to the measured decrease of thermal conductivity.

Compressive testing has further been performed for the modified cement samples prepared by varying the HNT:hydroxyethylcellulose ratio while keeping the overall loading of hydroxyethylcellulose-funtionalized HNTs at 2 wt.%. **Figure VII. 10** plots the stress *versus* strain plots. The unmodified cement sample has a compressive strength of 13.75 MPa, which given the short drying time (7 days) and size of the sample (5.1 cm diameter, 6.1 cm height) is within the range of values measured for thermal cements. For the samples incorporating hydroxyethylcellulose-modified HNTs, the 1:1 sample has a compressive strength of 12.81 MPa, the 2:1 sample has a strength of 13.08 MPa, the 4:1 sample has a compressive strength of 14.56 MPa, and the 8:1 sample has a compressive strength 15.71 MPa. The observed compressive strength values attests that even with incorporation of polymer functionalized HNTs within the matrix, the compressive strength is not deleteriously modified thereby yielding a sample with substantially

reduced thermally conductivity that retains the compressive strength of the material. The incorporation of nanoscopic enclosed voids that can increased phonon boundary scattering without weakening the host matrix underpins the observed desirable combination of thermal and mechanical properties.

VII.4 Conclusions

The available palette of thermal cements is rather sparse despite the urgent need for low-thermal-conductivity cement for applications such as SAGD wherein heat loss to the external environment represents a considerable expense. The inclusion of additives to form nanocomposites to reduce thermal conductivity without deleteriously impacting load-bearing ability has been examined across a multidimensional compositional space (type, loading %, ratio of filler/polymer). The inclusion of polymer-modified fillers has been examined for three distinct fibrous additives: CNTs, HNTs, and jute fibers; and three distinct polymers hydroxyethylcellulose, PVA, and poly(acrylic acid). Hydroxyethylcellulose-modified fibrous composites can be cured without discernible microannulus formation and exhibit a porous microstructure. CNTs bring about an enhancement of thermal conductivity, whereas jute fibers and HNTs substantially reduce thermal conductivity. The diminution of thermal conductivity is most pronounced for HNTs as a result of the nanoscale voids and the phonon boundary scattering at multiple interfaces. The thermal conductivity appears to be lowest below the percolation threshold. Modified cement nanocomposites incorporating HNTs along with hydroxyethylcellulose in a 8:1 ratio with an overall loading of 2 wt.% exhibit the lowest

measured thermal conductivity of 0.212 ± 0.003 W/m·K, which is substantially reduced from the thermal conductivity of unmodified cement (1.252 W/m·K). The mechanical properties of the hydroxyethylcellulose-HNT nanocomposite cements are not deleteriously impacted. The development of novel nanocomposite cements with reduced thermal conductivity fulfills a substantial need for well cementing in the SAGD process.

VII.5 References

(1) Lavrov, A.; Torsæter, M., *Physics and Mechanics of Primary Well Cementing*. Springer: 2016.

(2) Shah, A.; Fishwick, R.; Wood, J.; Leeke, G.; Rigby, S.; Greaves, M., A review of novel techniques for heavy oil and bitumen extraction and upgrading. *Energy Environ. Sci.* **2010,** 3, 700-714.

(3) Butler, R., Application of SAGD, related processes growing in Canada. *Oil Gas J.* **2001,** 99, 74-74.

(4) Dusseault, M. B.; Shafiei, A., Oil Sands. In *Ullmann's Encyclopedia of Industrial Chemistry*, Wiley-VCH Verlag GmbH & Co. KGaA: 2000.

(5) O'Loughlin, T. E.; Martens, S.; Ren, S. R.; McKay, P.; Banerjee, S., Orthogonal Wettability of Hierarchically Textured Metal Meshes as a Means of Separating Water/Oil Emulsions. *Adv. Eng. Mater.* **2017,** 19.

(6) O'Loughlin, T. E.; Waetzig, G. R.; Davidson, R. E.; Dennis, R. V.; Banerjee, S., Modifying Base Metal Substrates to Exhibit Universal Non-Wettability: Emulating

Biology and Going Further. In *Encyclopedia of Inorganic and Bioinorganic Chemistry*, John Wiley & Sons, Ltd: 2011.

(7) Schneider, J.; Sylvestre, C. J., Challenges While Performing Infill Cementing Amongst Existing SAGD Wells. In *SPE Heavy Oil Conference Canada*, Society of Petroleum Engineers: 2012.

(8) Brown, J.; Kenny, N.; Slagmulder, Y. In *Unique Cement Design to Mitigate Trapped Annular Pressure TAP Between Two Casing Strings in Steam Injection Wells*, SPE Heavy Oil Conference and Exhibition, 2016; Society of Petroleum Engineers: 2016.

(9) Iremonger, S. S.; Cheung, B.; Carey, J. In *Direct Strain Mapping of a Cement Sheath; A New Tool for Understanding and Preventing Cement Failure in Thermal Wells*, SPE Thermal Well Integrity and Design Symposium, 2017; Society of Petroleum Engineers: 2017.

(10) Bentz, D. P., Three-Dimensional Computer Simulation of Portland Cement Hydration and Microstructure Development. *J. Am. Ceram. Soc.* **1997,** 80, 3-21.

(11) Bye, G. C., *Portland cement: composition, production and properties*. Thomas Telford: 1999.

(12) Tennis, P. D.; Jennings, H. M., A model for two types of calcium silicate hydrate in the microstructure of Portland cement pastes. *Cem. Concr. Res.* **2000,** 30, 855-863.

(13) Lothenbach, B.; Winnefeld, F., Thermodynamic modelling of the hydration of Portland cement. *Cem. Concr. Res.* **2006,** 36, 209-226.

(14) Iremonger, S. S.; Bolt, M.; Lawrence, S. C. In *Enhanced thermal well integrity through the use of a new cement tensile strength-enhancing fiber*, SPE Canada Heavy Oil Technical Conference, 2015; Society of Petroleum Engineers: 2015.

(15) Chen, S. J.; Wang, W.; Sagoe-Crentsil, K.; Collins, F.; Zhao, X. L.; Majumder, M.; Duan, W. H., Distribution of carbon nanotubes in fresh ordinary Portland cement pastes: understanding from a two-phase perspective. *RSC Adv.* **2016,** 6, 5745-5753.

(16) Lu, Z.; Hou, D.; Meng, L.; Sun, G.; Lu, C.; Li, Z., Mechanism of cement paste reinforced by graphene oxide/carbon nanotubes composites with enhanced mechanical properties. *RSC Adv.* **2015,** 5, 100598-100605.

(17) Farzadnia, N.; Ali, A. A. A.; Demirboga, R.; Anwar, M. P., Effect of halloysite nanoclay on mechanical properties, thermal behavior and microstructure of cement mortars. *Cem. Concr. Res.* **2013,** 48, 97-104.

(18) Lvov, Y.; Wang, W.; Zhang, L.; Fakhrullin, R., Halloysite clay nanotubes for loading and sustained release of functional compounds. *Adv. Mater.* **2016,** 28, 1227-1250.

(19) Yu, L.; Wang, H.; Zhang, Y.; Zhang, B.; Liu, J., Recent advances in halloysite nanotube derived composites for water treatment. *Environ. Sci. Nano* **2016,** 3, 28-44.

(20) Lecomte, I.; Henrist, C.; Liegeois, M.; Maseri, F.; Rulmont, A.; Cloots, R., (Micro)-structural comparison between geopolymers, alkali-activated slag cement and Portland cement. *J. Eur. Ceram. Soc.* **2006,** 26, 3789-3797.

(21) Li, G. Y.; Wang, P. M.; Zhao, X., Mechanical behavior and microstructure of cement composites incorporating surface-treated multi-walled carbon nanotubes. *Carbon* **2005,** 43, 1239-1245.

(22) Banthia, N.; Nandakumar, N., Crack growth resistance of hybrid fiber reinforced cement composites. *Cem. Concr. Compos.* **2003,** 25, 3-9.

(23) Savastano, H.; Warden, P.; Coutts, R., Brazilian waste fibres as reinforcement for cement-based composites. *Cem. Concr. Compos.* **2000,** 22, 379-384.

(24) Dennis, R. V.; Patil, V.; Andrews, J. L.; Aldinger, J. P.; Yadav, G. D.; Banerjee, S., Hybrid nanostructured coatings for corrosion protection of base metals: a sustainability perspective. *Mater. Res. Exp.* **2015,** 2, 032001.

(25) Wu, H.; Zhao, W.; Hu, H.; Chen, G., One-step in situ ball milling synthesis of polymer-functionalized graphene nanocomposites. *J. Mater. Chem.* **2011,** 21, 8626-8632.

(26) Warrier, P.; Yuan, Y.; Beck, M. P.; Teja, A. S., Heat transfer in nanoparticle suspensions: modeling the thermal conductivity of nanofluids. *AlChE J.* **2010,** 56, 3243-3256.

(27) Pop, E.; Mann, D.; Wang, Q.; Goodson, K.; Dai, H., Thermal conductance of an individual single-wall carbon nanotube above room temperature. *Nano Lett.* **2006,** 6, 96-100.

(28) Koziol, K. K.; Janas, D.; Brown, E.; Hao, L., Thermal properties of continuously spun carbon nanotube fibres. *Physica E Low Dimens. Syst. Nanostruct.* **2017,** 88, 104-108.

(29) Thapa, S.; Zhao, Y.; Lvov, Y.; Weiss, L. In *Halloysite clay nanotubes with pcm for thermal energy storage and efficiency*, ASME 2013 International Mechanical Engineering Congress and Exposition, 2013; American Society of Mechanical Engineers: 2013; pp V06BT07A068-V06BT07A068.

(30) Kim, G. M.; Yang, B. J.; Ryu, G. U.; Lee, H. K., The electrically conductive carbon nanotube (CNT)/cement composites for accelerated curing and thermal cracking reduction. *Compos. Struct.* **2016,** 158, 20-29.

(31) Bandyopadhyay, S.; Ghose, P.; Bose, S.; Mukhopadhyay, U., The Thermal Resistance of Jute and Jute-blend Fabrics. *J TEXT I* **1987,** 78, 255-260.

(32) Scrivener, K.; Füllmann, T.; Gallucci, E.; Walenta, G.; Bermejo, E., Quantitative study of Portland cement hydration by X-ray diffraction/Rietveld analysis and independent methods. *Cem. Concr. Res.* **2004,** 34, 1541-1547.

(33) Trezza, M. A., Hydration study of ordinary Portland cement in the presence of zinc ions. *Mater. Res.* **2007,** 10, 331-334.

(34) Ylmén, R.; Jäglid, U.; Steenari, B.-M.; Panas, I., Early hydration and setting of Portland cement monitored by IR, SEM and Vicat techniques. *Cem. Concr. Res.* **2009,** 39, 433-439.

(35) Waetzig, G. R.; Cho, J.; Lacroix, M.; Banerjee, S., Building on Sub-Arctic Soil: Geopolymerization of Muskeg to a Densified Load-Bearing Composite. *Sci. Rep.* **2017,** 7, 14711.

(36) Carranza, P. H.; Vázquez, S. M.; García, J. G.; Pérez, S. C.; Sosa, R. Á.; Velasco, C. O., Elaboration and characterization of antifungal properties of biodegradable film

added with cinnamon oil. *Antimicrobial research: Novel bioknowledge and educational programs (A. Méndez-Vilas, Ed.)* **2017**, 385-391.

(37) Catauro, M.; Papale, F.; Lamanna, G.; Bollino, F., Geopolymer/PEG hybrid materials synthesis and investigation of the polymer influence on microstructure and mechanical behavior. *Mater. Res.* **2015,** 18, 698-705.

(38) Hsiao, M.-H.; Lin, K.-H.; Liu, D.-M., Improved pH-responsive amphiphilic carboxymethyl-hexanoyl chitosan–poly (acrylic acid) macromolecules for biomedical applications. *Soft Matter* **2013,** 9, 2458-2466.

(39) Zhou, C.; Liang, Y.; Gong, Y.; Zhou, Q.; Chen, Y.; Qiu, X.; Wang, H.; Luo, W.; Yan, C., Modes of occurrence of Fe in kaolin from Yunnan China. *Ceram. Int.* **2014,** 40, 14579-14587.

CHAPTER VIII

DISSERTATION SUMMARY AND OUTLOOK

VIII. 1 Conclusions

In this dissertation, rational design and development of next generation photocatalytic architectures interfacing light-harvester quantum dot and charge acceptor nanowires are explored. **Chapter II** focuses on the ligand-mediated modulation of dimensional control over methylammonium lead bromide ($MAPbBr_3$) nanoplatelets down to monolayer layer thickness level. Dimensional confinement of semiconducting nanocrystals in proximity to exciton Bohr radius (2 nm for $MAPbBr_3$; nm for $CsPbBr_3$; nm for CdSe) represent an alternative means to alter the energy bandgap and corresponding photoluminescent emission wavelength of optically active semiconducting materials. Surface-capping ligands generally deployed in a colloidal synthesis of nanocrystals allows for precise control of nucleation and growth kinetics of crystals by controlling supersaturation of monomer, monomer diffusion, and nucleation and growth kinetics. The surface-capping ligands are bound on the surface of nanocrystals indeed modulate the monomer addition to nuclei and growth kinetics of nanocrystals. Steric hindrance and concentration of surface capping ligands allows for modulation of the degree of vertical oligomerization and tuning the photoluminescent emission feature across the visible range of 430—520 nm.

Chapter III explores more robust all-inorganic $CsPbBr_3$ nanoplatelets, alternative to $MAPbBr_3$. Dimensional reduction, particularly in proximity of the Bohr

exciton radius, allows for substantial tunability of the photophysical properties of this material as a result of quantum confinement. The use of surface passivating ligands, particularly alkylammonium cations, has been developed as a means of inducing directional growth and facilitates dimensional confinement of the obtained perovskite nanocrystals. The ligand packing dictated by thermodynamics and kinetics of ligand shell assembly strongly influences the extent of dimensional confinement for obtained nanoplatelets. The interplay between enthalpic stabilization from crystalline packing and entropic loss from loss of configurational degrees of freedom provides substantial opportunity to tune the parameter space as a function of ligand structure and reaction variables. Mechanistic understanding of thermodynamic and kinetic regimes provides a means to rationally optimize synthetic parameters to obtained desired dimensionality and thus allows for control over nanocrystal thickness in precise increments.

Chapter IV illustrates a navigation of cesium—lead—bromine ternary phase diagram and establishes synthetic control of structural dimensiontily of lead halide perovskite nanocrystals. Ligand-mediated navigation of the ternary phase diagram is demonstrated that distinctive regimes can be stabilized from 3D $CsPbBr_3$ to 0D Cs_4PbBr_6 nanocrystals. The denticity, steric bulk, and concentration of aliphatic amine ligands strongly modifies the supersaturation of lead monomers, scaling proportionately to their complexation coefficients and ability to form ordered passivating ligand shells. The added ligands strongly alter the trajectory of nucleation and growth processes, stabilizing either Pb-rich or Pb-deficient compositions across the ternary phase diagram. These parameters furthermore exert considerable influence on the physical dimensions

of the obtained nanocrystals. By altering the monomer supersaturation and dynamics of crystal growth, the molecular amines thus provide a means of controlling both structural dimensionality and nanocrystal size. The reversible interconversion of $CsPbBr_3$ and Cs_4PbBr_6 is furthermore illustrated upon the ligand-mediated addition/leaching of $PbBr_2$.

Chapter V studies on the interfacial charge transfer kinetics of $M_xV_2O_5$/QDs heterostructures (M = Pb, Sn and QDs = CdS, CdSe, CdTe) with two distinctive interfaces using time-resolved ultrafast transient absorption (TA) spectroscopy. A vast matrix of potential compositions of $M_xV_2O_5$/QD heterostructures with tunable properties are successfully stabilized, differing for example in the intercalative cation M of nanowires and its stoichiometry *x*, the composition and size of various quantum dots, the nature of interface between nanowires and quantum dots, and the doping of nanowires and quantum dots. These variables provide tremendous design space which is central to the idea of programmable heterostructures. Collaborative integration of first principles theory, combinatorial material synthesis, high-throughput screening, and analytics allows for precise prediction of energetic offset, improvement of band alignment of heterostrutures, and ultimate exploits of the opportunities for programmability available in the target heterostructures with desired functionality.

Chapter VI further explores the energetic offset of V_2O_5 polymorph functionalized with CdSe quantum dot heterostructures with distinctive type II interface modulated as a function of the V-O connectivity and open frameworks of V_2O_5 nanowires. Careful band alignment of thermodynamic driving force across the interface is achieved for rapid charge separation and charge transfer kinetics. The type II

semiconductor heterostructure comprised of polymorph V_2O_5 and CdSe quantum dots (QDs) is successfully prepared using two distinctive approaches: linker-assisted assembly (LAA) and successive ionic layer adsorption and readction (SILAR). The thermodynamic driving force is correlate to charge transfer kinetics within type II interface based on relative band alignment of semiconductor heterostructure. SILAR-derived V_2O_5/CdSe heterostructure based on type II configuration facilitate the rapid charge separation with elongated carrier lifetime up to few microsecond.

Chapter VII demonstrates the modification of thermal conductivity of cement nanocomposites *via* incorporation of polymer-functionalized fillers into cementitious matrix. The nanocomposite materials are successfully designed with careful regard to a number of constraints. The cementitious materials deployed in steam-assisted gravity drainage (SAGD) wellbores have to endure the severe thermal cycling inherent in the SAGD process in which the temperature of steam fluctuates up to 275°C; the oilwell cement must further be flexible and yet dense in order to avoid microannulus formation, adhere conformally to metal tubing, and provide zonal isolation. We have been able to achieve a pronounced reduction in thermal conductivity without deleteriously impacting critically important mechanical properties such as ultimate compressive strength. Development of low-thermal-conductivity cement indeed provide a combination of enhanced thermal insulation and mechanical resilience upon thermal cycling which lead to better energy efficiency and mechanical robustness in SAGD process.

As a future direction for designing of next-generation photocatalysts, **Figure VIII. 1** sketches the broad compositional, structural, and interfacial palette available in

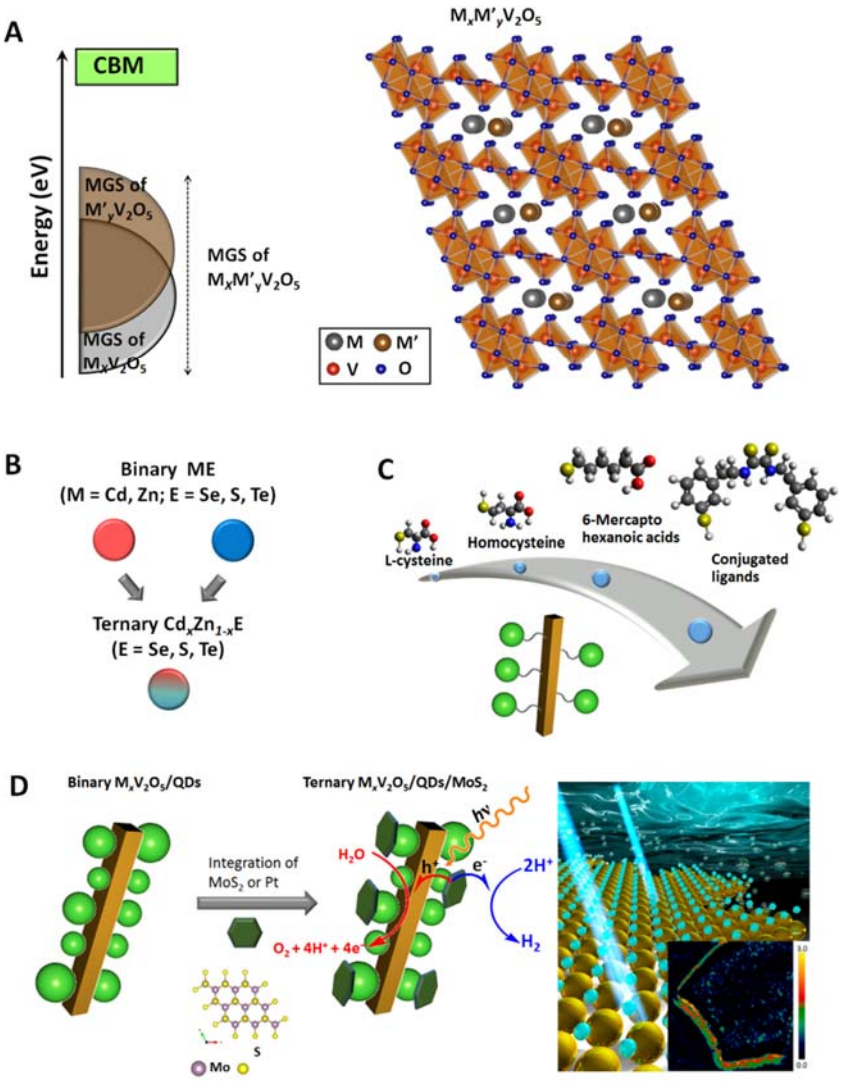

Figure VIII. 1 Future outlook for elaboration of heterostructure catalysts to further enhance photocatalytic activity. (A) schematic illustration of the modulation of energy positioning and dispersion of midgap states within $M_xM_y'V_2O_5$ nanowires *via* intercalation of multiple cations with steroactive lone pairs or periodic ordering of cations in distinctive sites within the tunnels (combinations of monovalent and trivalent ions, e.g., In^{3+} and Sb^{3+} represent a particularly attractive strategy); (B) engineering of the valence and conduction band edges of QDs *via* alloying of the cationic and anionic sublattices and quantum confinement; (C) ligand engineering based on selection of ligand molecules with different alkyl chain-lengths and functionality to modulate tunneling across the interfaces; and (D) integration of hydrogen evolution catalysts (HER) such as Pt and MoS_2 to build ternary heterostructure photocatalysts; the right panel illustrates hydrogen evolution from the edges of MoS_2 nanosheet (the inset shows a scanning transmission X-ray microscopy image of edge states in MoS_2)[1]; Panel (D) is reprinted with permission from ref 1. Copyright 2018 American Chemical Society.

our scheme to design heterostructures that satisfy the demanding constraints imposed by thermodynamics and kinetics for viable light harvesting, charge separation, and redox catalytic processes. DFT calculations benchmarked with electronic structure measurements (HAXPES, resonant inelastic X-ray scattering and X-ray absorption spectroscopy measurements) allow for mapping of thermodynamic parameters; in turn, TA spectroscopy and photoelectrochemistry measurements provide a measure of the relevant kinetic parameters. Taken together the computational and experimental data provide a rich set of input parameters and descriptors (e.g., valence band energetic offsets, interfacial separation, bandgaps) that can further be deciphered with assistance from machine learning algorithms. While an algorithm that identifies optimal descriptors to meet the multiple constraints of photocatalysis remains to be developed and clearly requires a more extensive elaboration of the compositional, structural, and interfacial palette beyond existing configurations, statistical learning methods have begun to guide navigation of the design space. For instance, Bayesian image analysis of hyperspectral X-ray microscopy data has been pivotal to the development of intercalation methods for homogeneously inserting cations within ζ-V_2O_5[2]; similarly, efficient navigation of synthetic design space to prepare QDs with the desired size to facilitate efficient harvesting of the solar spectrum has been achieved by identifying diffusion constant of passivating ligands as a key descriptor.[3]

Benchmarking of DFT calculations to experimentally measured electronic structure is imperative to increase its predictive power and to address known limitations of DFT in predicting energy level alignments and bandgaps.[4] In order to provide

meaningful information on thermodynamic driving forces, DFT calculations need to accurately capture electron correlation, relativistic effects, spin-orbit coupling, and lone-pair hybridization, which is non-trivial given the large unit cells and possibilities for interfacial hybridization. Valence band spectroscopy measurements performed at different excitation energies have been critical to quantitatively examine the orbital contributions and energy positioning of lone-pair-derived states and to determine the choice of hybrid functionals that most accurately capture the energetic offsets in these systems. Such integration of modeling and measurements has played a key role in guiding synthetic prioritization and will be imperative to more efficient navigation of the design space. Future work will explore mixed cation β-$M_xM'_yV_2O_5$ bronzes (**Figure. VIII. 1A**) as well as other (double-layered or puckered single-layered) frameworks of $M_xV_2O_5$ to determine the most optimal energy dispersion and positioning of stereoactive lone-pair states that can facilitate hole extraction from photoexcited QDs. Similarly compositional modulation of QDs through alloying of the cation or anion lattice[5] holds promise for tunability of the VB and CB edges of the light harvesting element (**Figure. VIII. 1B**), which in turn would allow for alteration both of thermodynamic driving forces for charge transfer as well as the kinetics of charge separation in a programmable manner. Direct bandgap perovskite semiconductors with high oscillator strengths and size-tunable spectra hold further promise as light harvesting components of the heterostructures.

Predicting excited-state charge transfer reactivity from first principles represents a formidable challenge but would provide highly complementary information on the

foundational principles and descriptors underpinning charge transfer dynamics and thereby guide synthetic prioritization of possible $M_xV_2O_5$/QD interfaces. Towards this end, time-dependent density functional theory-molecular dynamics methods explicitly including time-domain evolution of the electronic states that have recently become available hold promise for providing meaningful simulations of the charge transfer processes.[6] Notably, standard molecular dynamics simulations based on Born—Oppenheimer or Car—Parinnello methods that model evolution of the electronic ground state cannot be used to examine excited-state charge transfer reactivity of the heterostructures. Based on empirical considerations, ligand chain length provides a means of tuning interfacial coupling terms with interfacial coupling tunable as per Marcus theory, as illustrated in the distinctive differences in electron transfer rates when cysteine and homocysteine are used as bridging ligands. Ligand engineering, specifically increasing the separation between the $M_xV_2O_5$ and QD components of LAA-assembled heterostructures by varying the carbon chain length, holds great promise for increasing the differential between ultrafast hole transfer and relatively slower electron transfer reactions, thereby diminishing electron—hole recombination. **Figure VIII. 1C** shows mercapto acids with varying chain lengths. Furthermore, the installation of aromatic and conjugated residues in the bridging ligands can be used for enhancing light harvesting and to achieve further modulation of hole and electron transfer dynamics.

The design of ternary heterostructures incorporating HER catalysts further provides a mechanism for reducing electron—hole recombination since electrons can be consumed rapidly to mediate proton reduction reactions. **Figure. VIII. 1D** illustrates

further interfacing of the QD components of the $M_xV_2O_5$/QD heterostructures with well-known Pt or MoS_2 reduction co-catalysts to form ternary heterostructures. The reduced overpotential of the HER reaction engendered by interfacing these catalysts is expected to further facilitate more effective utilization of photoexcited electrons for catalysis while diminishing electron—hole recombination.

In summary, the account describes a conceptual framework and rich sandbox for tuning semiconductor heterostructures to meet the stringent constraints of photocatalytic water splitting. The ability to position stereoactive lone pair states through soft chemical intercalation chemistry provides a powerful means of tuning the energetics and dispersion of mid-gap states, enabling close overlap with chalcogenide-derived valence band edges of light-harvesting QDs. The nature of the interface determines the efficacy of charge separation. Viable photocatalysts for water splitting have been prepared with high Faradic efficiencies for H_2 production and continue to be improved in an evolutionary manner exploiting the multiple compositional, structural, and interfacial degrees of freedom available in these constructs.

VIII. 2 References

(1) Parija, A.; Choi, Y.-H.; Liu, Z.; Andrews, J. L.; De Jesus, L. R.; Fakra, S. C.; Al-Hashimi, M.; Batteas, J. D.; Prendergast, D.; Banerjee, S., Mapping Catalytically Relevant Edge Electronic States of MoS_2. *ACS Cent. Sci.* **2018,** 4, 493-503.

(2) Horrocks, G. A.; Parija, A.; De Jesus, L. R.; Wangoh, L.; Sallis, S.; Luo, Y.; Andrews, J. L.; Jude, J.; Jaye, C.; Fischer, D. A., Mitigating cation diffusion limitations

and intercalation-induced framework transitions in a 1D tunnel-structured polymorph of V_2O_5. *Chem. Mater.* **2017,** 29, 10386-10397.

(3) Cho, J.; Jin, H.; Sellers, D. G.; Watson, D. F.; Son, D. H.; Banerjee, S., Influence of ligand shell ordering on dimensional confinement of cesium lead bromide ($CsPbBr_3$) perovskite nanoplatelets. *J. Mater. Chem. C* **2017,** 5, 8810-8818.

(4) Ernzerhof, M.; Scuseria, G. E., Assessment of the Perdew–Burke–Ernzerhof exchange-correlation functional. *J. Chem. Phys.* **1999,** 110, 5029-5036.

(5) Regulacio, M. D.; Han, M.-Y., Composition-Tunable Alloyed Semiconductor Nanocrystals. *Acc. Chem. Res.* **2010,** 43, 621-630.

(6) Bang, J.; Meng, S.; Sun, Y.-Y.; West, D.; Wang, Z.; Gao, F.; Zhang, S., Regulating energy transfer of excited carriers and the case for excitation-induced hydrogen dissociation on hydrogenated graphene. *Proc. Natl. Acad. Sci.* **2013,** 110, 908-911.

APPENDIX A

SUPPLEMENTARY FIGURES AND TABLES

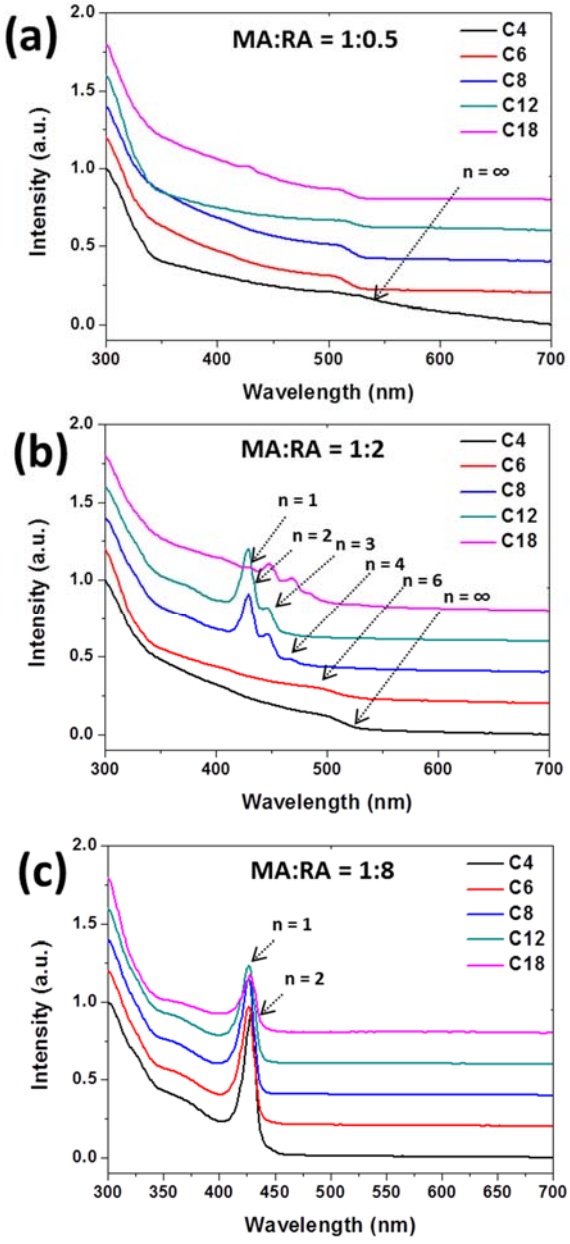

Figure A. 1 UV-visible absorption spectra of 2D perovskite nanoplatelets prepared using different chain lengths of capping ligands at varying MA:RA ratios of 1:*x* where (a) 1:0.5, (b) 1:2, and (c) 1:8.

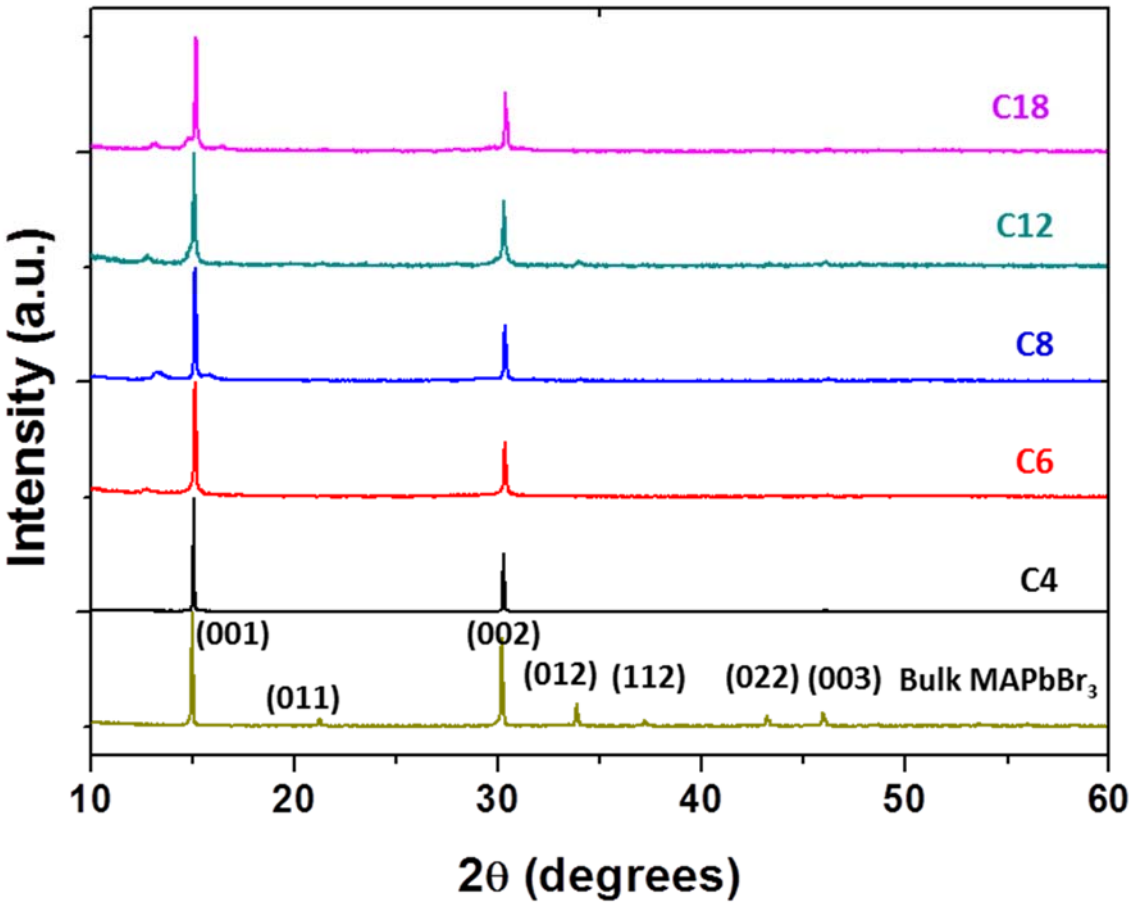

Figure A. 2 Powder XRD patterns acquired for perovskite nanoplatelets prepared at a MA:RA concentration of 1:2 for different chain lengths of alkylammonium cations. These patterns are contrasted to the pattern acquired for $MAPbBr_3$ precipitated by only using MABr and $PbBr_2$ as precursors without any added surfactants.

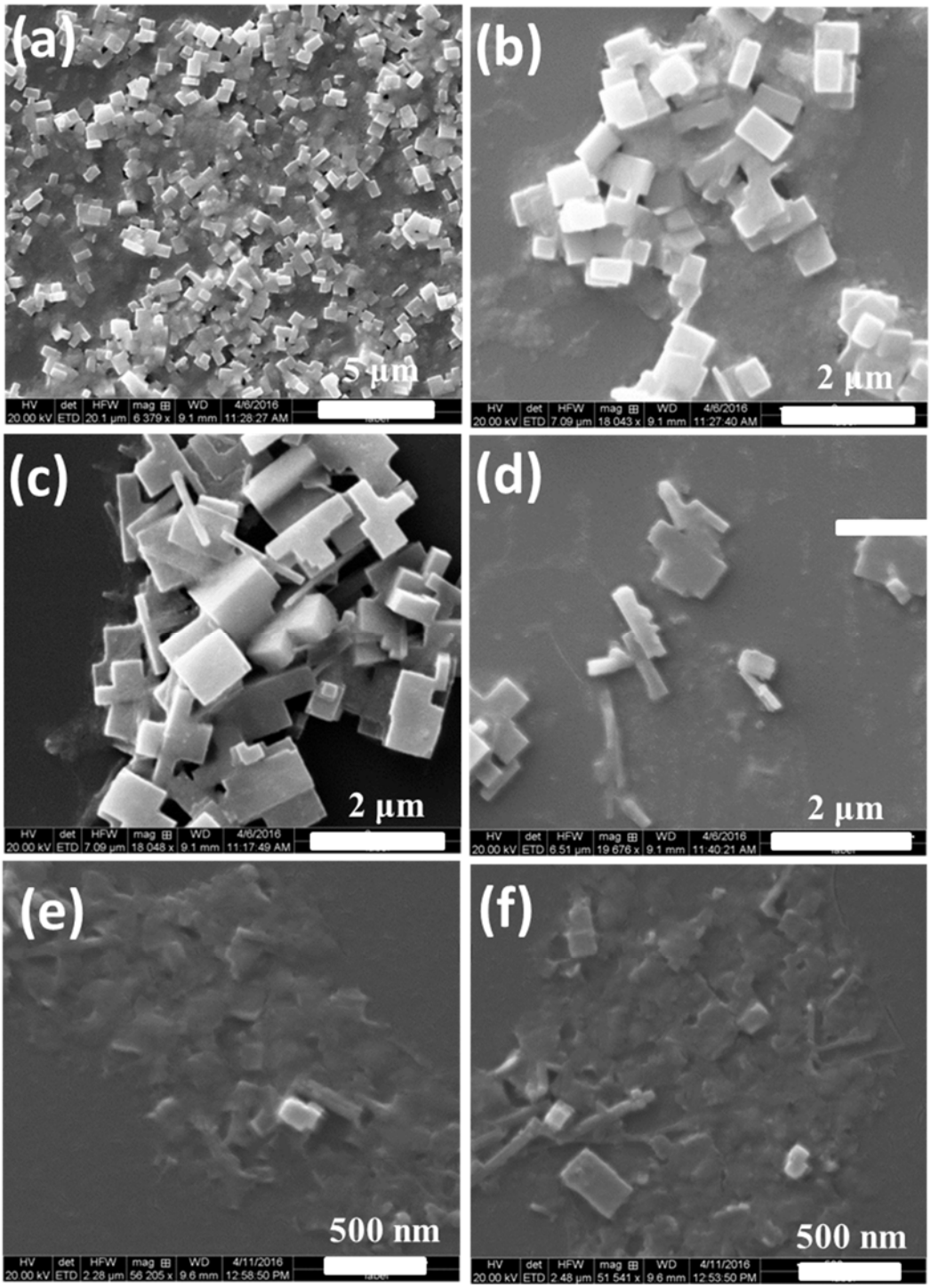

Figure A. 3 SEM images of perovskite $MAPbBr_3$ nanoplatelets obtained at different ratios of the capping ligand C8 OA, MA:OA = 1:*x* where a, b) *x* = 0.5; c, d) *x* = 1; and e, f) *x* = 2.

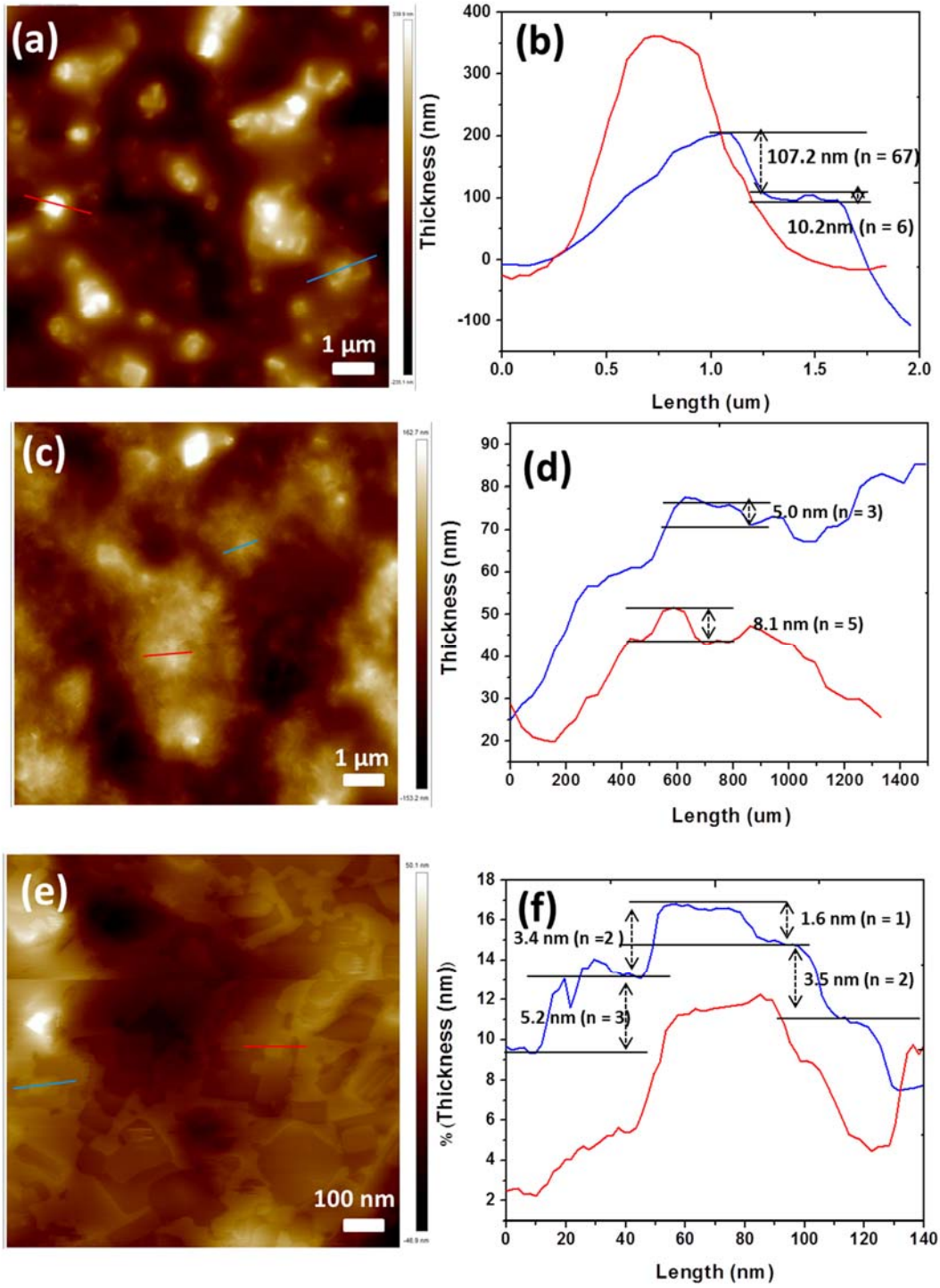

Figure A. 4 AFM topography images (left) and height profiles (right) measured for nanoplatelets obtained using the capping ligand C8 OA at different concentrations MA:OA 1:*x*: (a), (b) *x* = 1; (c), (d) *x* = 2; (e), (f) *x* = 4

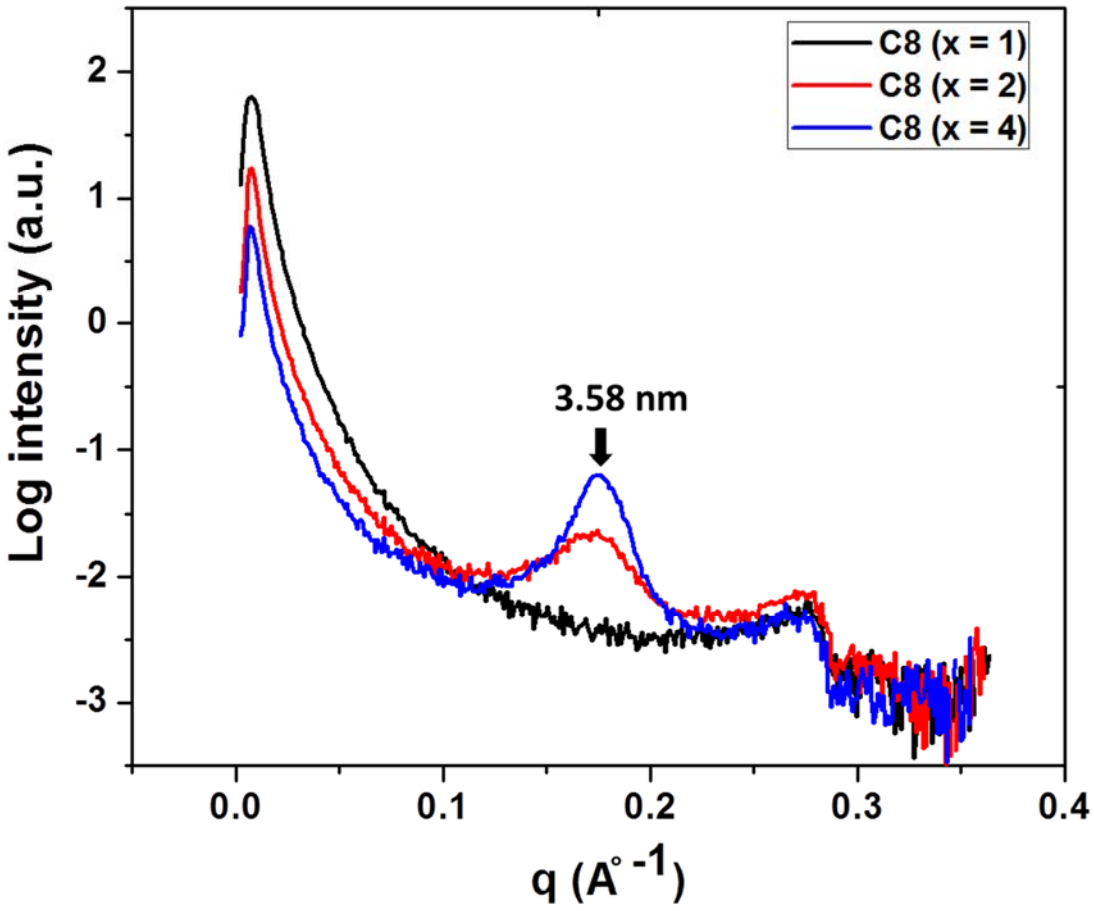

Figure A. 5 SAXS data acquired for perovskite nanoplatelets prepared using C8 OA surface binding ligands at different relative concentrations (MA: OA = 1:*x*); black (*x* = 1), red (*x* = 2), and blue (*x* = 4).

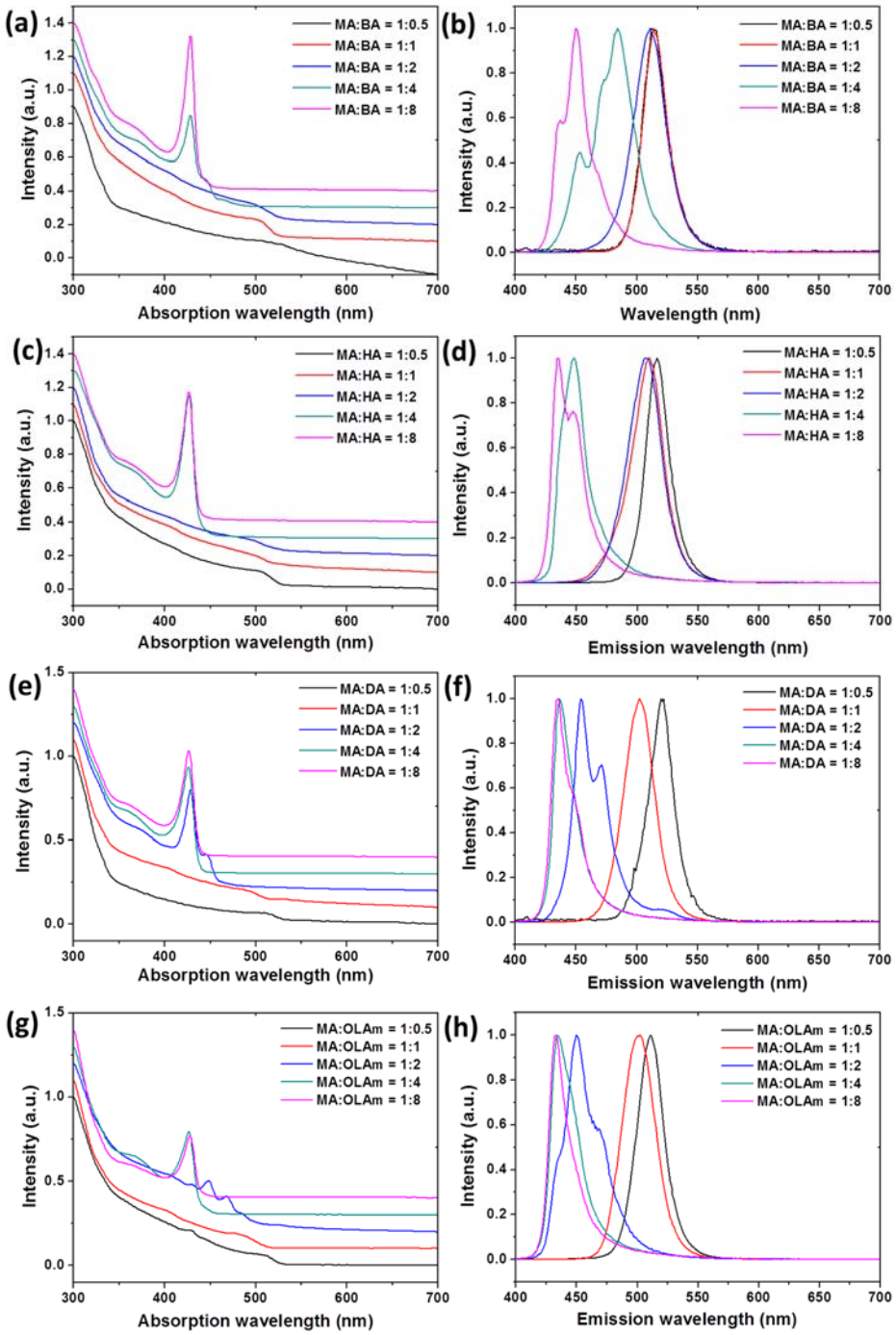

Figure A. 6 UV-visible absorption and photoluminescence emission spectra of 2D perovskite nanoplatelets prepared at varying MA:RA ratios using different alkylammonium groups: a,b) BA C4; c,d) HA C6; e,f) DA C12; and g,h) OLAm C18.

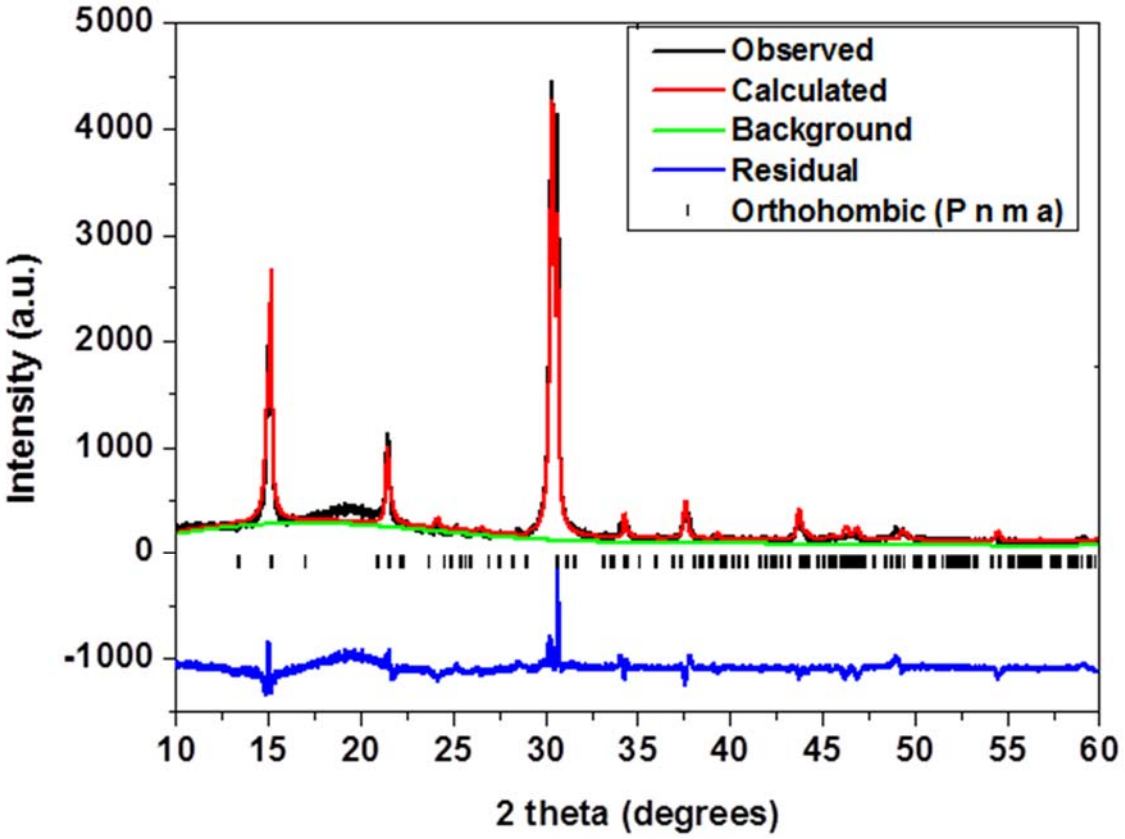

Figure A. 7 Rietveld refinement of powder XRD pattern of $CsPbBr_3$ nanoplatelets obtained using C8 at 150°; tick marks indicate the position of Bragg reflections corresponding to the *Pnma* orthohombic space group of $CsPbBr_3$.

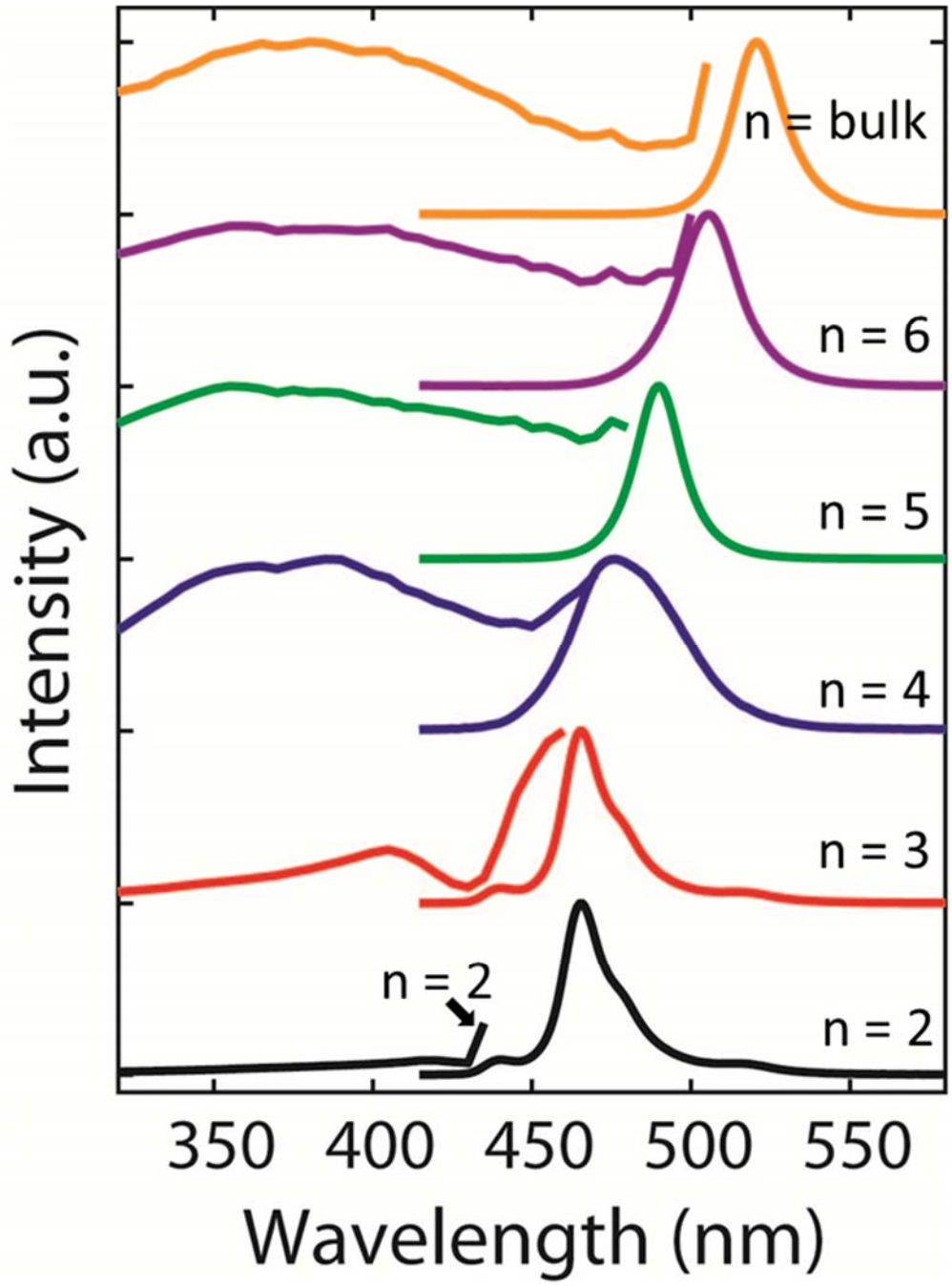

Figure A. 8 PL excitation spectra along with emission spectra for $CsPbBr_3$ nanoplatelets with different layer thickness (n = 2, 3, 4, 5, 6, and bulk): n = 2 and n = 3 nanoplatelets are obtained from dispersions prepared using C12 amine at 100°C; n = 4 and n =5 nanoplatelets are isolated from dispersions prepared using C12 amine at 150°C; and n = 6 and n = bulk nanoplatelets are isolated from samples prepared using C8 amine at 100°C.

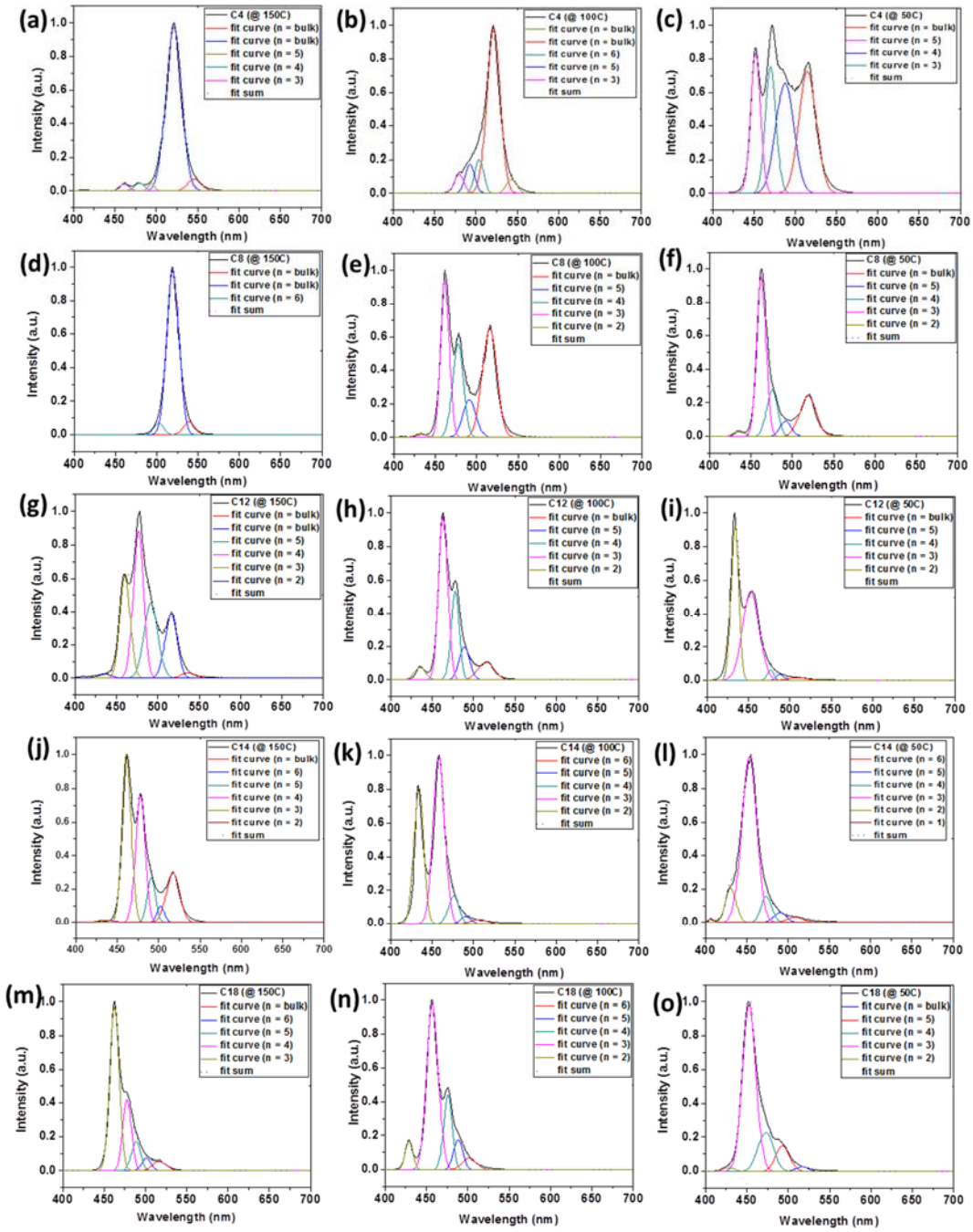

Figure A. 9 Deconvolution of ensemble PL emission spectra of $CsPbBr_3$ nanoplatelets to contributions from nanoplatelets of different layer thicknesses exemplified for spectra collected for nanoplatelets prepared using C4—C18 alkylamine ligands at 100°C. In each case, the spectra have been fitted to Gaussian peaks derived from n = 1, 2, 3, 4, 5, 6, and bulk species. The spectra correspond to nanoplatelets prepared at 150 (left), 100 (middle), and 50°C (right column) using (a-c) C4, (d-f) C8, (g-i) C12, (j-l) C14, and (m-o) C18.

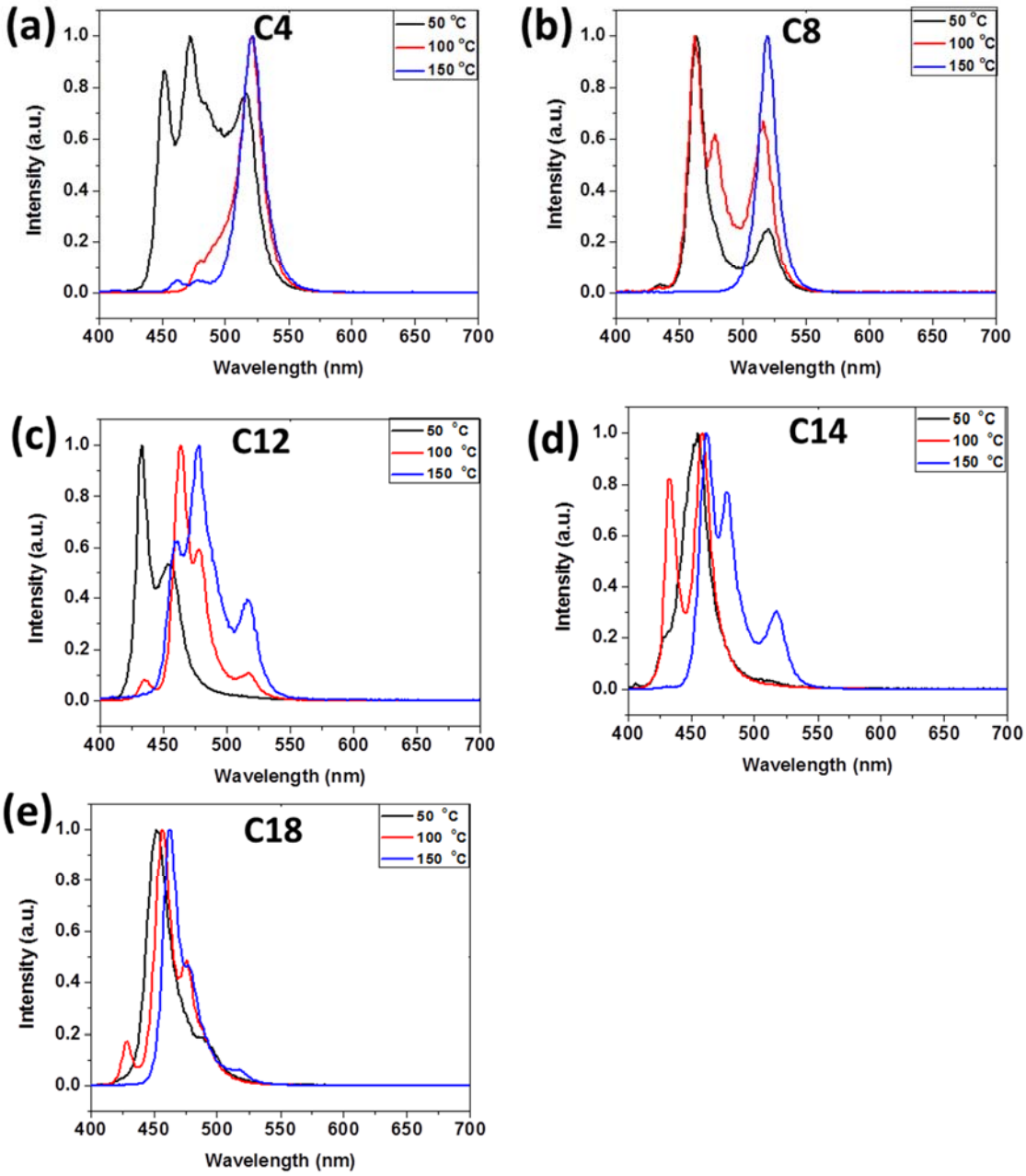

Figure A. 10 PL emission spectra of of $CsPbBr_3$ nanoplatelets plotted as a function of temperature for nanoplatelets obtained using (a) C4, (b) C8, (c) C12, (d) C14, and (e) C18 alkylamine ligands.

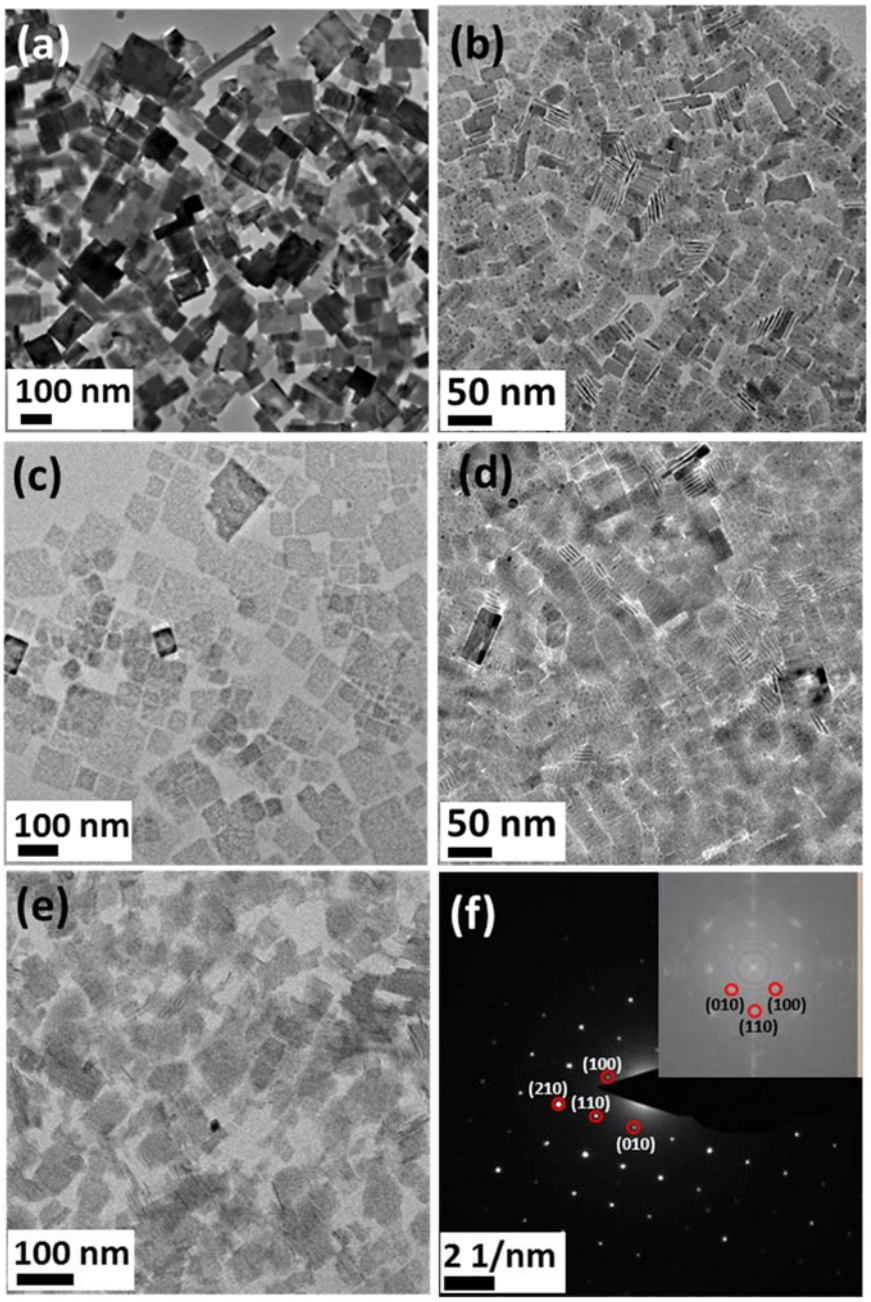

Figure A. 11 TEM images of $CsPbBr_3$ nanoplatelets prepared at 100°C using different alkylammonium chain-lengths of a) C4, b) C8, c) C12, d) C14, and e) C18. f) Selected area electron diffraction and its fast Fourier transform acquired for an individual $CsPbBr_3$ nanoplatelet prepared using a C4 amine.

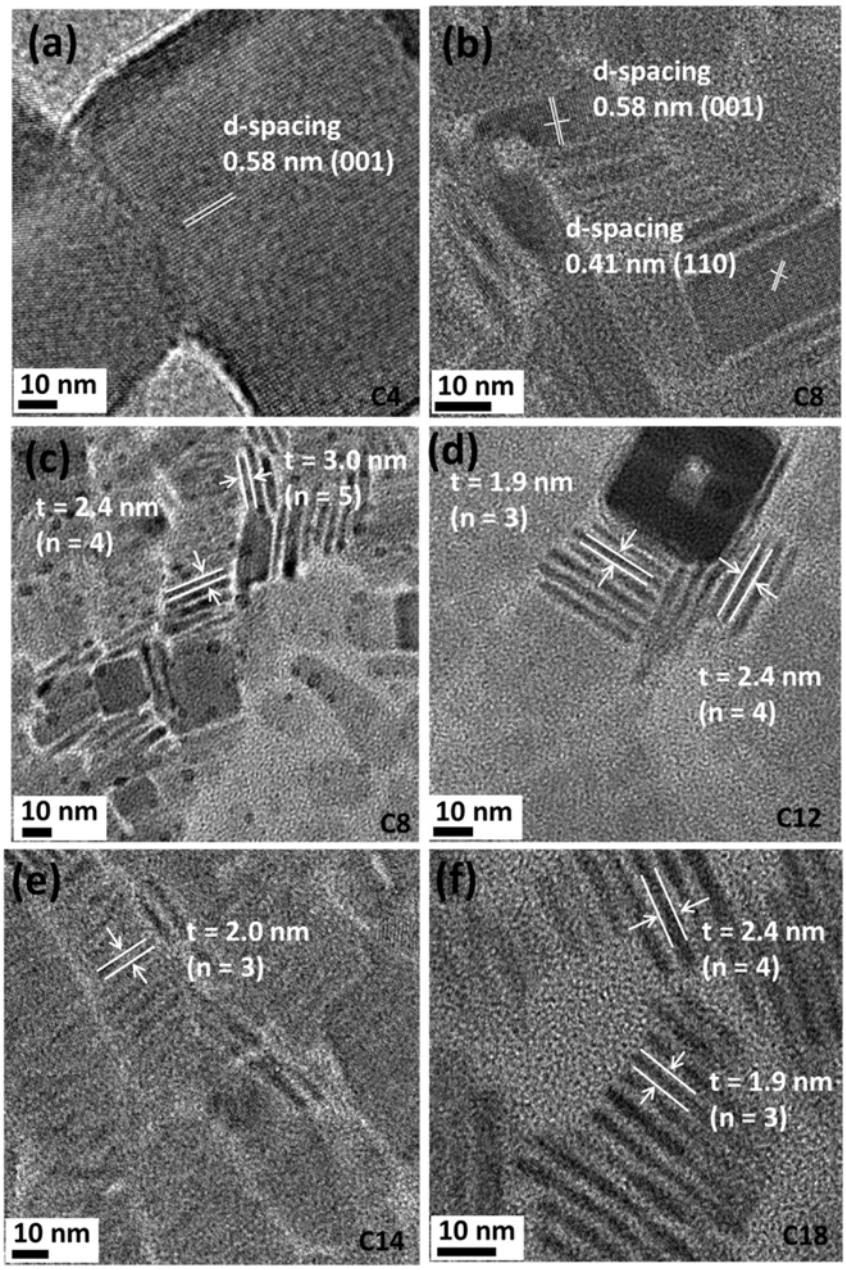

Figure A. 12 High-resolution TEM images of $CsPbBr_3$ nanoplatelets obtained using different chain-lengths of ligands and representative measurements of the thickness spans of nanoplatelets. The images correspond to $CsPbBr_3$ nanoplatelets prepared using: a) C4; b,c) C8, d) C12, e) C14, and f) C18.

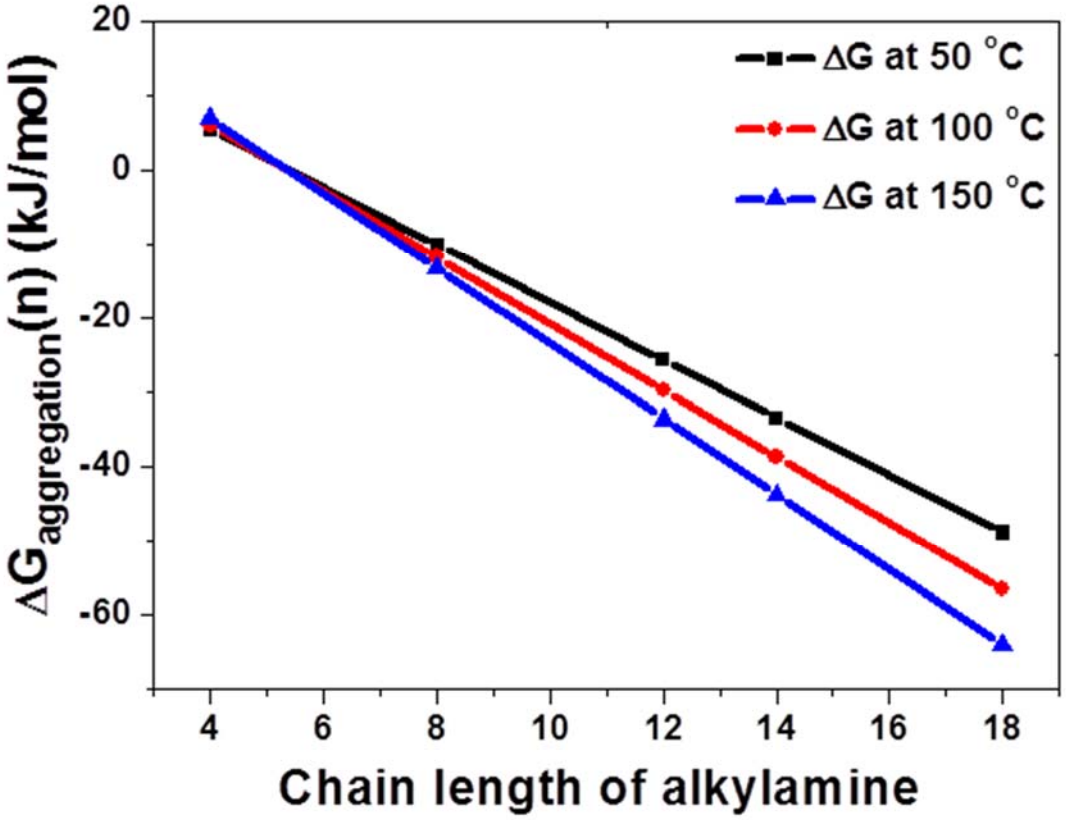

Figure A. 13 Gibbs free energy of aggregation of ligand packing as a function of chain-length at different reaction temperatures.

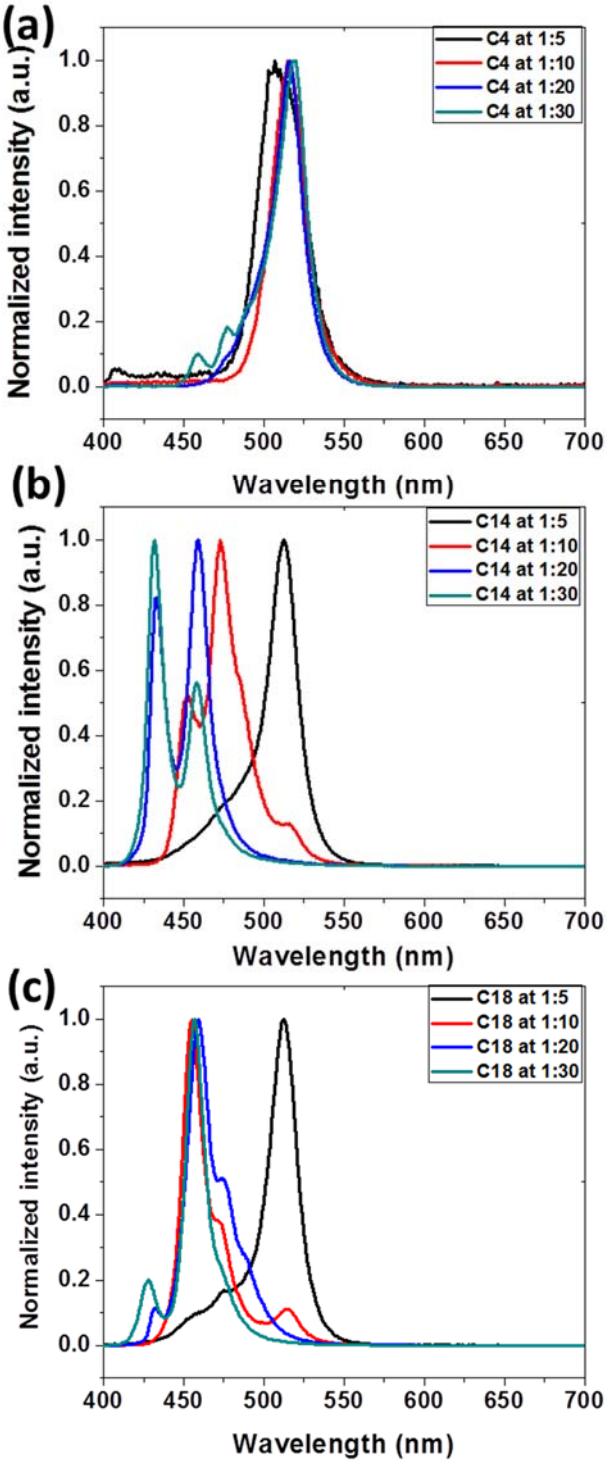

Figure A. 14 PL emission spectra of $CsPbBr_3$ nanoplatelets plotted as a function of ligand concentration (Pb-OA:RA=1:5—1:30) for nanoplatelets obtained using (a) C4, (b) C14, and (c) C18 at 100 °C.

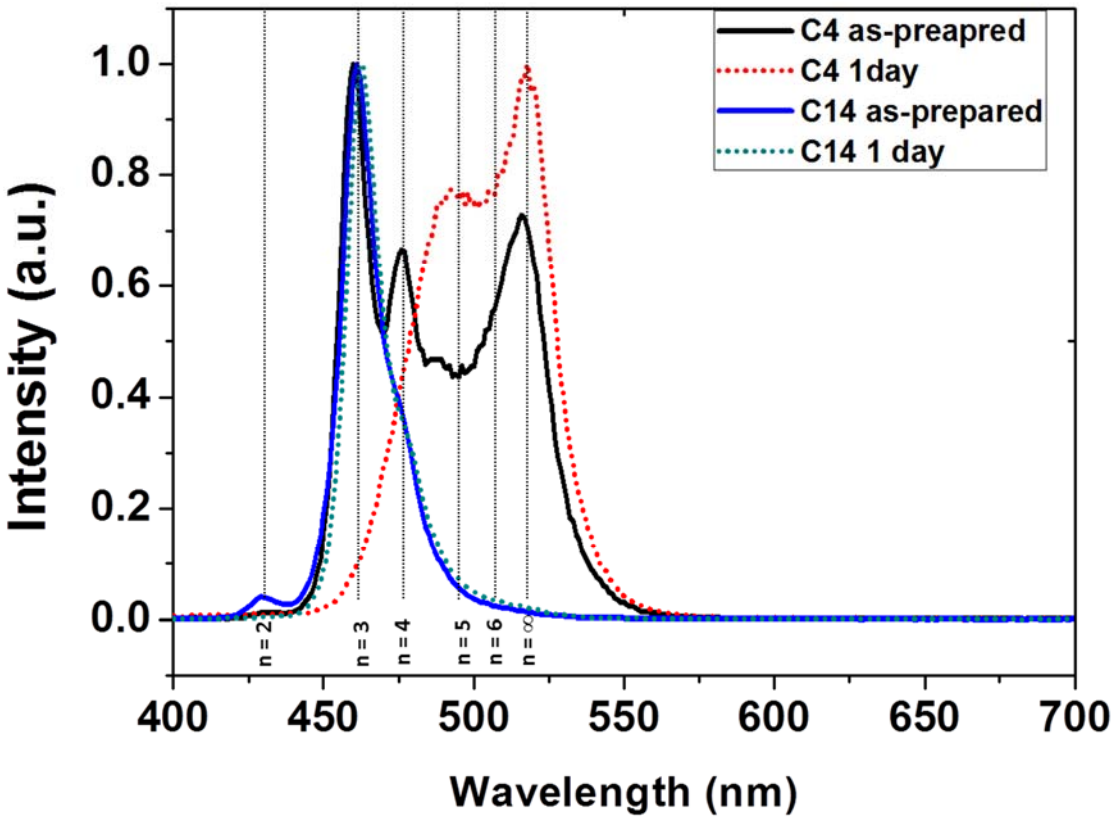

Figure A. 15 PL emission spectra of $CsPbBr_3$ nanoplatelets obtained immediately after synthesis (solid line) and after 1 day (dotted line) using C4 at 50°C and C14 at 80°C.

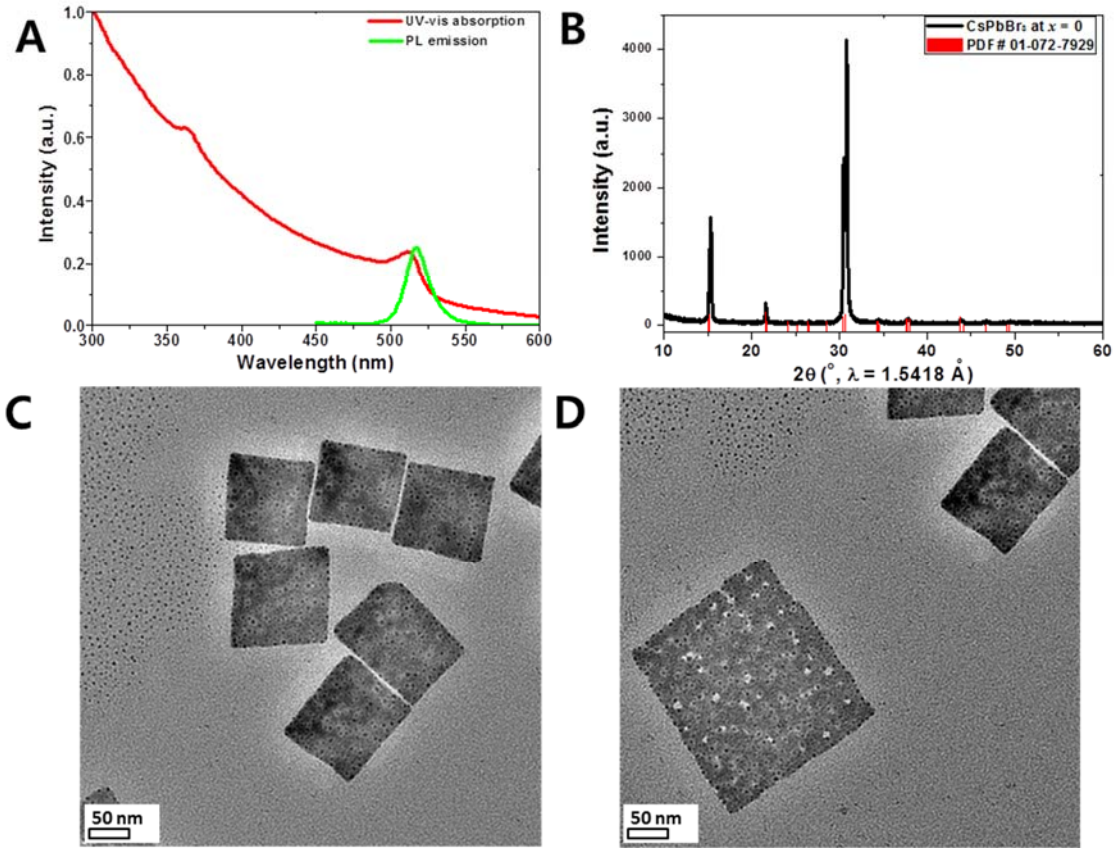

Figure A. 16 A) UV-vis absorption (red line) and PL emission spectrum (green line) ($\lambda_{ex.}$ = 360 nm), (B) XRD pattern, and C,D) TEM images of submicron-sized $CsPbBr_3$ particles stabilized in the absence of alkylamine ligands, corresponding to the x = 0 reaction as per the nomenclature noted in the text.

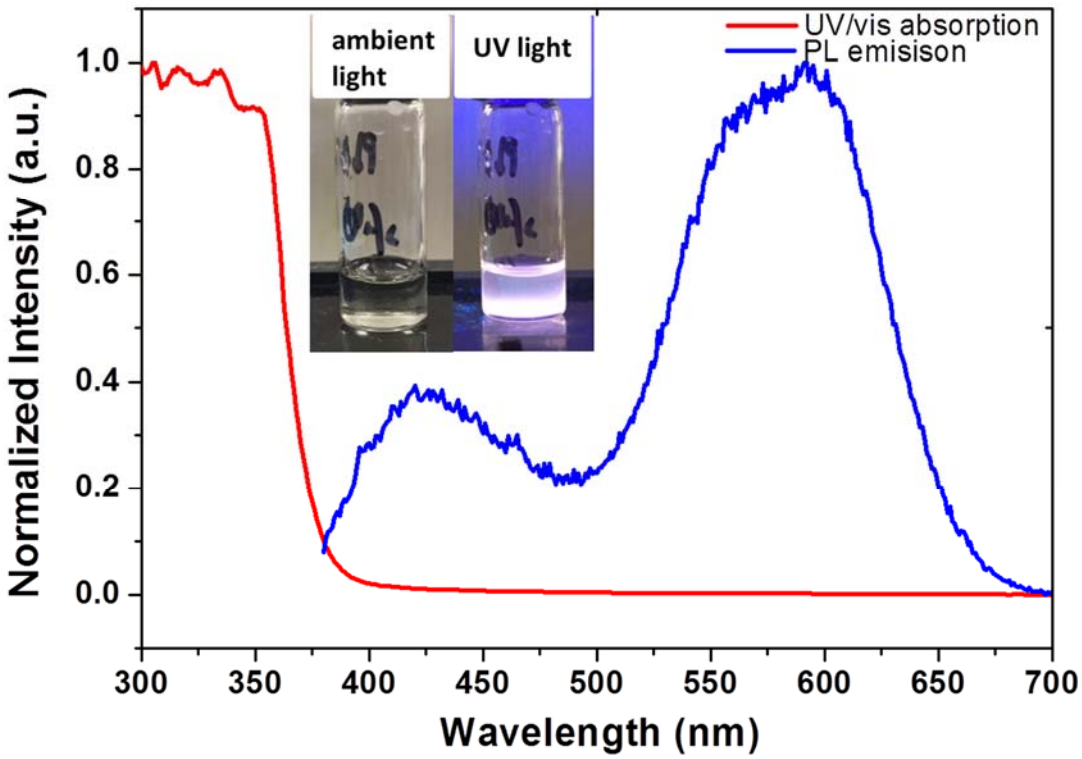

Figure A. 17 UV/Vis absorption and PL emission spectra for $PbBr_2$ complex with OA in DMF. The inset indicates digital photographs of the solution taken under ambient light (left) and 365 nm UV illumination (right).

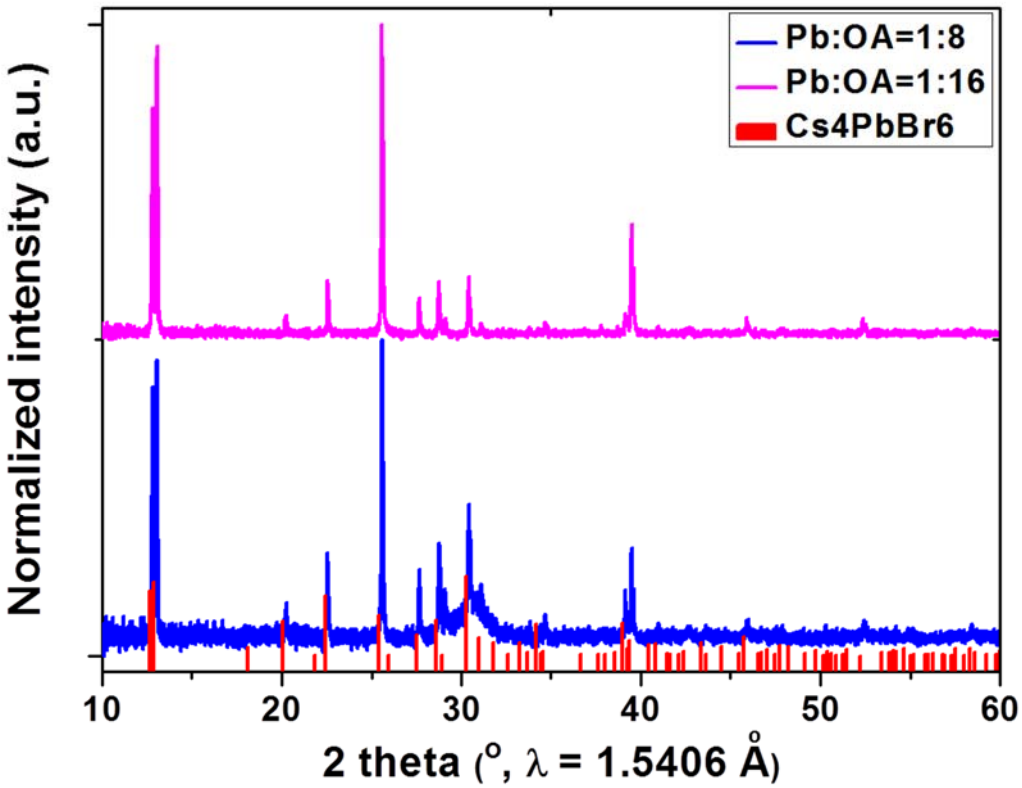

Figure A. 18 XRD patterns of cesium lead bromide samples acquired at OA concentration x = 8 and 16 after 24 h. The red tick mark correspond to reflections from rhombohedral Cs_4PbBr_6 (PDF# 01-073-2478).

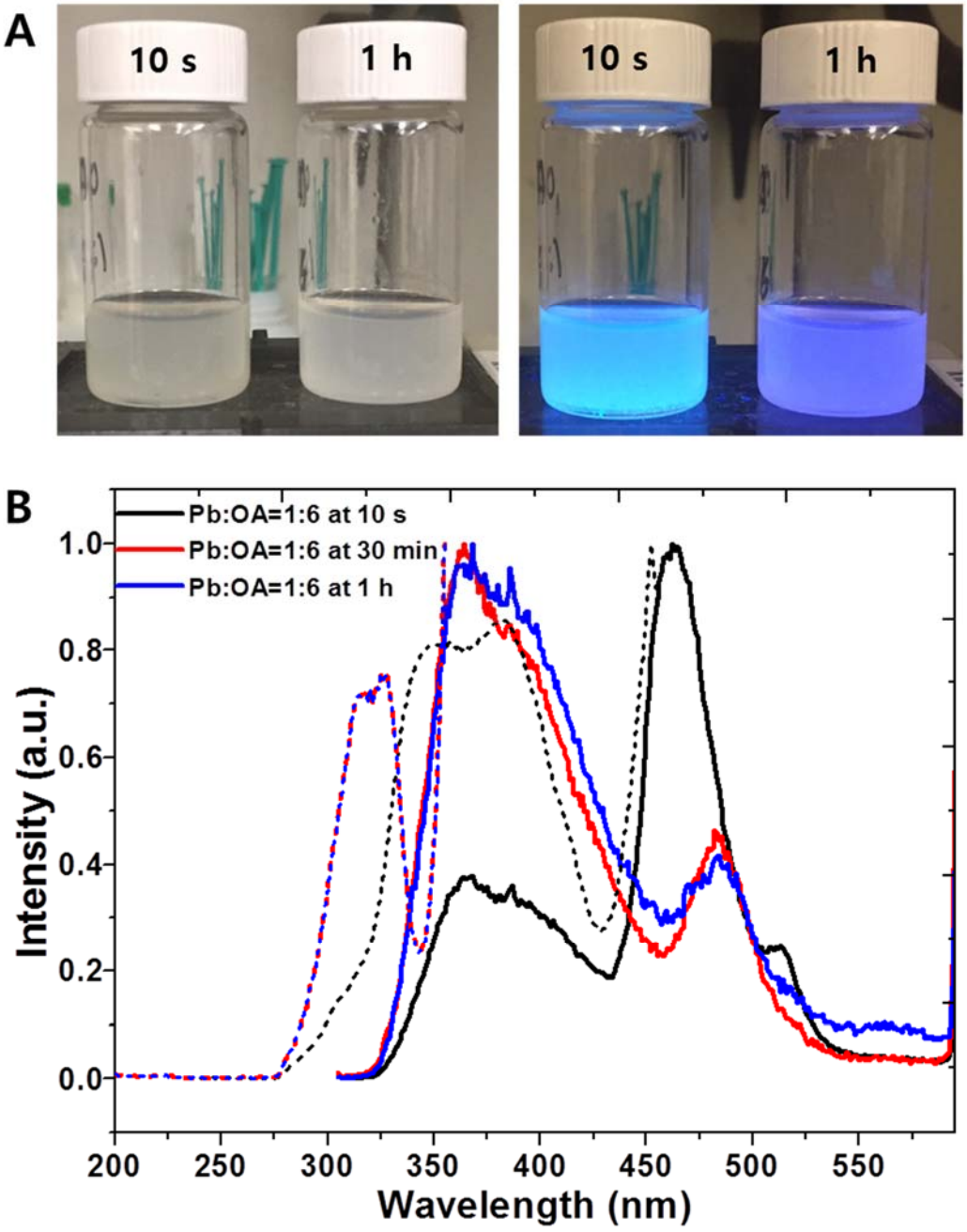

Figure A. 19 (A) Digital photographs of colloidal dispersions of cesium lead bromide nanocrystals immediately upon mixing (at ca. 10 s) and 1 h after mixing under ambient laboratory light (left) and upon 365 nm UV illumination (right); (B) time-course PL emission (solid line) and excitation (dotted line) spectra acquired after 10 s, 30 min, and 1 h of adding the precursor DMF solution to toluene.

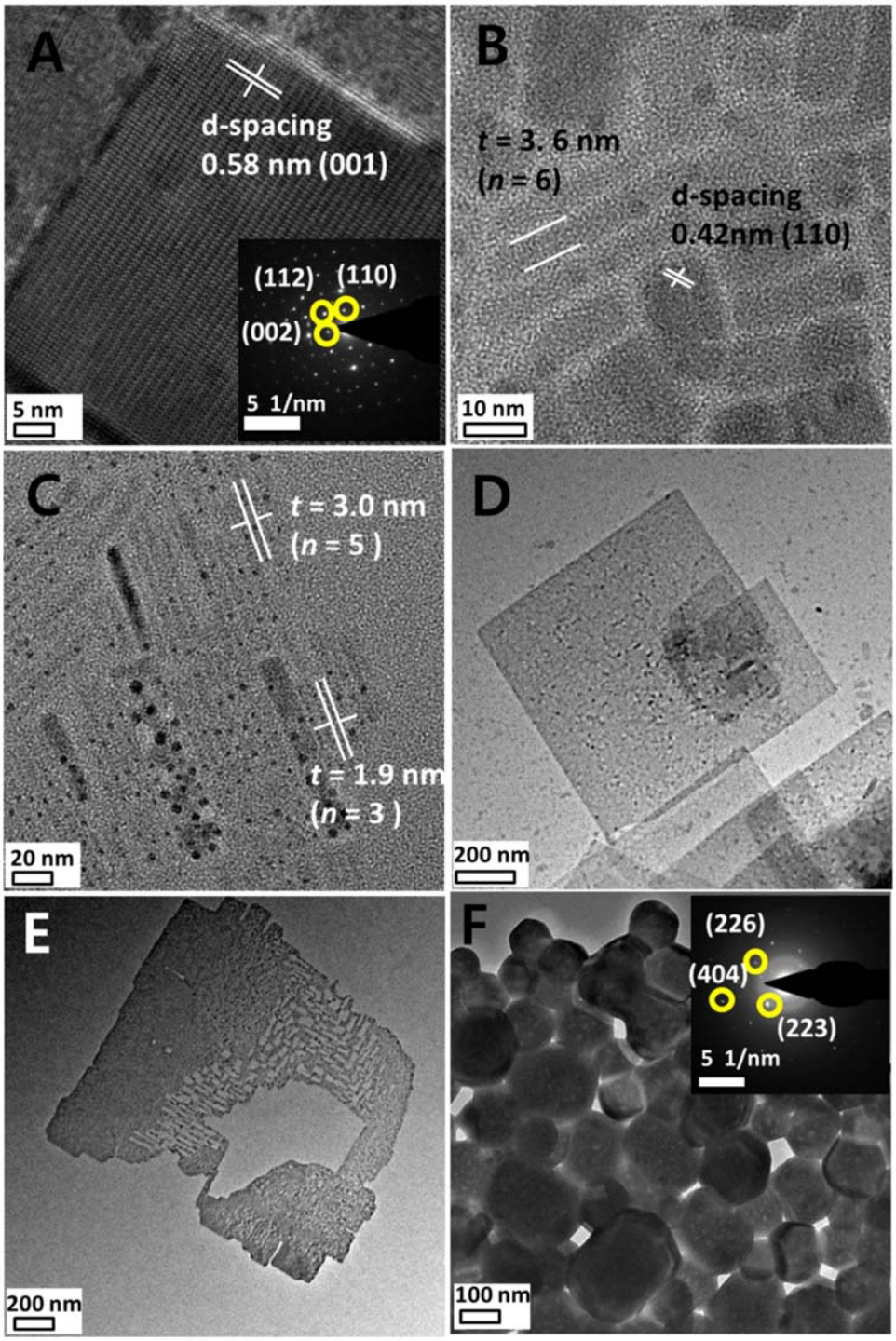

Figure A. 20 TEM images of cesium lead bromide nanocrystals obtained as a function of increasing OA concentration (x): (A) x = 0.5; (B) x = 1; (C) x = 2; (D) x = 4; (E) x = 6; and (F) x = 8. The insets of Figure A. 20A and F show SAED patterns acquired for the imaged $CsPbBr_3$ and Cs_4PbBr_6 nanocrystals, respectively.

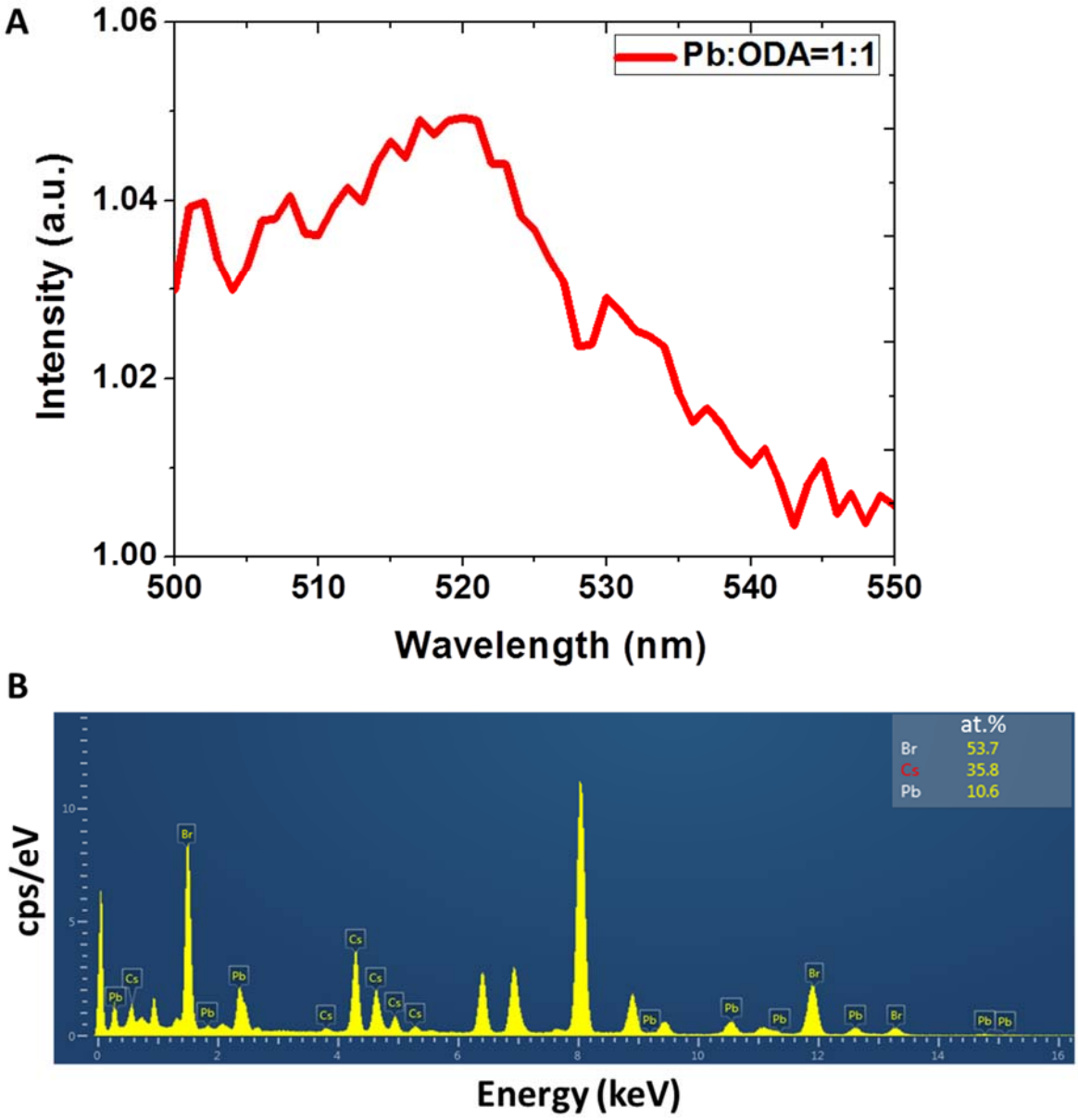

Figure A. 21 (A) PL emission spectrum of nanocrystals obtained at an ODA concentrations of $x = 1$ and (B) energy dispersive X-ray spectra (EDS) of the nanocrystals obtained at an ODA concentration of $x = 2$.

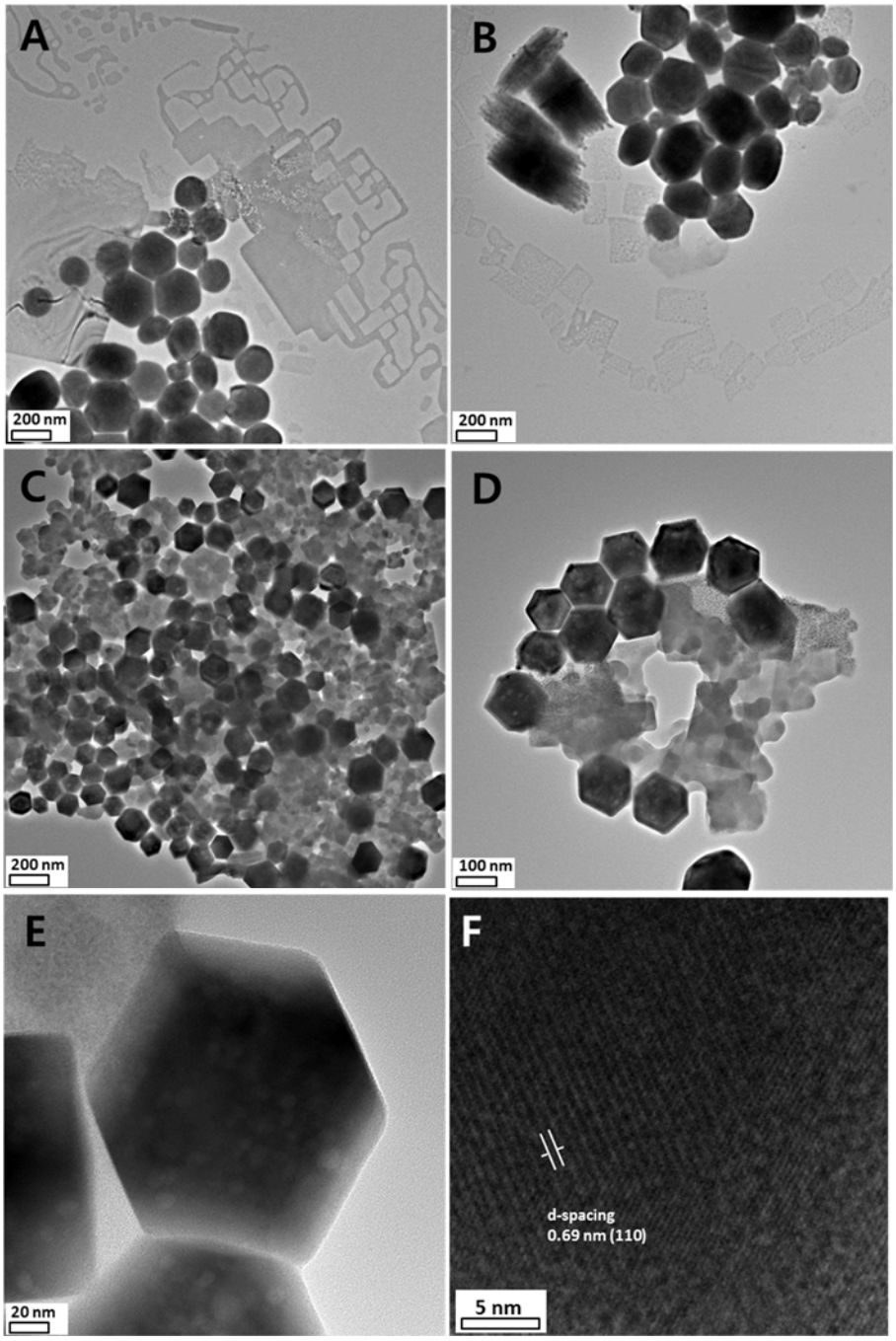

Figure A. 22 TEM images of cesium lead bromide perovskite nanocrystals obtained at different ODA concentrations: (A, B) x = 1 and (C—F) x = 2. Figure A. 22F shows a lattice spacing of 0.69 nm, corresponding to the separation between the (110) planes of Cs_4PbBr_6.

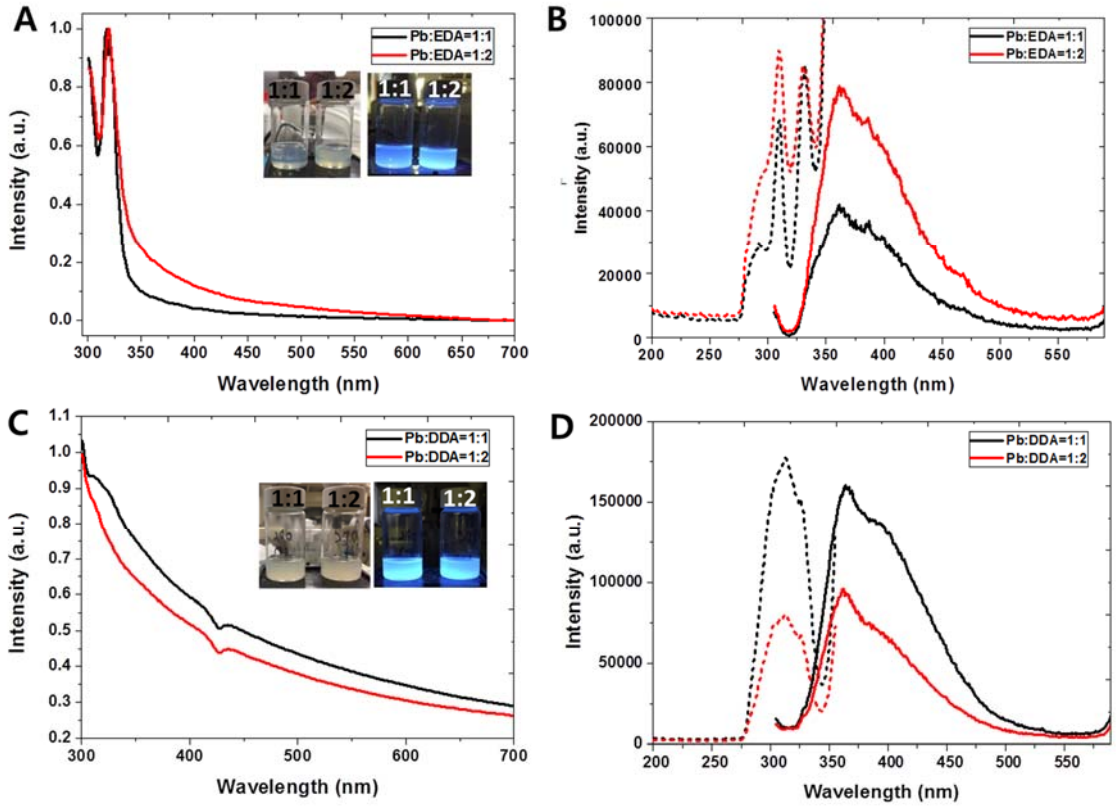

Figure A. 23 (A) UV-vis absorption spectra and (B) PL emission (solid line) and excitation spectra of Cs_4PbBr_6 nanocrystals stabilized at EDA concentrations of x = 1 and 2; (C) UV-vis absorption spectra and (D) PL emission (solid line) and excitation spectra of Cs_4PbBr_6 nanocrystals stabilized at DDA concentration of x = 1 and 2. The insets to Figures A21.A and C show digital photographs of colloidal dispersions of Cs_4PbBr_6 nanocrystals taken under ambient laboratory light (left) and 365 nm UV illumination.

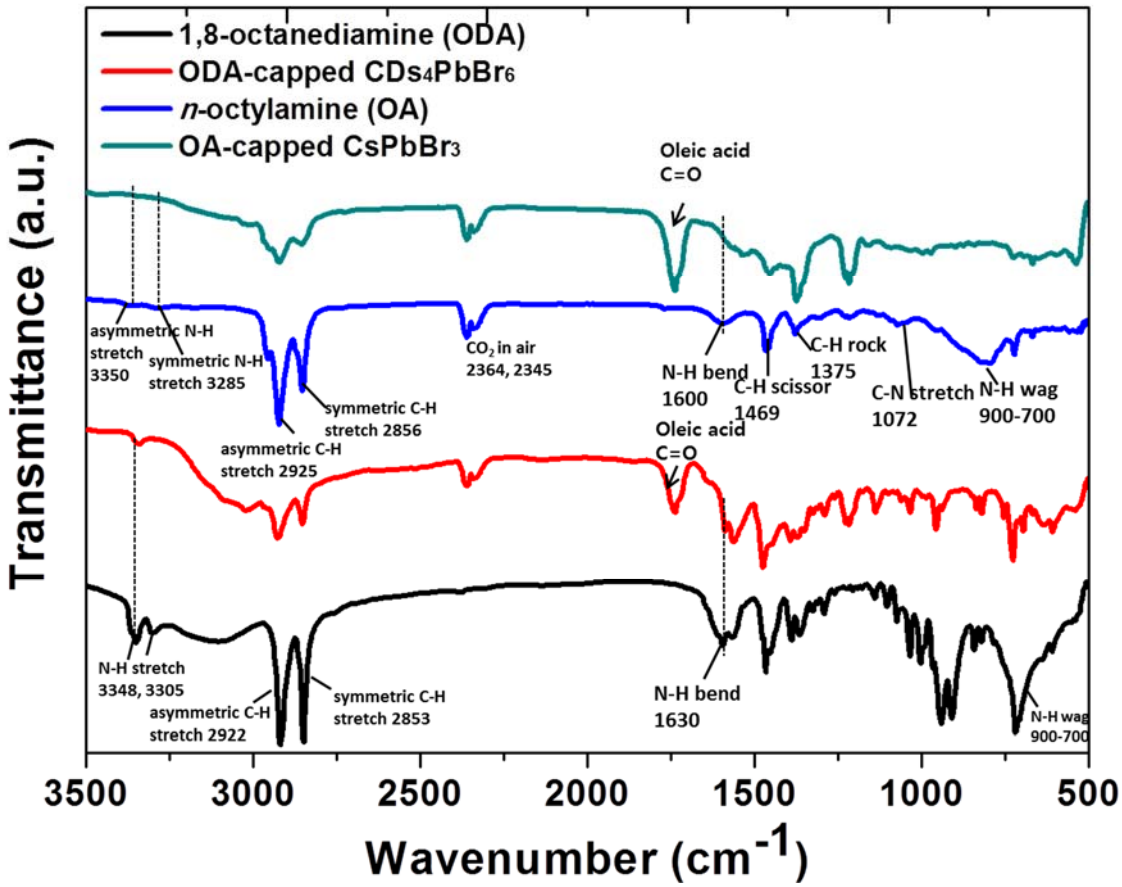

Figure A. 24 FTIR spectra of OA (olive), OA-capped $CsPbBr_3$ (navy blue), ODA (blue), and ODA-capped Cs_4PbBr_6 (magenta). The nanocrystal samples correspond to fixed ligand concentrations of $x = 2$. The relative intensity of the N-H stretching and bending vibration is increased upon changing from the monodentate alkylamine (OA) to the bidentate amine (ODA).

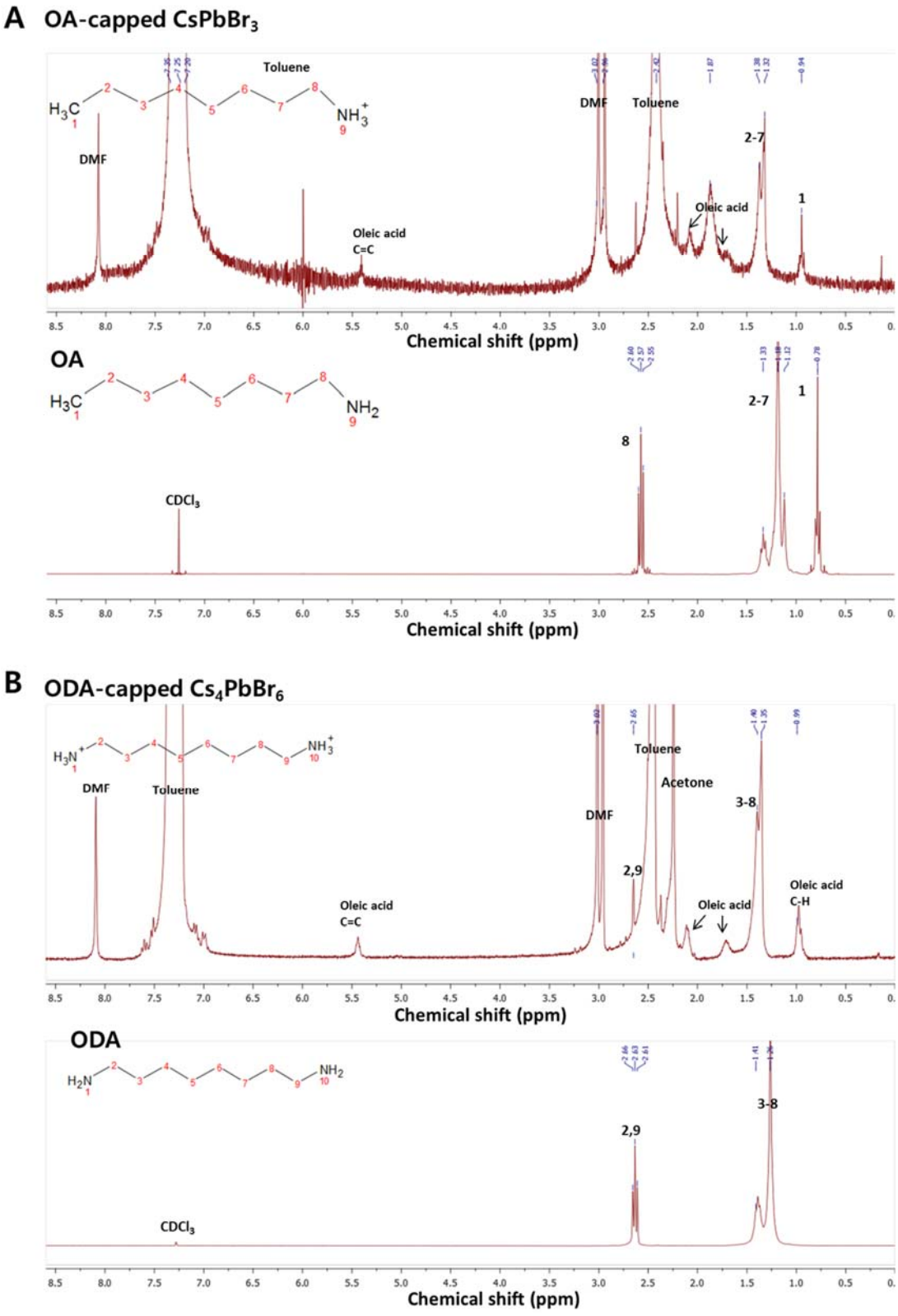
A
OA-capped CsPbBr3
Toluene
DMF
Oleic acid
C=C
Toluene
2-7
1
Oleic acid
Chemical shift (ppm)
OA
8
2-7
1
CDCl3
Chemical shift (ppm)
B
ODA-capped Cs4PbBr6
DMF
Toluene
Oleic acid
C=C
DMF
Toluene
Acetone
3-8
2,9
Oleic acid
Oleic acid
C-H
Chemical shift (ppm)
ODA
2,9
3-8
CDCl3
Chemical shift (ppm)

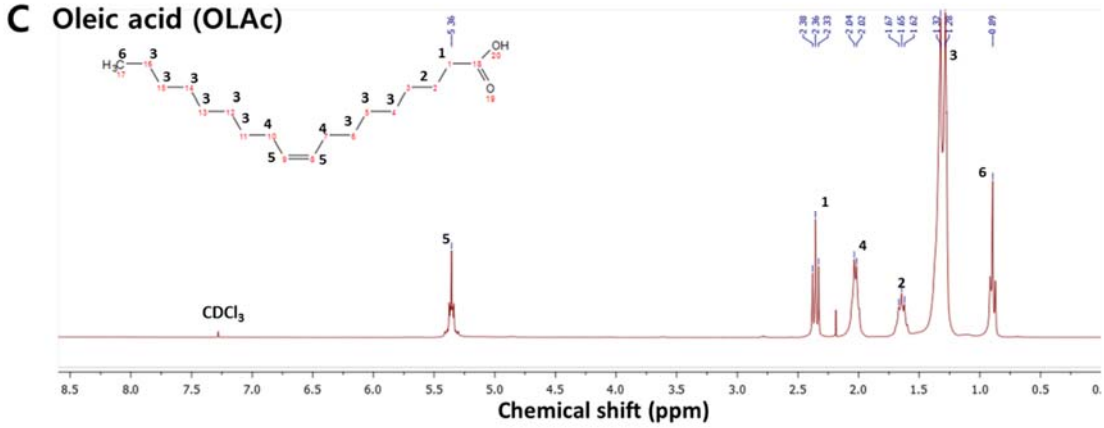

Figure A. 25 ^{1}H NMR spectra of (A) OA-capped $CsPbBr_3$ (top) and OA (bottom); (B) ODA-capped Cs_4PbBr_6 (top) and ODA (bottom); and (C) oleic acid (OLAc). The insets to Figures S7A—C indicate the molecular structures of OA, ODA, and OLAc, respectively.

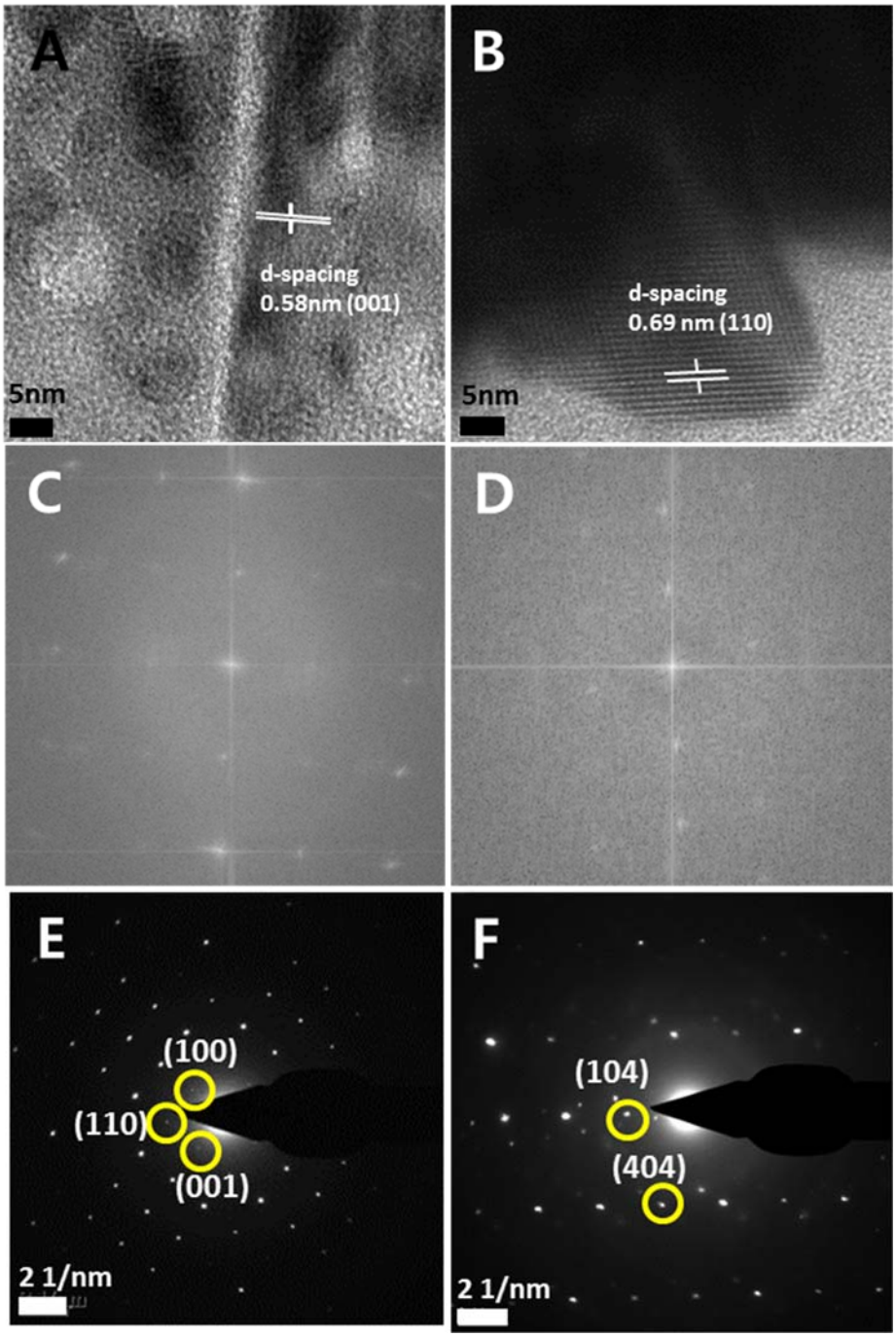

Figure A. 26 (A,B) High-resolution TEM image, (C,D) corresponding fast Fourier transform patterns, and (D,E) SAED patterns acquired for $CsPbBr_3$ nanoplatelets (A, C, E) and hexagonal Cs_4PbBr_6 platelets (B, D, F).

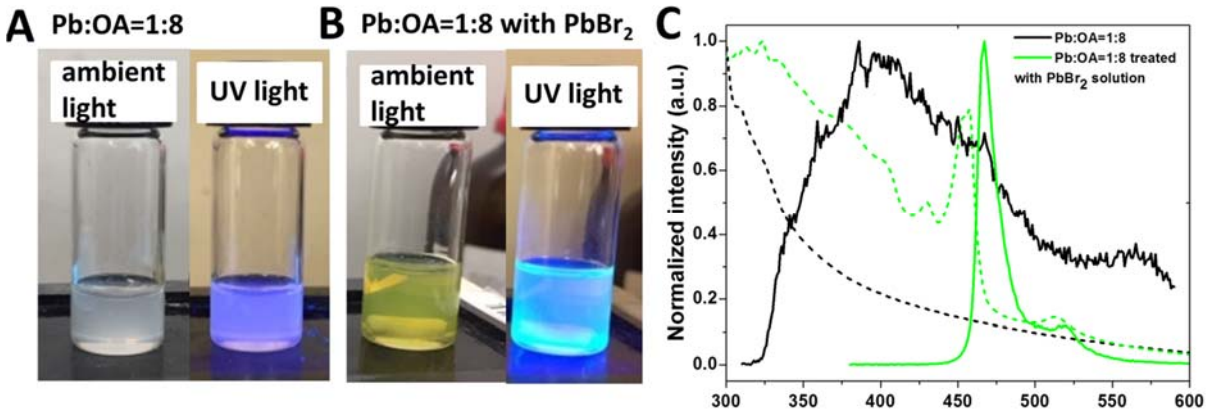

Figure A. 27 Digital photograph of lead halide perovskite nanocrystals prepared at an OA concentration of (A) $x = 8$ and (B) after treatment with $PbBr_2$ solution under ambient (left) and 365 nm UV illumination (right). (C) UV/vis (dotted line) and PL emission (solid) spectra of the colloidal nanocrystals before and after $PbBr_2$ treatment indicating recovery of the characteristic emission bands of $CsPbBr_3$ nanocrystals.

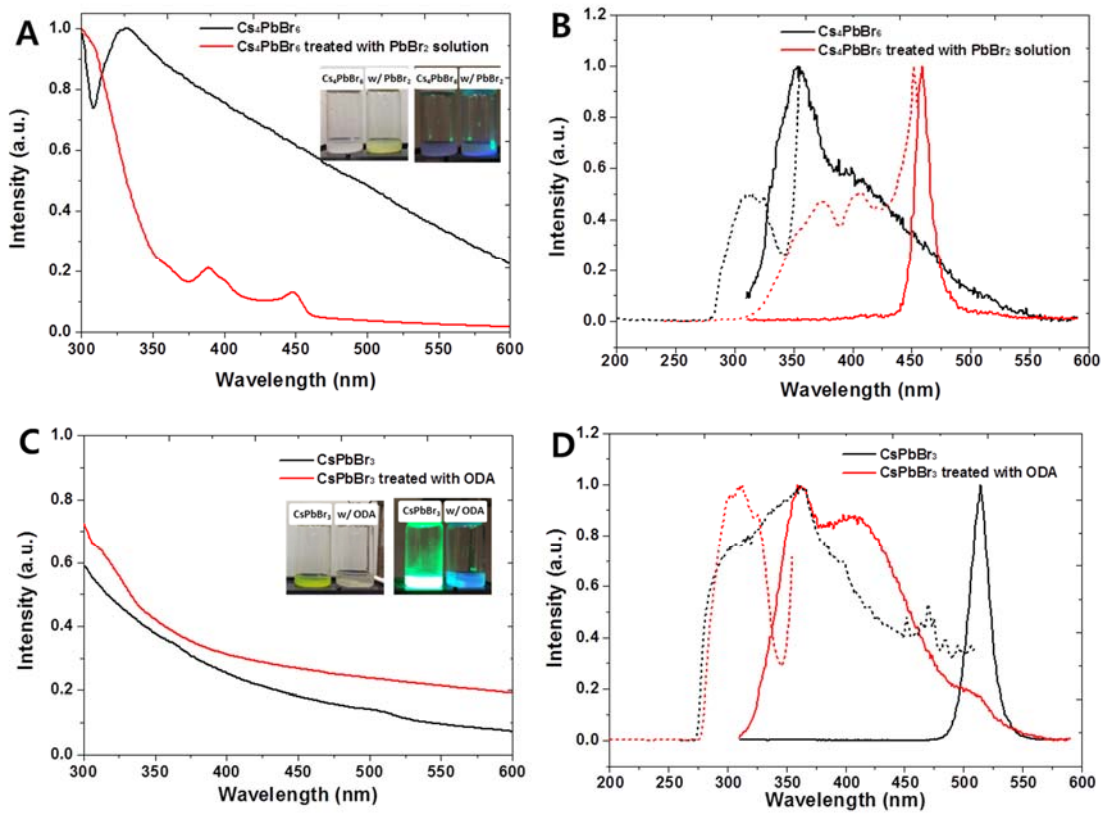

Figure A. 28 Reversible phase transformation from colloidal dispersion of $CsPbBr_3$ in toluene to Cs_4PbBr_6 and back to $CsPbBr_3$: A) UV-vis absorption spectra of Cs_4PbBr_6 and the Cs_4PbBr_6 after addition of $PbBr_2$ dissolved in OLAc and OLAm in toluene; the inset shows digital photographs taken under ambient laboratory light (left) and 365 nm UV illumination (right). (B) Corresponding PL emission (solid line) and excitation spectra (dotted line). (C) UV-vis absorption spectra of $CsPbBr_3$ nanocrystals and the $CsPbBr_3$ colloidal dispersion after reaction with ODA dissolved in OLAc; the inset shows digital photographs taken under ambient laboratory light (left) and 365 nm UV illumination (right). (D) Corresponding PL emission (solid line) and excitation spectra (dotted line).

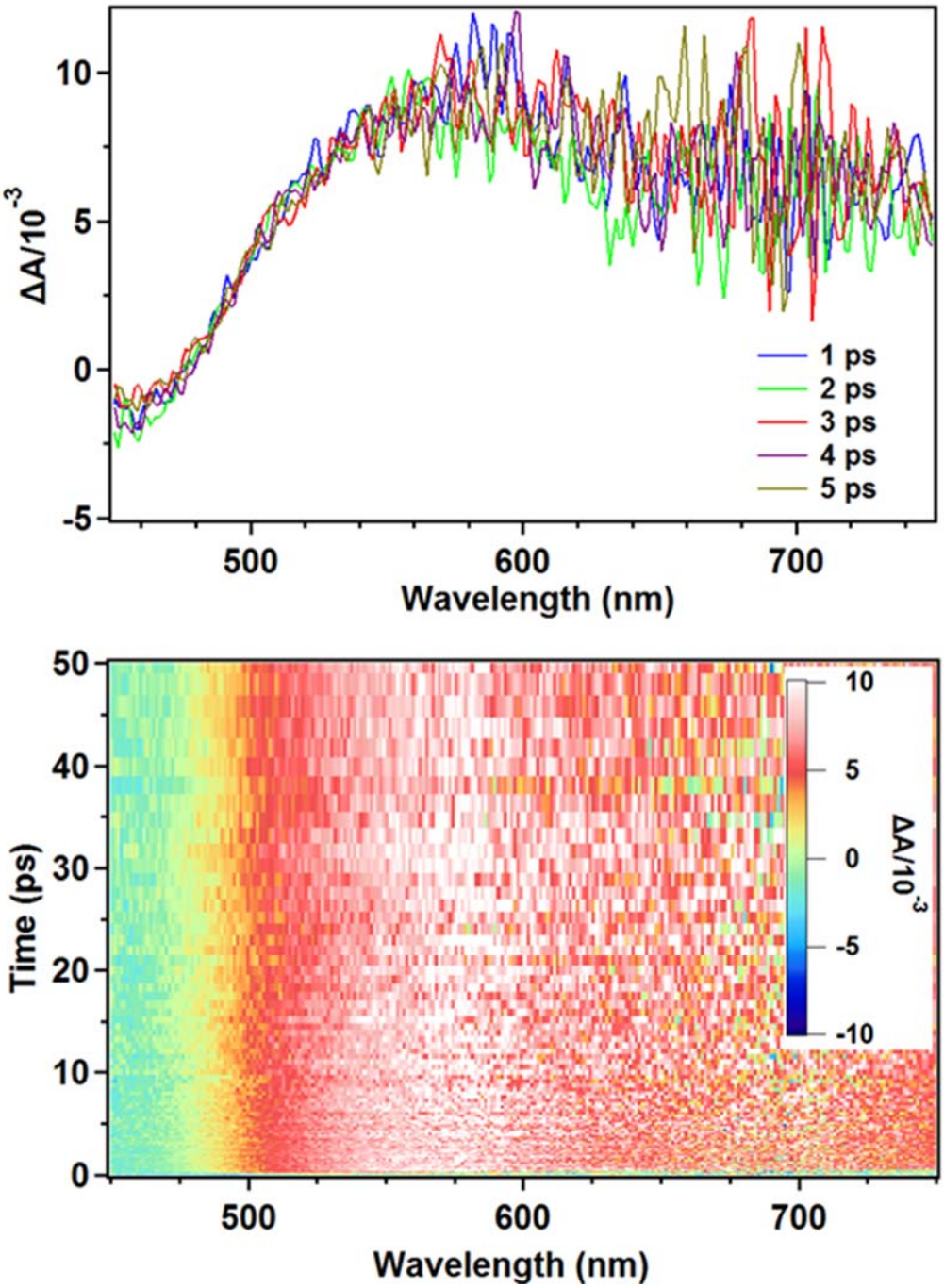

Figure A. 29 TA spectra of (top) bare β-$Pb_{0.33}V_2O_5$ NWs and (bottom) corresponding 3D color map illustrating the evolution of ΔA over a time interval of 0–50 ps as a function of the probe wavelength in the range of 425 – 850 nm (λ_{pump} = 360 nm).

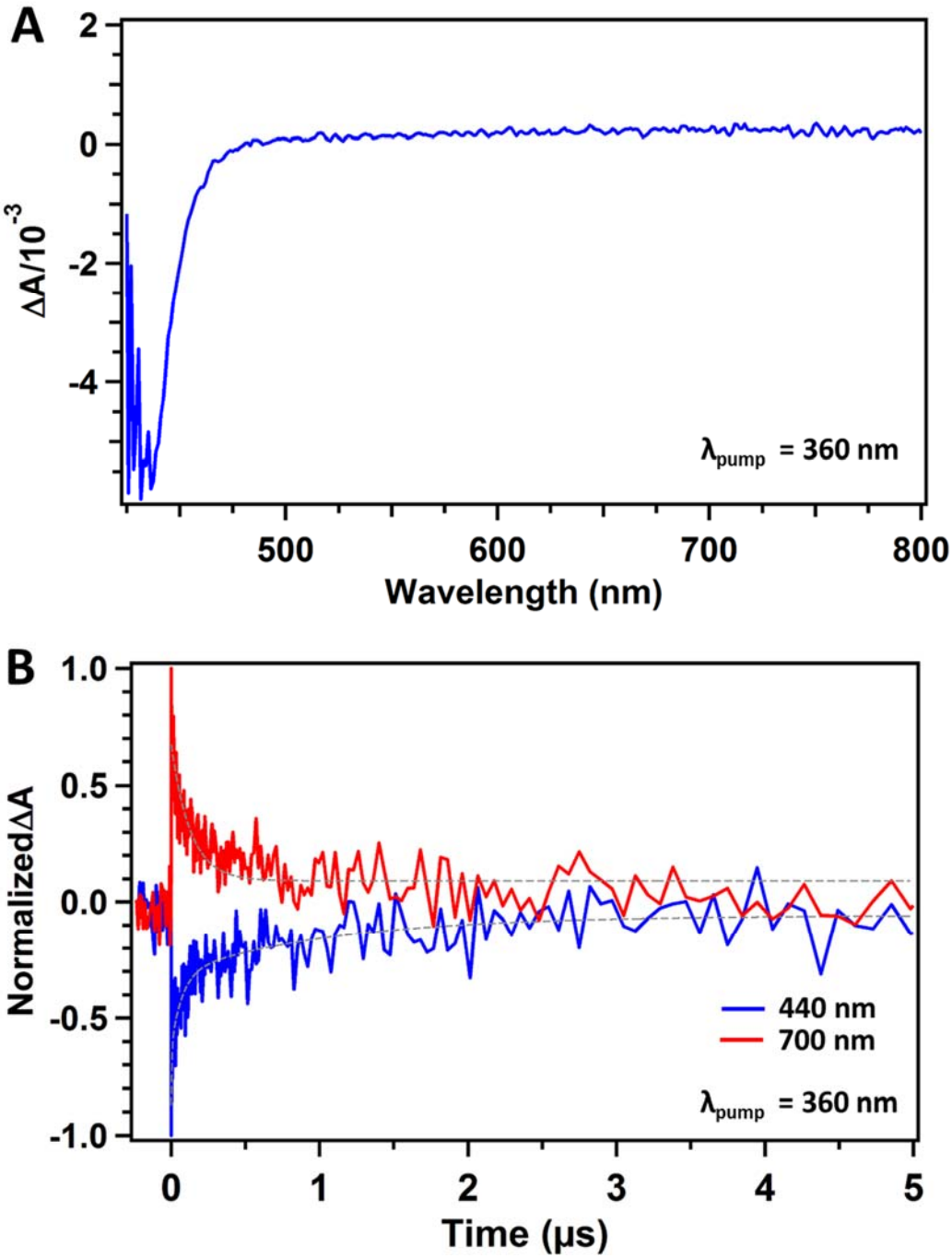

Figure A. 30 TA spectrum (A) of colloidal Cys-CdS QDs in aqueous dispersion averaged for delay times in the interval 0—10 ns; and (B) corresponding kinetic decay and biexponential fits obtained at probe wavelengths of 440 nm (blue) and 700 nm (red) with λ_{pump} = 360 nm.

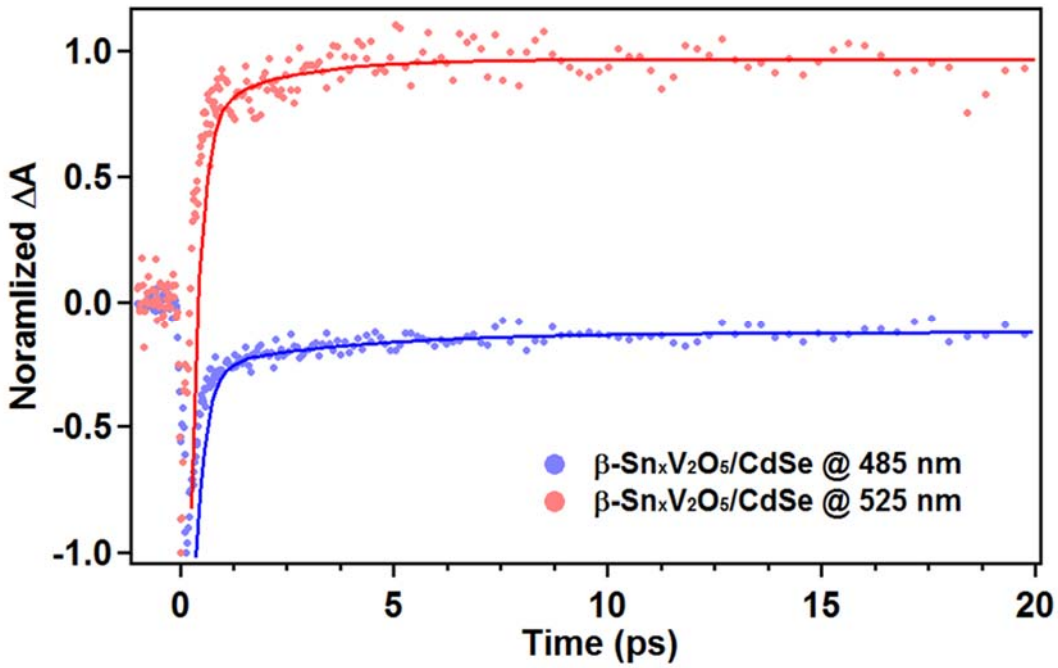

Figure A. 31 TA kinetic trace and multiexponential kinetic fitting for β-$Sn_xV_2O_5$/CdSe heterostructures at probe wavelength of 485 nm (only contribution from bleach feature of CdSe QDs) and 525 nm (contribution from both bleach feature of CdSe QDs and induced absorption of β-$Sn_xV_2O_5$ nanowires). The decay trace at the specific probe wavelength is marked as spread dots while the multiexponetial kinetic fit is indicated as a solid line.

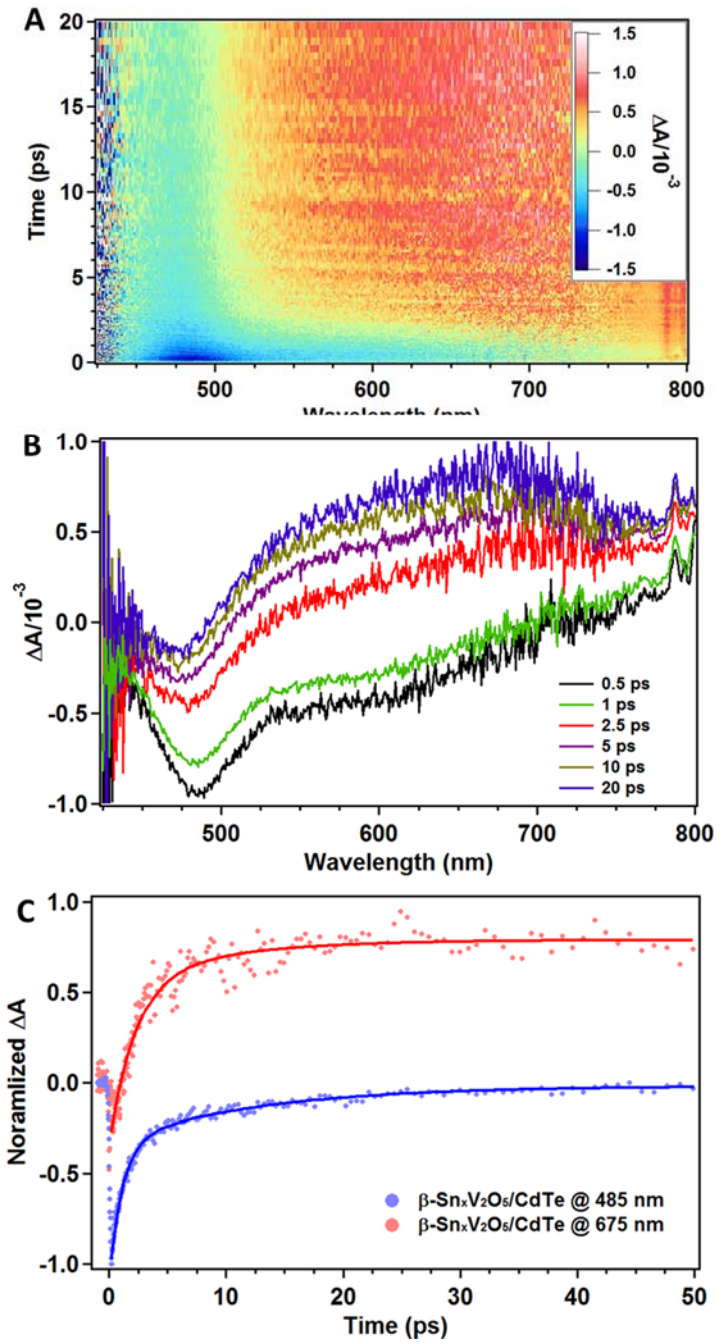

Figure A. 32 (A) TA 3D color map illustrating the evolution of difference spectra of β-$Sn_xV_2O_5$/CdTe heterostructures, (B) TA spectral evolution over a time interval of 0–20 ps, and (C) decay kinetic trace and multiexponential fitting at probe wavelengths of 485 nm (blue) and 675 nm (red) with λ_{pump} = 360 nm.

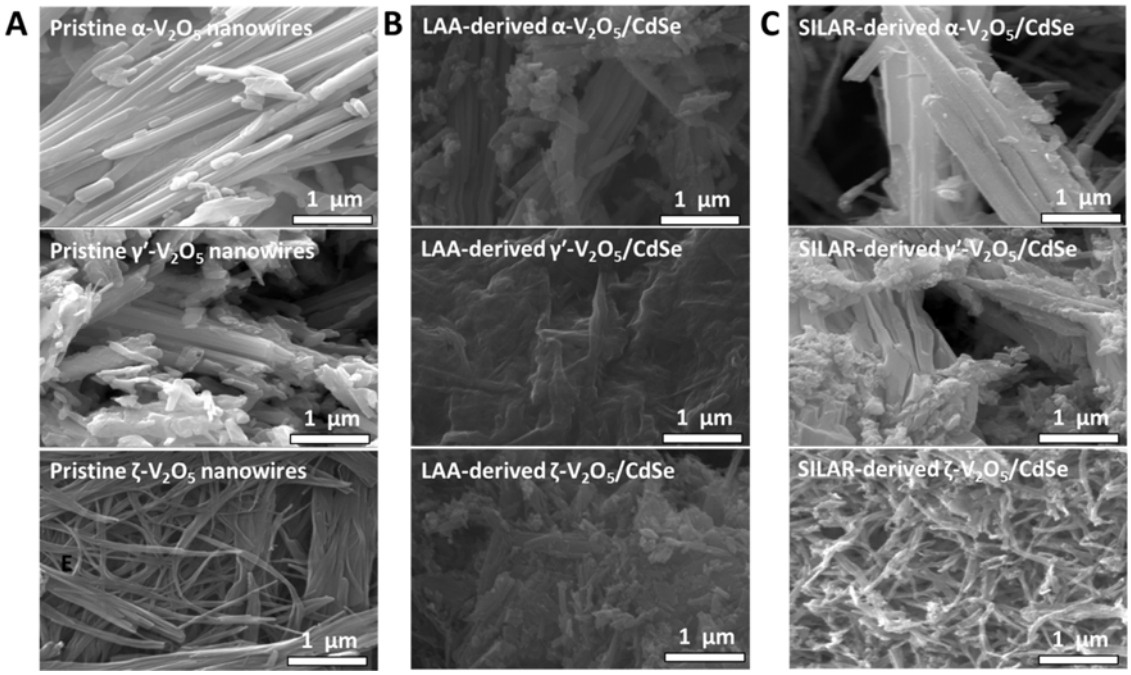

Figure A. 33 SEM images of (A) pristine V_2O_5 nanowires; (B) LAA-derived V_2O_5/CdSe heterostructures; and (C) SILAR-derived V_2O_5/CdSe heterostructures (top: α-V_2O_5, middle: γ'-V_2O_5, and bottom: ζ-V_2O_5).

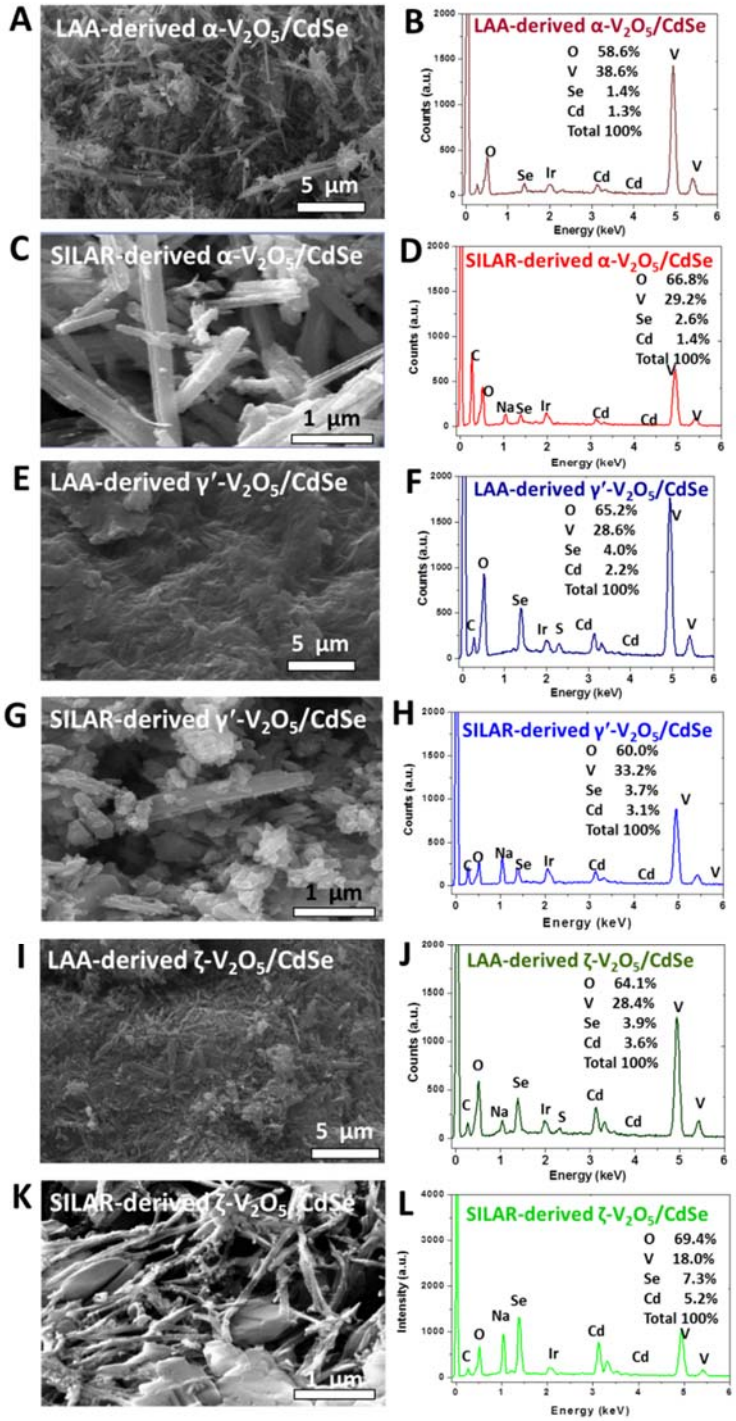

Figure A. 34 SEM images (left) and corresponding EDS spectra (right) obtained for (A, B) LAA-derived α-V_2O_5/CdSe; (C, D) SILAR-derived α-V_2O_5/CdSe; (E, F) LAA-derived γ′-V_2O_5/CdSe; (G, H) SILAR-derived γ′-V_2O_5/CdSe; (I, J) LAA-derived ζ-V_2O_5/CdSe; and (K, L) SILAR-derived ζ-V_2O_5/CdSe.

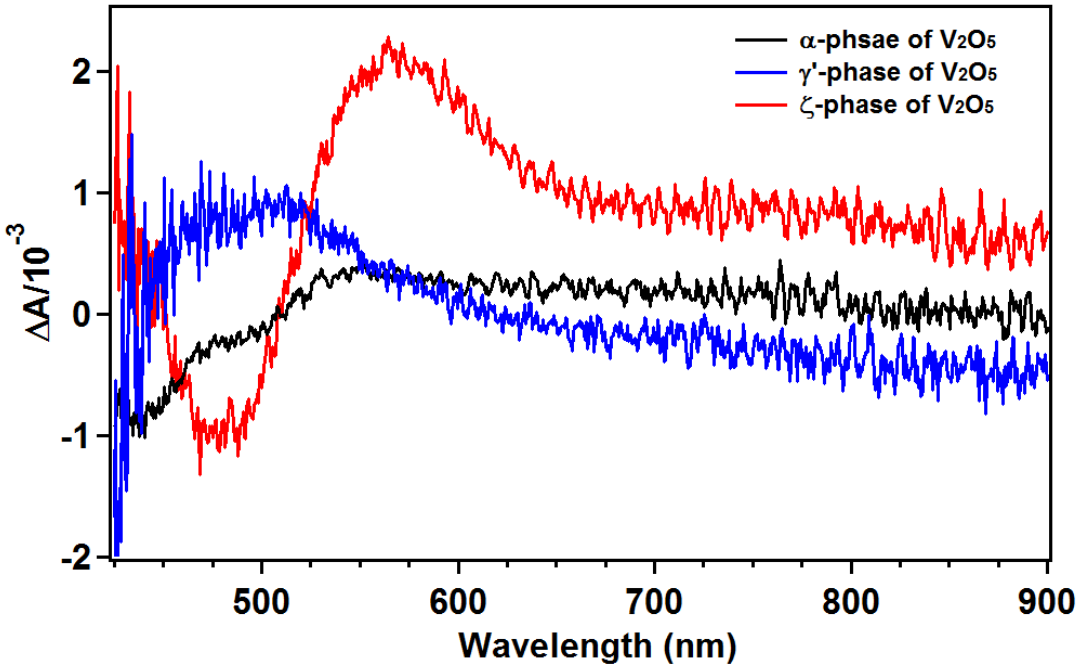

Figure A. 35 TA spectra acquired at 360 nm pump wavelength for α-, ζ- and γ'-V_2O_5 nanowires. The TA spectra have been averaged for delay times in the interval between 1.5—10 ns.

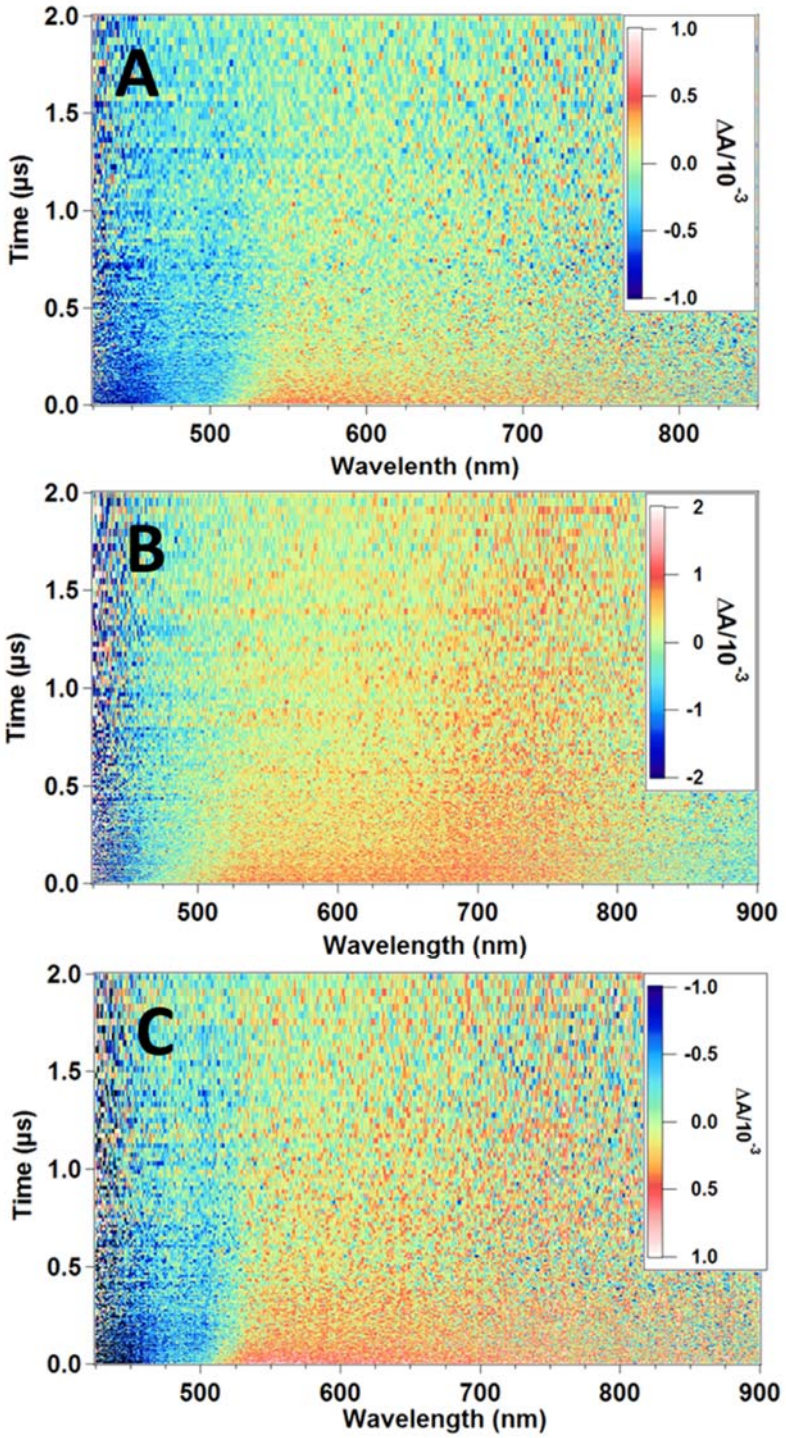

Figure A. 36 TA 3D color maps of (A) pristine α-V_2O_5 nanowires, (B) SILAR-derived α-V_2O_5/CdSe heterostructures, and (C) LAA-derived α-V_2O_5/CdSe heterostructures in the delay time range of 0-2 μs. Both heterostructures show longer-lived excited-states as compared to the pristine nanowires.

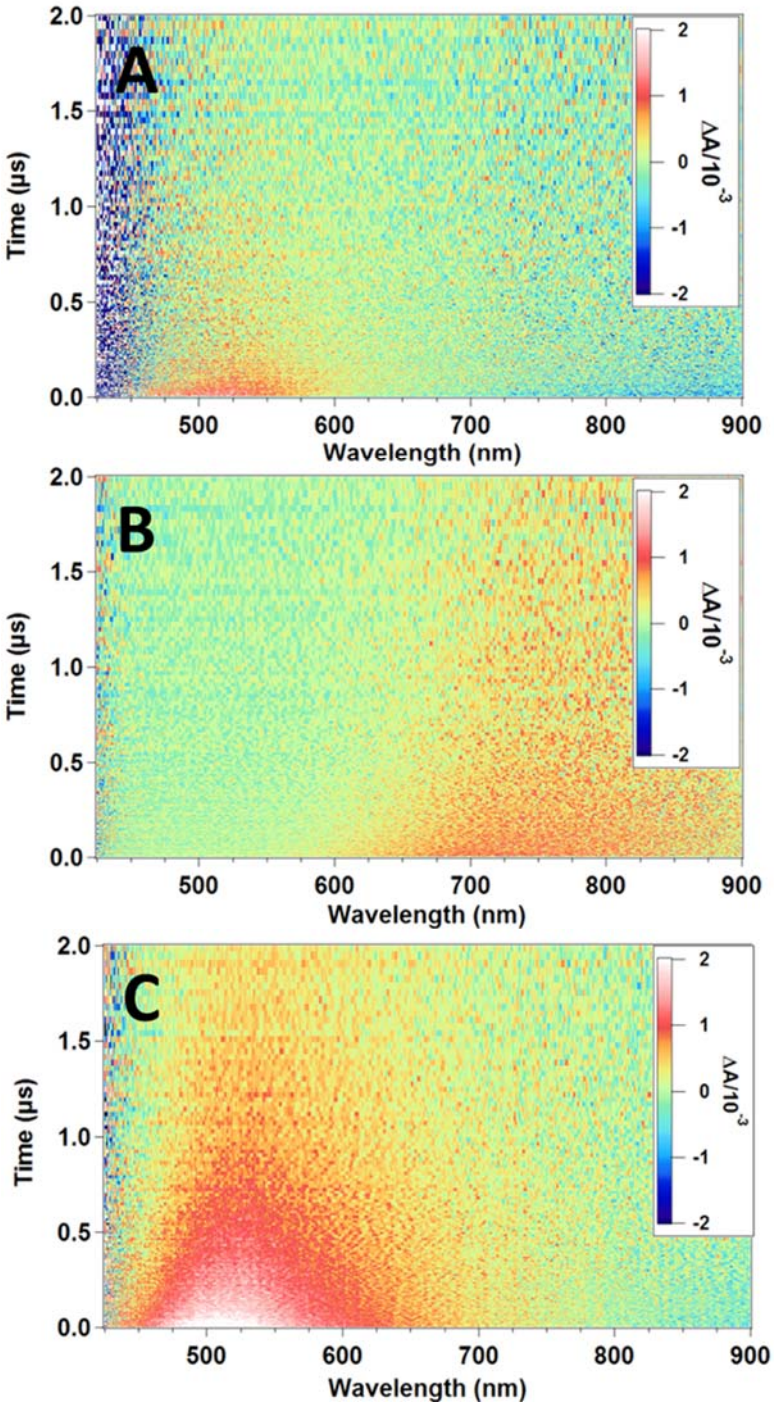

Figure A. 37 TA 3D color maps of (A) pristine γ′-V_2O_5 nanowires, (B) SILAR-derived γ′-V_2O_5/CdSe heterostructures, and (C) LAA-derived γ′-V_2O_5/CdSe heterostructures in the delay time range of 0-2 μs. Both heterostructures show considerably longer-lived excited-states as compared to the pristine nanowires.

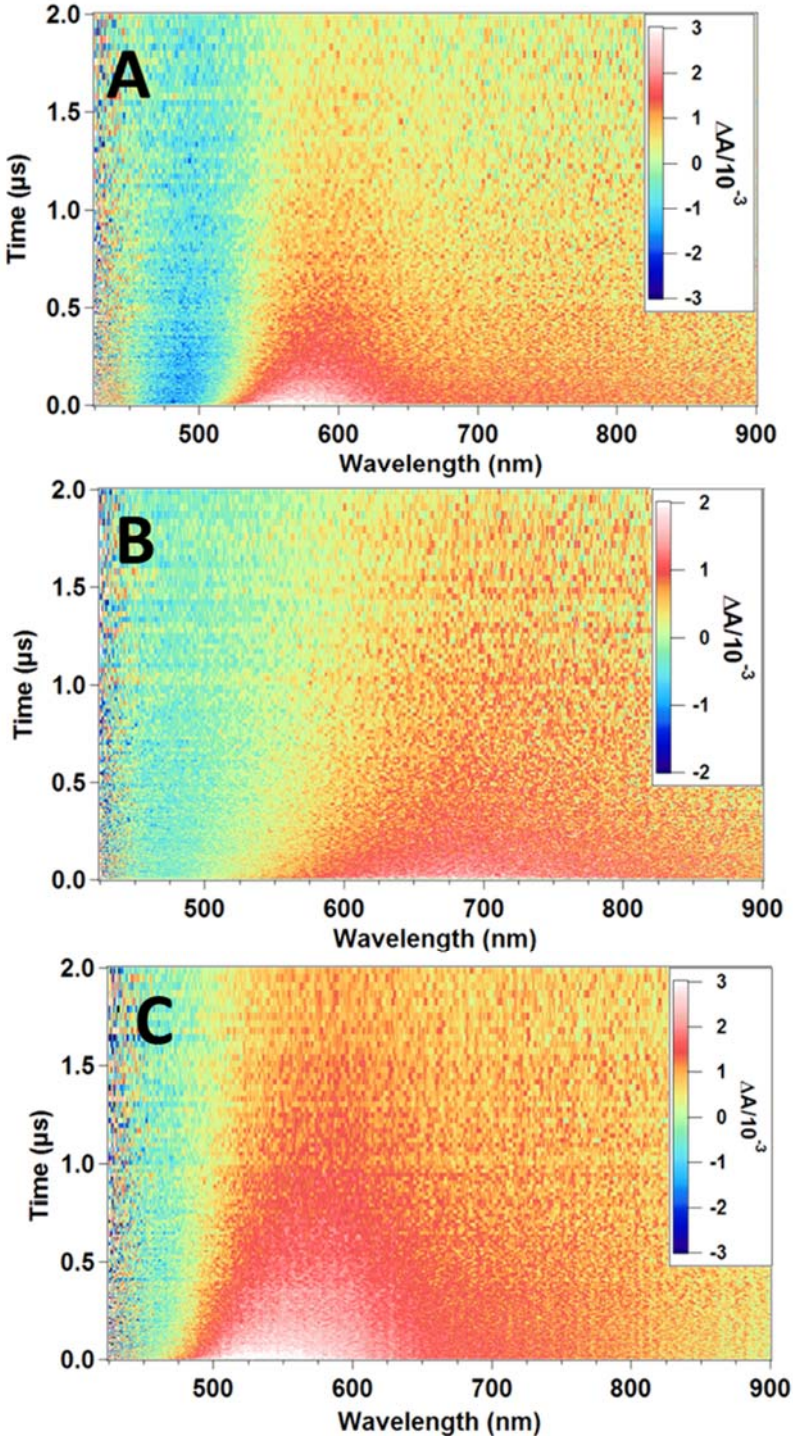

Figure A. 38 TA 3D color maps of (A) pristine ζ-V_2O_5 nanowires, (B) SILAR-derived ζ-V_2O_5/CdSe heterostructures, and (C) LAA-derived ζ-V_2O_5/CdSe heterostructures in the delay time range of 0-2 μs. Both heterostructures show longer-lived excited-states as compared to the pristine nanowires.

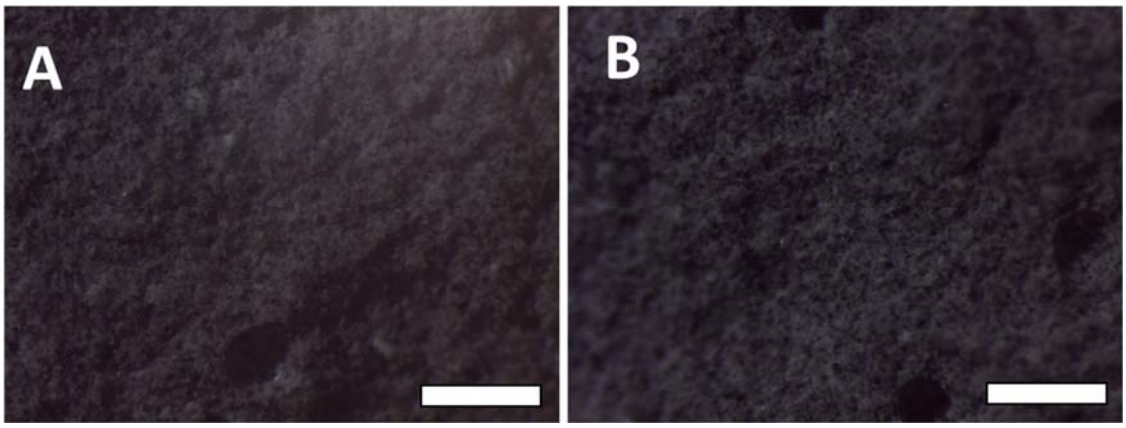

Figure A. 39 Stereomicroscopy Characterization of Modified Cement Nanocoposites. Stereomicroscopy images of modified cement nanocomposites incorporating a 2 wt.% loading of 2 wt.% of 4:1 polymer—fibrous additive ratio inclusions: (A) HNTs suspended in poly(acrylic acid) and (B) jute fibers suspended in poly(acrylic acid). Large voids spanning several hundred microns are discernible in both panels. Scale bar = 1 mm.

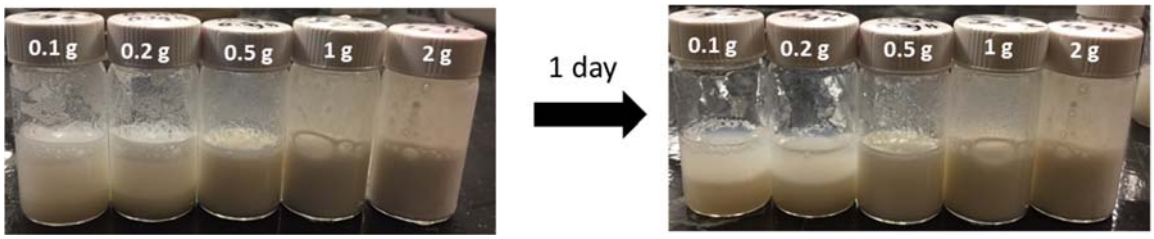

Figure A. 40 Colloidal Dispersion of HNT in Water in Aid of Hydroxyethylcellulose. Digital photographs of colloidal dispersions of HNTs dispersed in 10 mL water with the help of 0.5 g of hydroxylethylcellulose. The digital photographs in the left panel were taken immediately after mixing, whereas the panel on the right was photographed 24 h after mixing.

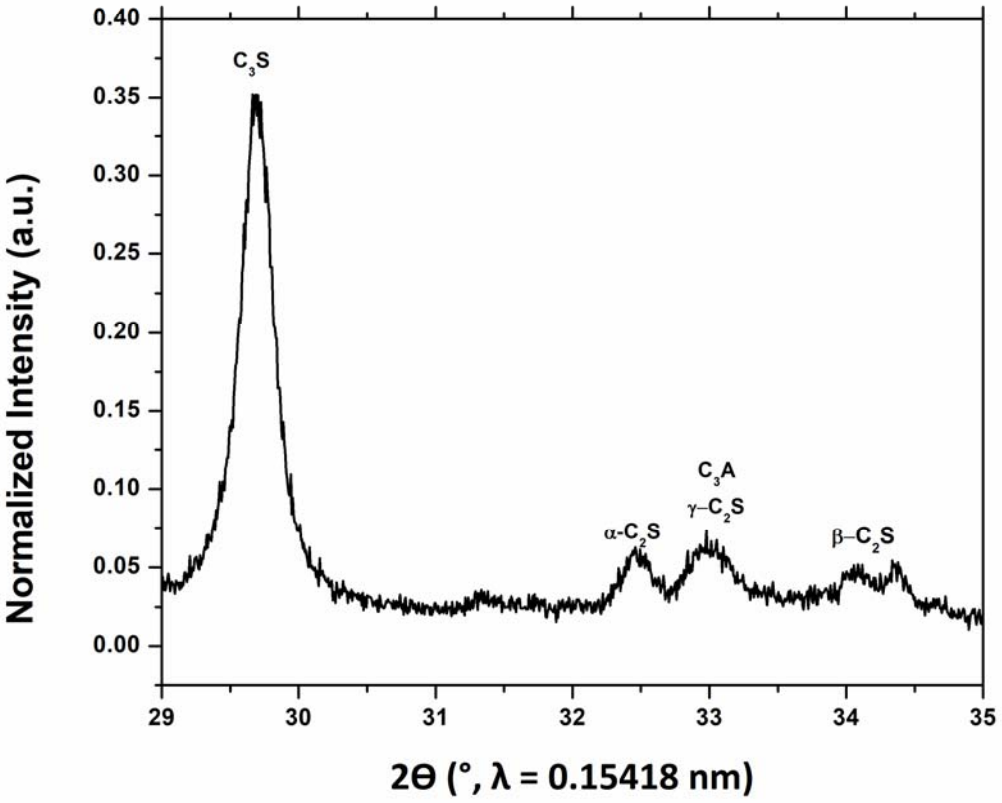

Figure A. **41** X-ray Diffraction Patterns of Cement. Magnified XRD pattern confirming the presence of four major phases of cement in the cured unmodified cement specimen.

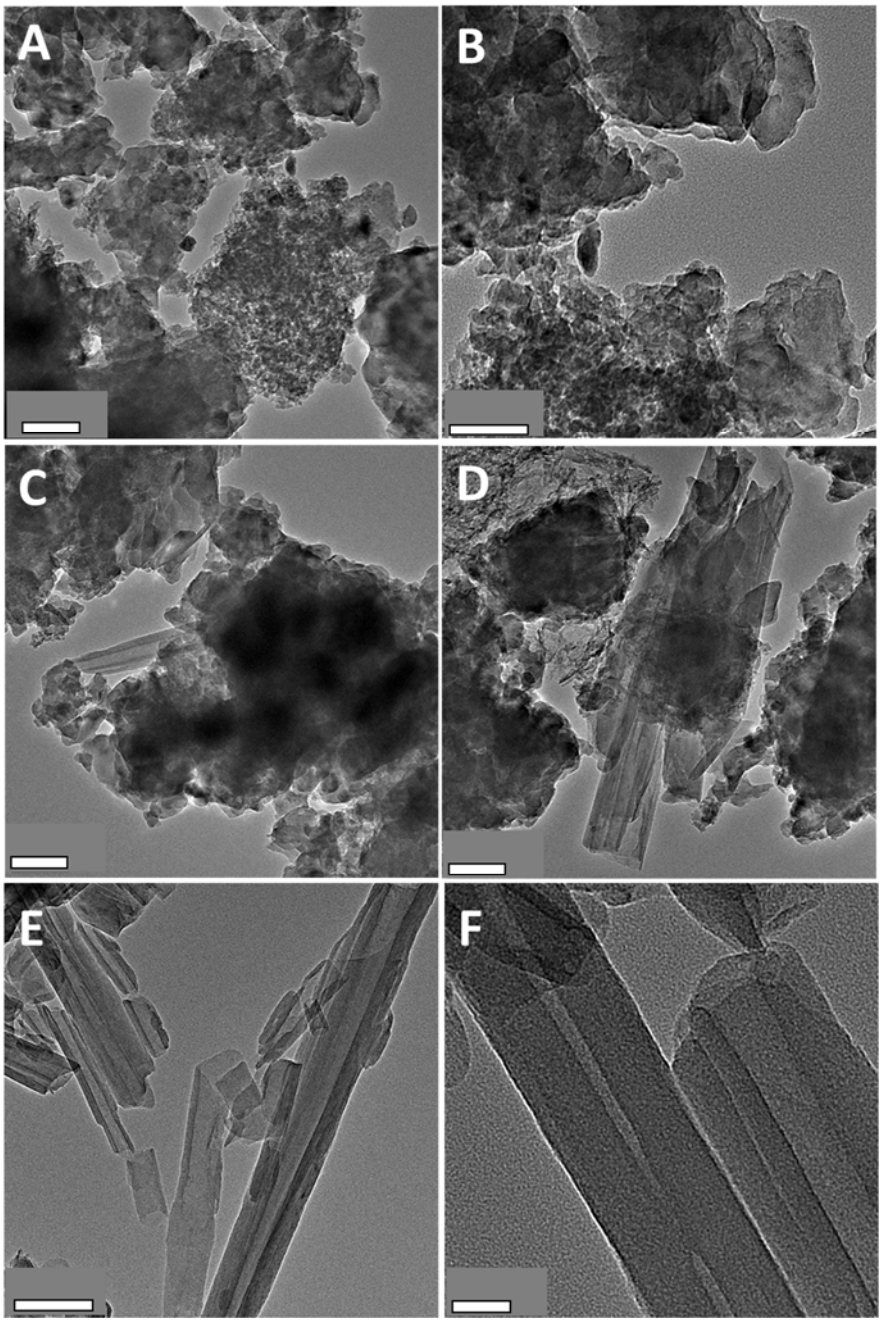

Figure A. 42 TEM Images of Cement Nanocomposites with Inclusion of Hydroxyethylcellulose-Modified HNTs. TEM images of A,B) unmodified cement and C,D) modified cement composites incorporating 2 wt.% of hydroxyethylcellulose-modified HNTs. E,F) TEM images of the HNT precursors. Scale bar = 100 nm for 4A,C,D,E; Scale bar = 50 nm for 4B; and Scale bar = 20 nm for 4F.

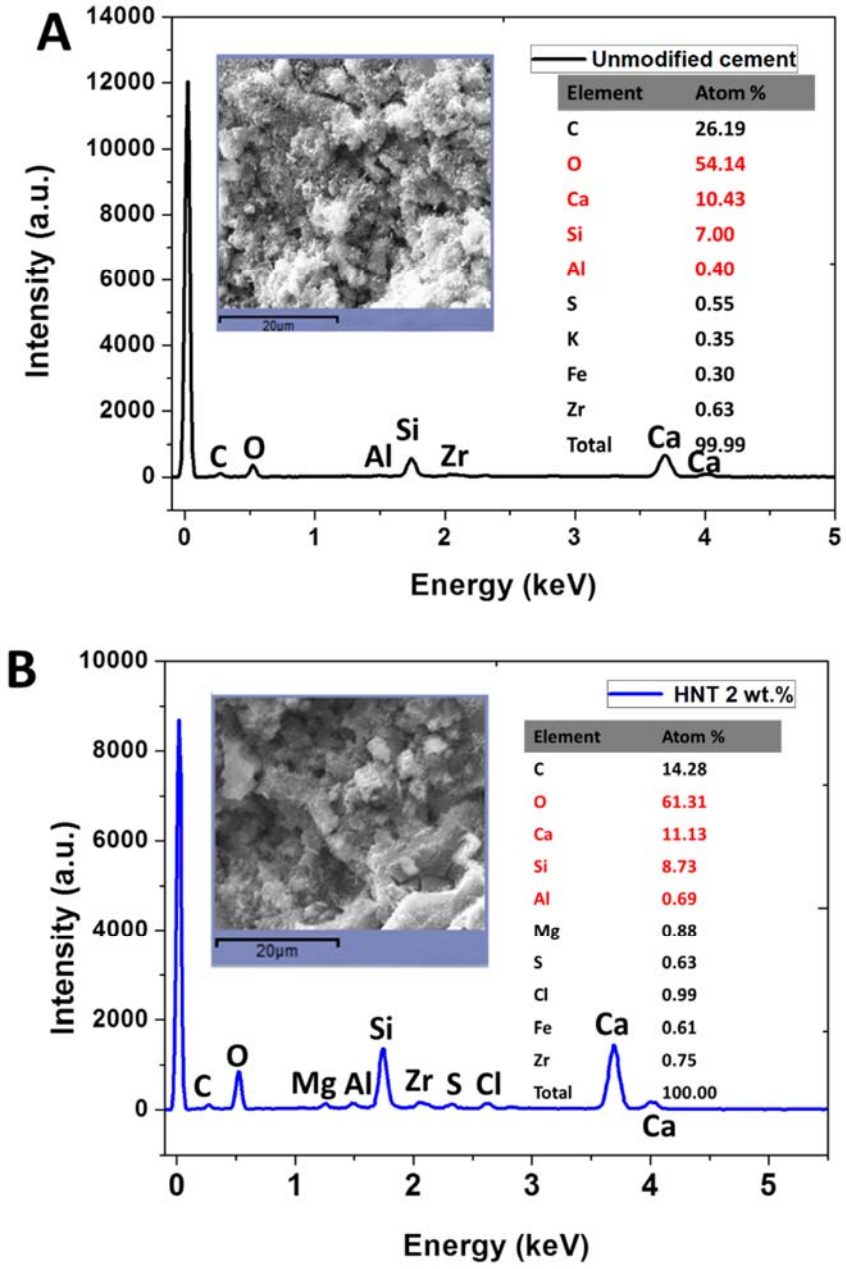

Figure A. 43 Elemental Analysis of Pristine Cement and Modified Cement Composites. EDS spectra of (A) an unmodified cement specimen and (B) a modified cement composite incorporating 2 wt.% of hydroxyethylcellulose-modified HNTs. The inset showed the SEM images of the samples measured and the table provided alongside lists the detailed elemental compositions in each case.

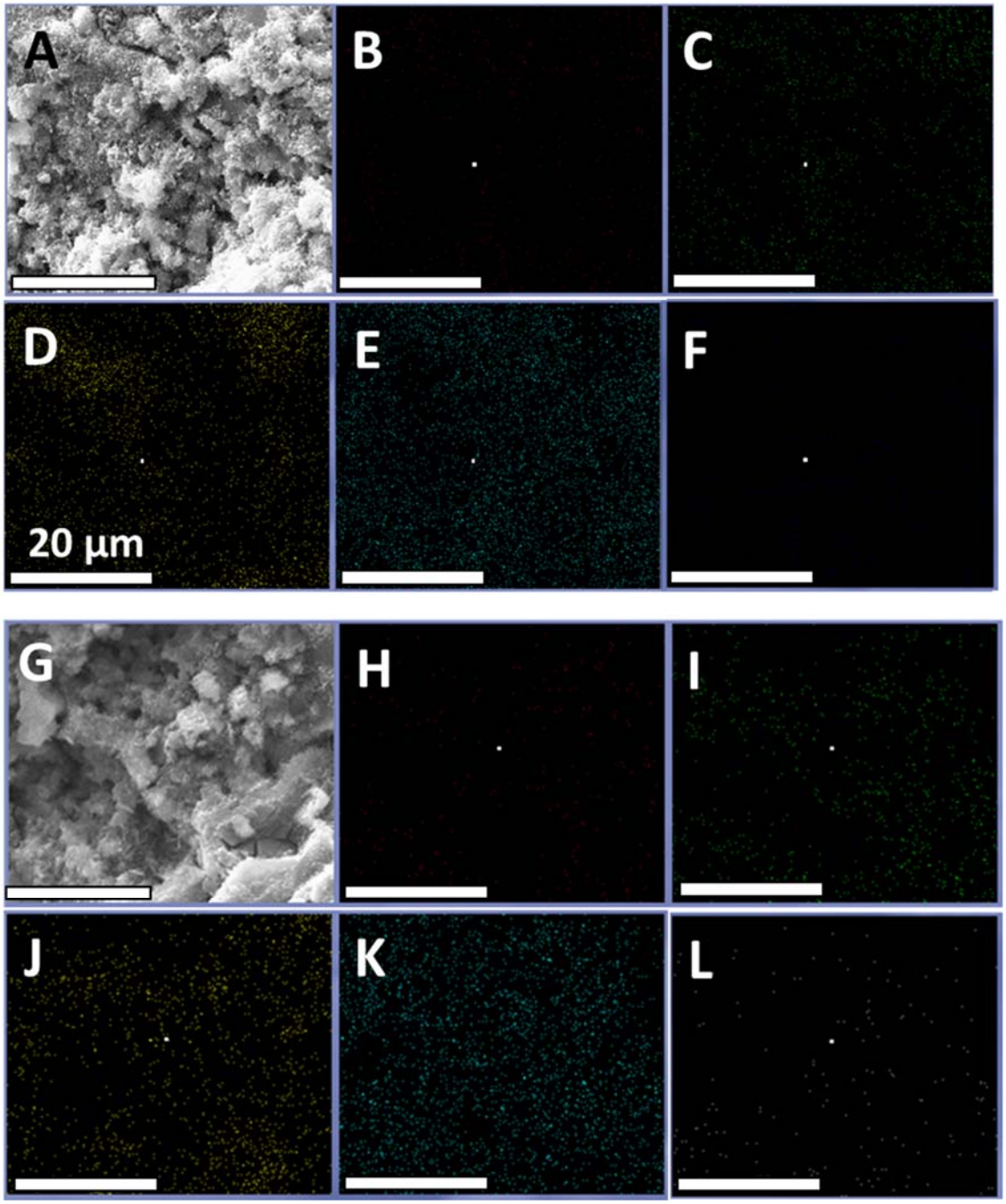

Figure A. 44 Homogenous Distribution of Elements in Modified Cement Nanocomposites. EDS elemental maps measured for A-F) unmodified cement and G-L) modified cement composite incorporating 2 wt.% of hydroxyethylcellulose-modified HNT: (A,G) SEM images, (B,H) C K-edge elemental maps (red); (C,I) O K-edge elemental maps (green); (D,J) Si K-edge elemental maps (yellow); (E,K) Ca K-edge elemental maps (cyan); (F,L) K K-edge elemental maps (grey). Scale bar = 20 µm.

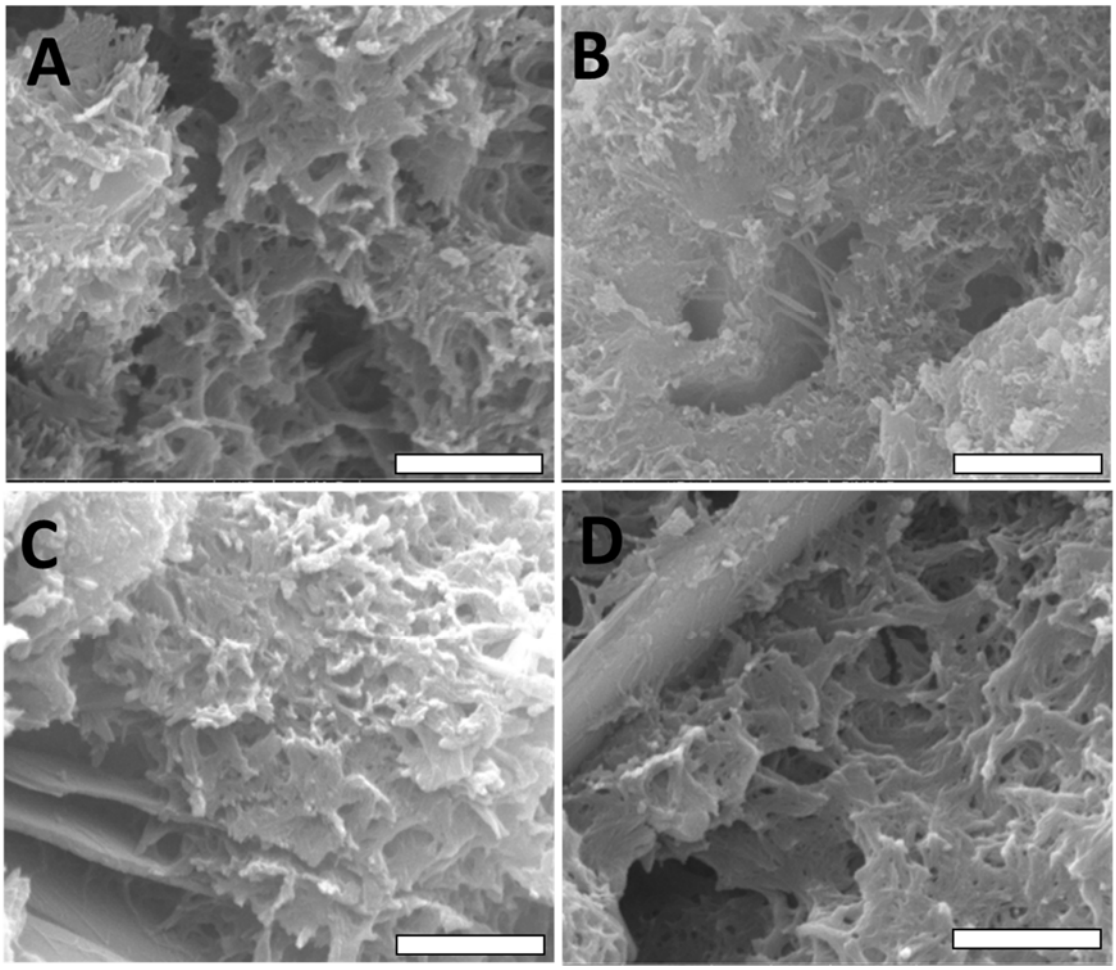

Figure A. 45 Microstructure Formation within Modified Cement Composites. SEM images of modified cement composites with varying loadings of hydroxyethylcellulose-modified HNTs at a fixed 4:1 stoichiometric ratio of HNTs: hydroxyethylcellulose: (A) 0.5 wt.%; (B) 1 wt.%; (C) 2 wt.%; and (D) 5 wt.%. Scale bar = 1 μm.

Unit cell layer number (n)	Emission maximum (nm), Experimental (*this paper*)	Emission maximum (nm), Ref. 18	Emission maximum (nm), Ref. 28	Emission maximum (nm), Ref. 50
1	433	427	-	442
2	450	454	-	-
3	474	469	-	456
4	485	482	475	482
5	490	490	490	492
6	505	-	504	-
∞	520	519	530	534

Table A. 1 PL emission maximum wavelength (nm) of 2D perovskite nanoplatelets and corresponding unit cell layer number (*n*) assignment obtained from Refs. 18 and 28.

Orthorhombic Fit: $CsPbBr_3$ (using C8 at 150°C)// Space Group: *Pnma* // Vol: 804.83(6) $Å^3$		
$\alpha = 90.000(0)°$	$\beta = 90.000(0)°$	$\gamma = 90.000(0)°$
$a = 8.2934\ (5)$	$b = 11.7941\ (4)$	$c = 8.2281(6)$
$\chi^2 = 5.809$	wRp = 0.1482	Rp = 0.1150

Table A. 2 Rietveld refinement parameters corresponding to the refinement of the power XRD pattern of $CsPbBr_3$ nanoplatelets obtained using C8 at 150°C as shown in Figure A. 7. Refinement statistics, including goodness of fit (χ^2), weighted goodness of fit (wRp) and the individual point residuals (Rp) show good agreement between the observed and calculated patterns. The orthorhombic structure provides a better fit to the diffraction data as compared to the cubic polymorph.

Thickness of nanoplatelts in terms of number of octahedra layers (*n*)	Experimental result based on emission maximum (nm), (*this paper*)	Emission maximum (nm), Ref. 18	Emission maximum (nm), Ref. 19	Emission maximum (nm), Ref. 29
1	406	-	405	-
2	430	-	435	-
3	458	438	462	452
4	475	450	477	478
5	490	459	488	489
6	505	-	-	-
Bulk	520	-	-	516

Table A. 3 PL emission maxima (nm) measured for 2D $CsPbBr_3$ nanoplatelets from single-particle PL emission spectroscopy experiments and assignments to layer thicknesses in terms of number of octahedral layers (*n*). The assignments are in good agreement with previous assignments available from Refs. 16 and 17.

Used Ligand chain length at reaction temperature	$n = 2$	$n = 3$	$n = 4$	$n = 5$	$n = 6$	$n =$ bulk	$n =$ bulk (larger species)
C4 at 150°C	-	461	479	493	-	520	546
C8 at 150°C	-	-	-	-	502	519	538
C12 at 150°C	435	460	476	491	-	516	539
C14 at 150°C	-	460	476	490	502	515	-
C18 at 150°C	-	462	477	489	502	516	-
C4 at 100°C	-	-	479	493	504	521	543
C8 at 100°C	432	461	477	491	-	515	-
C12 at 100°C	435	463	477	489	-	515	-
C14 at 100°C	433	458	476	490	506	-	-
C18 at 100°C	430	457	475	488	501	-	-
C4 at 50°C	-	452	470	487	-	515	-
C8 at 50°C	435	462	475	492	-	519	-
C12 at 50°C	432	455	475	489	-	510	-
C14 at 50°C	430	455	473	489	508	-	-
C18 at 50°C	433	453	476	488	-	510	-

Table A. 4 Deconvolution of PL emission spectra using Gaussian fitting results and emission peak position for different layer thickness (n = 1, 2, 3, 4, 5, 6, and bulk) at specific synthetic condition using various chain length amines at various temperature.

Table A. 5 Kinetic fitting parameters and calculated average lifetimes deduced from TA decay traces of colloidal CdS QD.

Sample	λ_{pump} (nm)	λ_{probe} (nm)	ΔA_0	C_1	τ_1 (ns)	C_2	τ_2 (ns)	$<\tau>$ (ns)	χ^2
Cys-CdS	360	440	-0.09 (±0.01)	-0.43 (±0.04)	20 (±10)	-0.35 (±0.02)	500 (±90)	230 (±45)	1.68
Cys-CdS	360	700	0.04 (±0.01)	0.33 (±0.26)	570 (±110)	0.46 (±0.03)	30 (±5)	250 (±210)	1.37

Table A. 6 Kinetic fitting parameters and calculated average lifetimes for TA decay traces of LAA-derived CdS QD/β-$Pb_{0.33}V_2O_5$ NW heterostructures.

Sample	λ_{pump} (nm)	λ_{probe} (nm)	ΔA_0	C_1	τ_1 (ps)	C_2	τ_2 (ps)	$<\tau>$ (ps)	χ^2	Non-resolvable Signal	Time-Resolvable Signal
Cys-CdS/β-$Pb_{0.33}V_2O_5$	360	455	-0.18 (±0.01)	0.49 (±0.09)	10.5 (±0.8)	0.51 (±0.08)	0.46 (±0.09)	5.4(±1.1)	0.015	-	-
Cys-CdS/β-$Pb_{0.33}V_2O_5$	360	600	1.13 (±0.01)	1.00 (±0.07)	5.3 (±0.7)	-	-	5.3 (±0.8)	0.127	76.3 %	23.7 %
Cys-CdS/β-$Pb_{0.33}V_2O_5$	360	740	1.01 (±0.01)	1.00 (±0.05)	5.1 (±0.5)	-	-	5.1 (±0.6)	0.117	68.3 %	31.7 %

Table A. 7 Kinetic fitting parameters and calculated average lifetimes for picoseond TA decay traces of β-$Sn_xV_2O_5$/CdSe and β-$Sn_xV_2O_5$/CdTe heterostructures.

Sample	λ_{pump} (nm)	λ_{probe} (nm)	ΔA_0	A_1	τ_1 (ps)	A_2	τ_2 (ps)	$<\tau>$ (ps)	χ^2
β-$Sn_xV_2O_5$/CdSe	360	485	-0.124 (±0.007)	-3.228 (±0.242)	0.248 (±0.012)	-0.156 (±0.016)	3.671 (±0.770)	0.406 (±0.053)	0.132
β-$Sn_xV_2O_5$/CdSe	360	525	0.968 (±0.009)	-5.110 (±0.433)	0.221 (±0.017)	-0.252 (±0.074)	1.925 (±0.655)	0.301 (±0.052)	1.082

β-$Sn_xV_2O_5$/CdTe	360	485	-0.023 (±0.004)	-0.734 (±0.013)	1.113 (±0.043)	-0.318 (±0.013)	11.77 (±0.835)	4.33 (±0.301)	0.123
β-$Sn_xV_2O_5$/CdTe	360	675	0.786 (±0.011)	-0.878 (±0.196)	2.222 (±0.443)	-0.248 (±0.203)	8.389 (±5.29)	3.578 (±0.811)	1.379

Table A. 8 Kinetic fitting parameters and calculated average lifetimes for nanosecond TA decay traces of individual V_2O_5 nanowires and SILAR-derived and LAA-derived V_2O_5/CdSe heterostructures.

Sample	**λ_{pump} (nm)**	**λ_{probe} (nm)**	**ΔA_0**	**A_1**	**τ_1 (μs)**	**A_2**	**τ_2 (μs)**	**$<\tau>$ (μs)**	**χ^2**
α-phase V_2O_5	360	550	-0.108 (±0.008)	0.599 (±0.069)	0.019 (±0.035)	0.629 (±0.037)	0.284 (±0.026)	0.155 (±0.025)	1.665
LAA-α-V_2O_5/CdSe	360	565	-0.026 (±0.009)	0.585 (±0.046)	0.058 (±0.009)	0.409 (±0.046)	0.585 (±0.098)	0.275 (±0.052)	1.641
SILAR-α-V_2O_5/CdSe	360	725	0.098 (±0.022)	0.205 (±0.044)	0.076 (±0.037)	0.568 (±0.032)	1.698 (±0.263)	1.266 (±0.224)	3.341
γ'-phase V_2O_5	360	520	-0.010 (±0.010)	0.609 (±0.050)	0.076 (±0.050)	0.295 (±0.051)	0.705 (±0.182)	0.281 (±0.078)	1.836
LAA-γ'-V_2O_5/CdSe	360	525	0.055 (±0.003)	0.205 (±0.011)	0.075 (±0.009)	0.674 (±0.010)	0.979 (±0.028)	0.768 (±0.027)	0.145
SILAR-γ'-V_2O_5/CdSe	360	725	0.094 (±0.012)	0.264 (±0.030)	0.058 (±0.015)	0.559 (±0.020)	1.372 (±0.123)	0.950 (±0.099)	1.299
ζ-phase V_2O_5	360	580	0.003 (±0.003)	0.406 (±0.014)	0.119 (±0.008)	0.529 (±0.014)	1.151 (±0.050)	0.703 (±0.036)	0.155
LAA-ζ-V_2O_5/CdSe	360	570	0.065 (±0.006)	0.266 (±0.016)	0.246 (±0.022)	0.624 (±0.014)	2.072 (±0.096)	1.527 (±0.084)	0.130
SILAR-ζ-V_2O_5/CdSe	360	700	0.070 (±0.009)	0.341 (±0.017)	0.103 (±0.012)	0.514 (±0.014)	1.842 (±0.132)	1.148 (±0.089)	0.477